

Clemson University

**TigerPrints**

---

All Dissertations

Dissertations

---

December 2020

## Nonlinear Modeling and Control of Driving Interfaces and Continuum Robots for System Performance Gains

Chengshi Wang

*Clemson University*, [chengsw@g.clemson.edu](mailto:chengsw@g.clemson.edu)

Follow this and additional works at: [https://tigerprints.clemson.edu/all\\_dissertations](https://tigerprints.clemson.edu/all_dissertations)

---

### Recommended Citation

Wang, Chengshi, "Nonlinear Modeling and Control of Driving Interfaces and Continuum Robots for System Performance Gains" (2020). *All Dissertations*. 2720.

[https://tigerprints.clemson.edu/all\\_dissertations/2720](https://tigerprints.clemson.edu/all_dissertations/2720)

This Dissertation is brought to you for free and open access by the Dissertations at TigerPrints. It has been accepted for inclusion in All Dissertations by an authorized administrator of TigerPrints. For more information, please contact [kokeefe@clemson.edu](mailto:kokeefe@clemson.edu).

NONLINEAR MODELING AND CONTROL OF DRIVING INTERFACES AND  
CONTINUUM ROBOTS FOR SYSTEM PERFORMANCE GAINS

---

A Dissertation  
Presented to  
the Graduate School of  
Clemson University

---

In Partial Fulfillment  
of the Requirements for the Degree  
Doctor of Philosophy  
Mechanical Engineering

---

by  
Chengshi Wang  
December 2020

---

Accepted by:  
Dr. John R. Wagner, Committee Chair  
Dr. Yue Wang  
Dr. Ian D. Walker  
Dr. Todd Schweisinger

## ABSTRACT

With the rise of (semi)autonomous vehicles and continuum robotics technology and applications, there has been an increasing interest in controller and haptic interface designs. The presence of nonlinearities in the vehicle dynamics is the main challenge in the selection of control algorithms for real-time regulation and tracking of (semi)autonomous vehicles. Moreover, control of continuum structures with infinite dimensions proves to be difficult due to their complex dynamics plus the soft and flexible nature of the manipulator body. The trajectory tracking and control of automobile and robotic systems requires control algorithms that can effectively deal with the nonlinearities of the system without the need for approximation, modeling uncertainties, and input disturbances. Control strategies based on a linearized model are often inadequate in meeting precise performance requirements. To cope with these challenges, one must consider nonlinear techniques. Nonlinear control systems provide tools and methodologies for enabling the design and realization of (semi)autonomous vehicle and continuum robots with extended specifications based on the operational mission profiles. This dissertation provides an insight into various nonlinear controllers developed for (semi)autonomous vehicles and continuum robots as a guideline for future applications in the automobile and soft robotics field. A comprehensive assessment of the approaches and control strategies, as well as insight into the future areas of research in this field, are presented.

First, two vehicle haptic interfaces, including a robotic grip and a joystick, both of which are accompanied by nonlinear sliding mode control, have been developed and studied on a steer-by-wire platform integrated with a virtual reality driving environment.

An operator-in-the-loop evaluation that included 30 human test subjects was used to investigate these haptic steering interfaces over a prescribed series of driving maneuvers through real time data logging and post-test questionnaires. A conventional steering wheel with a robust sliding mode controller was used for all the driving events for comparison. Test subjects operated these interfaces for a given track comprised of a double lane-change maneuver and a country road driving event. Subjective and objective results demonstrate that the driver's experience can be enhanced up to 75.3% with a robotic steering input when compared to the traditional steering wheel during extreme maneuvers such as high-speed driving and sharp turn (e.g., hairpin turn) passing.

Second, a cellphone-inspired portable human-machine-interface (HMI) that incorporated the directional control of the vehicle as well as the brake and throttle functionality into a single holistic device will be presented. A nonlinear adaptive control technique and an optimal control approach based on driver intent were also proposed to accompany the mechatronic system for combined longitudinal and lateral vehicle guidance. Assisting the disabled drivers by excluding extensive arm and leg movements ergonomically, the device has been tested in a driving simulator platform. Human test subjects evaluated the mechatronic system with various control configurations through obstacle avoidance and city road driving test, and a conventional set of steering wheel and pedals were also utilized for comparison. Subjective and objective results from the tests demonstrate that the mobile driving interface with the proposed control scheme can enhance the driver's performance by up to 55.8% when compared to the traditional driving system during aggressive maneuvers. The system's superior performance during certain



vehicle maneuvers and approval received from the participants demonstrated its potential as an alternative driving adaptation for disabled drivers.

Third, a novel strategy is designed for trajectory control of a multi-section continuum robot in three-dimensional space to achieve accurate orientation, curvature, and section length tracking. The formulation connects the continuum manipulator dynamic behavior to a virtual discrete-jointed robot whose degrees of freedom are directly mapped to those of a continuum robot section under the hypothesis of constant curvature. Based on this connection, a computed torque control architecture is developed for the virtual robot, for which inverse kinematics and dynamic equations are constructed and exploited, with appropriate transformations developed for implementation on the continuum robot. The control algorithm is validated in a realistic simulation and implemented on a six degree-of-freedom two-section OctArm continuum manipulator. Both simulation and experimental results show that the proposed method could manage simultaneous extension/contraction, bending, and torsion actions on multi-section continuum robots with decent tracking performance (e.g. steady state arc length and curvature tracking error of 3.3mm and  $130\text{mm}^{-1}$ , respectively).

Last, semi-autonomous vehicles equipped with assistive control systems may experience degraded lateral behaviors when aggressive driver steering commands compete with high levels of autonomy. This challenge can be mitigated with effective operator intent recognition, which can configure automated systems in context-specific situations where the driver intends to perform a steering maneuver. In this article, an ensemble learning-based driver intent recognition strategy has been developed. A nonlinear model

predictive control algorithm has been designed and implemented to generate haptic feedback for lateral vehicle guidance, assisting the drivers in accomplishing their intended action. To validate the framework, operator-in-the-loop testing with 30 human subjects was conducted on a steer-by-wire platform with a virtual reality driving environment. The roadway scenarios included lane change, obstacle avoidance, intersection turns, and highway exit. The automated system with learning-based driver intent recognition was compared to both the automated system with a finite state machine-based driver intent estimator and the automated system without any driver intent prediction for all driving events. Test results demonstrate that semi-autonomous vehicle performance can be enhanced by up to 74.1% with a learning-based intent predictor. The proposed holistic framework that integrates human intelligence, machine learning algorithms, and vehicle control can help solve the driver-system conflict problem leading to safer vehicle operations.

## DEDICATION

I dedicate this dissertation to my parents, and my sister, who supported me to pursue my doctoral degree and inspired me to be good. This dissertation is also dedicated to my niece Isla, who is the most beautiful baby girl in the world.

## ACKNOWLEDGMENTS

I would like to express the deepest appreciation to my committee chair Dr. John Wagner, who has the attitude and the substance of a genius: he continually and convincingly conveyed a spirit of adventure in regard to research and scholarship. Dr. Wagner's expertise was invaluable in the formulating of the research topic and methodology in particular. Without his guidance and persistent help this dissertation would not have been possible.

Besides my advisor, I would like to thank the rest of my dissertation committee members (Dr. Todd Schweisinger, Dr. Ian D. Walker, and Dr. Yue Wang) for their great support and invaluable advice. I would like to thank my committee member, Dr. Yue Wang an expert in human robot interaction (HRI) system, for her crucial remarks that shaped my final dissertation. In addition, a thank you to Dr. Todd Schweisinger, for providing me with opportunities to teach undergraduate courses, an experience which truly shaped me as a scholar and prepared me for future academic endeavors. I would particularly like to single out my committee member Dr. Ian D. Walker, who introduced me to the robotics. I want to thank you for your guidance and for all the opportunities I was given to conduct research on the control of continuum robots and further my dissertation.

Last but not least, I would like to express my deepest gratitude to my family and friends. This dissertation would not have been possible without their warm love, continued patience, and endless support.

## TABLE OF CONTENTS

	Page
TITLE PAGE .....	i
ABSTRACT.....	ii
DEDICATION .....	vi
ACKNOWLEDGEMENTS .....	vii
LIST OF TABLES .....	xi
LIST OF FIGURES .....	xiii
CHAPTER	
I. INTRODUCTION .....	1
1.1 Dynamic Systems.....	2
1.2 Model and Control Strategies .....	6
1.3 Dissertation Objectives .....	11
1.4 Innovation .....	12
1.5 Proposal Organization.....	14
II. EVALUATION OF ALTERNATIVE STEERING DEVICES WITH ADJUSTABLE HAPTIC FEEDBACK FOR SEMI- AUTONOMOUS AND AUTONOMOUS VEHICLES.....	15
2.1 Introduction.....	16
2.2 Steering System Model .....	21
2.3 Steering System Control Design .....	25
2.4 Hardware-in-the-Loop Platform .....	29
2.5 Operator-in-the-Loop Evaluation.....	31
2.6 Conclusion .....	38
III. EVALUATION OF ROBUST HAPTIC INTERFACE FOR SEMI- AUTONOMOUS VEHICLES.....	40
3.1 Introduction.....	41
3.2 Steering System Model .....	47
3.3 Control System Design .....	50

## Table of Contents (Continued)

	Page
3.4 Operator-in-Loop Evaluation.....	54
3.5 Conclusion .....	75
IV. USE OF CELLPHONE AS ALTERNATIVE DRIVER INPUTS IN PASSENGER VEHICLES .....	78
4.1 Introduction.....	79
4.2 Cellphone Vehicle Control .....	83
4.3 Vehicle Dynamics .....	85
4.4 Control Strategies for Portable HMI.....	90
4.5 Experimental Methods .....	100
4.6 Test Results .....	103
4.7 Conclusion and Future Study.....	119
V. DYNAMIC CONTROL OF MULTI-SECTION THREE- DIMENSIONAL CONTINUUM MANIPULATORS BASED ON VIRTUAL DISCRETE-JOINTED ROBOT MODELS .....	121
5.1 Introduction.....	122
5.2 Mathematical Model .....	127
5.3 Control Systems Design.....	132
5.4 Controller Simulation Results.....	135
5.5 Experiential Implementation.....	137
5.6 Conclusion .....	150
VI. HAPTIC ASSISTIVE CONTROL WITH LEARNING BASED DRIVER INTENT RECOGNITION FOR SEMI-AUTONOMOUS VEHICLES .....	153
6.1 Introduction.....	154
6.2 Vehicle Dynamics .....	158
6.3 Vehicle Control Methodologies.....	160
6.4 Driver Intent Recognition .....	166
6.5 Experimental Results and Discussion.....	179
6.6 Conclusion .....	190
APPENDICES .....	192
A. Publication List (As First Author) .....	192

Table of Contents (Continued)

	Page
REFERENCES .....	193

## LIST OF TABLES

Table	Page
2.1 Comparison of ground vehicle steering device functionality assuming a steer-by-wire configuration.....	20
2.2 Summary of hardware and model parameters .....	32
2.3 Summary of steering device and feedback conditions.....	34
2.4 Average performance improvement for alternative devices when compared with traditional steering wheel (C2).....	37
3.1 Average of all N=30 human subjects heading error, lateral error, and lateral acceleration results for three steering configurations, C1-C3, at 50 and 80 kph (highest value highlighted in bold, lowest value is underlined). Note that $e_{HRMS}$ , $e_{LRMS}$ and $\ddot{y}_{RMS}$ are the root mean square values, while $e_{Hmax}$ , $e_{Lmax}$ and $\ddot{y}_{max}$ are the maximum values for test subjects .....	67
3.2 ANOVA results for road course lateral error and questionnaire responses on confidence level; bold entries indicate statistically significant results. ....	73
4.1 Comparison of traditional steering wheel and cellphone functionality assuming a drive-by-wire configuration. ....	82
4.2 Summary of vehicle and control model parameters. ....	90
4.3 Summary of driver averaged performance for 15 subjects with cellphone device and steering wheel on city roadway. Note that $e_{HRMS}$ , and $e_{LRMS}$ are the root mean square values, while $e_{HMAX}$ , $e_{LMAX}$ are the maximum values for test subjects (lower values in bold font).....	116
5.1 Link Parameters for Virtual RRPR Robot Manipulator .....	129
6.1 Vehicle Operating variables and driver behavior indicators with corresponding feature code. ....	169



## List of Tables (Continued)

Table	Page
6.2 Average of all $N = 25$ human subjects' lateral acceleration $\dot{v}_y$ , applied human force $F_H$ , and intent recognition accuracy $R\%$ for driving configurations, C1-C3, on highway scenario. Note that the bar represents the RMS value, while subscript $max$ is the maximum value.....	182
6.3 Average of all $N = 25$ human subjects' lateral acceleration $\dot{v}_y$ , applied human force $F_H$ , intent recognition accuracy $R\%$ , and lateral error $e_y$ for driving configurations, C1-C3, on city road scenario. Note that the bar represents the RMS value, while subscript $max$ is the maximum value.....	187

## LIST OF FIGURES

Figure	Page
1.1 Four Research Thrust Areas Identified .....	2
1.2 Parameter and Variable Definitions For The Vehicle Model. ....	4
1.3 Three-Dimensional Constant Curvature Section Geometry Obtained Via Rotation About Initial Tangent Based on Virtual RRPR Discrete-Jointed Robot Model. ....	6
1.4 Laboratory Driving Simulator Schematic .....	12
2.1 Top view of vehicle configurations - (a) standard with five seats; and (b) autonomous with two benches .....	18
2.2 Close-loop system design for human/machine steering interface.....	21
2.3 Diagram to illustrate vehicle body forces .....	22
2.4 Single wheel with applied longitudinal and lateral tire forces, as well as tire rotation .....	24
2.5 Block diagram of classical controller for vehicle lane keeping .....	26
2.6 Hardware-in-the-loop haptic interface schematic .....	31
2.7 Haptic steering visualization environment - (a) straight highway; and (b) country road.....	33
2.8 Lateral RMS error for cases C1 to C5 - (a) Highway at low speed (50kph), (b) Highway at high speed(100kph), (c) Country road at low speed (50kph), (d) Country road at high speed (100kph) .....	38
3.1 Progression pathway of steering devices for ground vehicles along the SAE autonomy level; emergency operation of level 4 and 5 vehicles accommodated with a “plug & play” steering interface .....	42
3.2 Haptic steering device operation map - (a) steering wheel with brake and acceleration pedals, (b) joystick, (c) robotic grip.....	46
3.3 Closed-loop system design for human/machine steering interface.....	47

## List of Figures (Continued)

Figure	Page
3.4 Diagram to illustrate vehicle chassis dynamics .....	49
3.5 Sliding mode and classical control structures for vehicle lane keeping controllers .....	51
3.6 Lane keeping control system kinematics .....	52
3.7 Operator with robotic haptic interface .....	55
3.8 Virtual roadway with (a) lane change, and (b) slalom test. ....	57
3.9 ISO 3888-1 double-lane-change maneuver test track .....	58
3.10 Double lane change simulator scene in software animation .....	59
3.11 Human subject #16 data for three steering configurations, C1-C3, during a double-lane-change maneuver starting at 50kph- (a) vehicle trajectories, (b) steer angle, (c) lateral position error, (d) front tire slip angle, and (e) rear tire slip angle.....	62
3.12 Human subject #22 data for three steering configurations, C1-C3, during the winding country road scenario at 50 and 80kph: (a, d) steer angle, (b, e) heading error, and (c,f) lateral error. ....	63
3.13 Human subject #22 data for three steering configurations, C1-C3, during country road driving at 80kph- (a) front, and (b) rear tire slip angles.....	66
3.14 Snapshot of the vehicle on the slalom course .....	69
3.15 Human subject #16 data for three steering configurations, C1-C3, during a slalom maneuver starting at 50kph, (a) vehicle trajectories, and (b) yaw rate vs steer angle, the red asterisks represent slalom test marking cones. ....	70
3.16 Nine subjective measures for three steering devices based on human subjects' responses to the questionnaire in Table B1 normalized to 10.....	72
4.1 Evaluation of vehicle control – traditional steering wheel w/ brake and throttle pedal to cellphone.....	80

## List of Figures (Continued)

Figure	Page
4.2	Cellphone driving device with Arduino sensor support. .... 84
4.3	Parameter definitions for the vehicle model. .... 85
4.4	(a) Conventional hydraulic steering system with steering wheel, and (b) Steer-by-wire steering system with cellphone. .... 88
4.5	Lateral control design featuring feedforward and feedback actions embedded in the portable HMI ..... 94
4.6	Variable Steering ratio feedforward control: (a) Steering ratio of full- speed section varies with speed, (b) Corner correction factor change with the portable HMI steer angle, and (c) The corrected steering ratio with the vehicle speed and mobile control interface angle changes. .... 95
4.7	(a) Firing Conditions for three driver intention states: lane keeping, obstacle avoidance, and cornering/turning, and (b) Logic flow for the SF braking control; controller state transitions based on comparison of vehicle states with firing condition ..... 100
4.8	Driving simulator driving scene using cellphone. .... 101
4.9	Fixed-base driving simulator schematic ..... 102
4.10	Bandwidth test for driving controllers – (a) Steering wheel, (b) Cellphone. .... 105
4.11	(a) Three-dimensional virtual driving space featuring the obstacle avoidance event, and (b) ISO 3888-2 obstacle avoidance track and placing of cones (detailed lane width in Table 2) ..... 106
4.12	Driver #3 desired and actual vehicle trajectories when driving through the obstacle avoidance using the cellphone and steering wheel (steering wheel in solid line, cellphone in dashed line, desired trajectory in dotted line, and cones in asterisk)..... 107

## List of Figures (Continued)

Figure	Page
4.113 Driver #3 performance for the obstacle avoidance maneuver - (a) Steer angle, (b) Lateral error, (c) Lateral acceleration, and (d) Front tire slip angle (steering wheel in solid line, and cellphone in dashed line). .....	109
4.14 (a) Three-dimensional city road driving scenario, and (b) City road driving event track with distance travel markers displayed. ....	111
4.15 City roadway 15m radius right turn - Driver #8 performance for (a) Heading error, (b) Lateral error, and (c) Front tire slip angle (steering wheel in solid line, and cellphone in dashed line). ....	112
4.16 City roadway 25m radius left turn - Driver #8 performance for (a) Heading error, (b) Lateral error, and (c) Front tire slip angle (steering wheel in solid line, and cellphone in dashed line). ....	114
4.14 City roadway 20m radius switchback - Driver #8 performance for (a) Heading error, (b) Lateral error, and (c) Front tire slip angle (steering wheel in solid line, and cellphone in dashed line). ....	117
4.15 Yaw rate vs steering angle of steering wheel and cellphone during city road driving event. ....	118
5.1 Dynamically controlled OctArm, a pneumatically actuated continuum manipulator with three sections, following a desired configuration trajectory. ....	123
5.2 Block Diagram for Continuum robot control based on virtual robot models. ....	126
5.3 Three-dimensional constant curvature section geometry obtained via rotation about initial tangent based on virtual RRPR discrete-jointed robot model. ....	129
5.4 Block diagram for PID computed-torque controller designed for virtual RRPR robot. ....	133
5.5 Desired configuration variables arc length $s$ , curvature $k$ , and Orientation $\phi$ for simulation of the virtual robot computed torque control. ....	136

## List of Figures (Continued)

Figure	Page
5.6	Desired and actual continuum robot end-effector X, Y, and Z coordinates during simulation of the virtual robot computed torque control. .... 136
5.7	Desired and actual virtual RRPR robot joint variables $\theta_1$ , $\theta_2$ , $d_3$ , and $\theta_4$ during simulation of the virtual robot computed torque control. .... 137
5.8	Torques and force applied to each virtual RRPR robot joint - $\tau_1$ , $\tau_2$ , $f_3$ , and $\tau_4$ are the torques/force applied to $\theta_1$ , $\theta_2$ , $d_3$ , and $\theta_4$ during simulation..... 138
5.9	The OctArm manipulator with base, mid, and tip sections..... 139
5.10	OctArm actuator cross-section configurations for (a) tip (left), (b) mid (right) sections (Dotted lines show three control channels)..... 139
5.11	One section experiment (OctArm tip section) — Desired and actual arc length $s$ , curvature $k$ , and orientation $\phi$ in configuration space..... 142
5.12	One section experiment (OctArm tip section) — Arc length $s$ , and curvature $k$ error on OctArm in configuration space..... 143
5.13	One section experiment (OctArm tip section) — Desired and actual $\theta_1$ , $\theta_2$ , $d_3$ , and $\theta_4$ of the virtual RRPR rigid-link model in OctArm joint space. .... 143
5.14	One section experiment (OctArm tip section) — Actuation torques/force $\tau_1$ , $\tau_2$ , $f_3$ , and $\tau_4$ , applied to the corresponding joint space variables $\theta_1$ , $\theta_2$ , $d_3$ , and $\theta_4$ in virtual RRPR model. .... 143
5.15	Experimental control loop block diagram for two section OctArm decoupled virtual discrete-jointed model dynamics control. .... 144
5.16	Two section experiment 1 (OctArm tip and mid sections) — Desired and actual arc length $s$ , curvature $k$ , and orientation $\phi$ in configuration space.. .... 146
5.17	Two section experiment 1 (OctArm tip and mid sections) — Arc length $s$ , and curvature $k$ error in configuration space. .... 146

## List of Figures (Continued)

Figure	Page
5.18 Two section experiment 1 (OctArm tip and mid sections) — Desired and actual $\theta_1, \theta_2, d_3, \theta_4, \theta_5, \theta_6, d_7$ , and $\theta_8$ of the virtual discrete-jointed model in the joint space; the variables $\theta_1, \theta_2, d_3, \theta_4$ represents the mid-section virtual RRPR model and the variables $\theta_5, \theta_6, d_7, \theta_8$ represents the tip-section virtual RRPR model.....	148
5.19 Two section experiment 1 (OctArm tip and mid sections) — Actuation torques/force applied to the corresponding joint space variables: $\tau_1$ to $\theta_1, \tau_2$ to $\theta_2, f_3$ to $d_3, \tau_4$ to $\theta_4, \tau_5$ to $\theta_5, \tau_6$ to $\theta_6, f_7$ to $d_7$ , and $\tau_8$ to $\theta_8$ .....	148
5.20 Two section experiment 2 (OctArm tip and mid sections) — Desired and actual arc length $s$ , curvature $k$ , and orientation $\phi$ in configuration space .....	150
5.21 Two section experiment 2 (OctArm tip and mid sections) — Arc length $s$ , and curvature $k$ error in configuration space .....	151
5.22 Two section experiment 2 (OctArm tip and mid sections) — Desired and actual $\theta_1, \theta_2, d_3, \theta_4, \theta_5, \theta_6, d_7$ , and $\theta_8$ of the virtual discrete-jointed model in the joint space; the variables $\theta_1, \theta_2, d_3, \theta_4$ represents the mid-section model and the variables $\theta_5, \theta_6, d_7, \theta_8$ represents the tip-section model.....	151
5.23 Two section experiment 2 (OctArm tip and mid sections) — Actuation torques/force applied to the corresponding joint space variables: $\tau_1$ to $\theta_1, \tau_2$ to $\theta_2, f_3$ to $d_3, \tau_4$ to $\theta_4, \tau_5$ to $\theta_5, \tau_6$ to $\theta_6, f_7$ to $d_7$ , and $\tau_8$ to $\theta_8$ .....	152
6.1 The illustration of the haptic assistive control framework with learning-based intent recognition.....	158
6.2 NMPC closed-loop control structure.. .....	162
6.3 Driver-in-the-loop simulation platform with joystick for throttle, brake, and steering commands.....	167
6.4 Driving intent recognition process implemented using ensemble learning approach.....	172

## List of Figures (Continued)

Figure	Page
6.5	Misclassification of the test data (left vertical axis) and training time of 209,791 observations (right vertical axis) as a function of the number of trained trees in the ensemble.. 173
6.6	A confusion matrix from true labels and predicted labels with number of trees $N = 45$ . Class labels: 1=Lane keeping (LK), 2=Left lane change (LLC), 3=Right lane change (RLC), 4=Left obstacle avoidance (LOA), and 5=Right obstacle avoidance (ROA). 174
6.7	Ensemble model recognition result in the design scenario: vehicle trajectory on the left column and lane changing intention recognition result on the right column. Recognition Intent labels: 1=Lane keeping (LK), 2=Left lane change (LLC), 3=Right lane change (RLC), 4=Left obstacle avoidance (LOA), and 5=Right obstacle avoidance (ROA) 175
6.8	Updated vehicle trajectory for driver intended maneuvers on three-lane highways: (a) lane change, and (b) obstacle avoidance. The red circle and asterisk are the start and the end of the maneuver..... 178
6.9	Highway scenario — (a) Test track, and (b) Animated simulator scene... 181
6.10	Driver #12 response — (a) Desired and actual vehicle trajectories, (b) Wheel steer angle, (c) Applied human force onto the joystick, and (d) Lateral acceleration when driving through the highway track with speed of 90kph under configurations C1-C3 for vehicle left obstacle avoidance of highway roadway ..... 184
6.11	Driver #5 response — (a) Desired and actual vehicle trajectories, (b) Wheel steer angle, (c) Applied human force onto the joystick, and (d) Lateral acceleration when driving through the highway track with speed of 90kph under configurations C1-C3 for left lane change of highway roadway ..... 185
6.12	City road scenario — (a) Test track, and (b) Animated simulator scene... 187
6.13	Driver #8 response — (a) Lateral error, (b) Applied human force on joystick, and (c) Lateral acceleration when driving through the city with a speed of 30kph for configurations C1-C3..... 188



## List of Figures (Continued)

Figure	Page
6.14	Nine subjective measures for three driving configurations C1-C3 based on human subjects' responses to the questionnaire in Table III normalized to 10. Symbols O1 to O3 correspond to Table III and capture the steering characteristic behind driver assessment..... 190

## CHAPTER ONE

### INTRODUCTION

A control system uses sensory measurement of the plant's behavior to influence the input for the realization of an altered response. Both linear and nonlinear control methods exist for the underlying mathematical model that describes the dynamics. Governed by nonlinear differential equations, nonlinear control theory applies to more real-world systems, as they tend to be nonlinear. A variety of nonlinear controller designs exist including gain scheduling, backstepping, and robust control. Two significant areas for nonlinear control applications are semi-autonomous ground vehicles and continuous robotic systems. While linear controllers may be typically adequate for these systems, it is often found that the underlying dynamics are nonlinear, and a linear controller will not satisfy the performance requirements. This research focuses on feedback nonlinear control of alternative driving interface and continuum robots through mathematical modeling, numerical simulation, and experimental testing. The proposed approach utilizes several nonlinear control methodologies including sliding mode control, adaptive control, switched system control, and feedback linearization. Model-free control and the corresponding deep reinforcement learning algorithms are also implemented and integrated with the model-based approach to achieve intelligent semi-autonomous ground vehicle control. Four thrust areas, shown in Figure 1.1 have been identified, namely alternative

steering devices with haptic feedback, use of portable HMI as driver inputs, driver intent-based autonomous driving, and control of continuum robots.


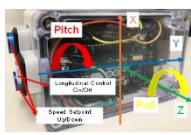

<div> <div>Nonlinear Modeling and Control of Driving Interfaces and Continuum Robots for System Performance Gains</div> </div>				
Research Thrusts				
Titles	Alternative Steering Devices with Haptic Feedback	Use of Portable HMI as Driver Inputs	Driver Intent Based Autonomous Driving	Control of Continuum Robots
Designs			Haptic Shared Vehicle Control via Deep Reinforcement Learning	
Modeling and Simulation	Vehicle Kinematics and Dynamics + Haptic Interface	Vehicle Kinematics and Dynamics + Portable HMI	Vehicle Kinematics and Dynamics + Driver Intent Inference	Continuum Robot Kinematics and Dynamics
Nonlinear Control	Sliding Mode Control	Adaptive Control	Model-Free and Model-Based Control	Feedback Linearization and Computed Torque Control
Experimental Testing	Human-in-the-loop Driving Simulator Testing	Human-in-the-loop Driving Simulator Testing	Human-in-the-loop Driving Simulator Testing	Cases Studies on "OctArm"
Contributions	Haptics and Robotic Grip Improve Operation Safety with Steering Feedback	Novel Design Interface	Application of Deep Reinforcement Learning Methods for Haptic Shared Control	Control Via "Virtual" Rigid Link Robot Model With Innovative Parameterization

Figure 1.1 Four Research Thrust Areas Identified

## 1.1 Dynamic Systems

To comprehend the ground vehicle and continuum robot movements, a mathematical model may be constructed. Such a dynamic model lays the foundation for designing control algorithms and is vital for the practical implementation of semi-

autonomous features and continuum robot hardware. The vehicle dynamics model describes the longitudinal and lateral vehicle platform characteristics. Robot dynamics are concerned with the relationship between the forces and torques acting on a robot mechanism and the accelerations they produce resulting in motion. This section introduces the formulation of the dynamic systems for both ground vehicles and continuum robots.

### *1.1.1 Chassis and Steering Systems*

A two-track seven-degree-of-freedom (7-DoF) vehicle chassis model, as shown in Figure 1.2, was used for the controller development presented in this dissertation. The lateral and longitudinal velocities of the vehicle ( $v_x$  and  $v_y$ , respectively) and the yaw rate  $\dot{\psi}$  constitute three degrees-of-freedom (DoF) related to the vehicle body. The wheel velocities of four wheels ( $\omega_{fl}$ ,  $\omega_{fr}$ ,  $\omega_{rl}$ , and  $\omega_{rr}$ ) constitute the other four DoF. Note that the first subscript in the symbols for the wheel velocities is used to denote the front or rear wheel, and the second subscript is used to denote the left or right wheel. Similar to the models considered in Alleyne (1997), Dugoff et al. (1970), and Rajamani (2006), roll and pitch motions were neglected while still accommodating the steering and individual wheel braking. The vehicle model contains nonlinear and coupled dynamics that make it unsuitable for linear controller development. The presence of nonlinearities in the vehicle model is the main factor in the selection of control algorithms for their real-time regulation and tracking. Linear control is often inadequate in meeting precise performance requirements, and one must resort to nonlinear techniques.

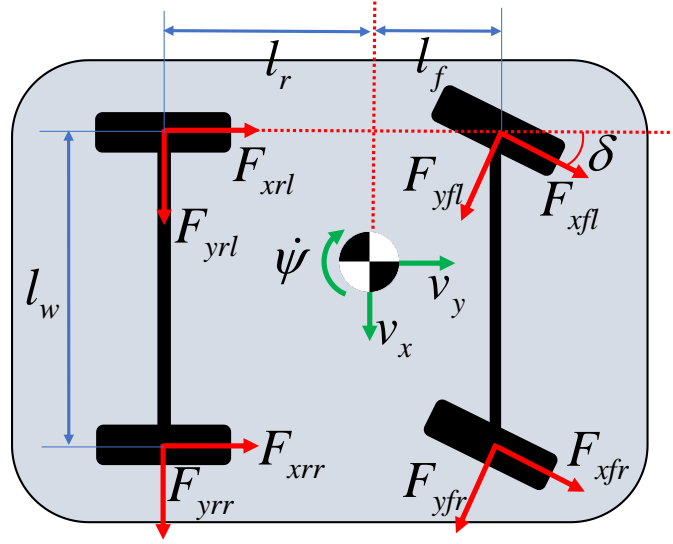


Figure 1.2. Parameter and variable definitions for the vehicle model.

The vehicle simulation requires the tire/road interface forces and moments for the wheels. In this study, the Dugoff tire model is used. This analytical tire model is presented in Dugoff et al. (1969), and has been updated for combined wheel slip in Gunta and Sankar (1980). Dugoff's model provides for the calculation of forces under combined lateral and longitudinal tire force generation. It assumes a uniform vertical pressure distribution on the tire contact patch (Rajamani, 2006a). In this simplified model the effects of camber and turn slip are neglected, and a uniform vertical pressure distribution is assumed in the tire. The advantage of this model is that it does not demand many parameters. Moreover, since it is an analytical model, these parameters can be derived intuitively. However, the drawback of this method is that the gradient cannot be computed directly since there are different equations for sliding and pre-sliding. Furthermore, the model is a relatively simplified representation. Therefore the shape of the tire curve is limited, such that a peak in the tire curve cannot be modelled (van Ginkel, 2014).

Vehicle steering systems translate the driver's steering commands into the rotation of the steered wheels about their kingpin axes. In this study, a steer-by-wire (SBW) configuration is considered for steering system dynamics. In a conventional steering system, the front road wheels are turned using a handwheel via the steering column, bevel gearbox, and rack. In steer-by-wire systems, the steering wheel is mechanically decoupled from the road wheels. The driver's steering commands are delivered electronically to an electric motor to actuate the wheels. As innovative driving interfaces can leverage drive-by-wire technology, an analytical mathematical model should be developed to describe the steering subsystem. To facilitate the investigation of a vehicle's lateral responsiveness and power consumption for SBW configuration, a suite of lumped parameter nonlinear steering system mathematical models developed by Mills and Wagner (2003) will be used.

### *1.1.2 Continuum Robot System*

Incorporating the dynamics of the continuum robot is vital for model-based dynamic control of continuum structures. The dynamic equations of motion, which provide the relationships between actuation and the acceleration, form the basis for several computational algorithms that are fundamental in control and simulation. In this work, we propose a novel approach to model continuum robot by reducing computational complexity using a virtual, conventional rigid link robot with discrete joints. Specifically, the above approach is validated from model development to hardware implementation for control of a multi-section spatial continuum robot. The continuum robot is approximated as a serial rigid-link Revolute-Revolute-Prismatic-Revolute (RRPR) joint spatial robot with an out-of-plane rotation, two in-plane rotations, and a translation in the same plane to create a 3D

virtual rigid-link robot (see Figure 1.3). For motion control, the dynamic model of a virtual RRPR mechanism is conveniently described by Lagrange dynamics represented in the joint-space formulation. Similarly, the dynamic model for a two-section continuum robot can be modeled by combining two virtual RRPR robots into an 8-DoF RRPRRRPR rigid-link robot. The task space to joint space inverse kinematics are obtained via a desired virtual joint vector which forms the error vector with the actual virtual joint space variables derived from the continuum robot configuration space. The approach mentioned above assumes the constant curvature (CC) approximation (Hannan and Walker, 2003) for the configuration space model.

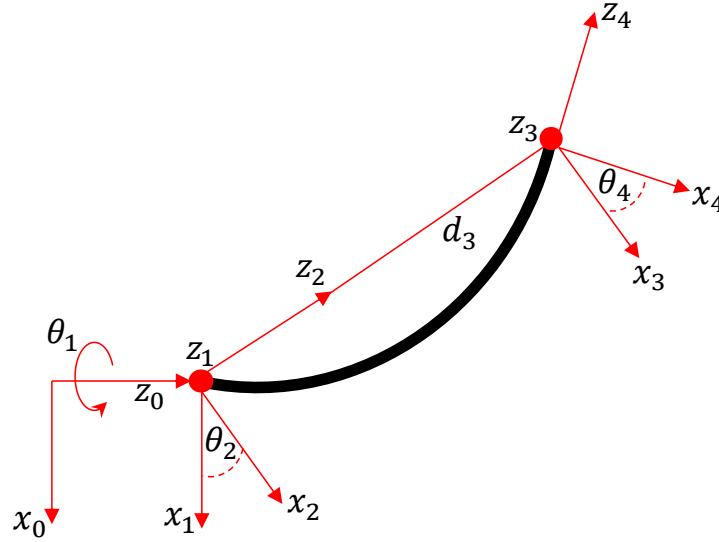


Figure 1.3: Three-dimensional constant curvature section geometry obtained via rotation about initial tangent based on virtual RRPR discrete-jointed robot model.

## 1.2 Model and Control Strategies

In recent years, there has been a resurgence of interest in developing improved control and identification strategies for nonlinear ground vehicle and continuum robot systems. The renewed interest has been motivated by several developments:

1. Advances in nonlinear systems theory which has led to controller design methods that are applicable to broad classes of nonlinear control problems.
2. The developments of efficient identification methods for empirical nonlinear models and their widespread availability in software packages like MATLAB.
3. Continued improvements in the capability of computer-controlled hardware and software, making it feasible to incorporate complex nonlinear models in control systems synthesis.
4. Need for enhanced safety and operation for autonomous vehicles.

In this section, the nonlinear control strategies utilized for the four research thrust areas are introduced.

#### *1.2.1 Sliding Mode Control (Thrust 1: Alternative Steering Devices with Haptic Feedback)*

A nonlinear higher-order sliding-mode controller (SMC) will be considered for the steering system to provide lateral feedback to the driver and assist lane-keeping. Sliding mode theory provides a methodology to design trajectory tracking and control systems for ground vehicle systems with all of their associated features. Sliding mode control algorithms ensure that the desired system dynamics is insensitive to parameter variations, system perturbations and external disturbances (Vepa, 2017). The motivation of using sliding mode control is to achieve the ability to guarantee the control robustness against the system uncertainties and varying road conditions (Freeman et al., 2015). Sliding mode control remains the most successful approach in handling bounded uncertainties/disturbances and parasitic dynamics (Davila et al., 2005). The control concept



is based on the introduction of a sliding variable function which is designed to become equal to zero. The main features of the sliding mode are its insensitivity to external and internal disturbances matched by the control, ultimate accuracy, and finite-time convergence of the sliding variable to zero. However, chattering is a problem impeding its implementation. The modified sliding mode control with boundary layer undergoes the degradation of tracking performance and robustness while reducing the chattering effect. Second-order sliding mode control is a viable solution to reduce the chattering effect without affecting the tracking accuracy and robustness. For higher-order systems a super-twisting algorithm can address the chattering problem.

### *1.2.2 Adaptive Control (Thrust 2: Use of Portable HMI as Driver Inputs)*

Adaptive control provides such nonlinear class of techniques that are particularly suitable for application in ground vehicle applications. Adaptive control refers to a set of techniques that provide a structured or systematic approach for automatically and continuously adjusting the parameters of a controller in real-time (Vepa, 2017). When the parameters of the plant dynamic model are unknown or change in time, adaptive control achieves or maintains a certain desired level of system performance. An adaptive controller is one that can modify the system's closed-loop behavior in response to changes in the dynamics of the manipulator due to changes in the configuration, external constraints, and disturbances. In this study, an adaptive variable steering ratio control strategy will be proposed that provides lateral compensation to the driver and assists with lane-keeping (Shimizu et al., 1999; Heathershaw, 2000; Nozaki et al., 2012). Specifically, a gain-scheduling PID controller is developed as the feedback control for the portable HMI-

steered vehicle to accomplish this task. The gain scheduling technique, an adaptive control method, is based on the adjustment of controller parameters in response to the vehicle's longitudinal speed and portable HMI steer angle variations.

### *1.2.3 Model-Free and Model-Based Control (Thrust 3: Driver Intent-Based Autonomous Driving)*

Autonomous and semi-autonomous electric robotic platforms represent the next generation of military vehicles with the challenge for seamless control switching (Kalinowski et al., 2014; Mandhata et al., 2012; Setlur et al., 2006; Stanton et al., 1997). Although these vehicles can undertake most driving tasks autonomously, the ability to infer operator intent and hence switch among different levels of autonomy (LoAs) is highly demanded, especially under complex urban or off-road circumstances. Advanced modalities of interaction such as a haptic interface that map operator commands to actions can be deployed to assist driver intervention in the vehicle cockpit. In this study, a haptic assisted vehicle control strategy enhanced by learning-based operator intent inference is introduced. The shared control strategy is capable of adapting vehicle behaviors to corresponding operators' preferences. The proposed operator intent inference algorithm for asset-level decision-making will exploit model-free deep reinforcement learning (DRL) techniques (Kim et al., 2017a; Kumar et al., 2013a; Li et al., 2016a; Polling et al., 2005). The DRL algorithm also serves as a logical rule that orchestrates switches among distinct LoAs, which forms a switched system (Lin and Antsaklis, 2009) for intelligent alteration of powertrain dynamics.

#### *1.2.4 Feedback Linearization and Computed Torque Control (Thrust 4: Control of Continuum Robots)*

The dynamic system of section 1.1.2 forms the basis for control approaches needed for continuum robots. We seek and exploit simple, relatively computationally inexpensive control methods used in (rigid-link) robot control systems to design the controller in the virtual RRPR robot coordinates (Webster and Jones, 2010). Multiple control methods, such as adaptive control (Frazelle et al., 2018), optimal and robust control (Kapadia et al., 2010), and learning control (Braganza et al., 2007), are widely used in robotics. Each control method has advantages and disadvantages. However, the main aim of the system is to provide stability and high-frequency updates. In this work, we adopt the computed-torque (Middleton and Goodwin, 1986), feedback linearization plus PID control, approach for the virtual robot. Specifically, sensing and actuation transformed from and to the continuum robot. The computed-torque control consists of an inner nonlinear compensation loop and an outer loop with an exogenous control signal,  $u$ . This control input converts a complicated nonlinear controller design problem into a simple design problem for a linear system consisting of several decoupled subsystems. One approach to the out-loop control  $u$  is the proportional–integral–derivative (PID) feedback. The reason why the PID controller is preferred in this article over the proportional-derivative (PD) controller is that the PID controller eliminates the steady-state error caused by environmental disturbances. In the PID control, the chosen parameters,  $K_p$ ,  $K_i$  and  $K_d$  remain constant during the process. Therefore, such a controller is inefficient because the controller contains ambiguity when environmental conditions or dynamics change. In

addition, it is inefficient because of time delays and nonlinearity conditions. Hence, we include the dynamics to linearize prior to the PID control.

### **1.3 Dissertation Objectives**

Research activities focus on the nonlinear control of alternative driving interface and continuum manipulators for enhanced tracking performance. The main objective of this first set of investigations is to improve the driver's confidence and driving safety in semi-autonomous vehicles. It will develop three vehicle driving interfaces, including a robotic grip, a joystick, and a portable HMI, which are accompanied by nonlinear control, and studied them on a steer-by-wire platform integrated with a virtual reality driving environment (see Figure 1.4). On the other hand, the innovative continuum robot control design, second set of study, aims to enhance robot configuration space tracking performance and deliver accurate, reliable, and energy-efficient control. Both quantitative and qualitative measures will be used to gain in-depth insight into the effectiveness and performance of the designed nonlinear controllers.

This research intends to achieve the following research objectives:

1. Develop three driving interfaces for physical and cognitive interaction of humans with (semi)autonomous vehicles.
2. Create a mathematical model for ground vehicle and continuum robot kinematics and dynamics.
3. Design appropriate nonlinear control strategies for the trajectory tracking and control of semi-autonomous vehicles and continuous robotic systems

4. Validate models and nonlinear controls through laboratory testing on three alternative driving interfaces and “OctArm”.

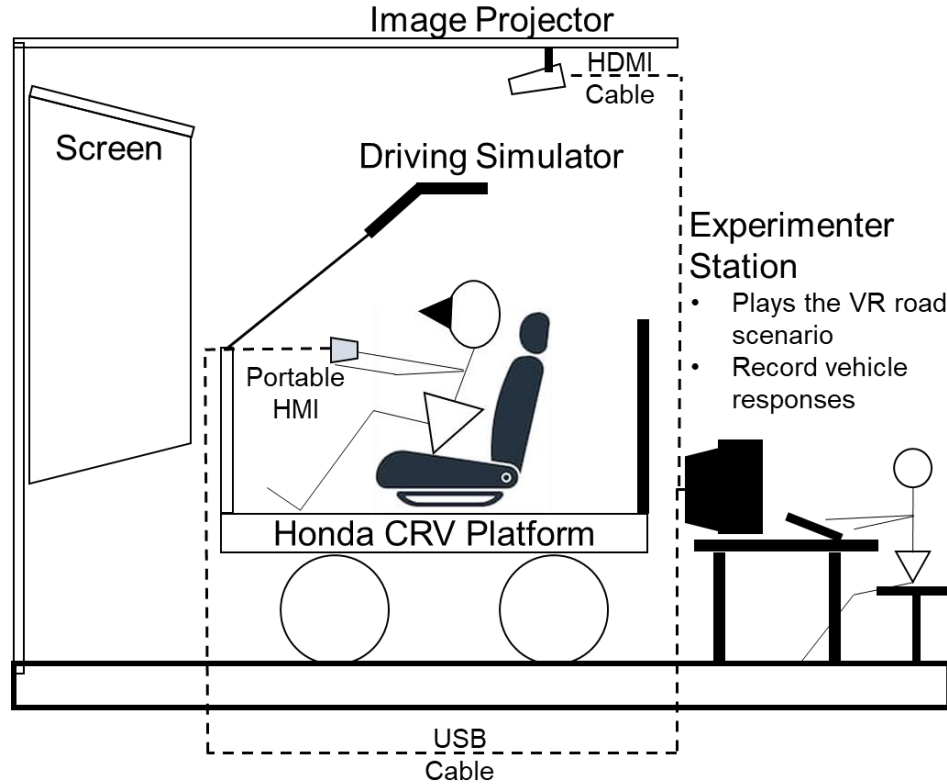


Figure 1.4: Laboratory Driving Simulator Schematic

#### 1.4 Innovation

To improve vehicle lateral performance, multiple lateral control strategies have been proposed by many researchers like Baviskar et al. (2009), Jensen et al. (2011), Mandhata et al. (2010), Petermeijer et al. (2015), and Shakeri et al. (2016). While this study provides insights on the lateral controller, especially in regard to nonlinear adaptive and sliding mode control, it devotes a large amount of attention to evaluating the performance of three alternative driving interfaces, including the portable HMI, joystick, and robotic grip, all of which provide nonlinear lateral feedback to the driver and assist in lane-keeping. In particular, research on alternative steering devices for semi-autonomous vehicles is notably

lacking. The replacement of the steering wheel on semi-autonomous vehicles is conceptually intriguing, and this project seeks to fill this gap by examining various potential haptic driving paradigms and benchmarking their performances against the steering wheel under different road scenarios and speed conditions. These hand-operated interfaces incorporate the directional control as well as the brake and throttle functionality into a single holistic device. Therefore, they broaden opportunities for people with disabilities to operate vehicles. These alternative driving devices also serve as a contingency when semi-autonomous vehicles encounter extreme maneuvers that are otherwise unable to be handled solely by the automated system without human intervention. Thus, their performances in aggressive driving conditions are investigated to determine the most applicable device for semi-autonomous vehicles.

Previous research has also examined the possibility of controlling a continuum structure via exploiting a “virtual” rigid link robot model. However, the methodologies were either applied only to the bending of a planar continuum section (Tang et al., 2019), or formulated using an under-parameterized model which involves merely bending and twisting without considering continuum robot extension/contraction (Katzschmann et al., 2019; Greigarn et al., 2019). In contrast, the work in this dissertation is the first attempt to accomplish three-dimensional control of continuum robots whose configuration space is parameterized by arc length, curvature, and rotational orientation. Such comprehensive parameterization accounts for simultaneous extension/contraction, bending, and torsion actions of continuum robots, therefore fully matching the control capability and motion complexity of continuum robots. In addition, we extend model-based dynamic control

research through the application of the computed torque approach that provides virtual rigid link robot dynamics decoupling for the control of multi-section continuum robots.

## **1.5 Dissertation Organization**

This document is organized into six chapters. Chapter 1 introduces the background of this study. Chapter 2 presents the evaluation of three alternative steering devices with adjustable haptic feedback for semi-autonomous and autonomous vehicles. Chapter 3 proposes a robust haptic interface for three alternative steering devices proposed in Chapter 2. A nonlinear and robust sliding mode controller is used to maintain the vehicle on the desired trajectory while minimizing the vehicle lateral and heading error. Chapter 4 demonstrates the use of portable HMI as alternative driver input device. Chapter 5 proposes a model-based dynamic feedback control architecture that has been specifically designed for controlling multi-section three-dimensional continuum robots. Lastly, Chapter 6 cover the study of haptic assistive control with learning based driver intent recognition for semi-autonomous vehicles.

## CHAPTER TWO

### EVALUATION OF ALTERNATIVE STEERING DEVICES WITH ADJUSTABLE HAPTIC FEEDBACK FOR SEMI-AUTONOMOUS AND AUTONOMOUS VEHICLES

Emerging autonomous driving technologies, with emergency navigating capabilities, necessitates innovative vehicle steering methods for operators during unanticipated scenarios. A reconfigurable “plug and play” steering system paradigm enables lateral control from any seating position in the vehicle’s interior. When required, drivers may access a stowed steering input device, establish communications with the vehicle steering subsystem, and provide direct wheel commands. Accordingly, the provision of haptic steering cues and lane keeping assistance to navigate roadways will be helpful. In this study, various steering devices have been investigated which offer reconfigurability and haptic feedback to create a flexible driving environment. A joystick and a robotic arm that offer multiple degrees of freedom were compared to a conventional steering wheel. To evaluate the concept, human test subjects interacted with the experimental system featuring a driving simulator with target hardware, and completed post-test questionnaires. Based on the data collected, drivers’ lane keeping performance was superior using a haptic robotic arm with haptic feedback to the joystick and steering wheel with an improvement of up to 70.18% during extreme maneuvers. Haptic feedback,



with a lane keeping algorithm, can assist the operator in steering the vehicle given the likely deterioration of driving skills when autonomous vehicles become prevalent.

## **2.1 Introduction**

The growing emphasis on autonomous vehicles and driver assistance subsystems have elevated the need for improved human-vehicle interfaces (Jensen et al., 2011). The introduction of haptic feedback in driver system can introduce greater road awareness and accommodate emergency scenarios that may arise in all ground transportation systems (Andonian et al., 2003). Future autonomous vehicles will have different interiors, refer to Figure 2.1, that enables the steering control device to be placed anywhere in the vehicle. If the driver can access the steering device, then alternative design can be readily considered. More importantly, the steering device could be stored while needed and simply plugged into a connector in the passenger pod. A robotic interface steering controller could provide benefits to the driver such as enhanced safety during a crash, greater vehicle control and steering ratio flexibility, and a more robust steering feel. The goal of this paper is to study the feasibility of replacing the current steering wheel with a new robotic interface device that can provide adjustable force feedback to the driver and a user-friendly experience for future autonomous and semi-autonomous vehicles.

In literature, various approaches have been presented within the scope of lane keeping assistance control and force feedback steering. In Saleh et al. (2011), a new model structure with inputs considering visual, haptic and kinesthetic perception, and neuromuscular dynamics was proposed. The model considers the torque applied to the

steering wheel as output and the steering angle in terms of driver intention. A model based predictive controller is developed for lane keeping assistance by Hwang et al. (2008) to minimize the effect of system overshoot caused by the time delay from the vision-based lane detection system. In a previous study, Black et al. (2011) used an advanced steering simulator to introduce supplemental haptic feedback for roadway avoidance notification and proposed a way to calculate the steering effort as a function of tire contact path friction torque. Ancha et al. (2007) validated the use of a chassis dynamic model to collect experimental data, model and compare steering systems. A Haptic intervention system for avoidance of lane departure was introduced by Pohl and Ekmark (2003). Chan (2011) has built a simulation analysis implementing electronic stability control that can help drivers maintain control in oversteer or understeer situations. Dadras (2017) has developed a control algorithm that helps the system converge to desired paths for autonomous vehicles. These methods described have proved their success in many aspects including consistency and precision.

Previous researchers have investigated various vehicle steering force feedback and feedforward steer assistance strategies. Mehdizadeh et al. (2011) proposed a novel approach for making force feedback which made use of virtual vehicle states through a linear vehicle model as the reference model. Vaddi et al. (2014) presented a vehicle steer assistance system based on yaw moment control. The feedforward steer assistance control with input of steering angle and vehicle speed is considered. Fahami et al. (2015) designed a LQR controller with gain scheduling based on steering wheel angle and vehicle speed function. The controller also provided better torque control that allowed rejection of the

uncertainty torque from a road condition. To improve the lane keeping performance on a curved road, Kang et al. (2016) developed a linear quadratic state feedback control using both the lateral offset error at the look-ahead distance and the integral of the lookdown lateral offset error. Katzourakis et al. (2011) developed a system that allowed the force feedback to be delivered to the driver through a speed-controlled three-phase brushless servomotor with a torque sensor on the motor shaft.

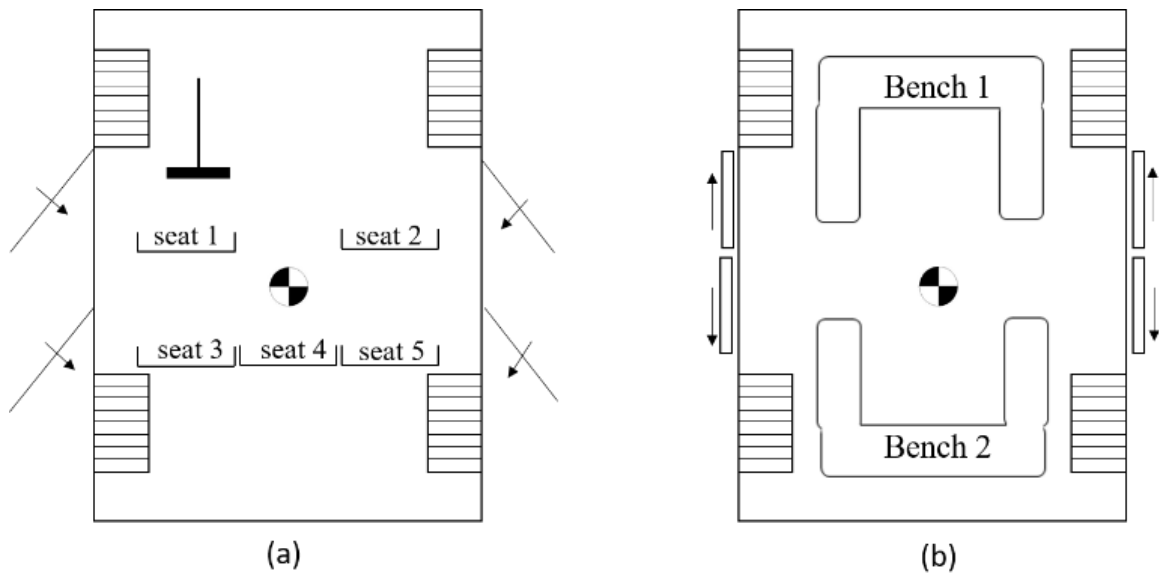


Figure 2.1: Top view of vehicle configurations - (a) standard with five seats; and (b) autonomous with two benches

In this study, a vehicle dynamics mathematical model that includes the vehicle body, wheel, and trajectory kinematics is presented. The model serves as a keystone for the computer simulation created in MATLAB/Simulink that provides the vehicle's longitudinal and lateral velocities, and yaw rate. Several customizable steering algorithms are implemented into the system that provided operators with not only varied levels of haptic steering “feel”, but more importantly, a force-feedback control design that enables

the steering device to provide a force feedback to the driver when they deviated from the lane. A feedback and pursuit behavior feedforward controller are established for the system. A high-level diagram of a vehicle's haptic force feedback steering system is shown in Figure 2.2. Several different steering devices, a few functionalities of which are compared in Table 1, are utilized in this research. The main steering device studied is a robotic interface grip device, the Novint Falcon, which is a three degree-of-freedom (DOF) haptic device that uses a delta-robot configuration with three servo-actuated parallel links connected to a moving plate. The delta configuration provides a mechanism with three rotational actuators mounted to the base plate, and a series of kinematic parallelograms to constrain the motion plate to three translational DOF only. The torques applied at the input link by the actuators to achieve proper haptic feedback may be calculated. All joints in the Falcon are one DOF revolute joints. The information between the device and the controlling computer is handled via USB connection. The Falcon sends the position data to the computer that returns a force vector. Position is measured using encoders and the force vector is created by feeding the supplied currents to the servomotors in each parallel link (Rodríguez and Velázquez, 2012). Fu et al. (2016) created a mathematical model for a Falcon device which led to dynamic equations that allowed the design of an adjustable haptic experience. Vehicle driving visualization is also realized thanks to the MATLAB 3D Animation toolbox. Case studies on two different driving environments, a straight highway and a meandering path of country road, were conducted to validate the fidelity of the lane keeping assistance control.

Table 2.1: Comparison of ground vehicle steering device functionality assuming a steer-by-wire configuration

<b>Devices</b> <b>Function</b>	Traditional Steering Wheel	Joystick	Robotic Interface Grip	Cellphone
Installation	Fixed	Portable		
Safety	Airbag Needed	Eliminate driver contact with steering wheel during crash		
Feedback	Tire/Road Interface Feel	Maybe	Yes	No
ADA Accommodating	Limited	High	High	Limited (Voice)
Space Required	High	Low	Low	Very low

This paper evaluated three different steering devices for future use by autonomous vehicles through quantitative and qualitative measures. The proposed system architecture has been assessed in a laboratory environment using a hardware-in-the-loop vehicle with steering devices, graphical display, and human subjects. The research hypothesis was: Can robotic steering input devices outperform the traditional steering wheel in terms of vehicle lane keeping control? The remainder of the article is organized as follows. The mathematical formulation and control structure are presented in Sections 2 and 3. The experimental setup and two case studies are described in Section 4, with the accompanying operator-in-the-loop test results summarized in Section 5. Finally, Section 6 offers the conclusion. A complete Nomenclature List exists in the Appendix.

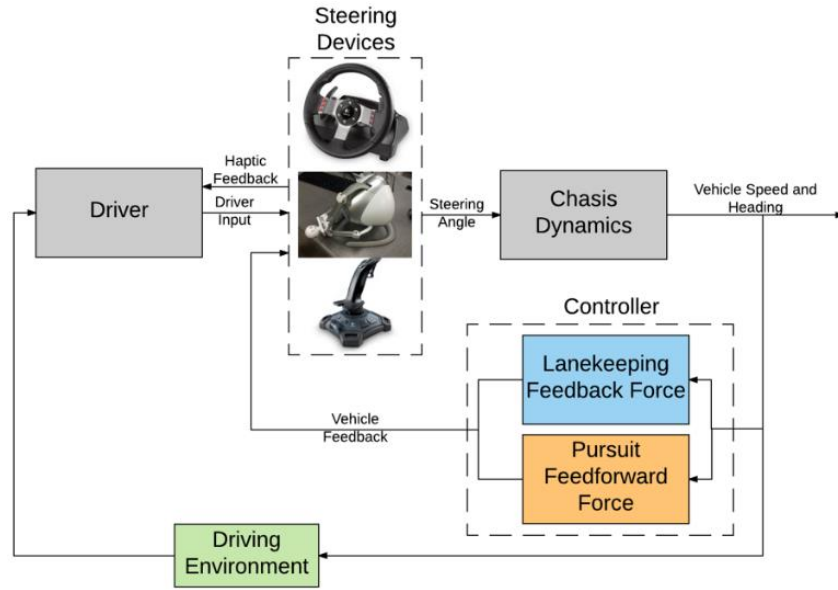


Figure 2.2: Close-loop system design for human/machine steering interface

## 2.2 Steering System Model

The steering system provides lateral control for ground vehicles using a dedicated steering assembly which turn the front wheels. For convenience, a single-track model will be considered. The chassis, wheel, and trajectory kinematics will be discussed in this section.

### 2.2.1 Ground Vehicle Body Modeling

To formulate the equations of transient motion for a vehicle body during a turning maneuver, it is essential to describe the absolute acceleration of the vehicle's center of gravity (CG) using the reference frame attached to the body.

A body fixed coordinate system will be considered to describe the longitudinal, lateral, and yaw motion of the chassis. Referring to Figure 2.3, for a vehicle having plane

motion, the equations of motion with respect to the axis fixed to the vehicle body are given by (Freeman et al., 2016)

$$\begin{aligned}\dot{v}_x &= \dot{\psi}v_y + \frac{1}{m} \left( (F_{xfl} + F_{xfr}) \cos \delta + F_{xrl} + F_{xrr} - (F_{yfl} + F_{yfr}) \sin \delta \right) \\ \dot{v}_y &= -\dot{\psi}v_x + \frac{1}{m} \left( (F_{xfl} + F_{xfr}) \sin \delta + F_{yrl} + F_{yrr} + (F_{yfl} + F_{yfr}) \cos \delta \right) \\ \ddot{\psi} &= \frac{1}{I_z} \left( l_f (F_{xfl} + F_{xfr}) \sin \delta + l_f (F_{yfl} + F_{yfr}) \cos \delta - l_r (F_{yrl} + F_{yrr}) \right)\end{aligned}\quad (2.1)$$

where  $\delta$  is the front wheel steering angle. The longitudinal and lateral velocities, and the yaw rate were obtained by integrating Eq. (2.1) - (2.3).

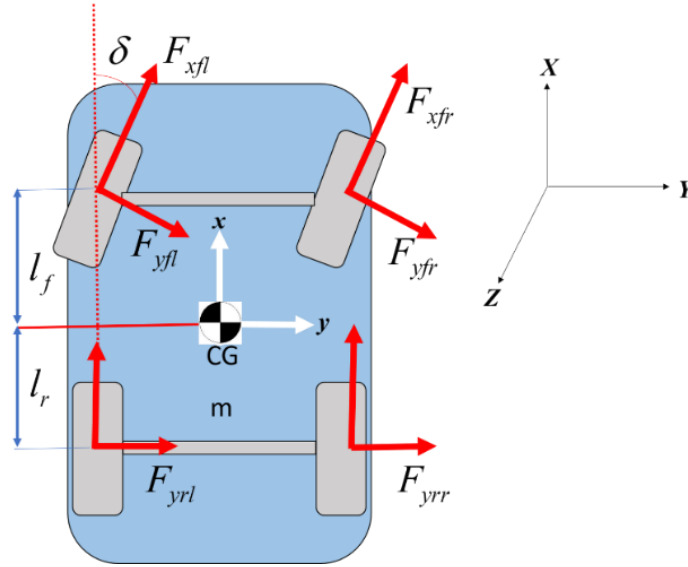


Figure 2.3: Diagram to illustrate vehicle body forces

### 2.2.2 Ground Vehicle Wheel Modeling

The simulation of vehicle dynamics for four wheels vehicle demands details of relating forces acting on the wheel. Dugoff's model is used in this paper. The analytical model in (Dugoff et al., 1969) has been altered for combined slip (Gunta and Sankar, 1980).

In Figure 2.4, the system variables and parameters are displayed to describe the wheel motions.

The longitudinal slip ratio for four wheels during braking and acceleration,  $s_x$  may be expressed as

$$s_{xi} = \begin{cases} \frac{r_{eff} \omega_{wi} - v_x}{v_x}, & v_x < r_{ref} \omega_{wi} \text{ brake} \\ \frac{r_{eff} \omega_{wi} - v_x}{r_{eff} \omega_{wi}}, & v_x > r_{ref} \omega_{wi} \text{ traction} \end{cases} \quad (i = fl, fr, rl, rr) \quad (2.2)$$

The subscripts  $fl, fr, rl$ , and  $rr$  refer to the front left, front right, rear left, and rear right wheels, respectively.

The slip angles for front and rear tires,  $\alpha_f$  and  $\alpha_r$ , are

$$\alpha_f = \delta - \frac{v_y + l_f \dot{\psi}}{v_x}, \quad \alpha_r = -\frac{v_y - l_r \dot{\psi}}{v_x} \quad (2.3)$$

where  $l_f$  and  $l_r$  correspond to the distance from the front and rear axles to the center of vehicle gravity.

The longitudinal and lateral tire force,  $F_{xi}$  and  $F_{yi}$ , may now be written as

$$\begin{aligned} F_{xi} &= C_\sigma \frac{s_{xi}}{1 + s_{xi}} f(\lambda_i) \\ F_{yi} &= C_{\alpha j} \frac{\tan \alpha_j}{1 + s_{xi}} f(\lambda_i) \end{aligned} \quad \begin{pmatrix} i = fl, fr, rl, rr \\ j = f, r \end{pmatrix} \quad (2.4)$$

where  $C_\alpha$  and  $C_\sigma$  are the cornering and longitudinal tire stiffness. The variable  $\lambda_i$  is given by

$$\lambda_i = \frac{\mu F_{zi} (1 + s_{xi})}{2 \sqrt{(C_\sigma s_{xi})^2 + (C_{\alpha j} \tan \alpha_j)^2}} \quad \begin{pmatrix} i = fl, fr, rl, rr \\ j = f, r \end{pmatrix} \quad (2.5)$$



and the function,  $f(\lambda_i)$ , may be stated as

$$f(\lambda_i) = \begin{cases} (2 - \lambda_i) \lambda_i; & \lambda_i < 1 \\ 1; & \lambda_i \geq 1 \end{cases} \quad (i = fl, fr, rl, rr) \quad (2.6)$$

The term  $F_z$  denotes the vertical force on the tire while the symbol  $\mu$  is the tire-road friction coefficient. The index  $j = f, r$  corresponds to the front and rear wheels.

The relationship between the drive and braking torques,  $T_{di}$  and  $T_{bi}$ , and the wheel rotation,  $\omega_i$ , of the four wheels can be written as.

$$I_w \dot{\omega}_{wi} = T_{di} - T_{bi} - r_{eff} F_{xi} \quad (i = fl, fr, rl, rr) \quad (2.7)$$

where  $I_w$  is the wheel inertia,  $T_d$  is the drive torque of the wheel,  $T_b$  is the brake torque of the wheel, and  $r_{eff}$  is the effective wheel radius.

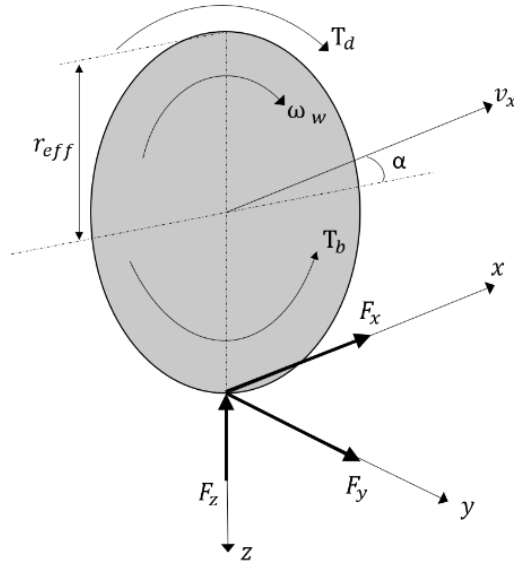


Figure 2.4: Single wheel with applied longitudinal and lateral tire forces, as well as tire rotation

### 2.2.3 Ground Vehicle Trajectory Kinematics

A vehicle trajectory calculation method is provided to estimate the planar response of the platform. The vehicle path is determined based on the vehicle's longitudinal velocity,  $v_x$ , yaw angle  $\psi$ , and yaw rate  $\dot{\psi}$ . To express the vehicle motion in global coordinates, the global frame must be considered. The vehicle velocities,  $V_X$  and  $V_Y$ , can be represented as

$$V_X = v_x \cos \psi - \frac{L}{2} \dot{\psi} \sin \psi, \quad V_Y = v_x \sin \psi + \frac{L}{2} \dot{\psi} \cos \psi \quad (2.8)$$

The position of vehicle in global-frame coordinates,  $X(t)$  and  $Y(t)$ , can be obtained by integrating Eq. (2.8) so that

$$X = \int V_X dt + X(t_0), \quad Y = \int V_Y dt + Y(t_0) \quad (2.9)$$

## 2.3 Steering System Control Design

In this study, the steering system controller encompasses feedforward and feedback components. The feedforward controller includes the pursuit behavior of human driver and the feedback controller is comprised of the compensate behavior. The input of feedforward component is longitudinal velocity and curvature. Feedback controller is a lane keeping compensation controller that applies correction to the vehicle's lateral position error and heading error based on the road conditions. Both feedforward and feedback controllers are summed up as steering signal that is received by haptic steering device to provide intuitive haptic cues to the driver. A high-level block diagram is presented in Figure 2.5.

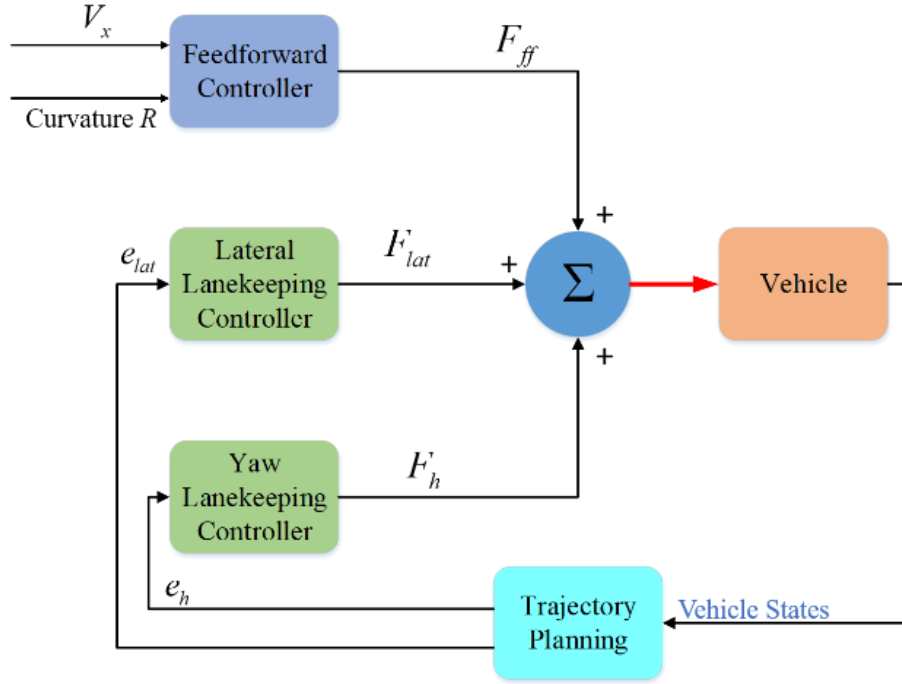


Figure 2.5: Block diagram of classical controller for vehicle lane keeping

### 2.3.1 Lanekeeping Feedback Force

For this study, a customizable steer-by-wire system is offered to the operator. The Falcon offers a haptic steering device input that provides the operator with direct force feedback when the vehicle is off the road. This not only warns the driver when the offset is small, but also assist them in restoring the vehicle to a safe position in its lane by adjusting the steering device to ensure safety. By introducing an underlying mathematical model, the feedback force may be properly estimated. The feedback controller is based on a proportional-derivative (PD) structure. PD control creates a virtual spring and damper between the estimated and reference vehicle positions. The reference trajectory includes the road center coordinate and ideal vehicle heading. Measured trajectory information,

calculated by sensors on the vehicle, include the current coordinate and heading of the vehicle.

The total force,  $F_t$ , applied to the robotic grip system is a combination of the driver and the electric motor in the lateral direction (e.g., steering commands occur in lateral manner while stop/go are communicated in longitudinal manner) so that

$$F_t = F_{fb} + F_{dr} = (F_c + F_l) + F_{dr} \quad (2.10)$$

where  $F_{dr}$  is the force actively given by the driver and is zero if the driver's hands are off the interface. The term  $F_{fb}$  is the summation of forces from two force feedback sources; a self-centering force  $F_c$ , and a lane keeping assistance force  $F_l$ . This research assumes that the robotic interface is linear.

Self-Centering Force: To recreate the feel of a traditional steering system, a self-centering force,  $F_c$ , can be added to match that of a mechanical steering system such that

$$F_c = -k_{p,c} y_{fal} - k_{d,c} \dot{y}_{fal} \quad (2.11)$$

where  $y_{fal}$  is the measured robotic grip's lateral position coordinate, while  $k_{p,c}$  and  $k_{d,c}$  are the proportional and the derivative gains.

Lane Keeping Force: The lane keeping assistance system is associated with the lateral error,  $e_{lat}$ , and the heading error,  $e_h$ , of the vehicle. These two errors can be expressed as

$$e_{lat} = Y - y_{ref}, \quad e_h = \psi - \psi_{ref} \quad (2.12)$$

where  $Y$  and  $\psi$  are the measured or estimated lateral position and vehicle heading, respectively. The terms  $y_{lat}$  and  $\psi_{ref}$  denote the desired lateral position and heading setpoint. The lane keeping assistance force,  $F_l$ , is equal to

$$F_l = F_{lat} + F_h = -(k_{p,l}e_{lat} + k_{d,l}\dot{e}_{lat}) - (k_{p,h}e_h + k_{d,h}\dot{e}_h) \quad (2.13)$$

with proportional gains  $k_{p,l}$  and  $k_{p,h}$ . Similarly, the derivative gains are  $k_{d,l}$  and  $k_{d,h}$ . Although a force feedback controller functions smoothly and effectively, it may have a time delay. In general, the effect of delays in closed-loop feedback systems resemble the impact of lowering the sampling frequency. To compensate for this scenario, a feedforward steering controller will be introduced.

### 2.3.2 Feedforward Force

Feedforward steering predicts the steering input to minimize tracking error. If a controller only includes feedback steering, the vehicle has to deviate from the path before the lane keeping system starts to drag the vehicle back to its lane. Thus, the addition of feedforward steering into the system will improve the performance since feedforward steering will steer the vehicle before it departs from the lane.

The expression for the feedforward steer angle,  $\delta_{ff}$ , required to negotiate a given curve (Wong, 2008) may be expressed as

$$\delta_{ff} = \frac{1}{R} \left( L + \frac{K_{us} v_x^2}{g} \right) \quad (2.14)$$

where  $L$  is the vehicle length,  $\frac{1}{R}$  is the curvature of the target path, and  $K_{us}$  is the vehicle understeer gradient. The feedforward force,  $F_{ff}$ , may be represented by introducing a stiffness gain,  $k_{ff}$ , that multiplies the feedforward steer angle,  $\delta_{ff}$  so that

$$F_{ff} = k_{ff} \delta_{ff} \quad (2.15)$$

## 2.4 Hardware-in-the-Loop Platform

To explore the real-time performance of operators using all three steering input device studied in this paper, a fixed based hardware-in-the-loop experimental test bench was created. The components included the haptic steering devices, a high-resolution image projector, and a Honda CR-V. Mathematical models, simulating the target vehicle dynamics and tire/road interactions, were integrated into the system through MATLAB/Simulink. The test bench core was the driver/haptic interface architecture and dedicated controller. The visual environment, created using the V-Realm Builder 2.0, was rendered by the Simulink 3D Animation toolbox. The resulting images were projected on a large screen for the devices. The Simulink environment recorded the vehicle behavior in real-time and simultaneously controlled the steering wheel actuator. The software package used to communicate with Falcon was the QUARC<sup>®</sup> Real-Time Control Software which includes a Simulink library block. The position readings are used in vehicle dynamics model.

The test bed functionality, shown in Figure 2.6, was presented to the human subjects in the laboratory (Mandhata et al., 2012). After evaluating the vehicle's current trajectory in vehicle dynamics block, the operator delivers the necessary force command

through the driver interface to guide the vehicle lane control tasks. The steering angle of the vehicle, recorded by the haptic steering device, was transmitted to the vehicle dynamics block theoretically corresponding to the remote vehicle. The embedded system model evaluates vehicle longitudinal velocity, vehicle heading, and vehicle steering angle to compute the resulting tire/road interface forces and moments, and update the trajectory and orientation in real-time. The test bed utilized in this study is a static driving simulator. Results may differ if a dynamic driving simulator is used. The average speed driving on a dynamic driving simulator will be lower than the average speed driving on a static driving simulator, because the driver will adapt to a more conservative driving style under the dynamic motion feedback. Also, the driver may experience more motion sickness such as cold sweat, dizziness, nausea and eye strain due to vertical head dynamics on a dynamic driving simulator.

The force feedback/feedforward measure block uses the simulated vehicle information such as vehicle lateral location and velocity to compute the steering feedback and feedforward forces, which then actuated the robotic grip's end effector by providing corresponding commands to the device motor. In the meantime, the virtual reality generator in MATLAB 3D Animation processed the vehicle information to represent a three-dimensional driving environment that was rendered on the screen by the image projector. This enables the operator to visualize the environment during the driving process. After receiving the visual feedback from the image projector in front of the driver, the driver can send his input force to the haptic steering device to get involved into system. The throttle

signal and brake signal of the robotic grip and joystick is delivered through the longitudinal push and pull of their end effector.

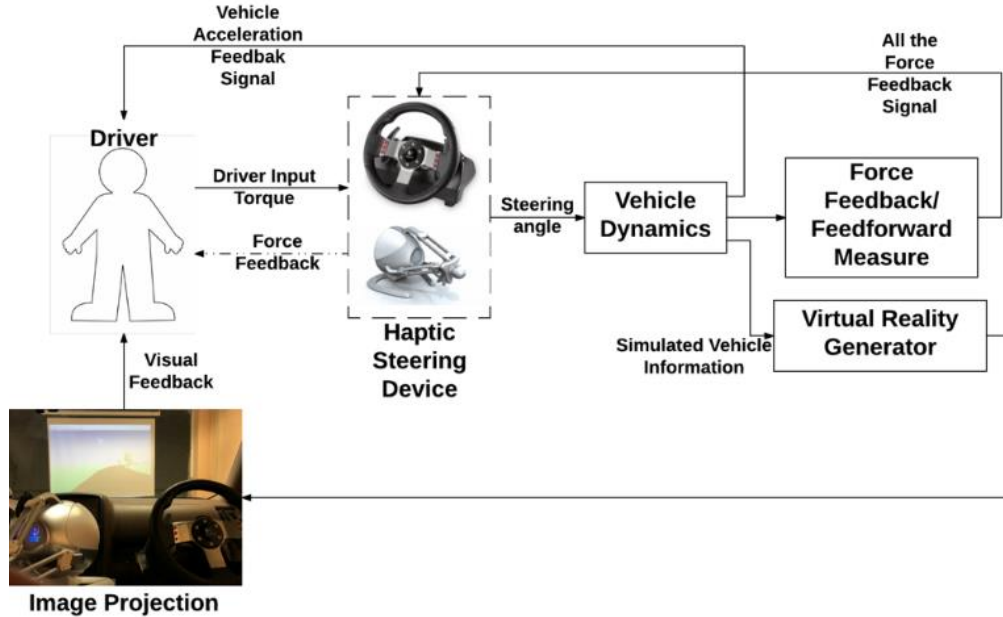


Figure 2.6: Hardware-in-the-loop haptic interface schematic

## 2.5 Operator-in-the-Loop Evaluation

To evaluate the practicability and performance of the alternative steering systems, eight human test subjects drove the experimental system and completed post-test questionnaires. A summary of the system parameters and their respective values are listed in Table 2. The test subjects first drove on the given roadways (refer to Figure 2.7) at the target speed with each steering device for several minutes to practice. The two different road profiles consisted of a highway and country road scenario. A Latin square design was used to ensure a randomized order of testing the different steering devices and road scenarios. A tradeoff exists between model sophistication and execution speed, so the scenery is somewhat limited. The operator is asked to use the respective steering devices



to drive on the divided road and maintain a position in the right lane. A questionnaire was completed after each test to offer feedback.

Table 2.2: Summary of hardware and model parameters

Symbol	Value	Units	Symbol	Value	Units
$C_{\alpha f}$	$5.04 \times 10^4$	N/rad	$k_{p,h}$	2.50	N/rad
$C_{\alpha r}$	$3.36 \times 10^4$	N/rad	$k_{p,l}$	8.60	N/m
$C_{\sigma}$	$1.42 \times 10^4$	N	$K_{us}$	0.027	Rad
$g$	9.80	m/s <sup>2</sup>	$L$	3	m
$I_w$	2.70	kg · m <sup>2</sup>	$l_f$	1.40	m
$I_z$	$1.89 \times 10^3$	kg · m <sup>2</sup>	$l_r$	1.60	m
$k_{d,c}$	0.17	N/rad	$m$	1500	Kg
$k_{d,h}$	0.03	N/rad	$R$	10.82	m
$k_{d,l}$	0.10	N/m	$r_{eff}$	0.41	m
$k_{ff}$	-23.34	N/rad	$\mu$	0.70	
$k_{p,c}$	2.10	N/rad			

To investigate the performance of each steering device and the effects of haptic feedback, five configurations were considered as shown in Table 3. Each participant was asked to operate the vehicle using a joystick, steering wheel, and robotic interface. Coupled with self-centering force feedback, the steering wheel, C2, has a OEM steering feel tuning. Two different cases, C3 and C4, were proposed for the robotic interface. Similar to C2, C3 also has a self-centering feedback force added to the grip to compare with the steering wheel under same control condition. Design of configuration C3 and C4 differs in the lane keeping feedback and forward controller discussed in Section 3. Design of steering wheel case C5 also includes the lanekeeping feedback and feedforward controller to study the impact of lanekeeping algorithm on the steering wheel.

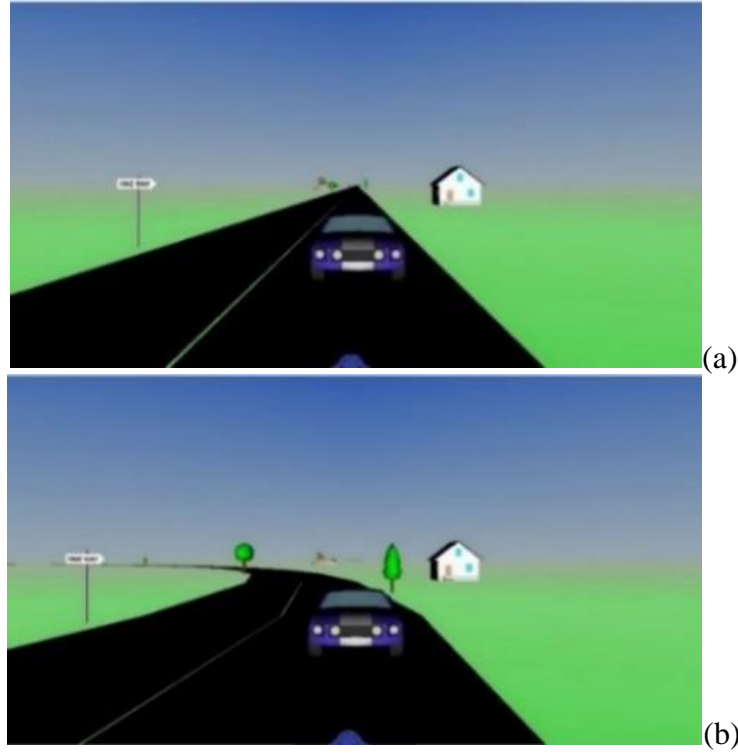


Figure 2.7: Haptic steering visualization environment - (a) straight highway; and (b) country road

During each test, the recorded crucial measurements included the vehicle lane position data (i.e., longitudinal and lateral coordinates), yaw angle and rate, longitudinal velocity, and driver input steering wheel angle. The driving trajectory of the operator was used to evaluate the performance of each participant. Following the test, the operators' actual trajectory is recorded and compared to the desired trajectory. The root mean square (RMS) of lateral error,  $e_{lat}$ , between the recorded and desired trajectory is calculated for each human subject. The RMS level of the lateral error in the case of a set of  $N$  values is

$$e_{lat}^{RMS} = \sqrt{\frac{1}{N} \sum_{j=1}^N |e_{lat}|^2}.$$

Table 2.3: Summary of steering device and feedback conditions

<i>Case</i>	<i>Description</i>	<i>Control Scenario</i>
C1	Joystick	None
C2	Steering Wheel	Self-Centering
C3	Robotic Interface Falcon	Self-Centering
C4	Robotic Interface Falcon	Self-Centering+ Lane keeping Feedback and Feedforward Forces
C5	Steering Wheel	Self-Centering+ Lane keeping Feedback and Feedforward Forces

As mentioned above, the goal of the highway drive test was to assess the lane keeping performance when driving on a straight road. The results of these tests are summarized according to steering input device and control scenario (refer to Figure 2.8a and 2.8b). For the eight different drivers using the joystick with no force feedback algorithm (C1), the average lateral error was 35.50 centimeters (50kph) and 40.04 centimeters (100kph). This average error was greater than that of the steering wheel (C2) which has the average lateral error of 27.48 centimeters (50kph) and 31.24 centimeters (100kph), and robotic grip (C3) which has the average lateral error of 27.40 centimeters (50kph) and 28.75 centimeters (100kph). After the addition of lanekeeping feedback and feedforward forces to both steering wheel and robotic grip, a dramatic lateral error decrease of 10.99 (50kph) and 12.91 (100kph) centimeters for robotic grip (C4) and 12.07 (50kph) and 11.2 (100kph) centimeters for steering wheel (C5) is observed. This decrease in lateral error indicates that the driver safety is significantly improved with some level of force feedback when driving with the steering wheel and the robotic grip. Furthermore, the

steering wheel with feedback C5 has a better performance than robotic grip C4 in low speed condition while robotic grip C4 exhibit superior lanekeeping than steering wheel C5 under high speed. Also, because there was no noticeable variation in terms of the RMS lateral error after an increase of speed, the effect of speed change on steering devices' performance on highway road scenario is inconclusive. The force applied to the robotic grip C4 ranged from -2.81N to 2.43N on highway.

The country roadway allowed the driver to perform on multiple curves to be evaluated at low and high speeds. The ability to steer the vehicle while maintaining a constant speed for maneuvers enabled human-machine interface to be better understood. Figures 2.8c and 8d display the results for cases C1-C5 on the country road under low and high speeds. As expected, the robotic interface and steering wheel steering cases with lanekeeping forces C4 & C5 displayed in Figure 2.8(c) has the highest level of performances. Joystick case C1's performance varied considerably among all the drivers. Driver 1,3, and 5 performed better than the other drivers while driver 2 and 4's performance was relatively deficient. Although the overall RMS lateral error raised due to an increase of speed from 50kph to 100kph in Figure 2.8(d), robotic grip C4's lateral error was not substantially affected by the speed change due to lane keeping control while C1-C3's performance was considerably deteriorated. The robotic grip and steering wheel with lanekeeping forces, C4&C5, delivers similar tracking performance in low speed condition. But when the speed reaches 100kph, the robotic grip C4 is far superior than steering wheel C5 given that C4 has 10 centimeters less average RMS lateral error. The recorded feedback

force applied to the robotic grip C4 ranged from -5.69N to 5.31N on country roadway scenario.

The improvement rate for the joystick, C1, and the robotic grip, C3&C4, compared to a traditional steering wheel, C2, derived from operator's driving path can be seen in Table 4. The red font indicates deteriorated performance and green font represents an improvement compared to the steering wheel. The performance of the joystick, C1, in all road scenarios and speed conditions is worse than the steering wheel. The performance of robotic grip with the self-centering feedback, C3, does not improve at low speed condition compared to steering wheel, C2, with an improvement rate of only -3.16% and -5.26% on straight road and country sinuous road respectively. But when the driver increases the speed to 100 kph, C3, delivers better results than C2 with an improvement of 10.28% and 14.87%. This is because the robotic grip's superior maneuverability to the steering wheel is more apparent when driving at unstable high-speed conditions. Steering wheel case C5 displays a tremendous enhancement in lanekeeping capability comparing to traditional steering wheel C2, with an astounding improvement rate of 42.77% on average thanks to the addition of lanekeeping feedback and feedforward forces. Robotic grip with both the self-centering and the lane keeping algorithms applied, C4, shows dominating performance over all the other conditions averaging 70.18% improvement on the lateral error with respect to tradition steering wheel, C2. This improvement is more apparent on a sinuous country road scenario than a straight road.

There are three key findings learned from the operator-in-the-loop evaluation. First, some level of force feedback was required with the steering controller to successfully

complete the lanekeeping maneuver. Most of the drivers performed the worst with joystick that has no force feedback. Second, drivers used robotic interface differently than the steering wheel to steer the vehicle on sinuous country roads. The robotic grip required much less physical movement, and therefore less expended energy to steer the vehicle during this lanekeeping maneuver. Consequently, the robotic grip may allow for a faster response to emergency and extreme maneuvers from driver with slowed reflexes. This finding explains the why robotic grip offer superior performance than steering wheel during high speed (100kph) driving shown in Table 4. Last but not the least, steering wheel maintains a certain level of dominance in low and moderate speed conditions. Another significant observation can be made is that during the country road driving scenario, most drivers would perform fast, small amplitude movements with the robotic grip versus gradual, large amplitude movement with the steering wheel. This further indicate potential safety benefits of robotic interface in driving situations like sharp turn and lane change that require extreme maneuvering.

Table 2.4: Average performance improvement for alternative devices when compared with traditional steering wheel (C2).

Road Scenario	Speed (kph)	C1 (Joystick)	C3 (Robotic)	C4 (Robotic w/ Lanekeeping)	C5 (Steering Wheel w/ Lanekeeping)
Highway	50	-35.01%	-3.16%	35.94%	40.97%
	100	-33.69%	10.28%	45.49%	33.50%
Country	50	-51.32%	-5.26%	44.23%	48.90%
	100	-22.06%	14.87%	70.18%	47.72%

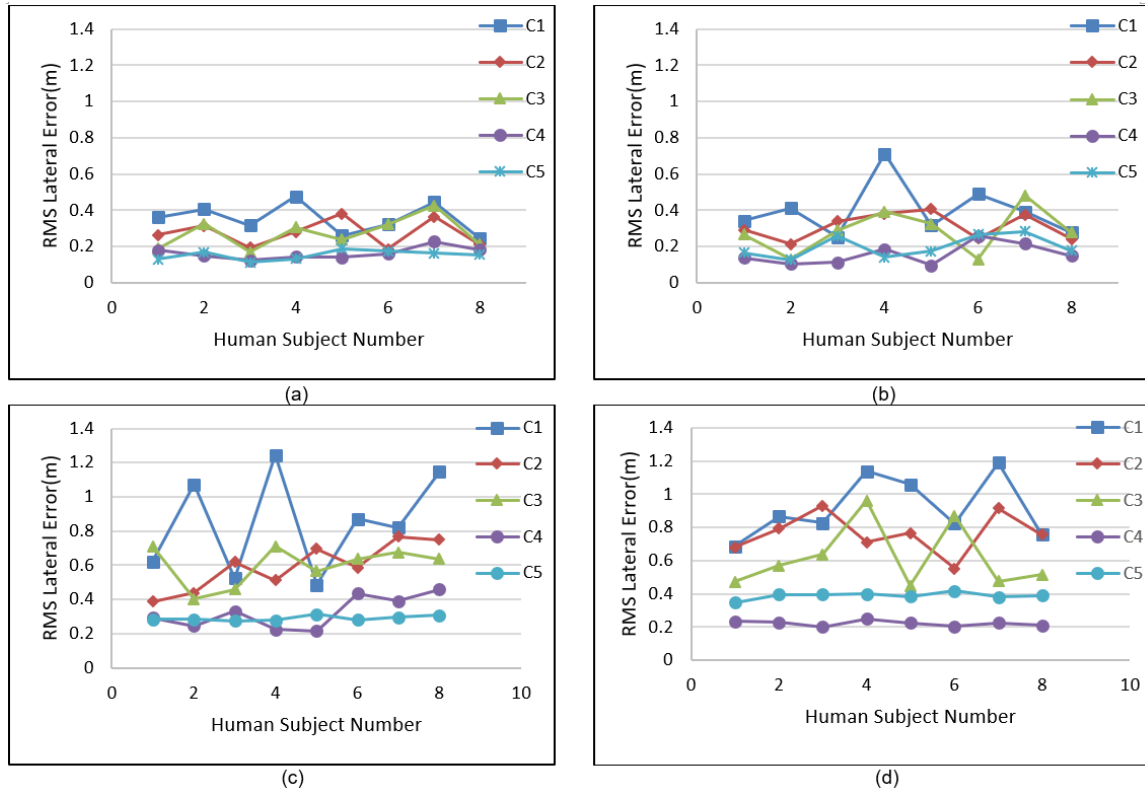


Figure 2.8: Lateral RMS error for cases C1 to C5 - (a) Highway at low speed (50kph), (b) Highway at high speed(100kph), (c) Country road at low speed (50kph), (d) Country road at high speed (100kph)

## 2.6 Conclusion

The growth in semi-autonomous and autonomous ground vehicles around the world has created a need for alternative steering input devices. The project objective was to compare driver performance when using a robotic interface mechanism versus a steering wheel and joystick in a driving simulator environment. The robotic interface was tested at two force feedback levels, while the steering wheel was used with self-centering feedback tuning. Human test subjects operated these interfaces for two road scenarios and two speed conditions. Subjective and objective results from the test demonstrate that the driver's experience can be enhanced up to 70.18% with a robotic steering input (e.g., Falcon) when

compared to the traditional steering wheel during extreme maneuvers. Laboratory results indicate that lane keeping efficacy is further boosted with the help of compensation feedback and preview feedforward forces added to the grip. The answer to the hypothesis put forth regarding the impact of robotic steering devices is: *yes, the lane keeping performance of the robotic steering input device surpasses that of the joystick and the steering wheel during emergency and extreme maneuvers.* The robotic interface steering devices, with adjustable feedback for future semi-autonomous and autonomous vehicle proposed in this study, falls in the Level 1 range of SAE's autonomy level definitions shown in Figure 2.9. Future work will include improving the control system design so that the execution of both vehicle steering and acceleration/deceleration through system alone can meet the Level 2 requirement.

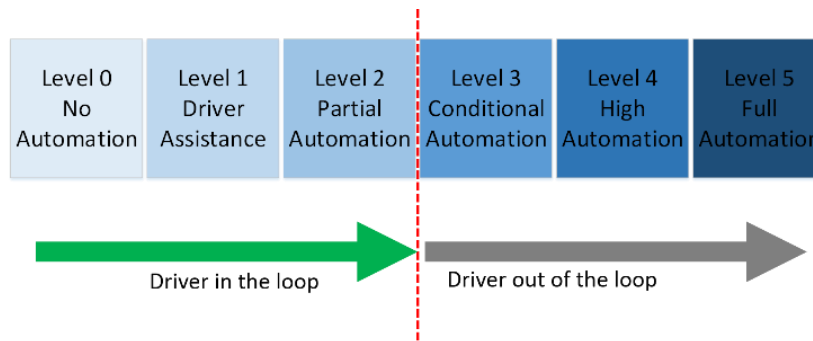


Figure 2.9: SAE (J3016) autonomy levels



## CHAPTER THREE

### EVALUATION OF A ROBUST HAPTIC INTERFACE FOR SEMI-AUTONOMOUS VEHICLES

The advent of steer-by-wire technologies has changed the driving paradigm for drivers and vehicle autonomy. Such technologies integrate electric motors to actuate the tire-road plus human-machine interfaces. Steer-by-wire vehicles can benefit from haptic concepts through the provision of tunable force feedback, coupled with nonlinear control, to introduce lane keeping and pathway following technologies that minimize and possibly eliminate driver actions. In this paper, two vehicle haptic interfaces, including a robotic grip and a joystick, both of which are accompanied by nonlinear sliding mode control, have been developed and studied on a steer-by-wire platform integrated with a virtual reality driving environment. An operator-in-the-loop evaluation that included 30 human test subjects investigated these haptic steering interfaces over a prescribed series of driving maneuvers through real time data logging and post-test questionnaires. A conventional steering wheel with the robust sliding mode controller was used for all the driving events for comparison. Subjective and objective results from the tests demonstrate that the driver's experience can be enhanced by up to 75.3% with a robotic grip steering input when compared to the steering wheel during extreme maneuvers. The robotic grip's superior performance in certain vehicle maneuvers indicates its potential as an alternative haptic steering adaptation for future semi-autonomous vehicles.

### **3.1 Introduction**

Lane departure crashes are one of the deadliest types of motor vehicle incidents. The U.S. Federal Highway Administration reports that such events account for 51% of motor vehicle deaths (U.S. Federal Highway Administration, 2018). A lane departure crash occurs when the vehicle leaves its lane, either moving into another lane or off the roadway itself. Although both automotive manufacturers and government agencies recognize the safety improvements needed for unintentional lane departures, relief may be offered through alternative steering devices that provide the driver with haptic cues such as lane departure warning vibration and lane keeping force feedback. The advent of haptic feedback steering in driver systems has the capacity to anticipate and compensate lane departure failures (which can be due to the driver, the vehicle, or the environment). Furthermore, the technology offers a pathway for autonomous vehicle operations. In this study, various steering devices have been investigated which provide haptic cues and reconfigurability to generate a flexible driving environment. The research goal is to replace the conventional steering wheel with a robotic interface device that provides adjustable haptic force feedback to the driver.

The ground vehicle SAE autonomy level with steering progression pathway has been displayed in Figure 3.1. The traditional steering wheel is the main device for Level 0 that offers no automation to the driver. After the development of drive-by-wire (DBW) technology (e.g. brake-by-wire, throttle-by-wire, steer-by-wire), autonomy levels 1 and 2 for driver assistance and partial automation are realized. The proposed alternative steering device, the robotic grip, is aimed at SAE autonomy level 3. It is designed to handle the situation that calls for an immediate response, such as evasive maneuvering. Such a device,

coupled with haptic feedback, provides immediate benefits to the driver, including enhanced safety during a crash with no risk of direct contact with a steering device, steering flexibility, and greater vehicle control (Andonian et al., 2003). The robotic grip naturally applies to levels 4-5 autonomy as well. When levels 4-5 suffer a fault and limp home operation is needed, the driver is responsible for the fallback performance of the dynamic driving tasks in which the operational envelope of the automated system is exceeded (Joshi, 2018). Assisting the human driver through haptic feedbacks, the robotic interface serves as a fallback steering controller which enables the avoidance and the mitigation of lane departure accidents (Wang et al., 2018b).

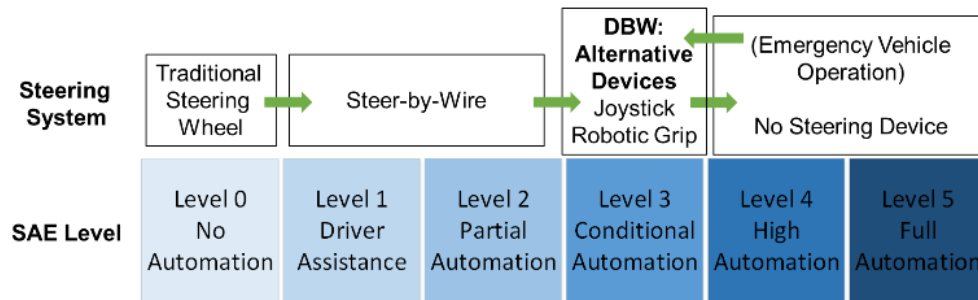


Figure 3.1: Progression pathway of steering devices for ground vehicles along the SAE autonomy level; emergency operation of level 4 and 5 vehicles accommodated with a “plug & play” steering interface

An extensive body of haptic force feedback steering research exists. Enriquez et al. (2001) proposed warning signals via pneumatic balloons on the steering wheel which inflated underneath the driver’s hand. Their approach had limitations: the pneumatic balloons were 10 cm long and thus provided only binary warnings. As observed by Beruscha et al. (2011), force (torque) feedback can remain unnoticed since it can be mistaken for driving related or “natural” torque caused by the tire/road interface. Medeiros-Ward et al. (2010) investigated the usability of a “sandpaper-like rubber tractor” on the

steering wheel under the index finger. They compared the effectiveness of auditory vs. tactile navigational instructions to the operator of a moving vehicle. Tactile shear cues were provided to the participants' index fingers as they gripped the steering wheel. Shakeri et al. (2016) conducted a user study to investigate the effectiveness of different haptic patterns. These patterns were presented on the outer rim of the steering wheel using three solenoids under each palm. They established a relationship between number of actuated solenoids and pattern identification rate. Wang et al. (2018) investigated various haptic steering devices and tested them on two road scenarios under two speed conditions. Results from the test indicated that the driver's performance can be improved with the haptic steering input when compared to the traditional steering wheel. Previous researchers have also investigated various force feedback steering assistance control strategies (Freeman et al., 2015; Jensen et al., 2013). For this paper, a sliding mode controller has been selected based on robustness and non-linearity.

The use of laboratory-based driving simulators as an alternative to field testing provides a safe, repeatable, and quick pathway to evaluate steering concepts. Despite these advantages, a laboratory-based driving simulator possesses several drawbacks. For instance, simulator discomfort such as motion sickness among certain groups may undermine training effectiveness and negatively impact the usability of simulators. Also, the physical and perceptual fidelity of a driving simulator is limited compared to a real vehicle. Zhang and Wang (2005) designed a hardware-in-the-loop steering simulator to study the effect of physical components, steering system dynamics, and other features such as soil stiffness on off-road vehicles. Setlur et al. (2003) assessed a hybrid vehicle steer-

by-wire system using hardware-in-the-loop and virtual reality environments. Most of the investigations involving human-subject simulators have focused more on driver behavior and performance instead of steering system design preferences. Norfleet et al. (2009) investigated three driving simulators in terms of their hardware and software, as well as their applications. The simulator capabilities reviewed varied from a fixed base to motion platform, desk top interface to in-vehicle cabin, and single to multiple computers to execute the software. Black et al. (2014) developed a high-fidelity steering simulator to support driver preference studies. The simulator SUV utilized features an electric power steering rack and pinion system and was validated using in-vehicle test data and two pilot studies. Andonian et al. (2003) created a fixed-base driving simulator with a 14-degree of freedom vehicle dynamics model to compare the lane tracking performance of test subjects using a joystick steering controller against a conventional steering wheel. They discovered that driver performance using a joystick was improved with the addition of force feedback.

To date, a considerable body of research has sought to develop lateral control strategies implemented in the form of steering torque to improve vehicle lateral performance. While this paper provides insights on the lateral controller, especially in regard to robust sliding mode control, it devotes a large amount of attention to evaluating the performance of three haptic steering interfaces, including the steering wheel, joystick, and robotic grip, all of which provide nonlinear lateral force feedback to the driver and assist in lane keeping. In particular, research on alternative steering devices for semi-autonomous vehicle is notably lacking. The replacement of the steering wheel on semi-autonomous vehicles is conceptually intriguing and this project seeks to fill this gap by

examining various potential haptic driving paradigms and benchmarking their performances against the steering wheel under different road scenarios and speed conditions. These haptic driving devices also serve as a contingency when semi-autonomous vehicles encounter extreme maneuvers that are otherwise unable to be handled solely by the automated system without human intervention. Thus, their performances in aggressive driving conditions are investigated to determine the most applicable device for semi-autonomous vehicles.

This paper evaluated three potential steering devices for implementation on Level 3 autonomous vehicles through quantitative and qualitative measures. These three steering systems have been procured from vendors in that they offer integrated feedback that may be computer controlled in real time. The steering wheel (Logitech G27) was secured from Logitech and offer a realistic experience with a known vehicle steering wheel device, throttle and brake pedal. On the other hand, the joystick (Logitech Wingman Force 3D) and robotic grip (Novint Falcon) are more modern and provided multi-channel for haptic feedback. The operation map for the three devices is shown in Figure 3.2. Steered in a one-handed manner with simpler functionality, the joystick and robotic grip devices require less effort and smaller motion from the driver compared to a traditional steering wheel. In addition, the joystick and robotic grip require much less space than a steering wheel. This size advantage leads to a more flexible steering device arrangement inside a semi-autonomous vehicle. The main steering device studied is a three degree-of-freedom (DOF) haptic robotic interface that uses a delta-robot configuration with three servo-actuated parallel links connected to a moving plate. The torques applied at the input link by the

actuators to achieve proper haptic feedback may be calculated. All joints in the robotic grip are one DOF revolute joints. The information between the device and the controlling computer is handled via USB connection. The robotic grip sends the position data to the computer that returns a force vector. Position is measured using encoders and the force vector is created by feeding the supplied currents to the servomotors in each parallel link (Rodríguez and Velázquez, 2012). A detailed forward and inverse kinematics model of the robotic grip can be found in (Fu et al., 2016).

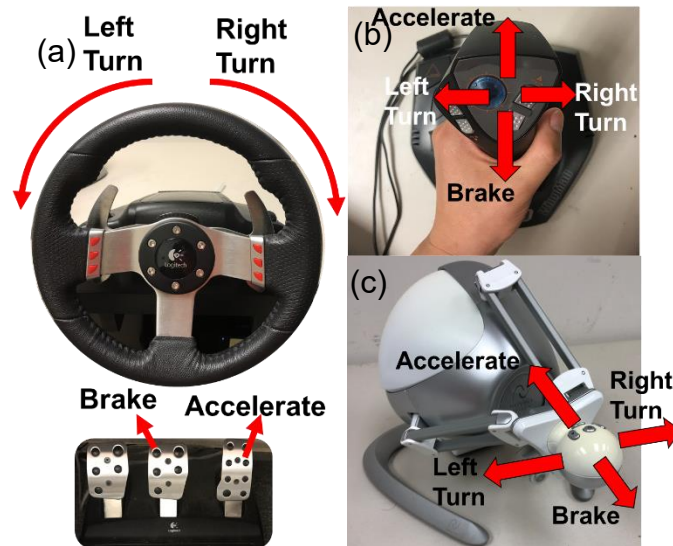


Figure 3.2: Haptic steering device operation map - (a) steering wheel with brake and acceleration pedals, (b) joystick, (c) robotic grip.

To evaluate vehicle handling performances, a nonlinear vehicle dynamics model implemented in the driving simulator includes the chassis dynamics and tire kinematics. The model generates the chassis response (e.g., longitudinal, lateral, and yaw velocities) and tire response (e.g., tire forces, moments, and slip angles). A high-level diagram of the system is shown in Figure 3.3. A human-in-the-loop study, involving 30 human subject

participants who are experienced drivers aged 18-30, was conducted to evaluate the effectiveness of the three haptic steering devices under different road scenarios.

Research Objective: *Can robotic inspired steering input devices with robust nonlinear control outperform the traditional steering wheel in terms of vehicle lane keeping?*

The remainder of the paper is organized as follows. The mathematical formulation and control structure are presented in Sections 2 and 3. The experimental setup with the accompanying operator-in-the-loop test results are summarized in Section 4. Finally, Section 5 offers the conclusion. The vehicle model and control parameter table, the test subject questionnaire, and a complete Nomenclature List appear in Appendices A, B, and C.

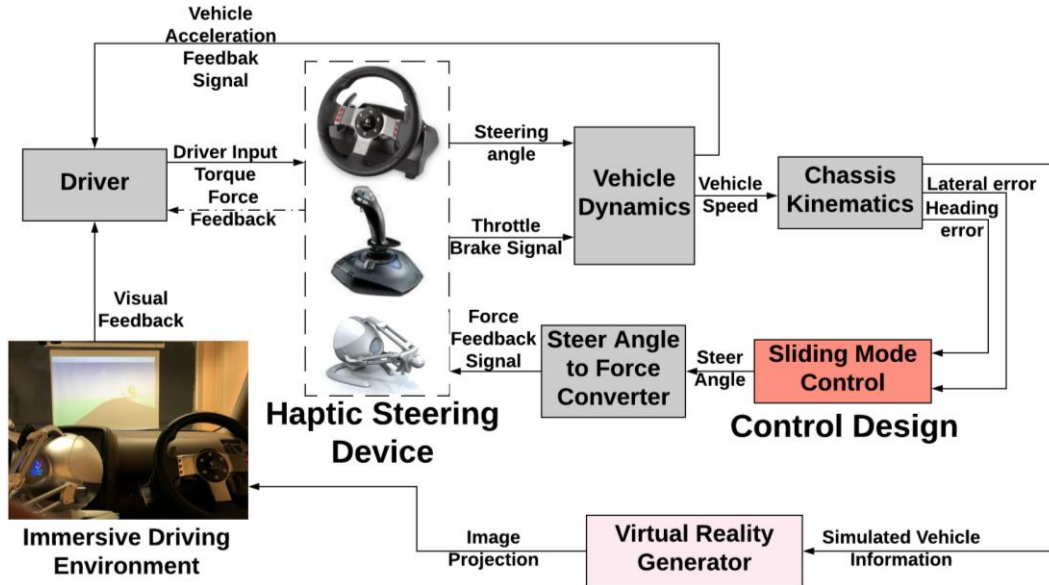


Figure 3.3: Closed-loop system design for human/machine steering interface

### 3.2 Steering System Model

The lateral characteristics of a semi-autonomous vehicle are influenced by the chassis dynamics and the front tires. The steering system provides lateral vehicle control



using a dedicated steering assembly which traditionally turns the front wheels. For convenience, a 7 DOF model that involves the longitudinal, lateral, and yaw motions, plus the four wheels rotations will be considered. The chassis, wheel and tire load interface, and lateral dynamics will be discussed in this section.

### 3.2.1 Vehicle Chassis

A nonlinear vehicle dynamic model has been implemented to evaluate control system performance. The three model states are the longitudinal velocity  $v_x$ , the lateral velocity  $v_y$ , and the yaw rate  $\dot{\psi}$ . Referring to Figure 3.4, the chassis dynamics may be expressed as (Freeman et al., 2016)

$$m\dot{v}_x = -m\dot{\psi}v_y + (F_{xfl} + F_{xfr})\cos\delta + F_{xrl} + F_{xrr} - (F_{yfl} + F_{yfr})\sin\delta \quad (3.1)$$

$$m\dot{v}_y = -m\dot{\psi}v_x + (F_{xfl} + F_{xfr})\sin\delta + F_{yrl} + F_{yrr} + (F_{yfl} + F_{yfr})\cos\delta \quad (3.2)$$

$$\begin{aligned} I_z\ddot{\psi} = & l_f (F_{xfl} + F_{xfr})\sin\delta + l_f (F_{yfl} + F_{yfr})\cos\delta - l_r (F_{yrl} + F_{yrr}) \\ & + \frac{l_w}{2} [(F_{xfr} - F_{xfl})\cos\delta + (F_{xrr} - F_{xrl}) + (F_{yfl} - F_{yfr})\sin\delta] \end{aligned} \quad (3.3)$$

where  $\delta$  denotes the front wheel steering angle,  $m$  is the vehicle mass, and  $I_z$  is the vehicle yaw moment of inertia. The longitudinal tire forces at the front left, front right, rear left and rear right tires are  $F_{xfl}$ ,  $F_{xfr}$ ,  $F_{xrl}$ , and  $F_{xrr}$ , respectively. Similarly, the lateral forces at the front left, front right, rear left, and rear right tires are by  $F_{yfl}$ ,  $F_{yfr}$ ,  $F_{yrl}$ , and  $F_{yrr}$ . The terms  $l_f$ ,  $l_r$ , and  $l_w$  refer to the distance from the center of gravity to the front wheels and rear wheels, as well as between the left and right wheels.



$$\alpha_{fl} = \alpha_{fr} = \delta - \frac{v_y + l_f \dot{\psi}}{v_x}, \quad \alpha_{rl} = \alpha_{rr} = -\frac{v_y - l_r \dot{\psi}}{v_x} \quad (3.5)$$

The longitudinal and lateral tire forces,  $F_{xi}$  and  $F_{yi}$ , may now be written as

$$F_{xi} = C_{\sigma i} \left( \frac{s_{xi}}{1 + s_{xi}} \right) f(\lambda_i), \quad F_{yi} = C_{\alpha i} \left( \frac{\tan \alpha_i}{1 + s_{xi}} \right) f(\lambda_i) \quad (3.6)$$

where  $C_{\alpha i}$  and  $C_{\sigma i}$  are the cornering and longitudinal tire stiffness. The variable  $\lambda_i$  and the function  $f(\lambda_i)$  are given by

$$\lambda_i = \frac{\mu F_{zi} (1 + s_{xi})}{2\sqrt{(C_{\sigma i} s_{xi})^2 + (C_{\alpha i} \tan \alpha_i)^2}}, \quad f(\lambda_i) = \begin{cases} (2 - \lambda_i) \lambda_i; & \lambda_i < 1 \\ 1; & \lambda_i \geq 1 \end{cases} \quad (3.7)$$

The term  $F_{zi}$  denotes the vertical force on the  $i$ th tire while the symbol  $\mu$  denotes the tire-road friction coefficient. The governing equation for the rotational speed of the wheels may be written as

$$I_w \dot{\omega}_{wi} = T_{di} - T_{bi} - r_{eff} F_{xi} \quad (3.8)$$

In this expression,  $I_w$  is the wheel inertia. The drive and braking torques are denoted as  $T_{di}$  and  $T_{bi}$ .

A summary of the vehicle and control model parameters is listed in Table A1 in the Appendix A.

### 3.3 Control System Design

A nonlinear higher order sliding-mode controller (SMC) will be considered for the steering system to provide lateral feedback to the driver and assist lane keeping. The nonlinear control structure designed to be integrated into all three haptic steering interfaces used in this study is shown in Figure 3.5. The motivation of using sliding mode control is

to achieve the ability to guarantee the control robustness against the system uncertainties and varying road conditions (Freeman et al., 2015).

The lane keeping assistance system considers the vehicle's lateral error,  $e_L$ , and the heading error,  $e_H$ , which may be defined as

$$e_L = y - y_{des}, \quad \ddot{e}_L = \dot{v}_y + v_x \dot{\psi} - \frac{v_x^2}{R}, \quad e_H = \psi - \psi_{des} \quad (3.9)$$

As shown in Figure 3.6,  $y$  is the measured or estimated vehicle lateral position. The term  $\psi_{des}$  is the desired yaw angle derived from the tangent of the road centerline. Similarly,  $y_{des}$  is the desired lateral position which is the lateral coordinate of the road centerline.

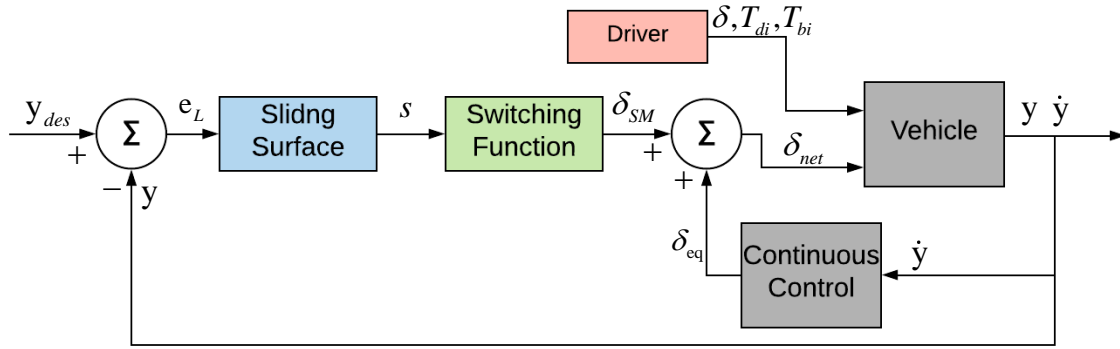


Figure 3.5: Sliding mode and classical control structures for vehicle lane keeping controllers

### 3.3.1 Sliding Mode (SMC)

Sliding mode control remains the most successful approaches in handling bounded uncertainties/disturbances and parasitic dynamics (Davila et al., 2005). The control concept is based on the introduction of a sliding variable function which is designed to become equal to zero. The main features of the sliding mode are its insensitivity to external and internal disturbances matched by the control, ultimate accuracy, and finite-time convergence of the sliding variable to zero. However, chattering is a problem impending

its implementation. The modified sliding mode control with boundary layer undergoes the degradation of tracking performance and robustness while reducing the chattering effect. Second order sliding mode control is a viable solution to reduce the chattering effect without affecting the tracking accuracy and robustness. For higher order systems a super-twisting algorithm can address the chattering problem.

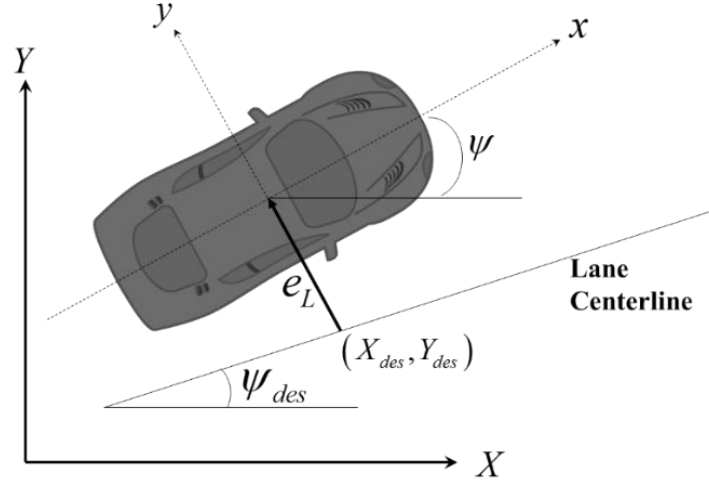


Figure 3.6: Lane keeping control system kinematics

Super-twisting sliding mode control begins with the dynamic system problem statement

$$\dot{x} = f(t, x) + g(t, x)u(t) \quad (3.10)$$

where  $x$  is the state vector,  $f$ ,  $g$  are continuous functions, and  $u$  is the control input. The sliding variable  $s$  may be defined so that the first-order time derivative of  $s$  yields

$$\dot{s}(t, s) = \phi(t, s) + \varphi(t, s)u(t) \quad (3.11)$$

The control authority (Alt et al., 2013; Kamal et al., 2014) may be written as

$$u = -k_a |s|^{\frac{1}{2}} \text{sign}(s) + v; \quad \dot{v} = -k_b \text{sign}(s) \quad (3.12)$$

which drives the sliding variable  $s$  and its derivative  $\dot{s}$  to zero in finite time. The terms  $k_a$  and  $k_b$  represent the sliding surface function gains and are positive constants.

Substituting Eq. (3.2) into Eq. (3.9) and simplifying yields

$$\ddot{e}_L = -\frac{C_{\alpha f} + C_{\alpha r}}{mv_x} \dot{y} - \frac{l_f C_{\alpha f} - l_r C_{\alpha r}}{mv_x} \dot{\psi} + \frac{C_{\alpha f}}{m} \delta - \frac{v_x^2}{R} \quad (3.13)$$

The control input is the steering wheel angle,  $u = \delta$ , and the control output is the lateral displacement,  $y$ . The objective of the control law is to eliminate the lateral displacement error,  $e_L$ . Select the sliding variable,  $s$ , as

$$s = \dot{e}_L + \lambda e_L \quad (3.14)$$

with a first-order time derivative  $\dot{s} = \ddot{e}_L + \lambda \dot{e}_L$ . Now substitute  $\ddot{e}_L$  per Eq. (3.9) so that

$$\dot{s} = -\frac{C_{\alpha f} + C_{\alpha r}}{mv_x} \dot{y} - \frac{l_f C_{\alpha f} - l_r C_{\alpha r}}{mv_x} \dot{\psi} - \frac{v_x^2}{R} + \frac{C_{\alpha f}}{m} \delta + \lambda \dot{e}_L \quad (3.15)$$

By correlating Eq. (3.11) and (3.15),  $\phi(t, s)$  and  $\varphi(t, s)$  can be represented as

$$\begin{aligned} \phi(t, s) &= -\frac{C_{\alpha f} + C_{\alpha r}}{mv_x} \dot{y} - \frac{l_f C_{\alpha f} - l_r C_{\alpha r}}{mv_x} \dot{\psi} - \frac{v_x^2}{R} + \lambda \dot{e}_L \\ \varphi(t, s) &= \frac{C_{\alpha f}}{m} \end{aligned} \quad (3.16)$$

Applying the super-twisting algorithm in Eq. (3.12), the control input becomes

$$\delta_{SM} = \delta_1 + \delta_2, \quad \begin{cases} \dot{\delta}_1 = -k_a |s|^{1/2} \text{sign}(s) + \delta_2 \\ \dot{\delta}_2 = -k_b \text{sign}(s) \end{cases} \quad (3.17)$$

To obtain a best estimate of the equivalent control for the sliding mode controller and to avoid important peaks in transient phases, a feedforward equivalent command  $\delta_{eq}$  obtained

by solving  $\dot{s} = 0$  that brings the system near to the sliding surface may be added to the control input (Tagne et al., 2016), and is given by

$$\delta_{eq} = \frac{C_{\alpha f} + C_{\alpha r}}{C_{\alpha f} v_x} \dot{y} + \frac{l_f C_{\alpha f} - l_r C_{\alpha r}}{C_{\alpha f} v_x} \dot{\psi} + \frac{m v_x^2}{C_{\alpha f} R} - \frac{m \lambda}{C_{\alpha f}} \dot{e}_L \quad (3.18)$$

Thus, the final steering angle representing the control input of the system should be

$$\delta_{net} = \delta_{SM} + \delta_{eq} \quad (3.19)$$

### 3.4 Operator-in-Loop Evaluation

An operator-in-loop (OIL) driving simulator environment has been created to assess the efficacy of the three haptic devices with accompanying controllers. In this section, the virtual environment, testing methodology, and experimental results will be presented.

#### 3.4.1 Test Environment

To explore the real-time performance of each operator using the steering input devices, a fixed-base hardware-in-the-loop experimental test bench was created. The driving simulator involves the synchronized operation of specialized hardware and software. The components included the haptic steering devices, a high-resolution image projector, and a Honda CR-V static vehicle. The visual environment, created using the V-Realm Builder 2.0, was rendered by the 3D Animation toolbox and projected on a large screen. The vehicle model, including wheels and chassis, and robust nonlinear controllers have been implemented in the MATLAB/Simulink environment [4]. All the steering devices are connected via USB to the main PC and communicate through QUARC® Real-Time Control Software to maintain timing and steering commands during the simulation.

The driving scenario selected for this study targeted influential sensory aspects of the lane keeping process, such as visual, audio, and steering feel, that could offer feedback and a sense of realism (refer to Figure 3.7). The vehicle speed was displayed on the screen, and the audio feedback played through the cabin speakers. The test bed utilized in this study is a static base driving simulator. Results may differ if a dynamic platform driving simulator is used. The average speed driving on a versus static driving simulator will be lower, since the driver will adapt to a more conservative driving style with dynamic motion feedback (Wang et al., 2018b).



Figure 3.7. Operator with robotic haptic interface

#### 3.4.2 Test Methodology

A total of 30 human subjects test drove the experimental system; they completed pre-test questionnaires that sought knowledge on operator's driving behavior characteristics and post-test questionnaires (refer to Table B1) after each scenario (Freeman et al., 2013). The research objective was to investigate the effects of three different steering devices, with integrated nonlinear sliding mode controller, on driver preference and performance. The test track profiles consisted of both straight and winding country roads; the latter features two circular paths with a radius of 200 and 100 meters as shown in Figure



3.8(a). A straight path was used to investigate the double lane-change maneuver, while the country road examines the curved path navigation capability. All 30 human subjects repeated these driving maneuvers for each of the three haptic steering interfaces. The drivers were requested to maintain the vehicle in the lane center. A slalom maneuver that is composed of a 300m straight road and 6 marking cones was also conducted to study the on-center handling behavior of the steering devices as shown in Figure 3.8(b). To control for learning that may arise from repeated activities, the sequence of scenarios was varied for each driver. A Latin square design ensured a randomized order of testing for the haptic steering devices. During each test, such objective measures as the vehicles lane position data (i.e., longitudinal and lateral coordinates), yaw rate, and lateral acceleration, along with the driver's input steering wheel angle, were recorded. After driving through each event, the drivers were requested to complete the post-test questionnaire and quantify the subjective measures of control and confidence, ease of driving, and safety.

The three different steering configurations, C1 = Steering Wheel, C2 = Joystick, and C3 = Robotic grip, all of which are integrated with the robust sliding mode control, were studied. All configurations are equipped with a self-centering mechanism to emulate original equipment manufacturer (OEM) steering feel. A tradeoff exists between model sophistication and execution speed, so the scenery is limited. The best performance corresponds to the case when an operator completes an assigned task with the smallest lateral position and heading error, and ideal handling performance (e.g., lateral acceleration, yaw rate). According to these criteria, the steering wheel that drivers are most familiar with may offer improved operation in comparison to the joystick and robotic grip at which

drivers are novice [4]. Based on these factors, three hypotheses have been proposed for the various steering configurations:

H1: The operator should be more confident in using the steering wheel, C1, due to familiarity.

H2: The joystick, C2, will require the least amount of physical driving efforts yet yield the highest lateral position tracking error.

H3: The robotic grip, C3, should offer higher lateral position error than the steering wheel, C1, but lower than the joystick, C2.

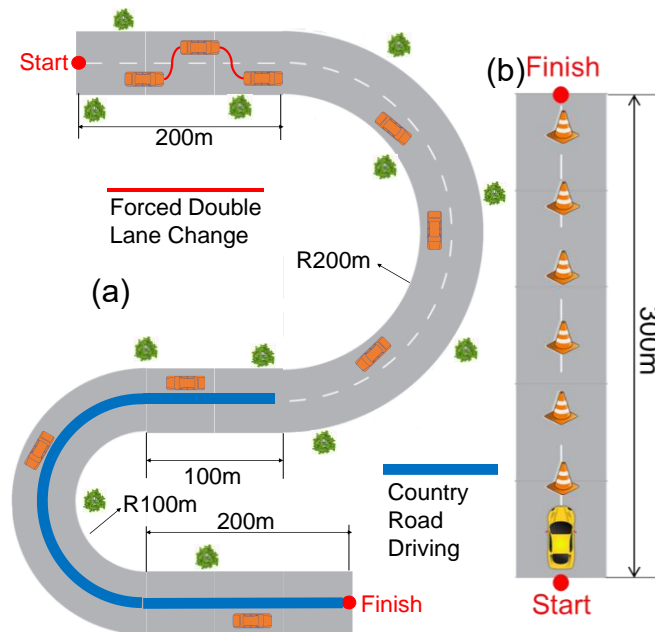


Figure 3.8. Virtual roadway with (a) lane change, and (b) slalom test.

### 3.4.3 Test Results

#### Double Lane Change Results

An aggressive double-lane-change maneuver per ISO 3888-1 (shown in Figures 3.9 and 3.10) was used to evaluate the effectiveness of each candidate steering device (ISO 3888-1, 1999). In this test, the vehicle enters the course at a speed of 50 kph and the

accelerator pedal is released. The driver then attempts to negotiate the course without striking the cones. The ISO double-lane-change maneuver is typically performed as a closed-loop driving test and is used to adjust the dynamics of a vehicle based on the subjective evaluations of professional drivers.

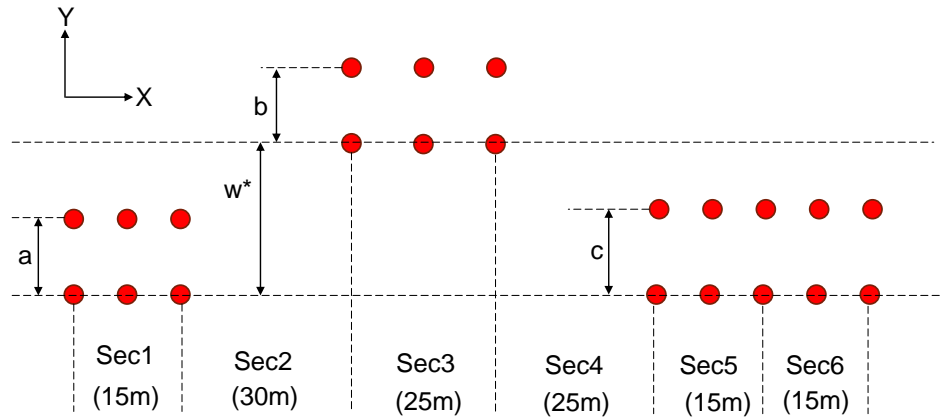


Figure 3.9. ISO 3888-1 double-lane-change maneuver test track [26]

The vehicle trajectories, steering angle, and lateral (y position) error of the 16th operator with steering devices and sliding mode feedback at 50kph, C1-C3, when driving through the double-lane-change maneuver are shown in Figure 3.11. The desired vehicle trajectory is shown in black dash-dotted line in Figure 3.11(a) (Jalali et al., 2013). The maneuver was successfully completed by the drivers using all steering devices, indicating the robustness and proficiency of the nonlinear haptic feedback. The steering wheel, C1, and the robotic grip, C2, understeered at the lane sections 2 and 4. The steering device steering angle response with respect to time is depicted in Figure 3.11(b). The steering angle for joystick and robotic grip was lower than the steering wheel, indicating that the steering efforts from the joystick are the lowest among all steering devices followed by the robotic grip. The steering wheel requires the largest steering effort during a double lane

change, a fact confirmed by the operators who were overwhelmed by the intensity of steering torque exertions they experienced from the sliding mode feedback. The lateral tracking error of the robotic grip, C3, was the lowest overall followed by steering wheel as shown in Figure 3.11(c). The joystick's lateral error is the highest, indicating the unreliability of the such devices in aggressive driving conditions. It is also clear that the robotic grip is an ideal steering device for the double lane-change maneuver.

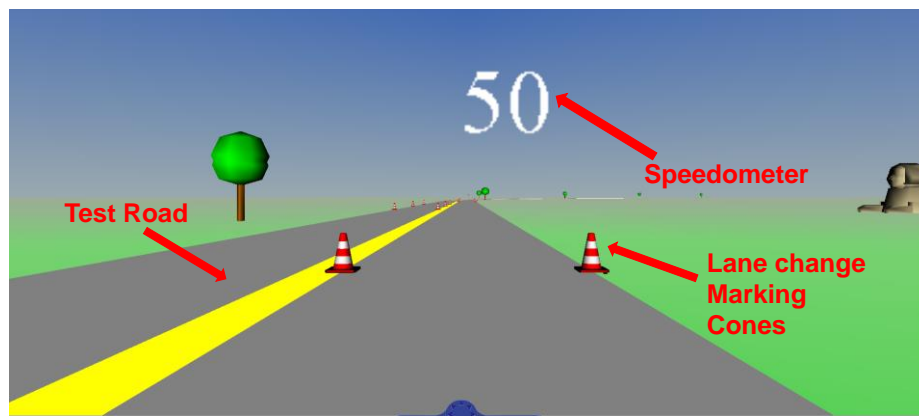
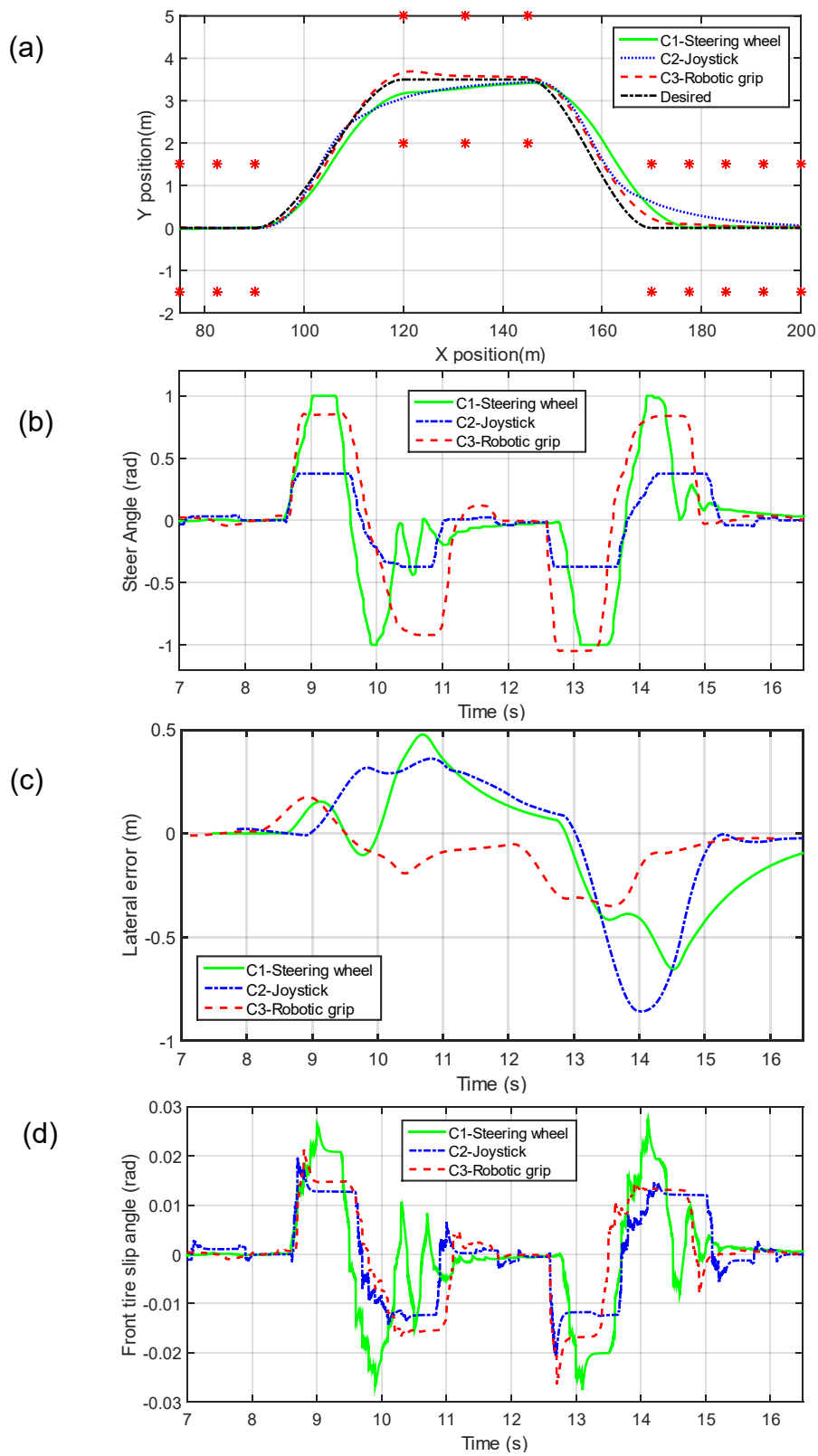


Figure 3.10. Double lane change simulator scene in software animation

The front and rear tire slip angle responses with respect to time in the driving environment during the double lane-change test at 50kph are displayed in Figures 3.11(d) and (e). The front tires generate a maximum 0.02-0.03 (rad) slip when entering the first left maneuver, and repeat again when returning to neutral yaw and vice versa. The deformation in the tire tread supports the vehicle dynamics through appropriate lateral force. The larger tire slip angle of the steering wheel indicates a higher tire lateral force, which in turn maximizes the vehicle's ability to grip. Thus, it can be deduced that the vehicle operated by the joystick has the worst traction during a double lane-change, due to the relatively lower tire slip angle. When the vehicle is entering the last straight road section (at 15s), the robotic grip and the steering wheel's front tire slip angles both settled from the overshoot

relatively fast. On the other hand, the joystick's settling time is the longest, indicating that the vehicle operated by the joystick recovers slower to a stable condition after the lane-change than the vehicles operated by the steering wheel and robotic grip.



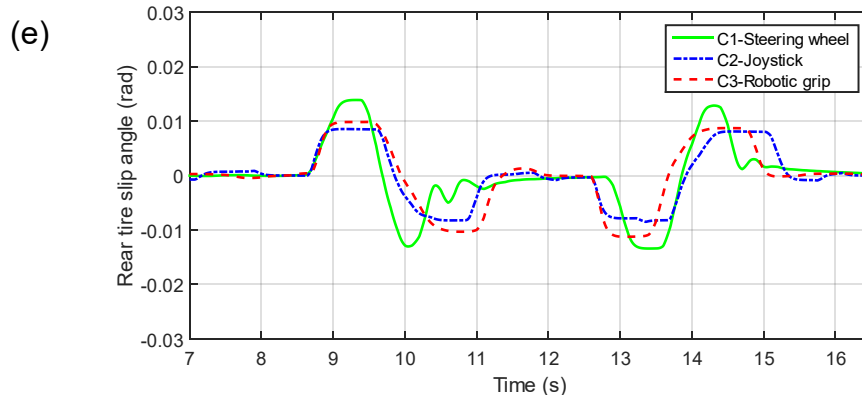


Figure 3.11. Human subject #16 data for three steering configurations, C1-C3, during a double-lane-change maneuver starting at 50kph- (a) vehicle trajectories, (b) steer angle, (c) lateral position error, (d) front tire slip angle, and (e) rear tire slip angle.

### Country Road Driving Results

After the completion of the double lane change maneuver, the drivers then traveled on a 200m radius curve before entering the country road driving sections which consisted of a 100m radius curve and two straight roads (refer to Figure 3.8(a)). This portion of the track served as a demonstration of the operators' ability to drive on a winding roadway under conditions C1-C3 at both 50kph and 80kph.

The country road driving vehicle responses from human subject #22 are presented in Figure 3.12. The vehicles' steering angle responses under low and high speed were plotted in Figure 3.12(a) and (d). Consistent with the trend from the double lane change maneuver, the joystick steering angle is the lowest during the circular path negotiation. This finding means that the driver's joystick steering effort is the lowest while more steering exertion needs to be applied to the steering wheel to navigate the same curve. When the vehicle is passing through the circular track, the steer angle response of the joystick is chattering severely. The main reason is that the sliding mode controller innate chattering feature is amplified by the fast steering response from the joystick. The vehicle

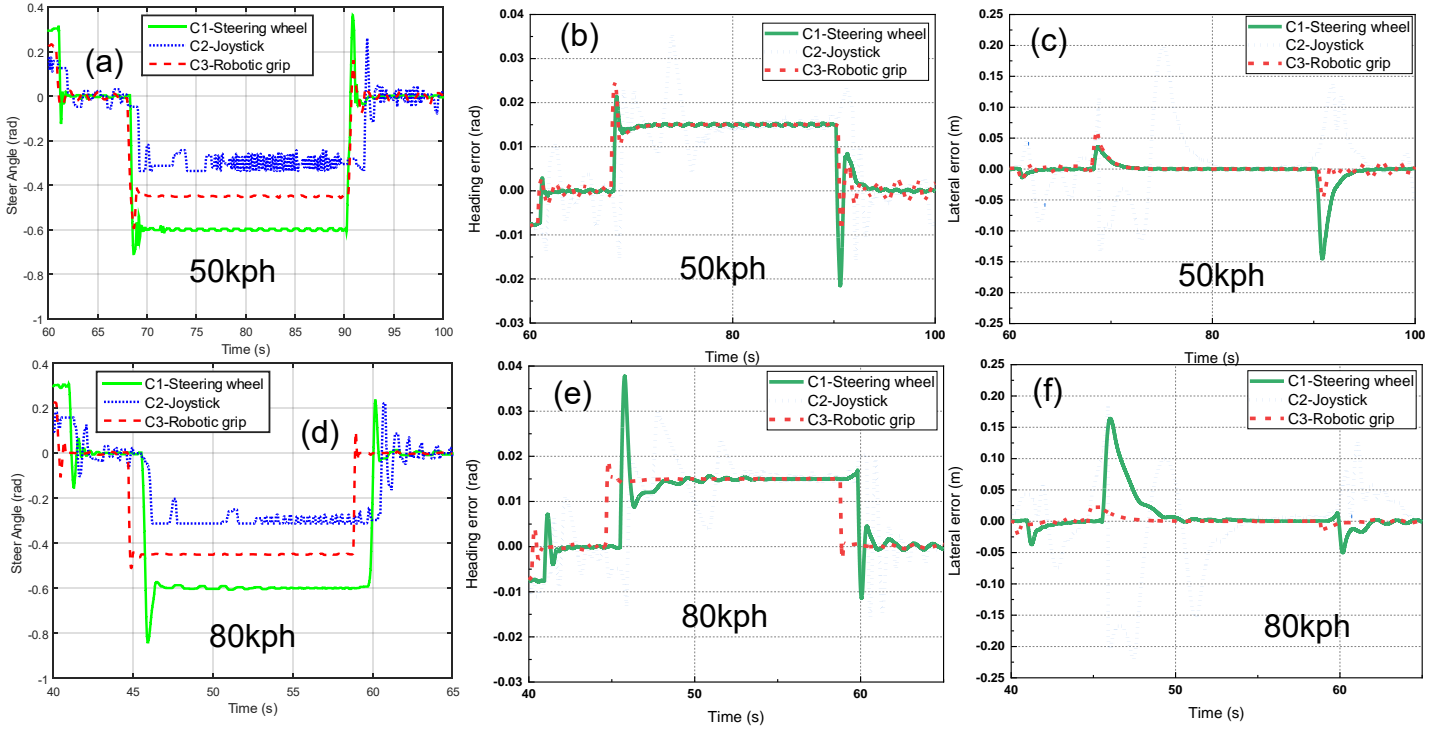


Figure 3.12. Human subject #22 data for three steering configurations, C1-C3, during the winding country road scenario at 50 and 80kph: (a, d) steer angle, (b, e) heading error, and (c, f) lateral error.

steer angle under 80kph in Figure 3.12(d) further verified excellent performance delivered by the robotic grip under both low and high-speed conditions. Not only was the robotic grip's steering angle the most stable during the whole navigation, but also its steer angle overshoot was the lowest at junction between 100-m radius circular path and straight road, a fact that ensures the best handling at the sacrifice of higher lateral acceleration.

Formed by the error between the actual heading angle of the vehicle and the tangential direction of the desired path, the vehicle heading error from human subject #22 under 50kph and 80kph can be found in Figures 3.12(b) and (e). During the cruising of two straight road segments (60s-68s and 92s-100s), the steering wheel, C1, exhibits the most stable condition followed by robotic grip, C3, whereas the joystick, C2, oscillates irregularly and reaches a marginally stable condition. On the circular path section (69s-



91s), both robotic grip and steering wheel devices reached a stable condition while the joystick reached a marginally stable condition. It is also noteworthy that the robotic grip has the lowest settling time from among all three devices, indicating its superior recovery capability from disturbances compared to other steering devices. Further, the robotic grip generated the lowest heading error overshoot during the junction between straight and circular path under both low and high speed conditions, guaranteeing a safer driving experience under high speed aggressive maneuvering.

The lateral error, which is the orthogonal distance from the center of gravity (CG) of the vehicle to the desired lane center, is depicted in Figures 3.12(c) and (f). Under the low speed condition displayed in Figure 3.12(c), all steering devices negotiate this segment efficaciously with lateral errors of 0.12m (C2), 0.04m (C1), and 0.06 (C3) at the first junction between the straight road and the circular path at 68s. At the second junction between the circular path and the straight road at 90s, only the robotic grip successfully completed this intense maneuver with maximum lateral error of merely 0.05m. During the circular path phase (70s-90s), the steering wheel and robotic grip exhibit a relatively steady error fluctuation, whereas the joystick did not reach a stable steady state condition, meaning that the vehicle operated by joystick experiences a lot of swaying. Under high speed condition in Figure 3.12(f), the robotic grip, C3, maintained its good performance, as its lateral error at the junction between straight road and circular path was the lowest among all three steering devices. The steering wheel, C1, also maintained a low lateral error on the straight path (41s-46s and 60s-65s), but its lateral error deteriorated at the junction between straight road and circular (46s and 60s) and became 0.17m and 0.05m at both

junctions respectively. The joystick, C2, continues its inferior performance, oscillating irregularly during all phases of the curve path navigation.

To further comprehend the vehicle handling performance under high speed country road driving, the vehicle's front and rear tire slip angle responses of the 22th operator driving at 80kph on the country road are displayed in Figure 3.13. With larger slip angles from the steering wheel, C1, during the junction (46s) between the straight road and the circular path, it will require more steering angle to sustain the desired path through the corner. Smaller slip angles on the front tires from the joystick, C2, and robotic grip, C3, will require less steering angle to maintain the desired cornering line. Unlike the rear tires, if the front tires develop a larger slip angle, the operator is free to turn the steering wheel a little farther and still maintain the desired direction of travel, a situation which is considered understeer. With the robotic grip, the driver operated the tires with the smallest slip angles and hence avoided the saturation of the front wheel lateral forces and excessive understeer. During the 100meter radius curve path driving (46s-58s), the front and rear tire slip of the steering wheel and robotic grip maintained a steady response while the joystick's front tire slip angle fluctuated in the latter half section, indicating that the front tire operated under joystick assisted by sliding mode controller will wobble during circular track negotiating that can cause severe tire damage. Finally, all three steering devices' front tire slip angles overshoot at the junction between circular track and straight road (60s). The robotic grip not only has the smallest overshoot, but also the least amount of settling time (1.2seconds), indicating the strong tire deformation recovery capability from the robotic interface. The steering wheel also recovered relatively fast (1.6 seconds) whereas the joystick's recovery

time is 5.1 seconds.

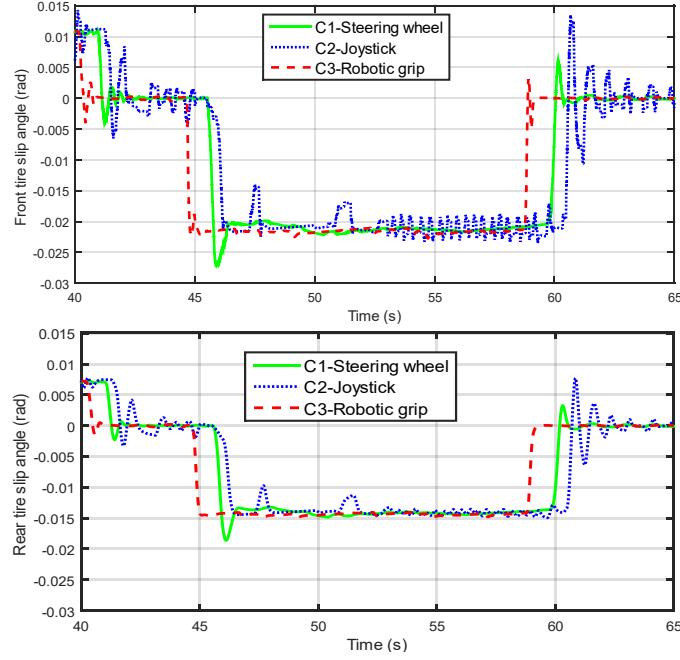


Figure 3.13. Human subject #22 data for three steering configurations, C1-C3, during country road driving at 80kph- (a) front, and (b) rear tire slip angles.

Following the completion of human subject tests, all 30 operators' actual trajectories are recorded and compared to the desired trajectory. The root mean square (RMS) of the heading error,  $e_{HRMS}$ , lateral error,  $e_{LRMS}$ , and lateral acceleration,  $\ddot{y}_{RMS}$ , are calculated and recorded for each human subject under low and high-speed conditions (50kph and 80kph) in Table 1. Along with the RMS values, the maximum value of heading error,  $e_{Hmax}$ , lateral error,  $e_{Lmax}$ , and lateral acceleration,  $\ddot{y}_{max}$  are also recorded for all configurations and speed conditions. Under the robust sliding mode controller, the robotic grip, an ideal steering device for extreme maneuvers, exhibited the lowest mean lateral error under both low and high-speed conditions at the sacrifice of relatively large lateral acceleration. The mean lateral error improvement of the robotic grip compared to the steering wheel is 75.3% under 80kph. The robotic grip presented the lowest average and

maximum lateral acceleration followed by the steering wheel under 50kph, indicating that the drivers' comfort during extreme maneuver can be guaranteed driving with robotic grip under low speed. The joystick, however, appears to produce the highest lateral acceleration among all three steering devices. The steering wheel, instead, outputs the lowest chassis lateral acceleration under 80kph, assuring the most comfortable ride for the driver at the expense of minor lateral deviation. The joystick delivers the poorest results in almost all variables that are recorded in the table, making it a highly undesirable steering device in most driving conditions.

Table 3.1: Average of all N=30 human subjects heading error, lateral error, and lateral acceleration results for three steering configurations, C1-C3, at 50 and 80 kph (highest value highlighted in bold, lowest value is underlined). Note that  $e_{HRMS}$ ,  $e_{LRMS}$  and  $\ddot{y}_{RMS}$  are the root mean square values, while  $e_{Hmax}$ ,  $e_{Lmax}$  and  $\ddot{y}_{max}$  are the maximum values for test subjects.

Test No.	Control Algorithm	Speed (kph)	Config	$e_{HRMS}$ (rad) ( $\times 10^{-3}$ )	$e_{Hmax}$ (rad) ( $\times 10^{-2}$ )	$e_{LRMS}$ (m) ( $\times 10^{-2}$ )	$e_{Lmax}$ (m) ( $\times 10^{-1}$ )	$\ddot{y}_{RMS}$ (m/s <sup>2</sup> ) ( $\times 10^{-2}$ )	$\ddot{y}_{max}$ (m/s <sup>2</sup> ) ( $\times 10^{-1}$ )
1	Sliding Mode Control	50	C1	<u>8.50</u>	<u>2.14</u>	<u>0.69</u>	<u>0.36</u>	0.57	0.81
2			C2	<b>9.50</b>	<b>3.55</b>	<b>3.91</b>	<b>1.97</b>	<b>1.48</b>	<b>1.27</b>
3			C3	8.60	2.47	1.26	0.60	<u>0.44</u>	<u>0.56</u>
4		80	C1	8.50	2.99	1.90	1.64	<u>0.66</u>	<u>0.48</u>
5			C2	<b>9.30</b>	<b>3.77</b>	<b>4.86</b>	<b>1.88</b>	<b>2.01</b>	<b>1.11</b>
6			C3	<u>8.40</u>	<u>1.88</u>	<u>0.45</u>	<u>0.24</u>	0.77	1.07

Some conclusions may be put forth based on the test results as follows:

1) The test condition associated with joystick, C2, exhibits an unfavorable handling performance compared to the steering wheel and the robotic grip. The corresponding heading error, lateral error, and lateral acceleration were highest in all test cases.

2) The steering wheel, C1, offers better performance than the robotic grip, C3, under low speed condition (50kph). Case C1 reduced the position tracking error by 45.2% when compared to C3. The robotic grip, C3, offers better performance than the steering wheel (C1) under high speed condition (80kph). Case C3 reduced the position tracking error by 75.3% when compared to C1.

3) The robotic grip, C3, is the most comfortable steering device to operate under low speed condition as its lateral acceleration is the lowest among all three devices. The steering wheel, however, becomes the ideal steering device under high speed condition in which its lateral acceleration is the lowest. It is important to stress that the lateral acceleration produced by all three steering devices under all speed conditions is less than 0.4g, which is the limit for ensuring driver's comfort during cornering, mainly thanks to the robustness of the sliding mode controller.

### Slalom Event Results

A slalom event, whose snapshot is displayed in Figure 3.14, was adopted to evaluate the on-center handling behavior of the three haptic steering devices. The slalom test is an open-loop procedure conducted on a test track that follows a straight-line path. The on-center handling represents that part of the straight-line directional stability characteristic of the vehicle existing at low lateral acceleration levels. In the slalom scenario, the drivers were requested to complete a weaving roadway at a constant speed of 50kph. A 300m long track with two 2.2m wide lanes was selected; 6 cones were placed at the intervals of 30m starting at 100m. A subset of 10 individuals in the test pool drivers were requested to complete this driving scenario.

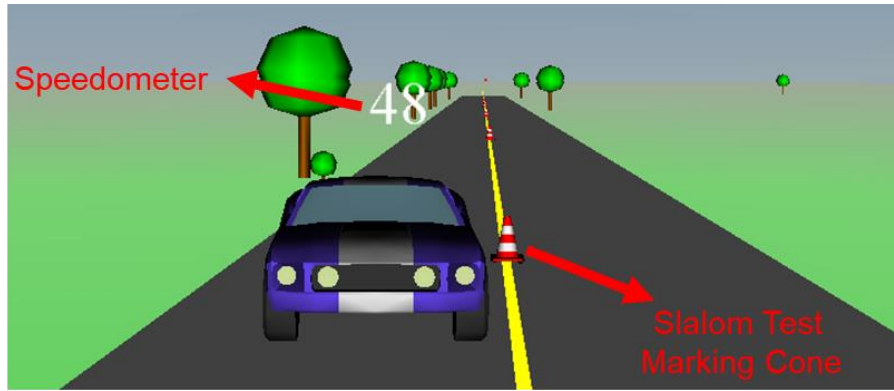


Figure 3.14. Snapshot of the vehicle on the slalom course

The vehicle trajectories, and yaw rate versus steer angle response of driver #16 with the haptic steering devices and sliding mode feedback at 50kph, C1-C3, when driving through the slalom maneuver are shown in Figure 3.15. The maneuver was successfully completed by the driver using all steering devices, indicating the trustworthiness and effectiveness of the nonlinear haptic feedback from the sliding mode control. As can be seen in Figure 3.15(a), although driver #16 is able to steer the vehicle through the slalom maneuver with the joystick, C2, the vehicle trajectory obtained from the joystick steering is uneven. On the other hand, the driver was able to negotiate the same maneuver much more easily and smoothly when steering with the steering wheel, C1 and the robotic grip, C3. This fact is confirmed in Figure 3.15(b), which illustrates the vehicle yaw rate with respect to steer angle. The closer this plot is to a straight narrow line, the more steering linearity the vehicle demonstrates, which indicates the best on-center handling performance driving with the steering wheel, C1. In addition, for on center steering, the joystick, C2, has a significantly faster response and higher yaw rate than the steering wheel, C1, and the robotic grip, C3. Consequently, the vehicle steered by the joystick is more responsive than the vehicle operated by the steering wheel and robotic grip. The high steering sensitivity

also explained the joystick-driven vehicle nonlinearity and deteriorated performance in the slalom test.

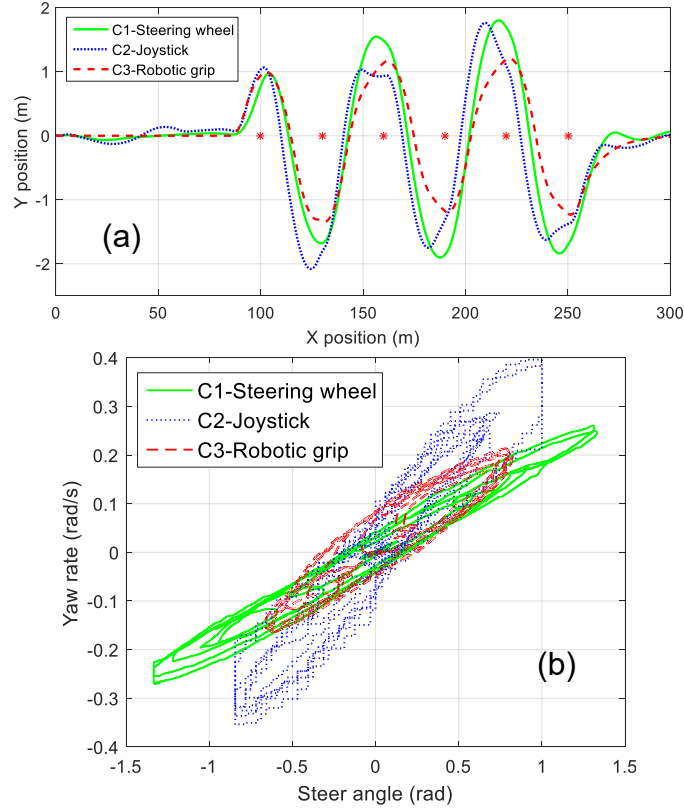


Figure 3.15. Human subject #16 data for three steering configurations, C1-C3, during a slalom maneuver starting at 50kph, (a) vehicle trajectories, and (b) yaw rate vs steer angle, the red asterisks represent slalom test marking cones.

### Post-Test Questionnaire Results

This section summarizes the information collected in both the initial demographic questionnaire and the post-task evaluation of the driving experience from each participant. The total number of participants for the study was 30, all of whom are students in the age range of 18 to 30 years, with the majority being between 18 to 21. Of the participants, 16 were male, and 14 were female. Self-identified as excellent drivers who have been driving for at least 3 years, all test subjects indicated they have used the cruise control feature in a

vehicle before. Only 11 individuals stated that they have driven in a driving simulator prior. When asked whether they had driven an autonomous or semi-autonomous vehicle that has been sold on the market, only 2 were noted to have any experience at all. Also, no driver has ever attended an advance driver training program that focused on safe driving practices.

Subjective reactions to the steering system feedback settings were evaluated through a questionnaire (refer to Table B1 in Appendix B) developed by factor-analyzing a set of nine questions, each rated by the test subjects, on a scale of 1 to 7 (Mandhata et al., 2012). The questions were grouped to evaluate three factors: (i) degree to which participants felt a sense of confidence and control over the steering system (Questions 1-4, symbol O1), (ii) perceived ease-of-use of the steering system (Questions 5 and 6, symbol O2), and (iii) perceived safety of the vehicle (Questions 7-9; symbol O3).

The subjective reaction measures for the three steering devices, C1-C3, and the driver observations, O1-O3, have been displayed in Figure 3.16 radar plot. It can be noticed that for the confidence and control measure, O1, the participants gave the highest rating to the steering wheel, C1, due to familiarity. Results also shows that the comfort for the robotic grip, C3, is the lowest mainly because the claw grip holding style from the robotic interface can be tiring for long-term driving. Additionally, the ease-of-use factor, O2, exhibited a novel pattern with joystick, C2, being most preferred followed by robotic grip, C3, and steering wheel, C1. The novel pattern of ease-of-use may be explained by the single-handed operation of joystick and robotic grip that demanded much less physical effort from the operator during both regular driving and evasive maneuvering. Lastly, a detail worth mentioning is that most operators rated high scores on the steering wheel, C1,



for being able to drive the vehicle safest at low speeds and also rated high scores on the robotic grip, C3, for being able to drive the vehicle safest at high speeds.

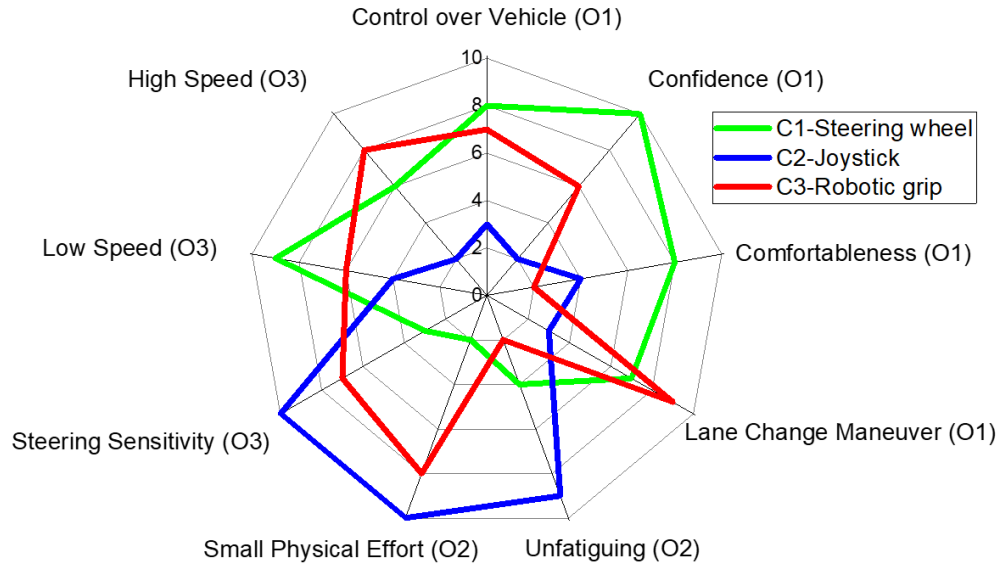


Figure 3.15. Nine subjective measures for three steering devices based on human subjects' responses to the questionnaire in Table B1 normalized to 10.

### ANOVA Statistical Analysis Results

Analysis of variance (ANOVA) is common technique adopted to examine a hypothesis concerning the means of multiple populations. A two-way repeated measure analysis of variance was used to separately analyze and determine whether there was a statistically significant effect by the two treatment factors studied in the Hypotheses H1-H3: speed and devices. The ANOVA results for the lateral error and the human subject confidence level for the road course are shown in Table 2. The first observation is that the steering devices and vehicle speed both individually had a significant effect on the lateral error magnitude generated by the participants. This result matches the expectation that the generated lateral error should increase with more speed and inferior steering devices as the lane keeping process becomes more difficult under these conditions. For interaction of the

speed and steering devices (Speed×Devices), it can be concluded that interaction between those two factors have a significant effect (p-value=0.0288). Moreover, the steering devices significantly impacted the confidence level of the participant drivers. This was another expected result as the different characteristics of the three steering devices created drastic variations in driving styles among the operators who expressed notably distinct confidence levels. Interestingly, the speed did not have a statistically significant impact on the drivers' confidence level during country road driving. Although initially unexpected, this lack of significant impact may result because the steering devices assisted by the sliding mode control feedback were robust against speed variations, causing the impact of speed to go unnoticed. Similarly, it can also be concluded that interaction Speed×Devices is significant on the driver's confidence level.

Table 3.2. ANOVA results for road course lateral error and questionnaire responses on confidence level; bold entries indicate statistically significant results.

Factors	Lateral Error		Confidence Level	
	F-ratio	p-value	F-ratio	p-value
Speed	4.8482	<b>0.0369</b>	1.9942	0.1564
Devices	7.7443	<b>0.0162</b>	8.6784	<b>0.0188</b>
Speed×Devices	5.7849	<b>0.0288</b>	7.3645	<b>0.0488</b>

### 3.4.3 Summary

The main objective of this study was to evaluate not only the tracking capability of three haptic steering devices in both straight-line and winding road driving, but also the on-center handling behavior of these devices. There are three key findings inferred from the operator-in-the-loop evaluations. First, tracking capability with the steering wheel and

robotic grip was superior to that of any of the joystick settings in both the double lane change and curve path navigation maneuvers. Second, drivers used the robotic grip differently than the steering wheel to steer the vehicle during extreme maneuvers. The robotic grip required much less physical movement, and therefore less expended energy to steer the vehicle during the lane change and curve path navigation maneuver. Consequently, the robotic grip may allow for a faster response to emergency and extreme maneuvers from driver with slower reflexes. This finding explains why the robotic grip offers superior performance than the steering wheel during high speed (80kph) driving in Table 1. Finally, the steering wheel maintains a certain level of dominance in low and moderate speed conditions and outperforms the joystick and robotic grip in terms of on-center handling linearity. Another significant observation can be made is that during the curve path navigation scenario, most drivers would perform fast, small amplitude movements with the robotic grip versus gradual, large amplitude movement with the steering wheel. This further indicates potential safety benefits of robotic interface in driving situations like sharp turn and lane change that require extreme maneuvering. Table 3 summarizes the advantages and disadvantages of each haptic steering device in detail.

In terms of hypotheses H1 through H3, these experimental results support that H1 and H2 are true within the 30 participants. However, H3 cannot be fully settled. Even though the steering wheel has lower RMS lateral error than the robotic grip under low speed conditions, the RMS lateral error of the robotic grip is still lower than that of the steering wheel under high speed conditions. More tests and statistical analysis are needed to prove the effectiveness of the haptic feedback device with different control strategies.

The test data from human subject #16 and #22 were selected and analyzed because these two drivers were most representative in terms of performance and demographic to display the data. All 30 drivers completed the double lane change maneuver, country road driving event, and slalom scenario successfully through the nonlinear robust haptic interfaces without severe hardware operation error or physiological discomfort.

### **3.5 Conclusion**

The growth in semi-autonomous and autonomous ground vehicles around the world has created a need for alternative steering input devices. The main objective of this paper was to compare driver performance when using a robotic interface mechanism versus a steering wheel and joystick in a driving simulator environment. All three haptic steering devices were tested under the robust sliding mode controller. Human test subjects operated these interfaces for a given track comprised of a double lane-change maneuver and a country road driving event under two speed conditions. Subjective and objective results from the test demonstrate that the driver's experience can be enhanced up to 75.3% with a robotic steering input when compared to the traditional steering wheel during extreme maneuvers such as high-speed driving and sharp turn (e.g., hairpin turn) passing.

The answer to the objective puts forth regarding the impact of robotic steering devices is:

*Yes, the lane keeping performance of the robotic steering input device with robust nonlinear control surpasses that of the joystick and the steering wheel during emergency and extreme maneuvers.*

One of the major challenges today for this growing area of research is semi-autonomous driving at high speed. The advent and implementation of robotic grip can increase the accuracy and tracking performance of semi-autonomous driving as an alternative steering device other than steering wheel.

Table 3.3: Comparison of different steering devices

Steering Device	Advantages	Drawbacks
Steering Wheel, C1	<ul style="list-style-type: none"> <li>• Dominant in low and moderate speed conditions</li> <li>• Superior steering linearity during on-center handling</li> <li>• Drivers are familiar with the device</li> <li>• Comfortable to drive during extreme maneuvers due to low lateral acceleration</li> </ul>	<ul style="list-style-type: none"> <li>• Slow response and more physical effort from the driver during extreme maneuvers.</li> </ul>
Joystick, C2	<ul style="list-style-type: none"> <li>• Driver's find the joystick easy to grab</li> <li>• Lightweight and easy to carry around</li> </ul>	<ul style="list-style-type: none"> <li>• Worst tracking performance driving along a pre-defined trajectory</li> <li>• Can cause serious human discomfort due the unstable and high lateral acceleration</li> </ul>
Robotic Interface, C3	<ul style="list-style-type: none"> <li>• Dominant in high speed extreme maneuvers.</li> <li>• Best tracking performance driving along a pre-defined trajectory</li> <li>• Faster response to emergency and extreme maneuvers from driver with slowed reflexes.</li> </ul>	<ul style="list-style-type: none"> <li>• Might cause human discomfort during extreme maneuvers due to relatively high lateral acceleration</li> </ul>

A tremendous amount of future research must be conducted before the robotic grip interface can be adopted as an alternative steering input device in industrial applications. First, the robotic interface must be tested in an actual vehicle to further validate the efficacy of driving with a robotic grip on semi-autonomous vehicles. Second, the robotic grip

biomechanics must be investigated to explore the effects of long-term robotic grip usage in terms of wrist injuries, etc. Third, steer-by-wire failsafe measures should be carefully investigated to ensure driver and occupant safety. Before the robotic grip, which relies heavily on steer-by-wire technology, may be used to operate a vehicle, advances in the digital technology and security protocol must occur. Fourth, the robotic grip needs to be evaluated under various road environments such as wet condition, whose friction coefficient might be as low as 0.1, to ameliorate the steering feel when the driver is assisted by the nonlinear haptic feedback. Last, additional robust control strategies such as  $H^\infty$  commands need to be implemented on the robotic grip to corroborate the effectiveness of the alternative haptic device.

## CHAPTER FOUR

### USE OF CELLPHONES AS ALTERNATIVE DRIVER INPUTS IN PASSENGER VEHICLES

Automotive drive-by-wire systems have enabled greater mobility options for individuals with physical disabilities. To further expand the driving paradigm, a need exists to consider an alternative vehicle steering mechanism to meet specific needs and constraints. In this study, a cellphone steering controller was investigated using a fixed-base driving simulator. The cellphone incorporated the direction control of the vehicle through roll motion, as well as the brake and throttle functionality through pitch motion, a design that can assist disabled drivers by excluding extensive arm and leg movements. Human test subjects evaluated the cellphone with conventional vehicle control strategy through a series of roadway maneuvers. Specifically, two distinctive driving situations were studied: a) obstacle avoidance test, and b) city road traveling test. A conventional steering wheel with self-centering force feedback tuning was used for all the driving events for comparison. Based on the lane position and vehicle response data collected, the operators' lane tracking capability during city road traveling was slightly inferior using a cellphone compared to traditional steering wheel. However, in extreme maneuvers like obstacle avoidance and sharp right turn, the lateral tracking performance of the cellphone was up to 12.07% better than that of the steering wheel. The cellphone's superior

performance during certain vehicle maneuvers indicates its potential as an alternative steering adaptation for disabled drivers.

#### **4.1 Introduction**

According to the World Health Organization, approximately 190 million people in the world live with a severe disability such as quadriplegia. Such disabilities and the resulting impairments present great challenges for operating a motor vehicle. With emerging technologies, it is possible to improve mobility and motor vehicle safety for people with disabilities (World Health Organization, 2011).

The introduction of computer controlled electro-mechanical systems in ground vehicles has fostered semi-autonomous operation which promotes greater availability, usability, and mobility options for disabled drivers (Elvin and Gambrell, 2002). Drive-by-wire systems including steering (Gambrell and Elvin, 2002), braking, and throttle offer a pathway from drivers to computer commanded inputs as well as performance improvements. Of interest is the integration of those three functions each operated with independent human-machine interface into a simple holistic device; a cellphone. The cellphone may feature steering through clockwise and counter-clockwise rotation for left and right turns. Similarly, throttle occurs by forward rotation of the phone while braking happens with backward rotation (refer to Figure 4.1). The amount of angular rotation in these two coordinates represents the value of steering angle, throttle, and brake input signals. As the mechanical connections between the input devices and vehicle is eradicated in drive-by-wire, the driver controls may be situated virtually anywhere in the vehicle



within the driver's grasp. The possibility exists then of substituting the traditional vehicle control system with a driving paradigm more applicable to all drivers.

A cellphone controller, whose comparison with traditional devices is listed in Table 1, could present advantages to the driver such as: more room, controller arrangement flexibility, enhanced safety during a car crash, and more accurate direction control. Moreover, the cellphone integrates the steering mechanism with throttle and brake control, thus eliminating the leg usage during longitudinal maneuvers, benefiting disabled drivers who could not maneuver their feet onto the gas and brake pedal. Despite these advantages, a cellphone-based driving scenario possesses several drawbacks. For instance, accidental or unintended cellphone deflections may occur while navigating a corner in addition to vertical and roll inputs from road disturbances as the driver must support the device with their hands. Such deflections can lead to unwanted longitudinal and lateral vehicle motion. Similarly, wrist fatigue may be experienced by drivers who must handle the device for long time periods.

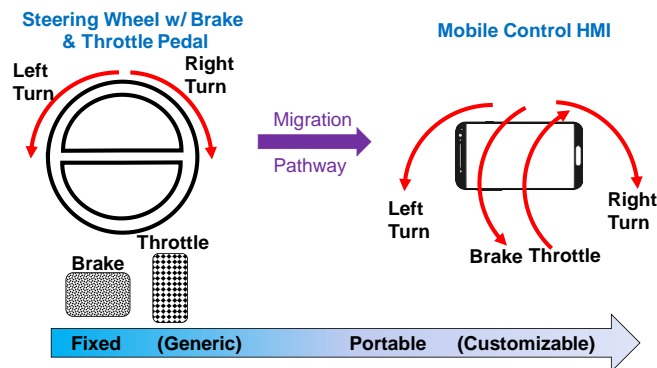


Figure 4.1. Evaluation of vehicle control – traditional steering wheel w/ brake and throttle pedal to cellphone.

Several studies have explored the drivers' response to a variety of steering system and driver input designs. Matsuura et al. (2004) developed a driver's joystick that was

compared with a conventional steering wheel by in-vehicle tests. The vehicle's motion was filmed by cameras and the driver's heart rate measured to examine their mental load while maneuvering. Shaw et al. (1999) designed a new steering control device, which included replacing the unyielding metal projections into the cabin with compliant plastic ones. This design produced lower peak contact pressure and less damage to the human chest, while maintaining sufficient rigidity to be useful. Zheng et al. (2016) investigated the difference between a joystick and steering wheel-based steer-by-wire (SBW) system. They discovered an angle transmission ratio with a constant yaw rate suitable for the steering wheel could not meet the requirement of the joystick steering. Nahak and Kota (2013) modeled, simulated, and analyzed the dynamic behavior of a joystick type articulated machine hydraulic steering system. Wang et al. (2018) investigated various steering devices (e.g. steering wheel, joystick, robotic grip) which offer lane keeping haptic feedback for the driver. The results demonstrated that the robotic arm was generally superior to the joystick and steering wheel.

The advancement in digital technology enables automotive systems to be studied in the laboratory using driving simulators. Ellensohn et al. (2018) applied a global optimization method to find the optimal motion for a nine degree-of-freedom (DOF) driving simulator. Freeman et al. (2013) developed an automotive simulator-based run-off-road (ROR) training program to instruct drivers on how to perform safe and effective vehicle recovery. Zhang and Wang (2005) created a hardware-in-the-loop steering simulator to study hydraulic power steering system with variable ratio rack and pinion gears. Setlur et al. (2003) presented an experimental hardware-in-the-loop steer-by-wire

real time simulator test environment to evaluate various human-machine interface designs. Black et al. (2014) developed a high-fidelity steering simulator to support driver steering preference studies with human subjects. Andonian et al. (2003) compared the lane tracking performance of test subjects using a joystick against a conventional steering wheel using a fixed-based driving simulator with a 14-degree of freedom vehicle dynamics model.

Table 4.1. Comparison of traditional steering wheel and cellphone functionality assuming a drive-by-wire configuration.

<b>Devices Function</b>	<b>Traditional Vehicle Control</b>	<b>Cellphone Control</b>
Directional Control	Steering Wheel	Roll Left and Right
Throttle Control	Gas Pedal	Pitch Forward
Brake Control	Brake Pedal	Pitch Backward
Safety	Airbag Needed	Eliminate Driver Contact with Steering Wheel during Crash
Installation	Fixed	Portable
Space Required	High	Very Low
Cost	\$\$\$	\$

In this study, a nonlinear vehicle description has been implemented that includes the chassis, wheel, tire, and steering dynamics. The models generate the chassis (e.g. longitudinal, lateral, and yaw velocities) and tire (e.g. tire forces, moments, and slip angles) responses. Two different steering devices (e.g. conventional steering wheel, cellphone) are studied. The emulated cellphone consists of a 3-axis accelerometer with communication link. The cellphone's real-time roll and pitch data, which serves as directional and throttle-brake control, can be determined from the raw acceleration data. An immersive virtual reality driving environment occurs using the Matlab 3D Animation toolbox. Case studies

on two different driving environments, including an obstacle avoidance, and a city roadway driving, were conducted in a driving simulator on 15 human subjects to explore the cellphone driving.

This study investigated the feasibility of using a cellphone as an alternative driver input device in passenger vehicles through quantitative and qualitative measures. The research hypothesis can be stated as:

*Can cellphone-inspired driving input devices outperform the traditional steering wheel in terms of driver performance and safety?*

The remainder of the paper is organized as follows. The cellphone human-vehicle interface design is discussed in Section 2. The vehicle dynamics mathematical formulation is contained in Section 3. The experimental methods are introduced in Section 4, followed by operator-in-the-loop test results and discussion in Section 5. Finally, Section 6 offers the conclusion. Additionally, a complete Nomenclature List can be found in the Appendix.

#### **4.2 Cellphone Vehicle Control**

The emulated cellphone driving device features a 3-axis accelerometer for motion-sensing (refer to Figure 4.2). The cellphone is capable of  $\pm 90^\circ$  in each of its three axes. For this research, only the pitch and roll are used. Communication between the cellphone and computer is accomplished through a USB interface, although a wireless link may be established readily. A cellphone interface program reads the  $X$ ,  $Y$ , and  $Z$  axis acceleration raw data, and converts it to roll and pitch motion. The roll and pitch signals serve as the steer angle and throttle-brake signal which are supplied to the vehicle dynamics model. The mapping of the commanded cellphone actions must now be established.

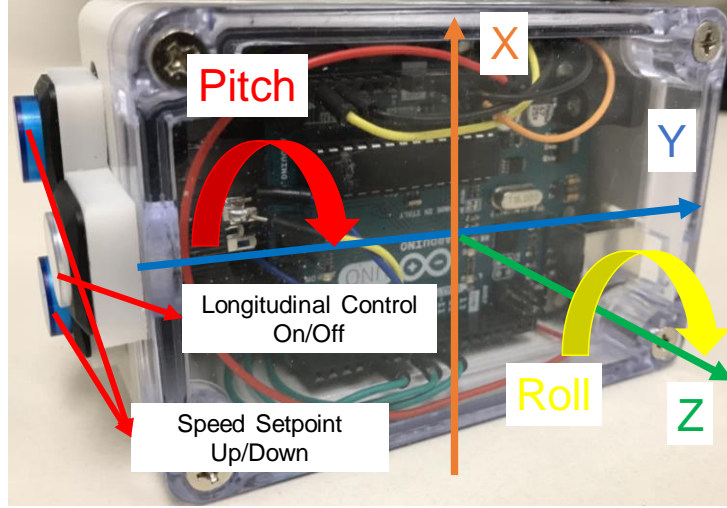


Figure 4.2. Cellphone driving device with Arduino sensor support.

The accelerometer can be used to determine the pitch and roll orientation angles (Pedley, 2013). The cellphone acceleration components  $G_x$ ,  $G_y$ , and  $G_z$  for the  $X$ ,  $Y$ , and  $Z$  axes, then the pitch,  $\theta_p$ , and roll,  $\theta_R$ , angles to be expressed as

$$\theta_p = \arctan\left(\frac{-G_z}{\sqrt{G_y^2 + G_x^2}}\right), \quad \theta_R = \arctan\left(\frac{G_y}{G_x}\right) \quad (4.1)$$

The pitch and roll angles, in the range of  $\pm 90^\circ$ , are transformed into vehicle commands to operate specific actuators. The conversion of the pitch and roll angles into the steering, brake, and throttle signals becomes

$$\theta_{in} = k_{in} \theta_p \quad (4.2)$$

$$T_{bi} = k_B \beta_B = k_B k_{BT} \theta_R; \text{ for } \theta_R \leq 0 \quad (4.3)$$

$$T_{di} = k_D \beta_T = k_D k_{BT} \theta_R; \text{ for } \theta_R > 0 \quad (4.4)$$

where  $\theta_{in}$  is the actual steering angle of the cellphone,  $k_{in}$  and  $k_{BT}$  is cellphone steering angle and brake throttle level gain, respectively. The variables  $\beta_B$  and  $\beta_T$  denote

the brake and throttle level percentages used in the respective brake,  $T_{bi}$ , and drive,  $T_{di}$  torques. The terms  $k_B$  and  $k_D$  represents the brake and drive torque gain.

### 4.3 Vehicle Dynamics

A numerical vehicle dynamics model simulates the longitudinal and lateral platform characteristics. The steer-by-wire system provides lateral vehicle control using a dedicated front wheel steering assembly. The model variables are defined in Figure 4.3.

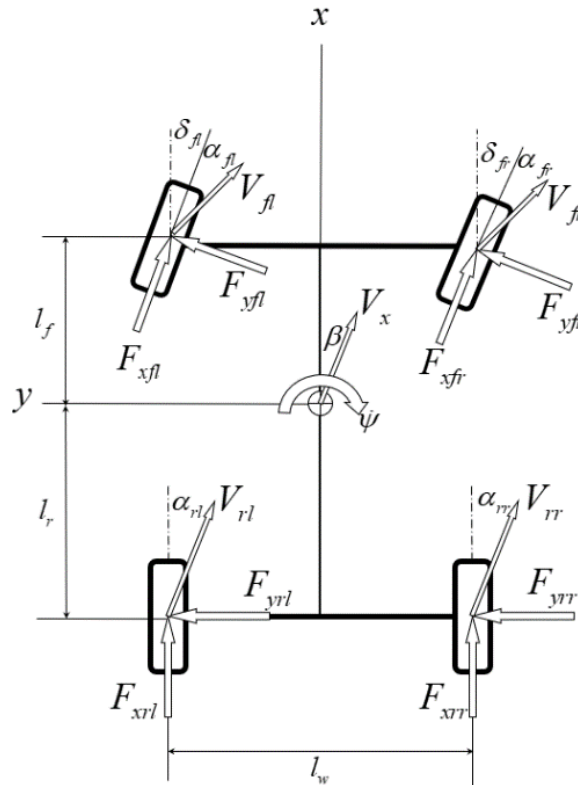


Figure 4.3. Parameter definitions for the vehicle model.

#### 4.3.1 Chassis Model

The governing equations of motion for the longitudinal velocity,  $v_x$ , lateral velocity,  $v_y$ , and yaw rate,  $\dot{\psi}$ , can be expressed as (2016)

$$m\dot{v}_x = -m\dot{\psi}v_y + (F_{yfl} + F_{yfr})\cos\delta + F_{xrl} + F_{xrr} - (F_{yfl} + F_{yfr})\sin\delta \quad (4.5)$$

$$m\dot{v}_y = -m\dot{\psi}v_x + (F_{xfl} + F_{xfr})\sin\delta + F_{yrl} + F_{yrr} + (F_{yfl} + F_{yfr})\cos\delta \quad (4.6)$$

$$\begin{aligned} I_z\ddot{\psi} = & l_f (F_{xfl} + F_{xfr})\sin\delta + l_f (F_{yfl} + F_{yfr})\cos\delta - l_r (F_{yrl} + F_{yrr}) \\ & + \frac{l_w}{2} [(F_{xfr} - F_{xfl})\cos\delta + (F_{xrr} - F_{xrl}) + (F_{yfl} - F_{yfr})\sin\delta] \end{aligned} \quad (4.7)$$

where  $\delta$  denotes the front wheel steering angle.

The longitudinal tire forces at the front left, front right, rear left, and rear right tires are  $F_{xfl}$ ,  $F_{xfr}$ ,  $F_{xrl}$ , and  $F_{xrr}$ , respectively. Similarly, the lateral forces at the front left, front right, rear left, and rear right tires are by  $F_{yfl}$ ,  $F_{yfr}$ ,  $F_{yrl}$ , and  $F_{yrr}$ . The terms  $l_f$ ,  $l_r$ , and  $l_w$  refer to the distance from the center of gravity to the front wheels and rear wheels, as well as between the left and right wheels.

#### 4.3.2 Vehicle Wheels and Tires

The vehicle simulation requires the tire/road interface forces and moments for the wheels. A general analytical tire model (Dugoff et al., 1969) has been updated for combined slip (Gunta and Sankar, 1980). The longitudinal wheel slip ratio,  $s_{xi}$ , becomes

$$s_{xi} = \begin{cases} \frac{r_{eff}\omega_{wi} - v_x}{v_x}, & v_x < r_{ref}\omega_{wi}; \text{ braking} \\ \frac{r_{eff}\omega_{wi} - v_x}{r_{eff}\omega_{wi}}, & v_x > r_{ref}\omega_{wi}; \text{ traction} \end{cases} \quad (4.8)$$

where the  $i$  subscript represents  $fl, fr, rl, rr$ . This notation refers to the front left, front right, rear left, and rear right wheels, respectively. The term  $\omega_{wi}$  represents the four wheels' rotational speed.

The tire sideslip angle,  $\alpha_i$ , becomes

$$\alpha_{fl} = \alpha_{fr} = \delta - \frac{v_y + l_f \dot{\psi}}{v_x}, \quad \alpha_{rl} = \alpha_{rr} = -\frac{v_y - l_r \dot{\psi}}{v_x} \quad (4.9)$$

The longitudinal and lateral tire force,  $F_{xi}$  and  $F_{yi}$ , may be written as

$$F_{xi} = C_{\sigma i} \left( \frac{s_{xi}}{1 + s_{xi}} \right) f(\lambda_i), \quad F_{yi} = C_{\alpha i} \left( \frac{\tan \alpha_i}{1 + s_{xi}} \right) f(\lambda_i) \quad (4.10)$$

where  $C_{\alpha}$  and  $C_{\sigma}$  are the cornering and longitudinal tire stiffness. Using the wheel slip ratio,  $s_{xi}$ , and tire sideslip angle,  $\alpha_i$ , the variable  $\lambda_i$  and the function  $f(\lambda_i)$  are given by

$$\lambda_i = \frac{\mu F_{zi} (1 + s_{xi})}{2 \sqrt{(C_{\sigma i} s_{xi})^2 + (C_{\alpha i} \tan \alpha_i)^2}}, \quad f(\lambda_i) = \begin{cases} (2 - \lambda_i) \lambda_i; & \lambda_i < 1 \\ 1; & \lambda_i \geq 1 \end{cases} \quad (4.11)$$

The term  $F_{zi}$  denotes the vertical force on the  $i$ th tire while the symbol  $\mu$  denotes the tire-road friction coefficient.

The governing equation for the rotational wheel speed,  $\omega_{wi}$ , may be written as

$$I_w \dot{\omega}_{wi} = T_{di} - T_{bi} - r_{eff} F_{xi}, \quad (i = fl, fr, rl, rr) \quad (4.12)$$

where  $I_w$  is the wheel inertia, and  $r_{eff}$  is the effective tire radius. The drive and braking torque are denoted as  $T_{di}$  and  $T_{bi}$ .

### 4.3.3 Steering System Dynamics

In a conventional steering system (refer to Figure 4.4a), the front road wheels are turned using a handwheel via the steering column, bevel gearbox, and rack. In steer-by-wire systems, the steering wheel is mechanically decoupled from the road wheels. The driver's steering commands are delivered electronically to an electric motor to actuate the wheels. As a cellphone-based steering device can leverage drive-by-wire technology, an



analytical mathematical model should be developed to describe the steering subsystem shown in Figure 4.4b (Mills and Wagner, 2003).

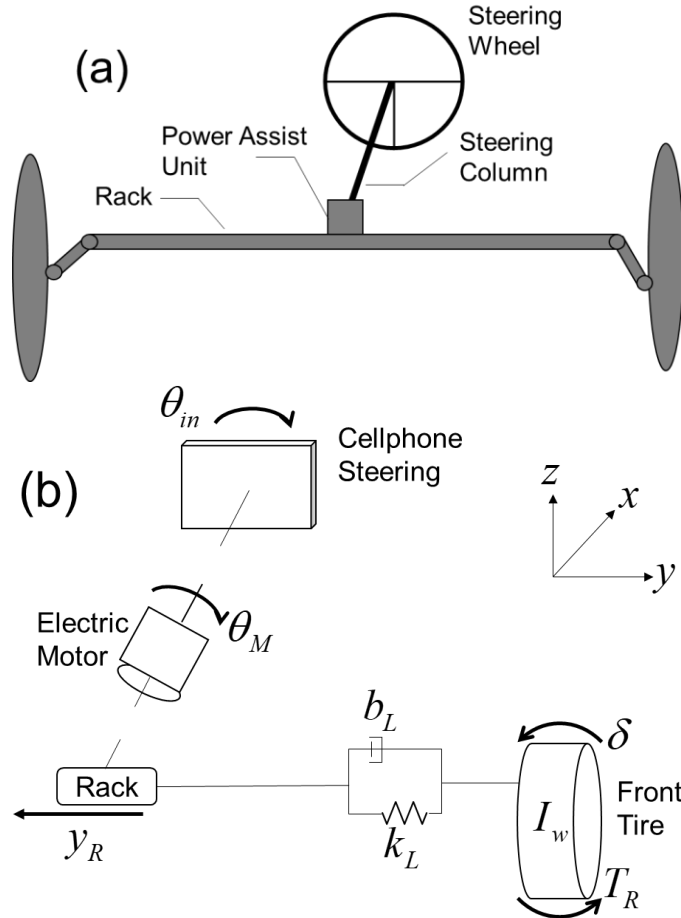


Figure 4.4. (a) Conventional hydraulic steering system with steering wheel, and (b) Steer-by-wire steering system with cellphone.

Unlike a conventional rack and pinion system, the directional control assembly of the steer-by-wire system replaces the steering column with a high torque servo-motor. The differential equation that describe the electric motor displacement,  $\theta_M$ , becomes

$$\ddot{\theta}_M = \frac{1}{I_M} \left[ -b_M \dot{\theta}_M - k_s \left( \theta_M - \frac{y_R}{r_p} \right) + T_M \right] \quad (4.13)$$

where  $I_M$  is the electric motor moment of inertia,  $b_M$  is the motor damping coefficient,  $k_S$  denotes the lumped stiffness of motor shaft and the torque sensor inserted between the rack and the motor, and  $r_P$  is the pinion gear radius. The torque produced by motor  $T_M = k_t i_a$  where the armature current,  $i_a$ , may be expressed as

$$\frac{di_a}{dt} = \frac{1}{L}(-Ri_a - k_M \dot{\theta}_M + V) \quad (4.14)$$

where  $L$  is the motor electrical inductance,  $R$  is the motor electrical resistance, and  $k_M$  is the motor electromotive force (e.m.f.) constant. The supply voltage,  $V$ , for this motor may be expressed as  $V = f(\theta_{in}, \delta)$ . The term  $\theta_{in}$  denotes the steering angle of input driving device (cellphone and steering wheel in this paper). The rack displacement,  $y_R$ , differential equation may be expressed as

$$\ddot{y}_R = \frac{1}{m_R}[-2k_L(y_R - r_L \delta) - k_S(y_R - r_P \theta_M)] \quad (4.15)$$

where  $m_R$  is the rack-piston lumped mass,  $k_L$  is steering linkage stiffness,  $r_L$  is the offset of kingpin axis at applied force.

The front wheel steering angle,  $\delta$ , second-order differential equation becomes

$$\ddot{\delta} = \frac{1}{I_w} \left[ -k_L \left( \delta - \frac{y_R}{r_L} \right) - b_L \dot{\delta} - T_R \right] \quad (4.16)$$

where  $b_L$  is the front wheel assembly damping coefficient, and  $T_R$  is the aligning torque at the road-tire interface.

A summary of the vehicle and control model parameters is listed in Table 4.2.

Table 4.2: Summary of vehicle and control model parameters.

Symbol	Value	Units	Symbol	Value	Units
$b_L$	900	$kg \cdot m/s$	$k_M$	$1.05 \times 10^{-3}$	$Vs/rad$
$b_M$	1.432	$kg \cdot m/s$	$k_S$	33.9	$Nm/rad$
$C_{\alpha f}$	$5.04 \times 10^{-4}$	$N/rad$	$k_t$	$2.65 \times 10^{-3}$	$Nm/A$
$C_{\alpha r}$	$3.36 \times 10^{-4}$	$N/rad$	$l_f$	1.18	$m$
$C_{\sigma i}$	$1.42 \times 10^4$	$N$	$l_r$	1.77	$m$
d	$1.1 \times W + 0.25$	$m$	$m$	1500	$kg$
e	$W + 1$	$m$	$m_R$	29.4	$kg$
f	$1.3 \times W + 0.25$	$m$	$r_{eff}$	0.41	$m$
$g$	9.80	$m/s^2$	$r_L$	0.118	$m$
$I_M$	0.075	$kg \cdot m^2$	$r_P$	$7.37 \times 10^{-3}$	$m$
$I_w$	2.7	$kg \cdot m^2$	$W$	1.91	$m$
$I_z$	$1.89 \times 10^{-4}$	$kg \cdot m^2$	$\mu$	0.85	
$k_L$	$48.8 \times 10^{-3}$	$N \cdot m$			

#### 4.4 Control Strategies for Portable HMI

##### 4.4.1 Longitudinal Control Design (Cruise Control)

Accurate throttle and brake control play an essential role to ensure that the automatic vehicle driving system achieves the desired longitudinal dynamic performance. To allow a portable HMI driven vehicle operating at a desired velocity setpoint, an optimal preview control which serves as a longitudinal speed-tracking controller based on reference and feedback velocities is introduced. The technique was first proposed by MacAdam in (MacAdam, 1980) for synthesizing closed-loop control of dynamic systems during tracking of previewed inputs is presented and was used to represents driver steering control behavior during path-following and obstacle avoidance maneuvers in (MacAdam, 1981).

The proposed control strategy is governed by the properties of the controlled vehicle longitudinal system and is obtained by elimination of the previewed velocity error at a single point ahead in time.

#### 4.4.1.1 Vehicle Longitudinal Dynamics

The longitudinal control aim is to minimize the vehicle longitudinal velocity concerning a given reference velocity. To implement the optimal preview control to the longitudinal vehicle dynamics, the vehicle longitudinal dynamics can be represented as

$$m\dot{v}_x = F_x - F_{aero} - F_{Rx} - mg \sin \theta \quad (4.17)$$

where  $F_x = K_{pt}u$  is the total longitudinal tire force,  $F_{aero}$  is the aerodynamics resistance force,  $F_{Rx}$  is the total rolling resistance force, and  $\theta$  is the road inclination angle. The term  $K_{pt}$  is the effective vehicle total tractive force and  $u$  is the commanded throttle/brake control signal.

The total rolling, driveline, and aerodynamic resistance  $F_r = F_{aero} + F_{Rx}$  can be modeled as

$$F_r = \tanh(v_x) \left( \frac{a_r}{v_x} + c_r v_x \right) + b_r \quad (4.18)$$

where  $a_r$  is the rolling resistance coefficient,  $b_r$  is the driveline resistance coefficient, and  $c_r$  is the aerodynamic drag coefficient.

The state space model can be written as

$$\begin{cases} \dot{z} = Az + B\bar{u}, \bar{u} = u - (m/K_{pt})g \sin \theta \\ y = Cz \end{cases} \quad (4.19)$$

Define the longitudinal position,  $x$ , and longitudinal velocity,  $v_x$ , so that the model states,  $z$ , can be expressed as

$$z = \begin{bmatrix} x \\ v_x \end{bmatrix}, A = \begin{bmatrix} 0 & 1 \\ 0 & F_r/m \end{bmatrix}, B = \begin{bmatrix} 0 \\ K_{pt}/m \end{bmatrix}, C = [0 \quad 1] \quad (4.20)$$

#### 4.4.1.2 Optimal Preview Control Design

The optimal preview control is implemented to find the optimal control,  $u^0(t)$ , which minimizes a local performance index (MacAdam, 1988)

$$J = \frac{1}{T} \int_t^{t+T} [v_{xref}(\eta) - y(\eta)]^2 d\eta \quad (4.21)$$

over the current preview interval  $(t, t + T)$  where  $v_{xref}$  is the previewed velocity reference input. The previewed output,  $y(t + T)$ , is related to the current state,  $z(t)$ , and fixed control,  $u(t)$ , over the previewed interval  $(t, t + T)$ , by

$$y(t+T) = b^* z(t) + a^* u(t) \quad (4.22)$$

where  $a^*$  and  $b^*$  are the driver prediction scalar and vector gain, respectively, and can be found as

$$a^* = TC \left[ I + \sum_{n=1}^{\infty} A^n T^n / (n+1)! \right] B \quad (4.23)$$

$$b^* = C \left[ I + \sum_{n=1}^{\infty} A^n T^n / n! \right] \quad (4.24)$$

The term  $T$  is the preview time window,  $I$  is the identity matrix, and  $n$  is the number of states. Thus, the necessary condition that the derivative of  $J$  with respect to the control variable,  $u$ , be zero, offer the optimal control,  $u^0$ , as

$$u^0(t) = u(t) + \frac{e(t+T)}{a^*} \quad (4.25)$$

where  $e(t + T) = v_{xref}(t + T) - y(t + T)$  is the previewed velocity error, which is being minimized in the original performance index in (21).

In order to account for the known neuromuscular delay of the driver, the resulting optimal control,  $u^0(t)$ , is assumed to be delayed an amount  $\tau$  seconds. Thus, the commanded throttle/brake control input,  $u(t)$ , becomes (MacAdam, 1981)

$$u(t) = u^0(t) e^{-s\tau} \quad (4.26)$$

where  $e^{-s\tau}$  is the driver transport time delay, and  $u^0(t)$  is given in (25).

#### 4.4.2 Lateral Control Design (Lane Keeping Control)

A variable steering ratio control strategy will be proposed that provides lateral compensation to the driver and assists with lane keeping (Shimizu et al., 1999; Heathershaw, 2000; Nozaki et al., 2012). The steering ratio reflects the ratio between the portable HMI steering angle  $\theta_{pH}$  the front wheel steering angle  $\delta$ . The vehicle steering lightness may be directly tuned given the absence of a mechanical connection in the steer-by-wire system. For instance, low and high-speed steering sensitivity can be adjusted to enhance the vehicle overall handling performance. The steering system lateral controller encompasses feedforward and feedback components. The feedforward element considers human driving behavior while the feedback action corrects for vehicle lateral placement in the roadway lane. Both control actions are summed to determine the steering ratio based on vehicle speed and position, commanded steering angle, and lane position desires. A high-level block diagram is presented in Figure 4.5.

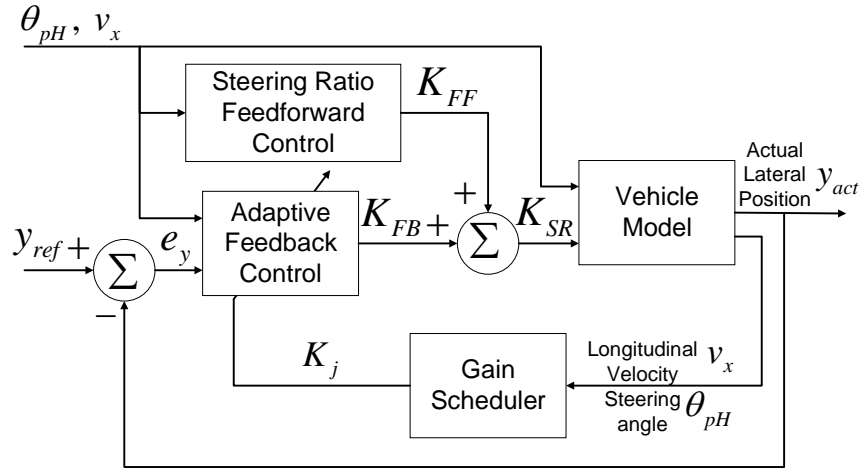


Figure 4.5. Lateral control design featuring feedforward and feedback actions embedded in the portable HMI

#### 4.4.2.1 Adaptive Feedback Control

The main task of the lateral control is to adjust the steering angle such that the deviation between the desired and actual vehicle speeds is compensated. Unlike the steering wheel which can regulate its wheel steering angle through force feedback to the driver, the emulated cellphone driving device can change the steered wheel direction by adjusting the steering ratio which in turn modifies the steering angle. A gain-scheduling PID controller is developed as the feedback control for the portable HMI-steered vehicle to accomplish this task. The gain scheduling technique, an adaptive control method, is based on the adjustment of controller parameters in response to the vehicle's longitudinal speed and steering angle variations.

The steering ratio feedback output,  $K_{FB}(t)$ , of the gain-scheduling classical controller is given by

$$K_{FB}(t) = K_1(t)e_y(t) + K_2(t)\int e_y(t) + K_3\dot{e}_y(t) \quad (4.27)$$

where  $e_y(t) = y_{act} - y_{ref}$  denotes the vehicle lateral error which is the orthogonal distance from the center of gravity (CG) of the vehicle to the desired lane center. The proportional,  $K_1(t)$ , integral,  $K_2(t)$ , and derivative,  $K_3(t)$ , gains of the gain scheduling controller have been determined to be time-varying parameters as follows

$$K_j = \sigma_j \left[ \tanh(\rho_j k_s(t) - \eta_j) + \xi_j \right], j = 1, 2, 3 \quad (4.28)$$

where  $\rho$  is the sigmoid logistic growth rate, and the  $j$  subscript represents each time-varying gain in the steering ratio output.

The speed sensitive steer ratio,  $k_s(t)$ , is a function of portable HMI steering angle,  $\theta_{pH}(t)$ , and vehicle longitudinal velocity,  $v_x(t)$ , so that

$$k_s(t) = \frac{\theta_{pH}(t)}{v_x(t)} \quad (4.29)$$

The terms  $\sigma_j = \frac{K_{jmax} - K_{jmin}}{2}$ ,  $\eta_j = \frac{K_{jmax} + K_{jmin}}{2}$ , and  $\xi_j = \eta_j / \sigma_j$  are positive constants. The parameters  $K_{jmax}$ , and  $K_{jmin}$  are the upper and lower thresholds of the proportional, integral, and derivative gains. Note that by defining  $k_s(t)$  directly proportional to the mobile interface steering angle  $\theta_{pH}$  and inversely proportional to the vehicle longitudinal velocity  $v_x(t)$ , the gain scheduler can adjust the gain to adapt to the variations of driver steering behavior and current vehicle state.

#### 4.4.2.2 Steering Ratio Feedforward Control

A feedforward steering ratio which varies according to the vehicle longitudinal speed as a fundamental characteristic is first considered. Then, compensation varying



according to the portable HMI steering angle is incorporated in the feedforward control to attain a desirable steering ratio level (Wu et al., 2018).

The adaptive steering ratio feedforward control features a standard steering ratio during medium speed driving. The steering sensitivity declines as the vehicle speed increases and vice versa while the vehicle is deaccelerating. Such design guarantees a steering sensitivity level to ensure turning flexibility during low-speed driving (e.g., parking). Also, at high road speeds, a much lower road wheel steering angle input is required than at low speeds. Thus, a limited steering sensitivity is desired to provide steering stability during highway driving. To satisfy those design objectives in different speed conditions and to secure a smooth transition between each speed range, a logistic function with an increasing value of the steering ratio growth factor up to a desired steering stability level has been implemented in this study.

The steering ratio,  $K_v$ , which is shown in Figure 4.6(a) is computed as a logistic function of the vehicle longitudinal velocity,  $v_x$ , as

$$K_v = \frac{a + de^{-b(v_x - c)}}{1 + e^{-b(v_x - c)}} \quad (4.30)$$

where  $a$  and  $d$  are the maximum and minimum steering ratio,  $b$  is the curve logistic growth rate, and  $c$  is the vehicle speed of the sigmoid midpoint.

The steering ratio feedforward control also features a decelerated gear ratio near the straight-ahead position with the steering ratio quickening as the portable HMI steering angle increased further. On the road, this translates into smooth, confidence building lane changes and increased maneuverability when parking. On the other hand, such a design

reduces steering sensitivity and enhances lateral stability during straight road driving. To accomplish such steering ratio changes concerning the portable HMI steering angle, a corner correction factor has been introduced. The corner correction factor,  $F_C$ , shown as Figure 4.6(b), is defined as a function of the portable HMI steering angle,  $\theta_{pH}$ , using the Gaussian distribution or

$$F_C = h_1 e^{-\left(\frac{\theta_{pH} + p}{s}\right)^2} + h_2 e^{-\left(\frac{\theta_{pH} - q}{w}\right)^2} \quad (4.31)$$

where  $e$  is the natural logarithm base, and the terms  $h_1$ ,  $h_2$ ,  $p$ ,  $s$ ,  $w$ , and  $q$  are constants.

To obtain the best estimate of the feedforward control for the adaptive controller to account for the variation in longitudinal vehicle velocity and portable HMI steering angle, the feedforward steering ratio (displayed in Figure 5(c)) that considers human behavior may be added to the control input

$$K_{FF} = F_C K_v \quad (4.32)$$

Thus, the final steering ratio representing the control input of the system should be

$$K_{SR} = K_{FF} + K_{FB} \quad (4.33)$$

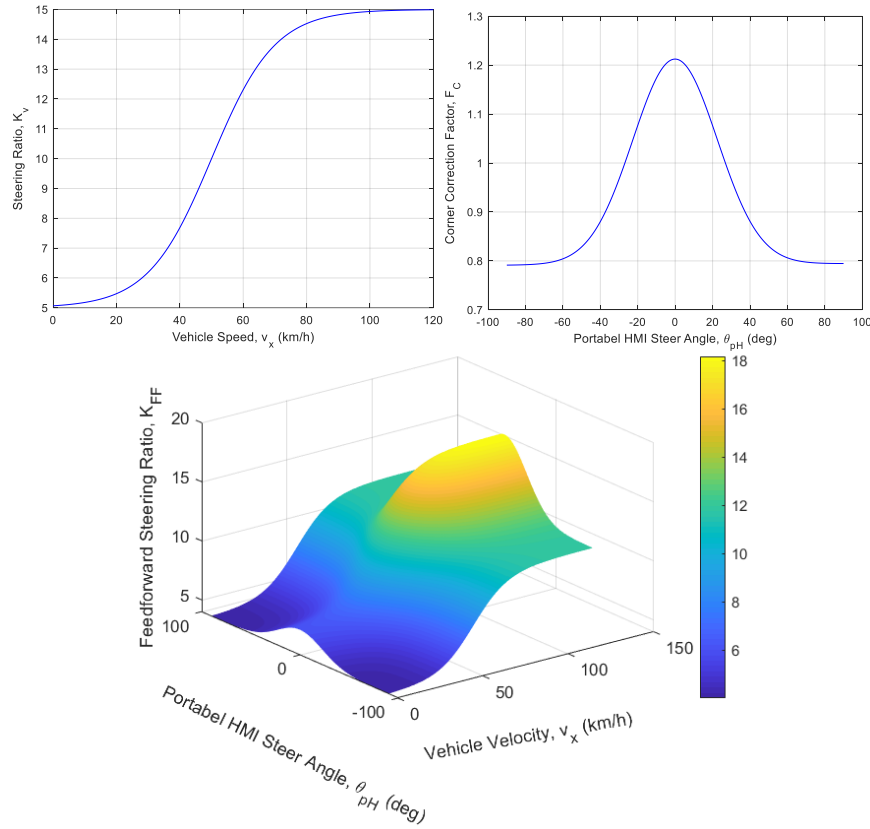


Figure 4.6. Variable Steering ratio feedforward control: (a) Steering ratio of full-speed section varies with speed, (b) Corner correction factor change with the portable HMI steer angle, and (c) The corrected steering ratio with the vehicle speed and mobile control interface angle changes

#### 4.4.3 State Flow Controller (Adaptive Cruise Control)

State flow control is a powerful logical strategy that utilizes state machines and flow charts to model reactive systems and control complex nonlinear systems (Freeman et al., 2015). A state flow controller observes certain system states and discretely switches between pre-programmed control outputs. In this study, the state flow controller applies differential braking to help control the vehicle's longitudinal dynamics. The state transition logic expressions also incorporated driver operating parameters to reflect real-time driver intentions. The inclusion of driver prediction is indispensable for the successful development of an intelligent driver assistance systems.

To develop the driver intention algorithm for portable HMI steering, a set of steering and vehicle system parameters were selected ( $\delta, \dot{\delta}, v_x, \dot{v}_y, \dot{\psi}$ ). In other words, the requested front wheel steering angle, front wheel steering angle speed, vehicle speed, vehicle lateral acceleration, and vehicle yaw rate. Collectively, this information serves as a significant reflection of the driver's intention. Steering angle—Zero to small steering angle typically indicates a pursue of lane keeping while large steering angle deflection marks the cornering or obstacle avoidance intent from the driver. Steering angle speed—High steering angle speed suggests that an extreme maneuver is ongoing while small steering angle speed hints the driver is performing a low-speed cornering or switchback. Yaw rates and lateral acceleration— Large values result of controlled steering maneuvers such as turning, which signify the need for increased cornering ability. Small yaw rates and lateral acceleration imply a lack of need for cornering capability and occur during lane keeping or obstacle avoidance.

Based on these discussions above and experimental results completed by Wang et al. (2019a), three firing conditions for select driver intention states derived from the iterative experimental process are displayed in Figure 4.7(a).

A state flow braking controller, based on driver intention prediction, was designed to help reduce vehicle speed during turning maneuvers and to maintain stability. The state flow braking controller coordinated with the other vehicle controllers by monitoring vehicle parameters and adjusting the brake torque,  $T_{bi}(i = 1,2,3,4)$ , accordingly. These individual wheel brake torques were constrained conforming to physical limitations appropriate for each individual system. Additionally, the firing condition for different

driver intention in Figure 4.7(b) serves as a transition condition that enables switching between different driving states while traveling various roadways. This strategy was implemented to help reduce controller complexity and mitigate the potential for instability at high speeds and large steering angles (Freeman et al., 2015).

The state flow braking controller consisted of three states, i.e.,  $S_{brake} = \{\text{Zero, Obstacle, Cornering}\}$ , with the decision-making framework described below and shown in Figure 4.7(b) as a Finite State Machine (FSM).

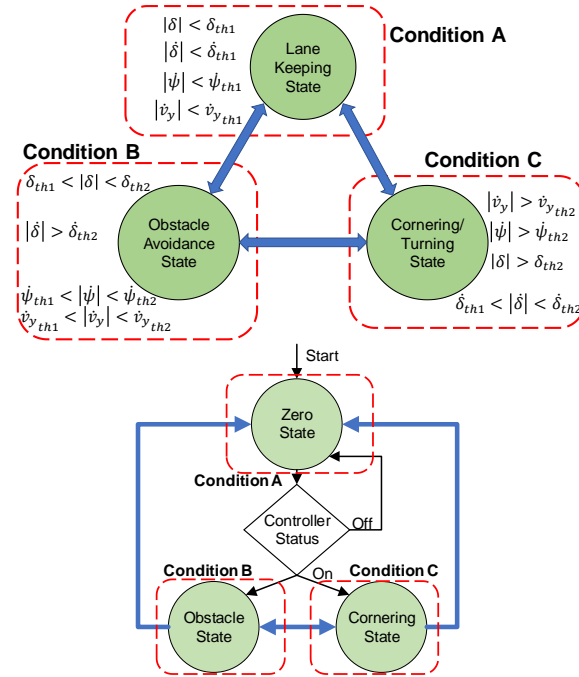


Figure 4.7. (a) Firing Conditions for three driver intention states: lane keeping, obstacle avoidance, and cornering/turning, and (b) Logic flow for the SF braking control; controller state transitions based on comparison of vehicle states with firing condition

#### 4.5 Experimental Methods

To explore the real-time performance of human subjects driving using the steering wheel and cellphone, a realistic fixed-base experimental simulator was created (refer to Figure 4.8). The simulator comprised the steering devices, a high-resolution image projector, and a Honda CR-V. To simulate the target vehicle dynamics and tire/road

interactions, mathematical models were integrated using MATLAB/Simulink®. In addition, the software handles the input/output from various systems (operator driving input, display output, chassis kinematics, and steering wheel self-centering feedback). The immersive virtual reality driving environment was created using the V-Realm Builder 2.0, imported, and rendered by the Simulink 3D Animation toolbox. The resulting road scene were projected on a large screen to provide the operators with visual feedback.



Figure 4.8. Driving simulator driving scene using cellphone.

The test bed functionality, shown in Figure 4.9, was experimented by the human subjects in the laboratory. The commanded roll and pitch data from cellphone were converted into the vehicle's steer angle (roll data) and throttle/brake signals (pitch data). The signals from either the steering wheel, throttle, brake, or cellphone were transmitted to the vehicle dynamics block. The virtual reality generator processed the vehicle information to represent a three-dimensional driving environment rendered on the projector.

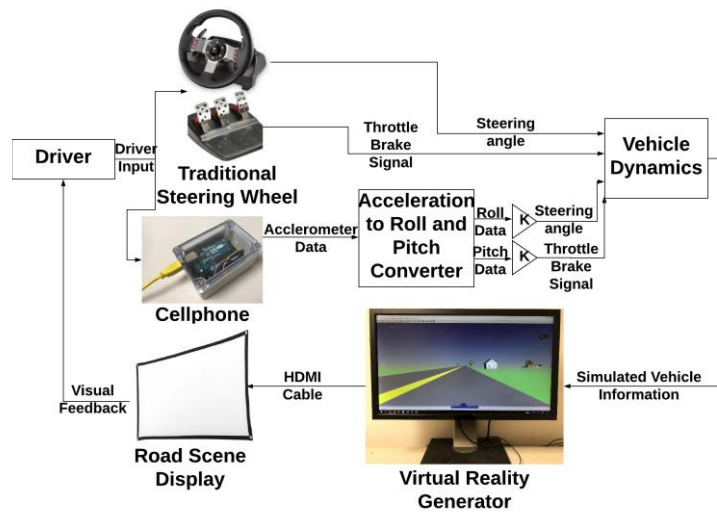


Figure 4.9. Fixed-base driving simulator schematic

A total of  $n=15$  subjects participated ranging in age from 18 to 31, with eleven males and four females. The concentration in age demographic corresponds to the university campus location. The average driving experience was 3.6 years. Ten subjects revealed that they have played racing games on a cellphone platform. In response to whether they had driven a semi-autonomous vehicle, only one subject was noted to have related experience. To control for learning that may arise from repeated activities, the driving sequence was varied for each driver. A Latin square design ensured a randomized order of testing the cellphone and steering wheel. Each test subject adhered to the following procedure:

1. Complete a demographic questionnaire to understand where each subject fit in the general population.
2. Subject practiced driving at the target speed for several minutes to familiarize themselves with the system.

3. Run a test and record steer angle, vehicle velocity, vehicle coordinate, lateral acceleration, yaw rate, four-tire slip angles.

4. Asked the subject to complete a post-test questionnaire for the specific driving event.

5. Change steering device and/or driving scenario and repeat.

#### **4.6 Test Results**

In this section, three studies including bandwidth, obstacle avoidance, and city road driving tests, were conducted to investigate the efficacy of the cellphone as an alternative driving device. The best performance was considered to correspond to when the operator completed the designed task with the smallest heading and lateral error. Intuitively, the steering wheel, to which operators are more familiar, should outperform the cellphone in terms of daily routine city driving. Moreover, the steering wheel is coupled with original equipment manufacturer (OEM) self-centering feedback. This means that the steering wheel can automatically return to its original state after a turning maneuver. On the other hand, cellphone steering requires less physical movement that may result in faster steering response. The driver's quicker response time can improve vehicle action during extreme maneuvers. Based on these factors, two hypotheses have been proposed for the driving configurations:

H1: The steering wheel will produce lower heading and lateral error than the cellphone in city road driving test.

H2: The cellphone will deliver the better performance during the obstacle avoidance driving test.



#### 4.6.1 Bandwidth Test

Bandwidth is the difference between the upper and lower frequencies in a continuous set of frequencies and is typically measured in Hertz (Hz). To examine the maximum speed that a cellphone and a steering wheel can be rotated during vehicle directional control, a bandwidth test of each steering configuration was conducted. In the driving simulator environment, the operator accelerated the vehicle to a speed of 20kph on a straight path, before they began to rotate the steering device in a sinusoidal manner with an amplitude of 90°. Meanwhile, the operator was slowly increasing the frequency of the rotation such that the steering angle input to the vehicle resembles a chirp sine wave signal. After the driver their steering devices' rotational limit, the test was terminated, and the steering angle response displayed (refer to Figure 4.7). The maximum and minimum frequencies of the steering wheel and the cellphone,  $f_{sw}$  and  $f_{cp}$ , are:

$$0.55 < f_{sw} < 1.2Hz, 0.42 < f_{cp} < 2.5Hz \quad (4.34)$$

The wider cellphone bandwidth indicates a unique property this new steering paradigm has over the conventional steering wheel: a faster steering direction adjustment speed by the human operators. This property enables the driver to react and respond more quickly in extreme emergency driving situations such as evasive maneuvering. As the steering wheel tends to be larger than a cellphone, difference in driving behavior were observed. Specifically, driver tended to have more gradual steering commands with the wheel while driver steering was more abrupt per Figure 4.10. Coupled with self-centering feedback, the steering wheel requires more efforts from the driver to turn compared to the cellphone, resulting in a slower device turning rate.

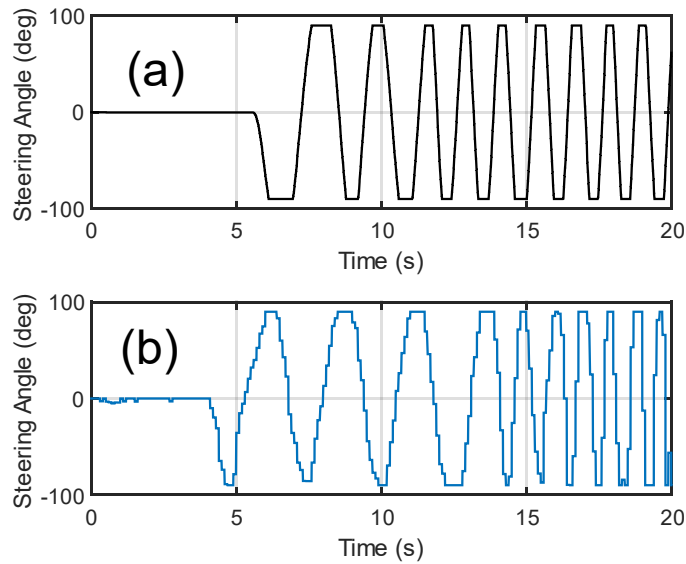


Figure 4.10. Bandwidth test for driving controllers – (a) Steering wheel, (b) Cellphone.

#### 4.6.2 Obstacle Avoidance Event

To determine the evasive maneuver performance of the cellphone, an obstacle avoidance driving event, ISO 3888-2 (2011) commonly known as the moose test, has been tested in the driving simulator (refer to Figure 4.11(a)). The dimensions for the track and cone placement are shown in Figure 4.11(b); the total track length is 61m. This maneuver is a dynamic process which involves driving from the original lane to a parallel lane, and then returning to the original lane without displacing the cones positioned alongside the track. After entering the track with an initial speed, the operator released the throttle and driver the remaining track with no throttle input or brake application. The intention of the obstacle avoidance is to allow the vehicle to attain a series of alternating high lateral accelerations such that the vehicle's lateral dynamics can be readily evaluated. The test results of Driver #3, who did not hit or bypass any cones driving with the cellphone or the steering wheel, will be discussed.

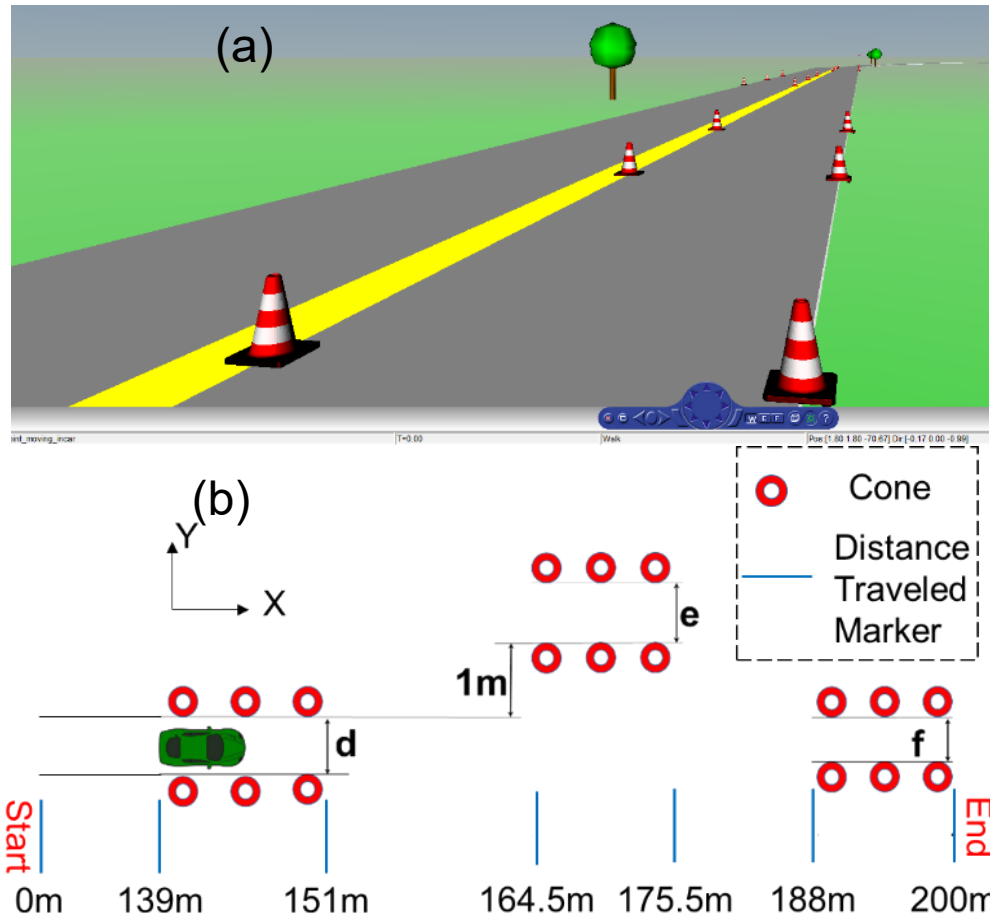


Figure 4.11. (a) Three-dimensional virtual driving space featuring the obstacle avoidance event, and (b) ISO 3888-2 obstacle avoidance track and placing of cones (detailed lane width in Table 2) (Jalali et al., 2013).

The performance of the cellphone driving controller will be presented by examining Driver #3 who entered the obstacle avoidance maneuver at an initial speed of 40 kph. As shown in Figure 4.12, the maneuver was successfully completed using both cellphone and steering wheel. The driver traveled the desired path (Jalali et al., 2013) successfully from 139m to 168m for the two steering devices. Once vehicle placement has been accomplished in the adjacent lane, the driver must begin returning to the original lane. During the return sequence (168m-190m), a noticeable steering difference between the steering wheel and the cellphone was observed. Specifically, the steering wheel-controlled vehicle's pathway

was above the ideal trajectory while the cellphone-controlled vehicle was marginally below. This difference can be explained through the discovery of the bandwidth test conducted prior. The cellphone has a faster steering directional adjustment speed than the steering wheel. Thus, when the cellphone and the steering wheel were performing an aggressive steering maneuver (168m-190m), the cellphone could accomplish it quicker in comparison to the steering wheel. Consequently, the commanded steer angle for the front wheel resulted in a sharp lane return. In extreme driving scenarios such as obstacle avoidance, both brake and steering action should be considered to return the vehicle to its original lane safely and smoothly.

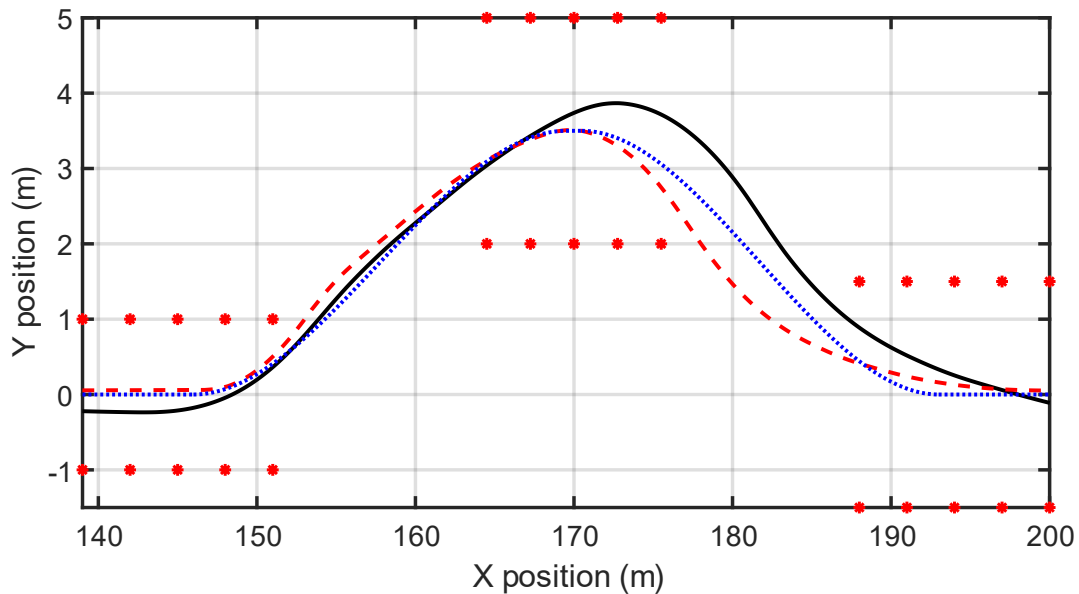


Figure 4.12. Driver #3 desired and actual vehicle trajectories when driving through the obstacle avoidance using the cellphone and steering wheel (steering wheel in solid line, cellphone in dashed line, desired trajectory in dotted line, and cones in asterisk).

The fast  $\pm 90^\circ$  traditional steering wheel action is performed quicker with a cellphone as shown in Figure 4.13(a) per the steering device angle versus the longitudinal distance traveled. While the steering wheel-controlled vehicle traveled 14m (173m-187m),

the cellphone-controlled vehicle traveled only 11m (170m-181m). Also, to drive the vehicle through the obstacle avoidance event, the driver used the steering wheel more aggressively, and at some points applied up to 1.61 rad (92 degrees). In contrast, cellphone driving required less effort as noted by 0.7 rad (40 degrees), resulting an easier and more comfortable steering experience. The lateral error, lateral acceleration, and the front tire slip angle are shown in Figure 4.13(b)-(d) for the same scenario. The steering wheel has a larger maximum lateral error of 0.758m compared to the 0.6891m of the cellphone. On the other hand, the cellphone ensured a lower lateral error at the expense of a much greater lateral acceleration. The maximum lateral acceleration the driver felt steering with the cellphone reaches 0.57g, which surpassed the lateral acceleration limit to assure driver comfort, 0.4g. When the driver operates the vehicle with the cellphone, the front tires generate a larger maximum 0.04-0.05 (rad) slip when entering the first left maneuver, and repeat again when returning to neutral yaw and vice versa. The larger tire slip angle of the cellphone indicates a higher tire lateral force, which in turn maximize the vehicle's ability to grip. Overall, the cellphone controlled vehicle offers better lateral performance and undemanding steering experience during the obstacle avoidance.

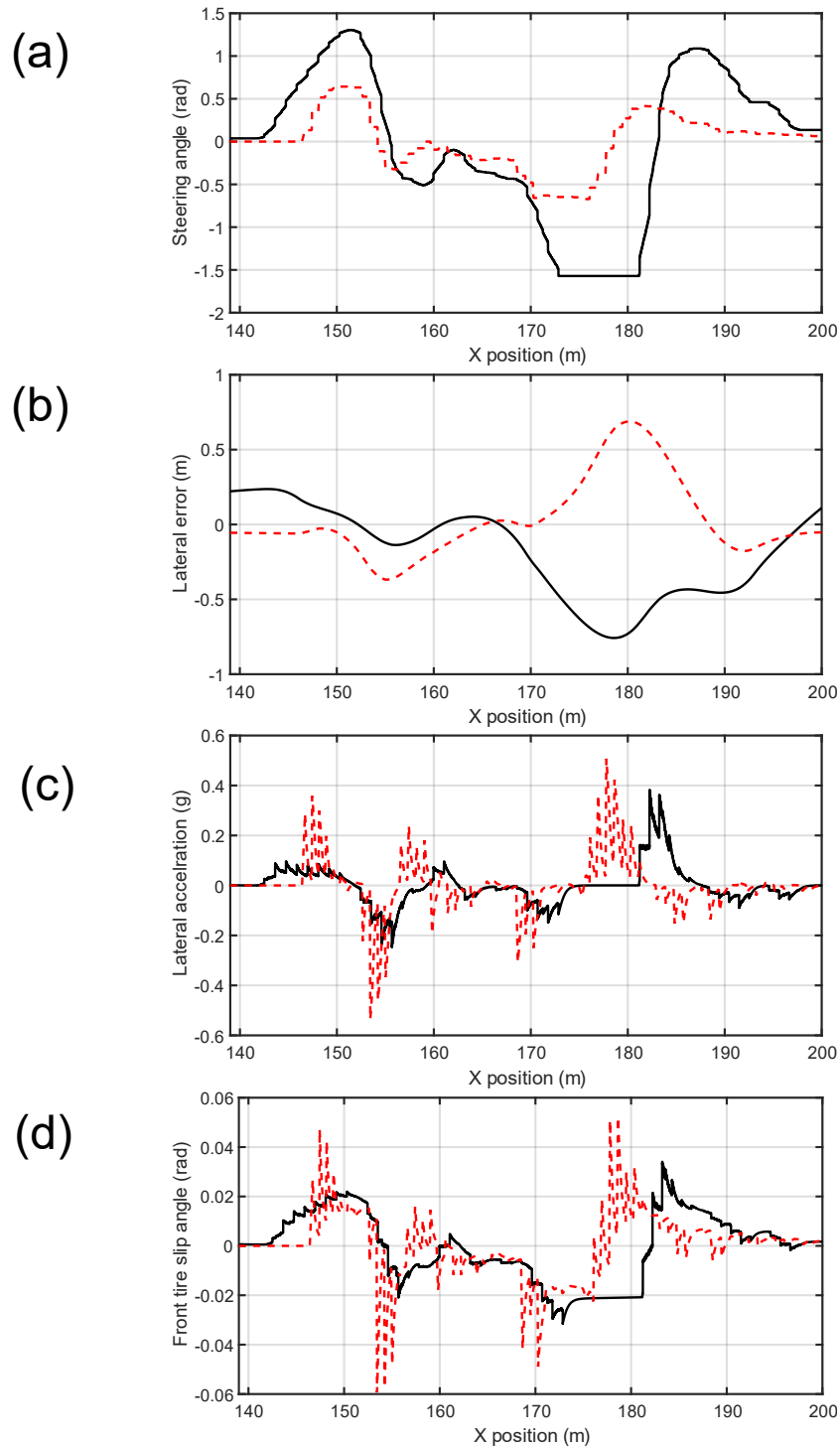


Figure 4.13. Driver #3 performance for the obstacle avoidance maneuver - (a) Steer angle, (b) Lateral error, (c) Lateral acceleration, and (d) Front tire slip angle (steering wheel in solid line, and cellphone in dashed line).

#### 4.6.3 City Road Driving Event

To measure the cornering capability of the cellphone driving device, a city roadway has been created as shown in Figure 4.14(a). This track environment features sharp curves which emphasizes vehicle handling. In Figure 4.14(b), the road features a 200m straight section to achieve an initial speed of 30kph (a common city street speed limit) and maintained throughout the event. The driver then encounters a 15m radius right turn, a 25m radius left turn, and a 20m radius switchback. Each turn is followed by a straight path section. The straight path sections serve two functions: (1) An assessment of the vehicle's traction and stability on the straight road after a turn, and (2) A buffer zone for the driver to recover before the next turn maneuver. The total distance traveled by the driver throughout the track has been displayed on the map.

##### Right Turn Maneuver (distance 200-323.6m)

The first roadway encountered by the driver is a 15m radius right turn maneuver, which is the sharpest turn in the city road driving event. Considering the driver is negotiating the turn at a speed of 30kph, this cornering maneuver is relatively extreme with a centrifugal acceleration of 0.472g and requires aggressive driving. To evaluate the lateral and yaw performance differences between the cellphone and the steering wheel, the vehicle's lateral and heading error for Driver # 8 are depicted in Figures 4.15(a) and (b). The heading error, actual heading angle of the vehicle vs the tangential direction of the desired path, of both the cellphone and the steering wheel peaked at 0.2rad at the end of the right turn (223.6m) and converged to zero on the straight section (223.6m-323.6m), indicating a decent yaw motion recovery. The steering wheel, with an absolute maximum

0.93m lateral error, has lower lane keeping performance than the cellphone during the turn (200m-223.6m). However, on the straight road following the turn (223.6m-323.6m), the steering wheel lateral error is much lower than the cellphone, suggesting that the steering wheel's self-centering feedback ensures that the vehicle will re-align with the road on the straight path section after a sharp turn. The front tire slip angle response, in Figure 4.15(c), show that the cellphone-operated vehicle required more cornering capability to the driver as requested.

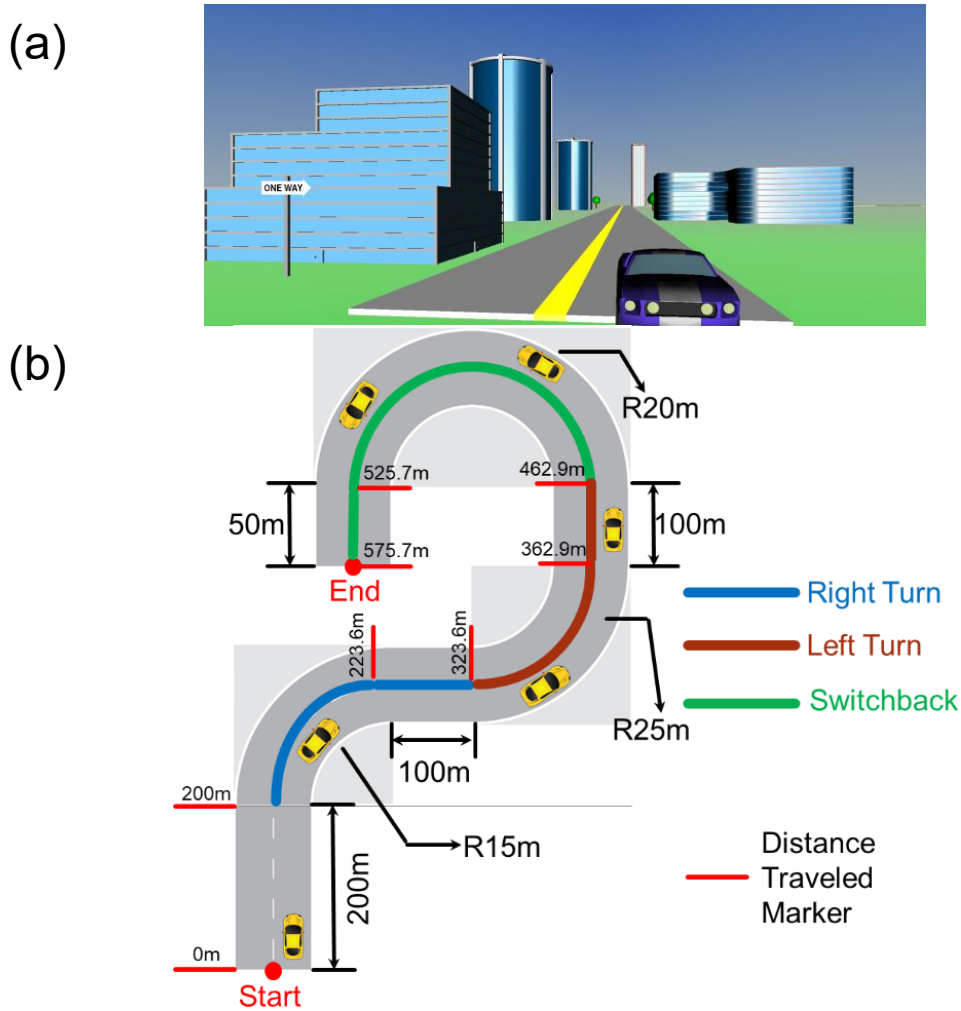


Figure 4.14. (a) Three-dimensional city road driving scenario, and (b) City road driving event track with distance travel markers displayed.



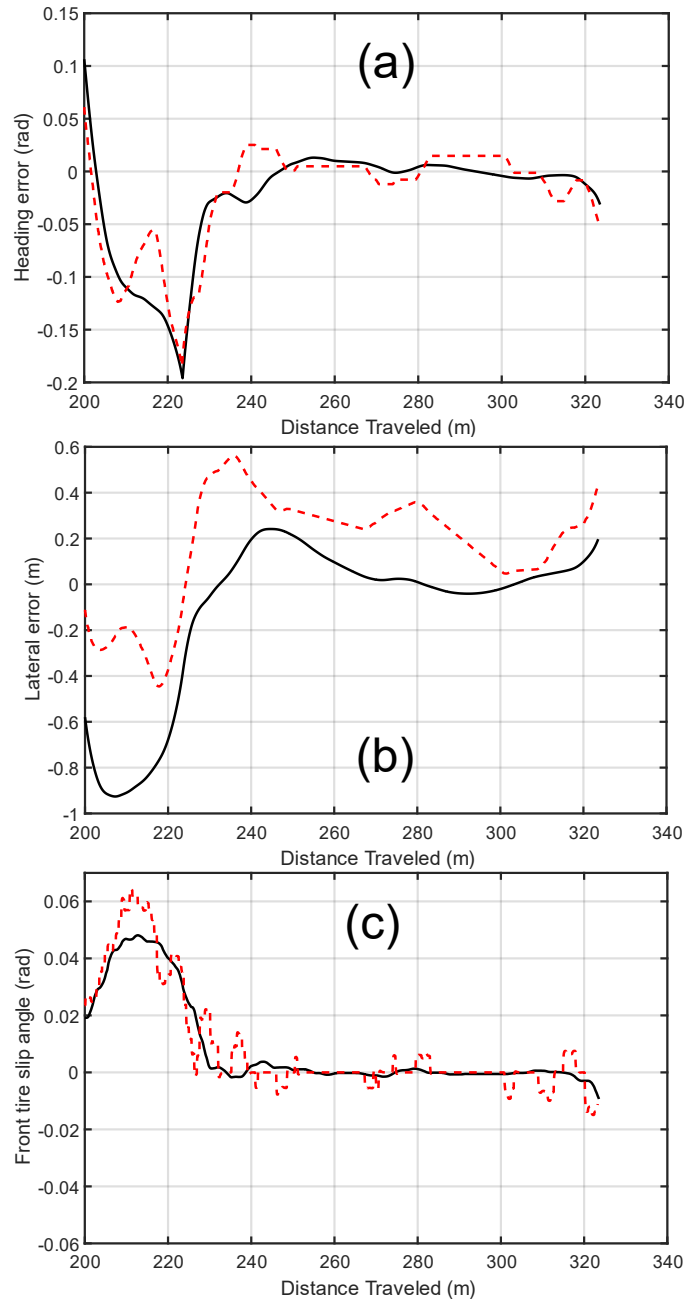


Figure 4.15. City roadway 15m radius right turn - Driver #8 performance for (a) Heading error, (b) Lateral error, and (c) Front tire slip angle (steering wheel in solid line, and cellphone in dashed line).

#### Left Turn Maneuver (distance 323.6-462.9m)

After a sharp right turn, the human subjects then encountered a 25m radius left turn.

The heading error of both controller devices is relatively similar in Figure 4.16(a). Their

lateral performance, on the other hand, is drastically distinct per Figure 4.16(b). During the left turn maneuver, the steering wheel not only outperformed the cellphone during the cornering (323.6m-362.9m), but also dominated the succeeding straight road, with an overall maximum lateral error of merely 0.24m against the cellphone's 0.64m. Considering the discussion of the cellphone in the previous section, it can be deduced that during a low radius moderate turn, the cellphone cannot accomplish the maneuver as effectively as the steering wheel since the vehicle driven by the cellphone is more responsive. However, such a quick vehicle response can lead to temporary chassis instabilities which is highly undesirable when a steady steering angle input is required during a moderate turn. The vehicle's instability is further evident by the unsettled front tire slip angle response in Figure 4.16(c). Another possible cause for the fluctuating tire slip angle is that the driver's hands tremor more when holding a cellphone compared to interacting with the steering wheel, an observation that needs to be considered when designing a cellphone driving controller.

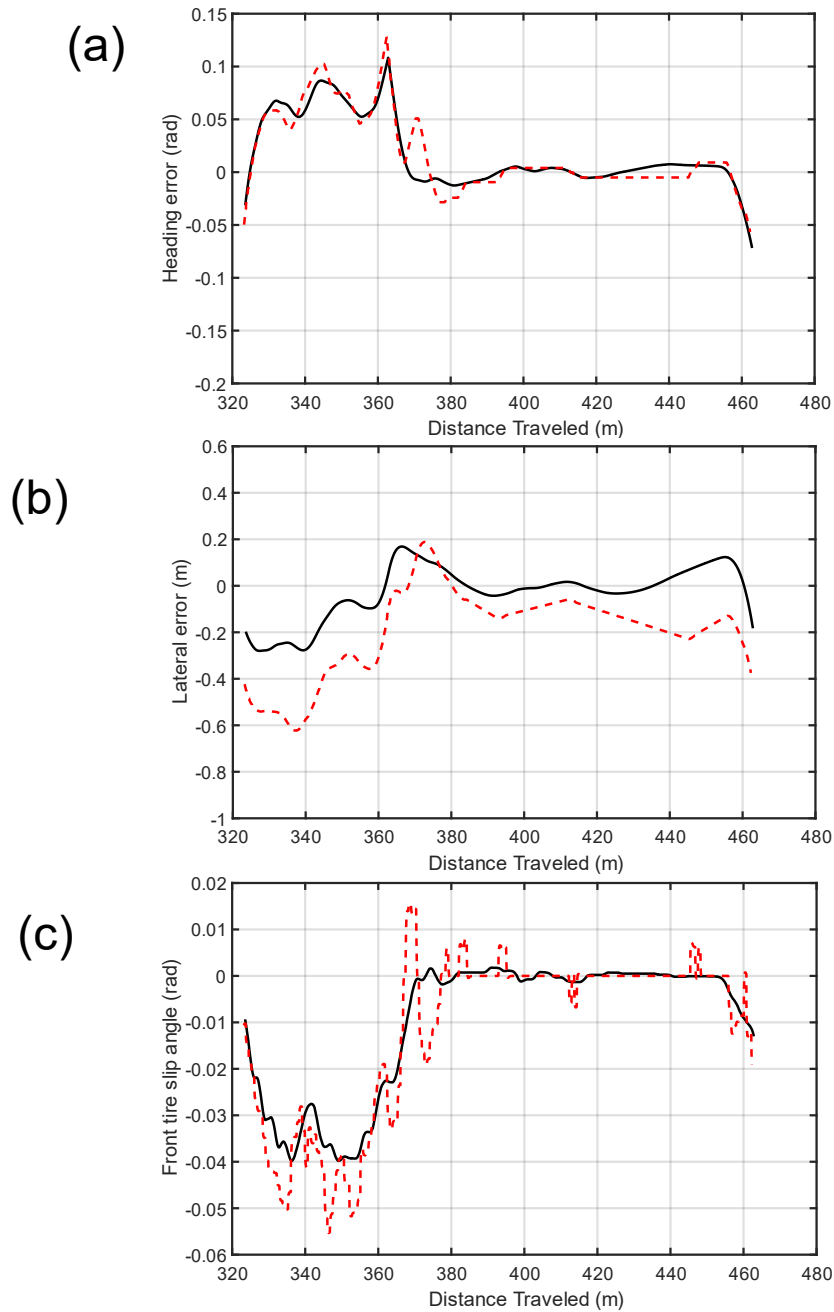


Figure 4.16. City roadway 25m radius left turn - Driver #8 performance for (a) Heading error, (b) Lateral error, and (c) Front tire slip angle (steering wheel in solid line, and cellphone in dashed line).

#### Switchback Maneuver (distance 462.9-575.7m)

The last road feature is a switchback, which is a 20m radius bend for vehicles to turn approximately  $180^\circ$  to continue on the path. As depicted in Figure 4.14(a), the heading

errors for the cellphone and steering wheel controller remain nearly the same across the 180° turn (462.9m-525.7m) and eventually converge to zero on the subsequent 50m straight path section (525.7m-575.7m). These results indicate a stable yaw motion for both controllers. When considering the lane keeping capability, the steering wheel controller outperforms the cellphone with lower average and maximum lateral error per Figure 4.14(b). Another notable observation is that the cellphone controller again exhibits some fluctuation in the front tire slip angle as shown in Figure 4.14(c).

#### 4.6.4 Summary of Findings

After completing the human subject tests, all 15 operators' actual trajectories in the city road driving event are recorded and compared to the desired trajectory. The root mean square (RMS) and the maximum average value of the heading error,  $e_{HRMS}$ ,  $e_{LMAX}$ , lateral error,  $e_{LRMS}$ ,  $e_{LMAX}$ , for all 15 human subjects is calculated and recorded in Table 3. The cellphone, an ideal steering device for extreme maneuvers, exhibited the lowest mean lateral error and heading error during the sharp right turn, with a mean lateral error improvement of 12.07% compared to the steering wheel. The steering wheel, on the other hand, appears to produce the lower errors during the left turn and switchback than the cellphone, assuring the minimal lateral and heading deviation during moderate driving conditions.

Three studies, including bandwidth test, obstacle avoidance test, and city road cornering operation, were performed and may be summarized as follows:

- 1) The cellphone steering bandwidth is larger than the traditional steering wheel, guaranteeing a faster steering response and more responsive vehicle handling.

- 2) Drivers utilized the cellphone device differently than the steering wheel during evasive maneuvers; the cellphone demanded less physical movement.
- 3) The traditional driving system maintains a certain level of dominance in cornering maneuvers; the gradual movement of the steering wheel ensures vehicle stability.

Table 4.3: Summary of driver averaged performance for 15 subjects with cellphone device and steering wheel on city roadway. Note that  $e_{HRMS}$ , and  $e_{LRMS}$  are the root mean square values, while  $e_{HMAX}$ ,  $e_{LMAX}$  are the maximum values for test subjects (lower values in bold font).

Road Scenario	Driving Device	$e_{HRMS}$ (rad)	$e_{HMAX}$ (rad)	$e_{LRMS}$ (m)	$e_{LMAX}$ (m)
Right Turn (15m radius)	Steering Wheel	0.116	0.196	0.806	0.926
	Cellphone	<b>0.102</b>	<b>0.185</b>	<b>0.295</b>	<b>0.446</b>
Left Turn (25m radius)	Steering Wheel	<b>0.065</b>	<b>0.108</b>	<b>0.196</b>	<b>0.28</b>
	Cellphone	0.069	0.128	0.462	0.623
Switchback (20m radius)	Steering Wheel	<b>0.077</b>	<b>0.141</b>	<b>0.425</b>	<b>0.617</b>
	Cellphone	0.081	0.143	0.631	0.812

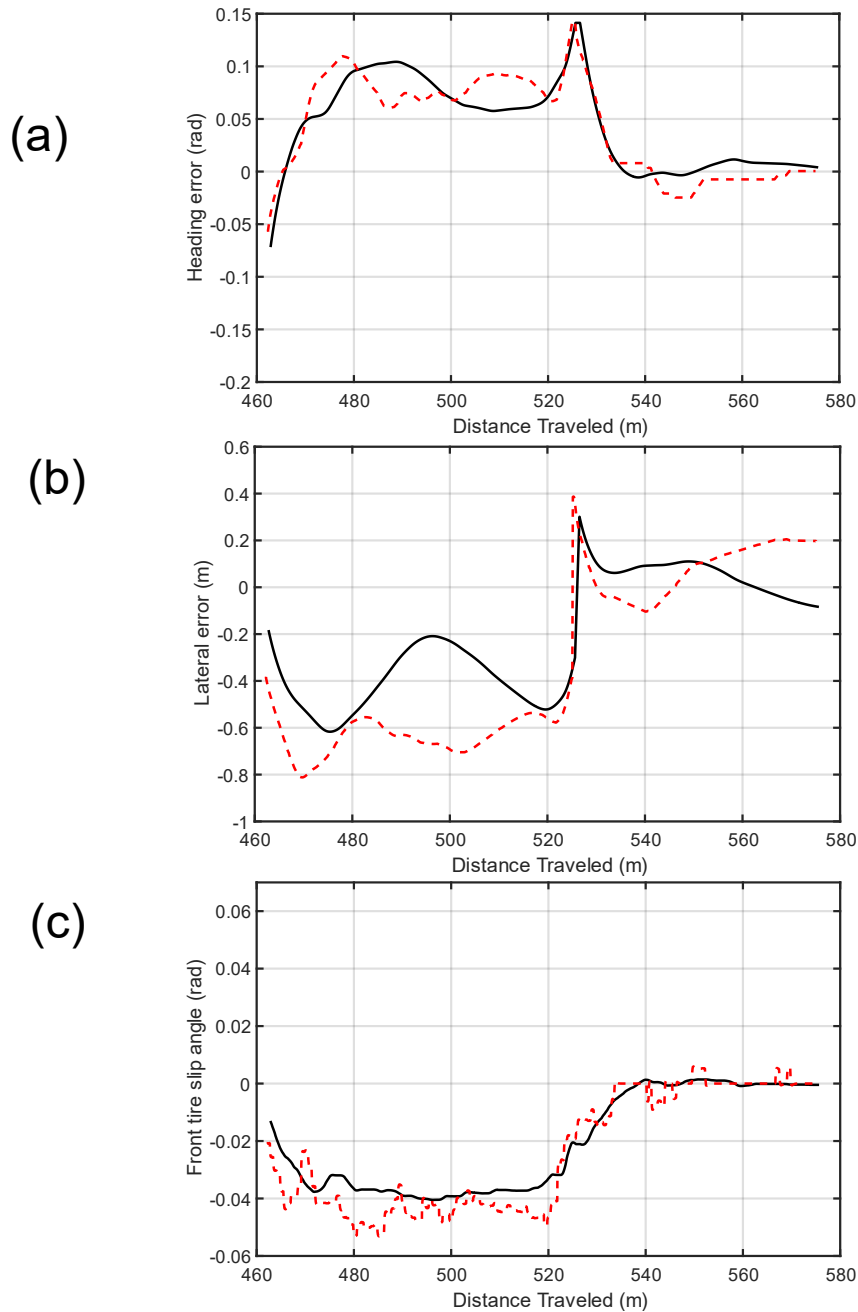


Figure 4.17. City roadway 20m radius switchback - Driver #8 performance for (a) Heading error, (b) Lateral error, and (c) Front tire slip angle (steering wheel in solid line, and cellphone in dashed line).

To investigate the vehicle's handling performance using the cellphone and the steering wheel, the yaw rate was plotted against the steering device angle in Figure 4.15. Both the cellphone and the steering wheel display a linear relationship, indicating decent

handling performances during cornering. For on center steering, the cellphone has a significantly faster response and higher yaw rate than the steering wheel. Consequently, the vehicle steered by the cellphone is more responsive than the vehicle operated by the steering wheel. This correlation also explained the cellphone-driven vehicle's faster response and higher controllability in the obstacle avoidance test.

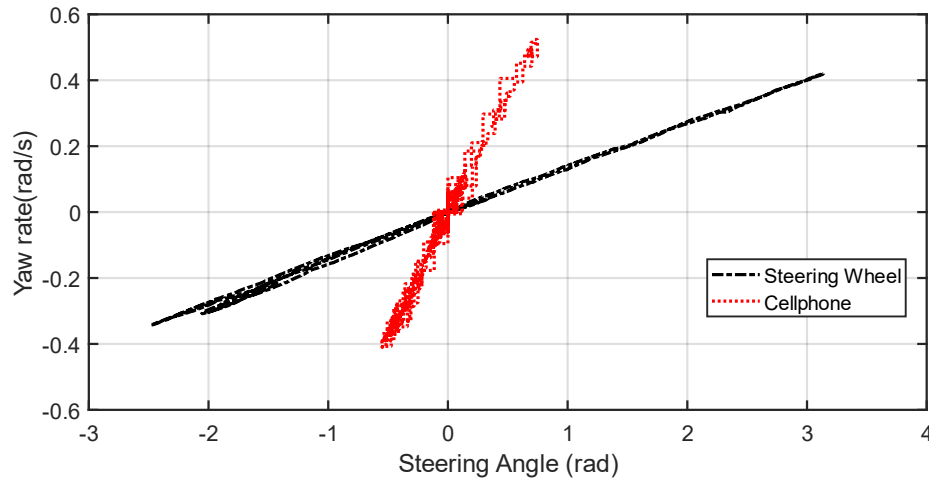


Figure 4.18. Yaw rate vs steering angle of steering wheel and cellphone during city road driving event.

The two hypotheses posed for the pilot studies have been answered. For H2, the experimental results support that it is true within the 15 participants. However, H1 cannot be fully settled. Although the steering wheel performed better in larger turning radius turns (e.g., left turn and switchback) in the city road driving event, the cellphone has a slight advantage in terms of lower lateral error compared to the steering wheel during sharp right turns. Therefore, further experimentation on different road conditions is required to explore the cellphone performance in a variety of driving environments. The steering wheel and cellphone used in this study governed the vehicle lateral motion with different steering ratios of 15:1 and 5:1 respectively due to rotational limitations (e.g.,  $225^\circ$  vs  $90^\circ$ ). More

tests and analysis are needed to investigate the effectiveness of cellphone driving through variable steering ratios.

#### **4.7 Conclusion and Future Study**

The global transportation industry needs to consider the widely accessible social media devices such as cellphone for vehicle control. Vehicle dynamics model that involves the chassis, tire and steering dynamics has been formulated and served as a cornerstone for the driving simulator designed for the operator-in-the-loop tests. Three studies, including bandwidth test, obstacle avoidance, and city road driving, have been conducted and the cellphone configurations effects on driver performance have been investigated and compared with traditional driving systems. Results from the pilot tests demonstrated that the cellphone has a 108.3% wider steering bandwidth, plus 9.1% less lateral error in extreme obstacle avoidance and 12.07% less lateral error during sharp right turn than the traditional driving system. The answer to the hypothesis puts forth regarding the impact of the cellphone driving devices is:

*Yes, the cellphone inspired driving input devices using a lower steering ratio can outperform the traditional driving system during evasive maneuvers and sharp turns.*

Fast growing semi-autonomous vehicles that use the human driver as the fallback system have created a need for alternative driving input devices. With its portability, compactness, and superior performance during extreme maneuvers, the cellphone driving device serves as a contingency driving device when semi-autonomous vehicles encounter situations that the automated system cannot handle and require human intervention. Also,



the integration of directional and propulsion control could largely solve most driving difficulties encountered by disabled drivers by excluding extensive arm and leg movements.

A tremendous amount of future research must be conducted before any cellphone-driven vehicle would be released to consumers. First, human factors studies shall be conducted to optimize cellphone placement, size, shape, as well as the safety features and the secondary functions that should be included on the device. Second, cellphone sensitivity tuning at various speeds, roadways and weather conditions need to be examined. For instance, the driver could benefit from a high steering sensitivity during low-speed driving (e.g., parking). Third, cellphone biomechanics must be investigated to explore the effects of long-term cellphone usage in terms of wrist injuries, etc. Last, steer-by-wire failsafe measures should be carefully investigated to ensure driver and occupant safety. Before a mobile telecommunication device may be used to operate a vehicle, advances in the digital technology and security protocol must occur.

## CHAPTER FIVE

### DYNAMIC CONTROL OF MULTI-SECTION THREE-DIMENSIONAL CONTINUUM MANIPULATORS BASED ON VIRTUAL DISCRETE-JOINTED ROBOT MODELS

Despite the rise of development in continuum manipulator technology and application, a model-based feedback closed-loop control appropriate for continuum robot designs has remained a significant challenge. Complicated by the soft and flexible nature of the manipulator body, control of continuum structures with infinite dimensions proves to be difficult due to their complex dynamics. In this paper, a novel strategy is designed for trajectory control of a multi-section continuum robot in three-dimensional space to achieve accurate orientation, curvature, and section length tracking. The formulation connects the continuum manipulator dynamic behavior to a virtual discrete-jointed robot whose degrees of freedom are directly mapped to those of a continuum robot section under the hypothesis of constant curvature. Based on this connection, a computed torque control architecture is developed for the virtual robot, for which inverse kinematics and dynamic equations are constructed and exploited, with appropriate transformations developed for implementation on the continuum robot. The control algorithm is validated in a realistic simulation and implemented on a six Degree-of-Freedom two-section OctArm continuum manipulator. Both simulation and experimental results show that the proposed method could manage

simultaneous extension/contraction, bending, and torsion actions on multi-section continuum robots with decent tracking performance (steady state arc length and curvature tracking error of merely 3.3mm and  $0.13\text{m}^{-1}$ , respectively).

## **5.1 Introduction**

A continuum robot (Robinson and Davies, 1999) is a bio-inspired slender hyper-redundant manipulator with theoretically infinite degrees-of-freedom (DoF) which provides remarkable capabilities for reach, manipulation, and dexterity in a cluttered environment. Recent progress toward biological systems has enabled continuum robotics research to expand rapidly, promising to extend the use of continuum robots into many new environments and providing them with capabilities beyond the scope of their rigid-link counterparts (Webster and Jones, 2010), (Trivedi et al., 2008). Long-term success for the practical application of continuum robots heavily relies on the development of real-time controllers that deliver accurate, reliable, and energy-efficient control. However, the development of high-performance model-based control strategies for continuum robots proves to be challenging due to multiple reasons. Since the manipulators must be modeled as continuous curves, the kinematic and dynamic models are difficult to derive. Also, control of continuum structures is complicated by the intrinsic underactuated nature of the backbone. Additionally, non-collocation of actuators with configuration space variables impedes the closed-loop control design (error calculation) in either space. The current scarcity of suitable local sensor technologies also contributes to the difficulty of direct internal sensing of backbone shape, which, in turn, hinders the control of continuum structures (Walker, 2013).



Figure 5.1: Dynamically controlled OctArm, a pneumatically actuated continuum manipulator with three sections, following a desired configuration trajectory.

Over the years, extensive model-based static control strategies have been proposed to design better and more reliable controllers for the continuum robots. Camarillo et al. proposed a closed loop configuration (D.B. Camarillo et al., 2009) and task space (David B. Camarillo et al., 2009) controller for tendon-driven continuum manipulators, experimentally validated with a 5-DoF per section kinematic model. Bajo et al. realized a configuration space controller which utilizes extrinsic sensory information about configuration and intrinsic sensory information about joint space (Bajo et al., 2011). An adaptation of the classic hybrid motion/force controller for continuum robots is presented and evaluated in both (Bajo and Simaan, 2016) and (Mahvash and Dupont, 2011). More complex kinematic formulations for continuum robots such as variable constant curvature (VCC) approximation were used by Mahl et al. for kinematic control of three-section manipulator with a gripper in (Mahl et al., 2014). Wang et al. presented visual servo control of a 2D image feature point in 3D space using the VCC model for a cable-driven soft conical manipulator (Hesheng Wang et al., 2013). Conrad et al. applied a closed-loop task

space controller on an interleaved continuum-rigid manipulator (Conrad and Zinn, 2015). Marchese and Rus achieved kinematic control of a pneumatic-actuated soft manipulator that is made from low durometer elastomer (Marchese and Rus, 2016).

Widely considered the most challenging field in the control of continuum robots (George Thuruthel et al., 2018), model-based dynamic controllers that consider the complete kinematics and dynamics of the whole manipulator have been explored by previous researchers. Gravagne and Walker validated feedforward and feedback proportional-derivative (PD) controller through simulations of a planar single multi-section continuum robot (Gravagne and Walker, 2002). Falkenhahn et al. implemented optimal control strategies that consider both the mechanical dynamics and the pressure dynamics to achieve trajectory optimization of continuum manipulators (Falkenhahn et al., 2014). Marchese et al. described a trajectory optimization scheme and dynamic model for a soft planar elastomer manipulator (Marchese et al., 2015). Falkenhahn et al. developed a dynamic controller in actuator space that provides actuator decoupling in combination with feedforward and feedback strategies (Falkenhahn et al., 2017).

In this work we propose a model-based dynamic feedback control architecture that has been specifically designed for controlling continuum robots, extending our previous work (Wang et al., 2018a) not only from two to three dimensions but also from one to two sections. The novel approach to continuum robot control discussed in this paper is motivated by reducing computational complexity using a virtual, conventional rigid link robot with discrete joints. The control strategy is developed in the virtual robot coordinates, taking advantage of the well-understood nature of conventional robot dynamics. The

virtual robot is selected such that its degrees of freedom are directly mapped to those of the real continuum robot for which control is desired.

Specifically, the above approach is validated from model development to hardware implementation for control of a multi-section spatial continuum robot. The continuum robot is approximated as a serial rigid-link Revolute-Revolute-Prismatic-Revolute (RRPR) joint spatial robot with an out-of-plane rotation, two in-plane rotations, and a translation in the same plane to create a 3D virtual rigid-link robot (Walker, 2013). A block diagram of the joint space dynamic controller by feedback linearization for closed-loop configuration space control is depicted in Figure. 5.2. The control attempts to achieve tracking of configuration space variables using a proportional integral derivative (PID) computed-torque controller in the joint space to calculate virtual torques that are translated into pneumatic pressure in the actuator space. The task space to joint space inverse kinematics are obtained via a desired virtual joint vector which forms the error vector with the actual virtual joint space variables derived from the continuum robot configuration space. The approach mentioned above assumes on the constant curvature (CC) approximation (Hannan and Walker, 2003) for the configuration space model.

Previous research has also examined the possibility of controlling a continuum structure via exploiting a “virtual” rigid link robot model. However, the methodologies were either applied only to the bending of a planar continuum section (Tang et al., 2019), or formulated using a under-parameterized model which involves merely bending and twisting without considering continuum robot extension/contraction (Katzschmann et al., 2019), (Greigarn et al., 2019). In contrast, the work in this paper is the first attempt to

accomplish three-dimensional control of continuum robots whose configuration space is parameterized by arc length  $s$ , curvature  $\kappa$ , and rotational orientation  $\phi$ . Such comprehensive parameterization accounts for simultaneous extension/contraction, bending, and torsion actions of continuum robots, therefore fully matching the control capability and motion complexity of continuum robots. In addition, we extend model-based dynamic control research through the application of the computed torque approach that provides virtual rigid link robot dynamics decoupling for the control of multi-section continuum robots.

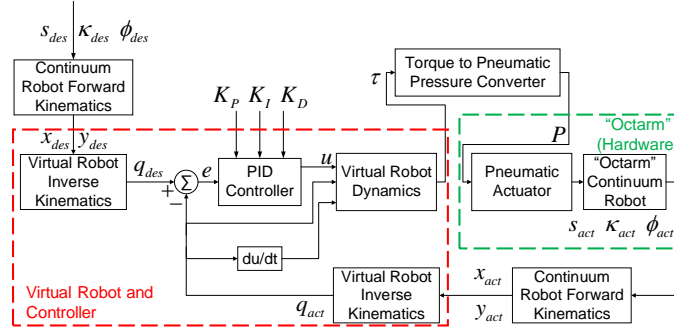


Figure. 5.2. Block Diagram for Continuum robot control based on virtual robot models.

This virtual discrete-jointed robot model-based controller for continuum manipulators is developed and applied and tested on the octopus biology inspired OctArm (Grissom et al., 2006), a three-section intrinsically pneumatic-actuated continuum manipulator with nine DoF (depicted in Figure. 5.1). Each OctArm section is constructed using pneumatic “McKibben” muscle extensors (Walker et al., 2005) with three control channels per section that provide bending, extension, and 360° of 3D rotation. A closed-loop task space dynamic controller (Kapadia and Walker, 2011) and a closed-loop configuration space control using a sliding mode controller (Kapadia et al., 2010),(Kapadia et al., 2014) were implemented on the OctArm. More recently, an adaptation-based

nonlinear control strategy was adopted for the OctArm (Frazelle et al., 2018), but until now, a dynamic controller based on virtual discrete-jointed robot model proposed in this paper remains undeveloped for the OctArm.

## 1.6 5.2 Mathematical Model

### 5.2.1 Spatial Continuum Robot Forward Kinematics

In order to comprehend the continuum robot movements, a forward kinematic model, which relates the configuration space (backbone shape) variables and task (e.g., tip) space variables, needs to be constructed. Such a model lays the foundation for designing control algorithms and is vital for the practical implementation of continuum robot hardware.

The approach to continuum robot forward kinematics in this article heavily exploits the CC sections feature. The CC feature assumes that the configuration space of a three-dimensional (3D) continuum architecture can be parameterized by three variables: arc length  $s$ , the curvature  $\kappa = 1/r$  as related to the radius  $r$  of a curve, and orientation  $\phi$  of the curve plane in space. The CC continuum bending can be decomposed into four discrete motions: (1) a rotation to “point” the tangent at the curve’s origin to the curve’s end point; (2) a translation from curve origin to end; (3) a second rotation identical with the first to realign with the tangent at the curve’s end; and (4) a rotation about the initial tangent; see Figure. 5.3. Given this observation, a “virtual” 3D four-joint rigid-link RRPR manipulator can be used to model the kinematic transformation along any CC backbone (Hannan and Walker, 2001). Consequently, the corresponding continuum robot forward kinematics model can be found using the conventional Denavit-Hartenberg (D-H) [29] convention for



the virtual robot; see Table I. The associated homogeneous transformation matrix of the virtual RRPR robot model is given as

$$H_4^0 = \begin{bmatrix} c_1 c_2 c_4 - c_1 s_2 s_4 & -s_1 & -c_1 c_2 s_4 - c_1 s_2 c_4 & -d_3 c_1 s_2 \\ s_1 c_2 c_4 - s_1 s_2 s_4 & c_1 & -s_1 c_2 s_4 - s_1 s_2 c_4 & -d_3 s_1 s_2 \\ s_2 c_4 + c_2 s_4 & 0 & -s_2 s_4 + c_2 c_4 & d_3 c_2 \\ 0 & 0 & 0 & 1 \end{bmatrix} \quad (5.1)$$

where  $s_l$  and  $c_l$  ( $l = 1, 2, 4$ ) denote  $\sin(\theta_l)$  and  $\cos(\theta_l)$  for the three revolute joints in the RRPR model, respectively and  $d_3$  is the length of the third, prismatic, joint in the RRPR model. The continuum robot kinematics can be readily developed by substituting the joint variables of the virtual robot with the corresponding configuration space variables of a continuous curve. Specifically (see Figure. 5.3),

$$\theta_1 = \phi, \quad \theta_2 = \theta_4 = \theta, \quad \kappa = \left( \frac{1}{r} \right) \quad (5.2)$$

We have

$$s = r(2\theta) = \frac{(2\theta)}{\kappa} = \frac{(\theta_2 + \theta_4)}{\kappa} \rightarrow (\theta_2 + \theta_4) = s\kappa \quad (5.3)$$

$$\frac{d_3}{2} = r \sin \theta = \frac{\sin \theta}{\kappa} \rightarrow d_3 = \frac{2 \sin \theta}{\kappa} \quad (5.4)$$

Substituting (3) and (4) into the model (1) and simplifying gives

$$H_4^0 = \begin{bmatrix} c_\phi c_{s\kappa} & -s_\phi & -c_\phi s_{s\kappa} & \frac{c_\phi - c_\phi c_{s\kappa}}{\kappa} \\ s_\phi c_{s\kappa} & c_\phi & -s_\phi s_{s\kappa} & \frac{s_\phi c_{s\kappa} - s_\phi}{\kappa} \\ s_{s\kappa} & 0 & c_{s\kappa} & \frac{s_{s\kappa}}{\kappa} \\ 0 & 0 & 0 & 1 \end{bmatrix} \quad (5.5)$$

where  $c_m$  and  $s_m$  ( $m = s, \kappa, \phi, s\kappa$ ), denote  $\cos(m)$  and  $\sin(m)$ , respectively. The model (5) describes the forward kinematic relationship (3 by 3 orientation, top left of (5), and 3 by 1 translation, top right) between continuum curve shape (arc length  $s$ , curvature  $\kappa$ , and orientation  $\phi$ ) and task space ( $x$ ,  $y$ , and  $z$  coordinates).

The forward kinematics for a  $n$ -section manipulator can then be generated by the product of  $n$  matrices of the form given in Eq. (5). For example, the forward kinematics for the continuum robot with its two sections can be calculated as

$$T_1^3 = T_1^2 T_2^3 \quad (5.6)$$

where  $T_a^{a+1} = H_4^0$  for section  $a$  of the manipulator.

TABLE 5.1

Link Parameters for Virtual RRPR Robot Manipulator

Link	$\theta$	$d$	$a$	$\alpha$
1	*	0	0	90
2	*	0	0	-90
3	0	*	0	90
4	*	0	0	-90

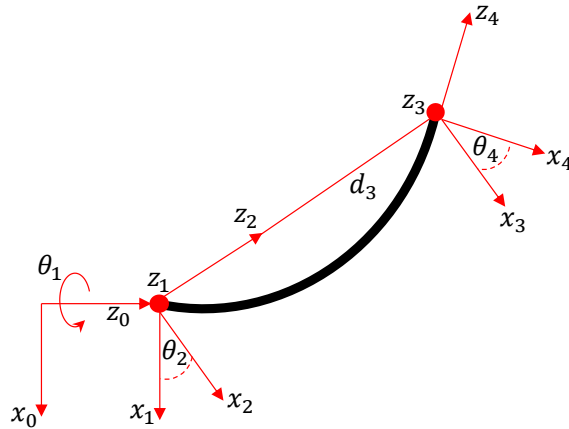


Figure. 5.3. Three-dimensional constant curvature section geometry obtained via rotation about initial tangent based on virtual RRPR discrete-jointed robot model.

### 5.2.2 Virtual Robot Inverse Kinematics

The inverse kinematics of the continuum robot can be approximated by that of the spatial RRPR virtual robot. After the task space coordinates of the continuum robot are derived from the continuum robot forward kinematics in (5), the  $x$ ,  $y$ , and  $z$  coordinates can then be substituted into the inverse kinematics of the RRPR robot model to obtain the desired joint space vector  $q_d = [\theta_1 \quad \theta_2 \quad d_3 \quad \theta_4]^T$ . From (1) we obtain

$$x = -d_3 c_1 s_2, \quad y = -d_3 s_1 s_2, \quad z = d_3 c_2 \quad (5.7)$$

Since

$$x^2 + y^2 + z^2 = d_3^2 \left[ (c_1 s_2)^2 + (s_1 s_2)^2 + (c_2)^2 \right] = d_3^2 \quad (5.8)$$

Thus

$$d_3 = +\sqrt{x^2 + y^2 + z^2} \quad (5.9)$$

The rotation  $\theta_2$  and  $\theta_4$  can be obtained from

$$\theta_2 = \tan^{-1} \left( \frac{s_2}{c_2} \right) = \tan^{-1} \left( \frac{\sqrt{x^2 + y^2}}{d_3} \bigg/ \frac{z}{d_3} \right) = \tan^{-1} \left( \frac{\sqrt{x^2 + y^2}}{z} \right) = \theta_4 \quad (5.10)$$

The rotation  $\theta_1$  can also be derived as

$$\theta_1 = \tan^{-1} \left( \frac{s_1}{c_1} \right) = \tan^{-1} \left( \frac{y}{-d_3 s_2} \bigg/ \frac{x}{-d_3 s_2} \right) = \tan^{-1} \left( \frac{y}{x} \right) \quad (5.11)$$

For a two-section continuum robot which can be modeled as an 8-DoF RRPRRRPR rigid-link robot, derivations of analytical inverse kinematics solutions can be extremely burdensome. Due to the high order polynomial nature of expressions and high redundancy, obtaining analytical inverse kinematic solutions for the full task space position for the two-

section continuum arms is computationally infeasible. Therefore, in this article, we apply the pseudoinverse solution to the virtual robot model to relate the rigid-link robot joint space to the continuum robot task space. After the Jacobian matrix  $J$  of an RRPRRRPR robot has been derived, the Moore-Penrose pseudoinverse of the Jacobian matrix  $J$  is readily defined as  $J^+ = J^T(JJ^T)^{-1}$  (Siciliano, 1990). Therefore, the joint space can be solved as

$$\dot{q}_{des} = J^+(q) \dot{x}_{des} \quad (5.12)$$

where  $\dot{x}_{des} \in \mathbb{R}^{3 \times 1}$  is the desired Cartesian coordinate vector  $[x \ y \ z]^T$  and  $\dot{q}_{des} \in \mathbb{R}^{8 \times 1}$  is the derived desired joint velocities vector. The inverse kinematic problem can then be readily solved through the integration of  $\dot{q}_{des}$  in (12).

### 5.2.3 Virtual Robot Dynamics

Incorporating the dynamics of the continuum robot is vital for model-based dynamic control of continuum structures. The dynamic equations of motion, which provide the relationships between actuation and the acceleration, form the basis for several computational algorithms that are fundamental in control and simulation. In this article, the virtual RRPR rigid-link robot dynamics is derived and exploited to approximate the dynamics of a 3D continuum architecture. For motion control, the dynamic model of a virtual RRPR mechanism is conveniently described by Lagrange dynamics represented in the joint-space formulation.

The Euler-Lagrange dynamics equations of the virtual RRPR manipulator can be written in a matrix form as

$$D(q)\ddot{q} + C(q, \dot{q})\dot{q} + g(q) = \tau \quad (5.13)$$

where  $q \in \mathbb{R}^{4 \times 1}$  is the joint variable vector for the virtual RRPR robot, the joint variables are  $q_1 = \theta_1$ ,  $q_2 = \theta_2$ ,  $q_3 = d_3$ , and  $q_4 = \theta_4$ . The vector  $\tau \in \mathbb{R}^{4 \times 1}$  is the torque applied to each joint variable. Specifically, the term  $\tau_1$  is the applied torque at the first revolute joint which drives the orientation of the continuum robot,  $\tau_2$  and  $\tau_4$  are the applied torques at the second and fourth revolute joints which form the shape (curvature) of the continuum robot, and  $f_3$  is the applied force at the third prismatic joint which elongates/shrinks the continuum robot. The detailed derivation process and derived terms of the inertia matrix  $D(q)$ , centrifugal and Coriolis matrix  $C(q, \dot{q})$  and gravity matrix  $g(q)$  in (13) can be found via the link <https://urlzs.com/wuEWb> for reference.

Similarly, the dynamic model for a two-section continuum robot can be modeled by combining two virtual RRPR robots into an 8-DoF RRPRRRPR rigid-link robot. The kinematics of this virtual robot is constructed in a way so that the interface between the two RRPR robots aligns the last/first z-axes (see Figure. 5.3), as the 8-DoF virtual robot needs to model the continuum case where the tangent between two sections are aligned. The authors have derived the dynamics model for the virtual 8-DoF robot model via the Euler-Lagrange approach to compute torques for continuum architecture control. For the sake of space and conciseness, the inertia matrix  $D(q)$ , centrifugal and Coriolis matrix terms in  $C(q, \dot{q})$ , as well as the gravity matrix  $g(q)$ , as derived by the authors for the 8-DoF virtual robot dynamics, is stored in the link <https://urlzs.com/vSmxy> for reference.

### 5.3 Control Systems Design

The modeling strategies of the previous section form the basis for control approaches needed for continuum robots. We seek and exploit simple, relatively

computationally inexpensive control methods used in (rigid-link) robot control systems [2] to design the controller in the virtual RRPR robot coordinates. Multiple control methods, such as adaptive control (Frazelle et al., 2018), optimal and robust control (Kapadia et al., 2010), and learning control (Braganza et al., 2007), are widely used in robotics. Each control method has advantages and disadvantages. However, the main aim of the system is to provide stability and high-frequency updates. In this work, we adopt the computed-torque (Middleton and Goodwin, 1986) (feedback linearization plus PID control) approach for the virtual robot, with the sensing and actuation transformed from and to the continuum robot, respectively.

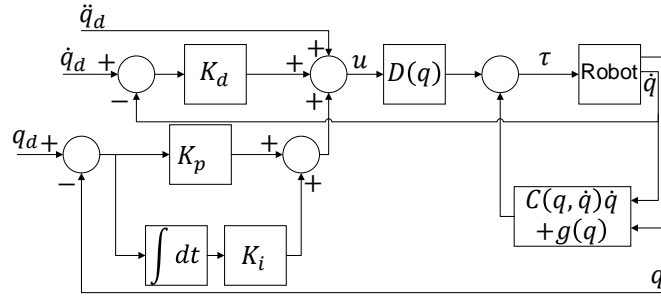


Figure. 5.4. Block diagram for PID computed-torque controller designed for virtual RRPR robot.

The computed-torque control consists of an inner nonlinear compensation loop and an outer loop with an exogenous control signal  $u$ . This control input converts a complicated nonlinear controller design problem into a simple design problem for a linear system consisting of several decoupled subsystems. One approach to the out-loop control  $u$  is the proportional–integral–derivative (PID) feedback. The reason why the PID controller is preferred in this article over the proportional-derivative (PD) controller is that the PID controller eliminates the steady-state error caused by environmental disturbances. In the PID control, the chosen parameters,  $K_p$ ,  $K_i$  and  $K_d$  remain constant during the process.

Therefore, such a controller is inefficient because the controller contains ambiguity when environmental conditions or dynamics change. In addition, it is inefficient because of time delays and nonlinearity conditions. Hence, we include the dynamics to linearize prior to the PID control.

The dynamic model of the virtual robot arm is given in (13). The errors of the robot variables are

$$e = q_d - q, \dot{e} = \dot{q}_d - \dot{q}, \ddot{e} = \ddot{q}_d - \ddot{q} \quad (5.14)$$

where  $e, \dot{e}, \ddot{e}$  express the position, velocity, and acceleration error vectors and  $q_d, \dot{q}_d, \ddot{q}_d$  expresses the desired position, velocity, and acceleration of the variables. The torques required for each joint of the virtual robot arm are calculated from (13) and the errors from (14). The linearization is achieved as follows

$$\tau = D(q)(\ddot{q}_d - u) + C(q, \dot{q})\dot{q} + g(q) \quad (5.15)$$

The control signal that is obtained from (15) is expressed as follows

$$u = \ddot{q}_d + D^{-1}(q)[C(q, \dot{q})\dot{q} + g(q) - \tau] \quad (5.16)$$

If the signal  $u$  is selected as the PID feedback controller, the torque value of each joint will be obtained from (17) and (18).

$$u = -K_d \dot{e} - K_p e - K_i \int e dt \quad (5.17)$$

$$\tau = D(q)(\ddot{q}_d + K_d \dot{e} + K_p e + K_i \int e dt) + C(q, \dot{q})\dot{q} + g(q) \quad (5.18)$$

where  $K_d$  is the derivative gain,  $K_i$  is the integral gain, and  $K_p$  is the proportional gain.

The overall controller of the virtual robot is shown in Figure. 5.4. The values of the controller gains, i.e.,  $K_d$ ,  $K_i$ , and  $K_p$ , were determined according to an iterative

experimental process to maximize controller performance. The input desired trajectory was represented in terms of Cartesian coordinates  $x$ ,  $y$ , and  $z$ , and was calculated from the continuum robot arc length  $s$ , curvature  $\kappa$ , and orientation  $\phi$  using the forward kinematics discussed in Section II. Subsequently the virtual robot variables: rotation  $\theta_1$ ,  $\theta_2$ ,  $d_3$ , and  $\theta_4$  were derived from the inverse kinematics in section II and fed into the control system as a desired reference input signal. Their derivatives and double derivatives were calculated and served as the inputs to the controller through  $\mathbb{R}^{4 \times 1}$  vectors  $q_d$ ,  $\dot{q}_d$ , and  $\ddot{q}_d$ . The output of the controller,  $u$ , is then used to establish the torque signal  $\tau$  along with systems  $D(q)$ ,  $C(q, \dot{q})$ , and  $g(q)$  matrices. The torque  $\tau$  was then converted to actuation space in the pressure form and applied to the physical continuum robot system which feeds back the current continuum robot shape configuration, subsequently converted to virtual robot rotation and translation  $\mathbb{R}^{4 \times 1}$  signal vectors  $q$  and  $\dot{q}$  which then input to the PID controller to form the error and drive the control action.

#### 5.4 Controller Simulation Results

A simulation study has been conducted to investigate the validity of the proposed control strategy based on the virtual rigid-link model. Simulations of the virtual robot computed torque control were executed in the Simulink environment. The input of the system is three reference signals in configuration space: the arc length  $s$ , curvature  $\kappa$ , and orientation  $\phi$ , which were fed into the continuum robot forward kinematics in (5) to form Cartesian coordinates  $x$ ,  $y$ , and  $z$ . In the simulation presented here, an OctArm-emulated reference arc length  $s$  is designated as a sinusoidal wave with range  $[0.35\text{m}, 0.41\text{m}]$  and frequency 3 rad/s as shown in Figure. 5.5. The continuum robot curvature  $\kappa$  reference is a



chirp signal in which the frequency increases with time to increase the control complexity. To simulate the full  $360^\circ$  rotation of the continuum robot, a ramp signal is assigned to the reference orientation  $\phi$ .

The comparison between desired and actual  $x$  and  $y$  coordinates of the continuum robot end effector is depicted in Figure. 5.5. There is a large overshoot observed when the end effector is attempting to reach the first desired  $x$ ,  $y$ , and  $z$  locations, but then the system becomes stabilized before following the desired task space successfully. The desired and actual joint space variables  $\theta_1$ ,  $\theta_2$ ,  $d_3$ , and  $\theta_4$  of the virtual RRPR robot can be observed in Figure. 5.7. All signals eventually reach an optimal stable condition. The corresponding torques/force applied to each joint, namely  $\tau_1$ ,  $\tau_2$ ,  $f_3$ , and  $\tau_4$  can be found in Figure. 5.8. Collectively, the convergence to reference values in both task and joint space not only marks decent accuracy of the virtual RRPR robot approximation model, but also reflect the effectiveness of the computed-torque approach in reaching desired continuum robot configuration.

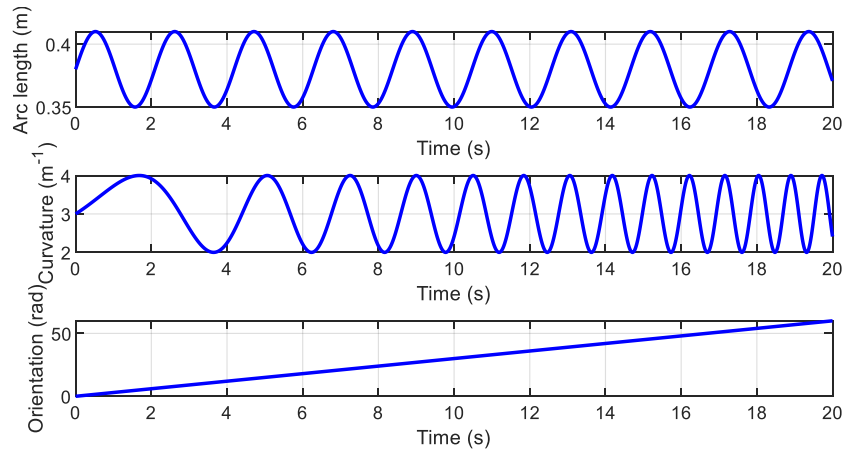


Figure. 5.5. Desired configuration variables arc length  $s$ , curvature  $k$ , and Orientation  $\phi$  for simulation of the virtual robot computed torque control.

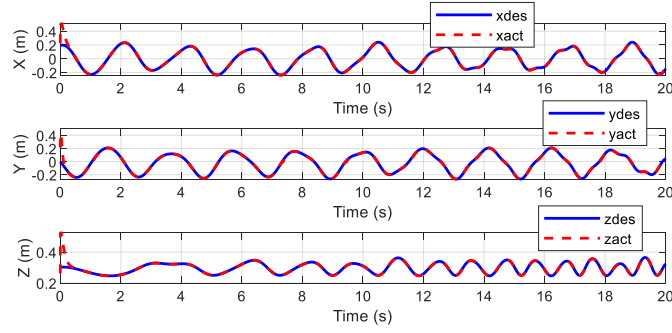


Figure. 5.5. Desired and actual continuum robot end-effector X, Y, and Z coordinates during simulation of the virtual robot computed torque control.

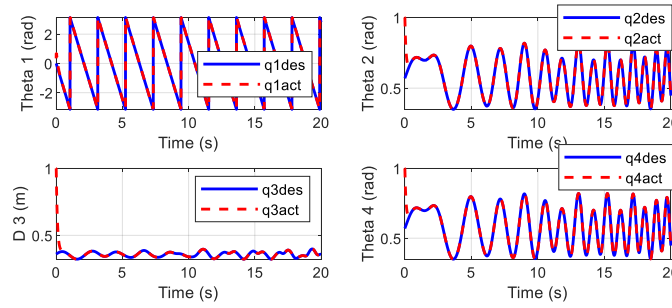


Figure. 5.7. Desired and actual virtual RRPR robot joint variables  $\theta_1$ ,  $\theta_2$ ,  $d_3$ , and  $\theta_4$  during simulation of the virtual robot computed torque control.

## 5.5 Experimental Implementation

### 5.5.1 Experimental Setup

To further demonstrate the validity of the proposed controller based on the virtual rigid-link dynamics model, the experiments are conducted on the tip and mid-sections of the OctArm continuum manipulator (Grissom et al., 2006), (Walker et al., 2005). The OctArm, whose structure is shown in Figure. 5.9, is a 9-DoF pneumatically actuated, extensible, continuum robot capable of motion in three dimensions. The kinematically redundant manipulator is comprised of three serially connected sections: base, mid, and tip-section. Each of the three sections can extend (with arc length  $s$ ) and bend in any direction (with curvature  $\kappa$  and orientation  $\phi$ ), providing three DoF for each section. The OctArm is constructed using compressed air-actuated McKibben extension muscles with

three control channels per section; see Figure. 5.10 (Grissom et al., 2006). The mid-section has three pairs of McKibben actuators spaced radially at  $120^\circ$  intervals, forming one control channel per pair. Such mid-section design leads the muscle actuators to be designed for a larger radius and results in higher stiffness and load capacity, though at the expense of manipulability. The tip-section of the device is comprised of three single McKibben actuators arranged radially at  $120^\circ$  intervals, resulting in greater manipulability as compared to the mid-section.

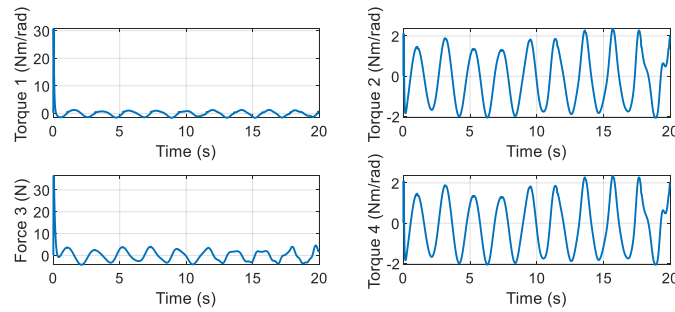


Figure. 5.8. Torques and force applied to each virtual RRPR robot joint -  $\tau_1$ ,  $\tau_2$ ,  $f_3$ , and  $\tau_4$  are the torques/force applied to  $\theta_1$ ,  $\theta_2$ ,  $d_3$ , and  $\theta_4$  during simulation.

A set of experiments utilizing the OctArm and the described model were implemented. The model and controller were implemented in MATLAB/Simulink environment (“Simulink - Simulation and Model-Based Design,” n.d.). Interfacing with the OctArm was accomplished using two Quanser Q8-USB data acquisition boards (“Q8-USB Data Acquisition Device - Quanser,” n.d.). State estimation of the system was provided through internal measurements of the OctArm via a series of string encoders that run along the length of each section muscle. After output torques and forces are computed from the proposed controller, they are converted to pneumatic pressures via a series of pressure regulators using an output voltage from the Quanser boards. The pressures are then applied onto the corresponding McKibben extension muscles, where one regulator is

assigned to one muscle or one muscle pair in the case of the mid-section. A full torque/force to pneumatic pressure conversion technique is formulated and discussed in Section V.B. Experiments on both one section (tip-section, 3-DoF) and two sections (tip and mid-sections, 6-DoF) are conducted in three-dimensional space to examine configuration space tracking performance of the proposed control method for multi-section continuum robots. Results of experiments are presented in Sections V.C and V.D and, with discussions and future research contained in Section V.E.



Figure. 5.9. The OctArm manipulator with base, mid, and tip sections.

### 5.5.2 Torque to Pressure Conversion

To facilitate the implementation of the proposed controller into pneumatically actuated continuum architectures like the OctArm, the computed torques  $[\tau_1 \ \tau_2 \ f_3 \ \tau_4]^T$  for controlling the virtual rigid-link robot model in (21) must be converted into applied pneumatic pressures onto each of the pneumatic “McKibben” muscles in the single tip-section. Such conversions can be inspired by the movements of the OctArm which can be categorized into three distinct motions: (1) extension/contraction which determines the continuum robot arc length  $s$ ; (2) bending which accounts for the OctArm curvature  $\kappa$ ; and (3) torsion which translates to continuum robot orientation  $\phi$ .

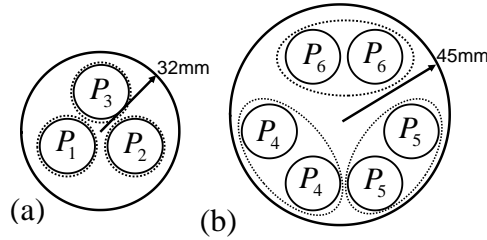


Figure. 5.10. OctArm actuator cross-section configurations for (a) tip (left), (b) mid (right) sections (Dotted lines show three control channels)

For pure extension/contraction motion, the calculated extension force  $f_3$  that results from the RRPR model is equally applied to the three muscles to achieve balanced pure extending movement. In order to generate simultaneous extending, bending, and torsion motions at the single tip-section of the OctArm shown in Figure. 5.10a, the controller generated torques  $\tau_1$ ,  $\tau_2$ , and  $\tau_4$  which are responsible for driving the rotation  $\phi$  and curvature  $\kappa$  need to be incorporated. Therefore, the pressure applied to the three McKibben muscle control channels can be represented as

$$\begin{aligned} P_1 &= k_p \left[ f_3 + \Delta\tau \cdot \cos(\phi + b \cdot \tau_1) \right] \\ P_2 &= k_p \left[ f_3 + \Delta\tau \cdot \cos(\phi + b \cdot \tau_1 + 120^\circ) \right] \\ P_3 &= k_p \left[ f_3 + \Delta\tau \cdot \cos(\phi + b \cdot \tau_1 - 120^\circ) \right] \end{aligned} \quad (5.19)$$

where  $\Delta\tau = (\tau_2 + \tau_4)/2$ ,  $\phi$  denotes the current rotation of the OctArm,  $k_p$  is the conversion gain from torque to pressure, and  $b$  is a constant. In (19), the terms  $f_3$ ,  $\Delta\tau$ , and  $\tau_1$  account for extending, bending, and torsion maneuvers, respectively. The difference of pressure given to three distinct sets of control channels will generate a bending effect of constant curvature that matches the continuum robot kinematics model. From the iterative experimental experiences, we identified a sinusoidal offset between the desired curvature  $\kappa_{des}$  and actual curvature  $\kappa$ , which occurs due to the OctArm tip-section inborn stiffness. Therefore, to compensate for this offset, the compensated pressure applied to the three muscles to achieve simultaneous extending, bending, and torsion are

$$\begin{aligned}
P_1 &= k_p \left[ f_3 + (\Delta\tau + C) \cdot \cos(\phi + b \cdot \tau_1) \right] \\
P_2 &= k_p \left[ f_3 + (\Delta\tau + C) \cdot \cos(\phi + b \cdot \tau_1 + 120^\circ) \right] \\
P_3 &= k_p \left[ f_3 + (\Delta\tau + C) \cdot \cos(\phi + b \cdot \tau_1 - 120^\circ) \right]
\end{aligned} \tag{5.20}$$

where  $C(\phi) = \alpha \sin \phi + \beta$  is the curvature compensator, and  $\alpha$  and  $\beta$  are both constants.

Pressure conversion of the two section OctArm which can be modeled as a virtual RRPRRRPR robot is achieved similarly to that of the one section. After the derivation of the torque vector  $[\tau_1 \ \tau_2 \ f_3 \ \tau_4 \ \tau_5 \ \tau_6 \ f_7 \ \tau_8]^T$ , whose first four terms model the mid-section and last four terms model the tip-section, the pressures on three mid-section control channels  $P_4$ ,  $P_5$ , and  $P_6$  (shown in Figure. 5.10b), are determined by substituting  $P_4$ ,  $P_5$ , and  $P_6$  for  $P_1$ ,  $P_2$ , and  $P_3$ , respectively, in (20). The pressures of the three tip-section control channels,  $P_1$ ,  $P_2$ , and  $P_3$ , are computed by substituting  $\tau_5$ ,  $\tau_6$ ,  $f_7$ , and  $\tau_8$  for  $\tau_1$ ,  $\tau_2$ ,  $f_3$ , and  $\tau_4$ , respectively, in (20).

### 5.5.3 One-section OctArm Experiment

The first experiment conducted on the OctArm manipulator reported here is simultaneous extension/contraction, bending, and torsion on one OctArm section. Detailed video footage of the experiment can be found via the link <https://urlzs.com/HiYMH>. In this experiment, the system is fed desired arc length  $s$  a sinusoid with an amplitude 0.03m and a frequency of 0.08Hz, as shown in Figure. 5.11. The desired curvature  $\kappa$  is also a sinusoidal signal with an amplitude of  $1m^{-1}$  and a frequency of 0.08Hz while the desired orientation  $\phi$  is a ramp function with a slope of 0.3 (rad/s) to generate a full 360° rotation on the tip-section. During the experiment, the OctArm initiated from its natural unpressurized length of 0.34m and rapidly converged to the desired arc length with minor

error in the crest of the sine wave. The actual arc length  $s$  and curvature  $\kappa$  settle relatively fast and no obvious overshoot or oscillations are detected. Possibly due to intrinsic settling nature of the PID controller, the high-frequency oscillatory motion observed in the first cycle of arc length and curvature sinusoid terminates after 7 seconds before the system reaches a steady state. Also, the robot accomplishes three full  $360^\circ$  rotations in conjunction with the sinusoidal arc length and curvature variations. Highlighting the effectiveness of the controller, the arc length and curvature error plot illustrated in Figure. 5.12 show that the control algorithm implemented on the OctArm only outputs arc length and curvature error of  $\pm 5\text{mm}$  and  $\pm 0.35\text{ m}^{-1}$ , respectively, which is considered within a reasonable range for such a complex maneuver with this robot.

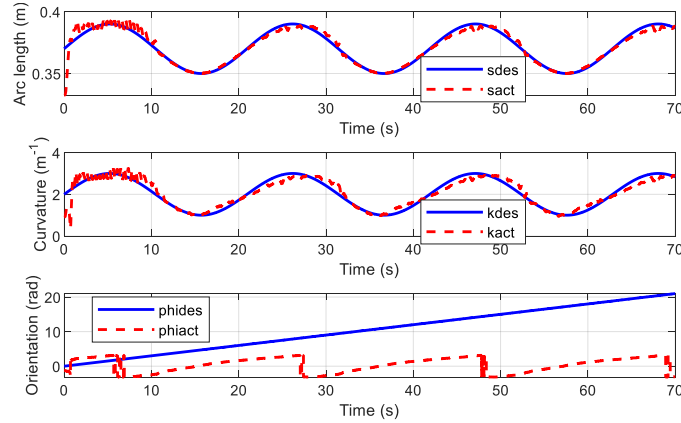


Figure. 5.11. One section experiment (OctArm tip section) — Desired and actual arc length  $s$ , curvature  $k$ , and orientation  $\phi$  in configuration space

To further demonstrate the control performance of the one section continuum robot during concurrent extending, bending, and rotation in joint space, the virtual RRPR joint variables and their corresponding applied torques/force responses of the OctArm tip-section are displayed in Figure. 5.13 & 14. Directly derived from the encoder generated OctArm configuration space variables, the joint space variables not only demonstrate the

efficacy of the controller but also reflect the accuracy of the proposed continuum architecture approximation using virtual RRPR rigid-link model. The actual joint variable values from the OctArm encoders track the desired joint variables from the virtual RRPR robot inverse kinematics relatively well. The oscillation at the beginning of the experiment, and minor error at the sinusoid crest observed in the configuration space occurred in the joint space as well. The torques/force depicted in Figure. 5.14 further confirms the source of the OctArm oscillatory motion at the beginning: all torques/force experience a high-frequency phase before following a stable sinusoidal pattern.

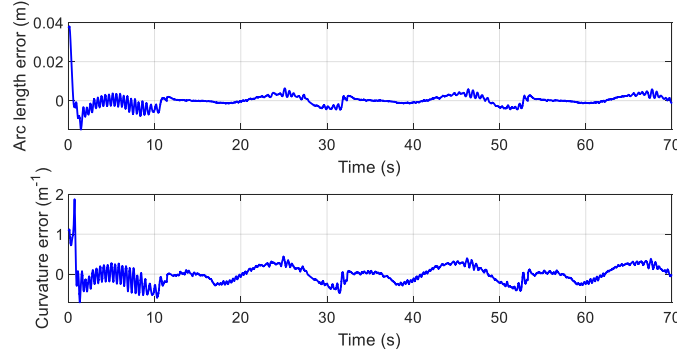


Figure. 5.12. One section experiment (OctArm tip section) — Arc length  $s$ , and curvature  $k$  error on OctArm in configuration space

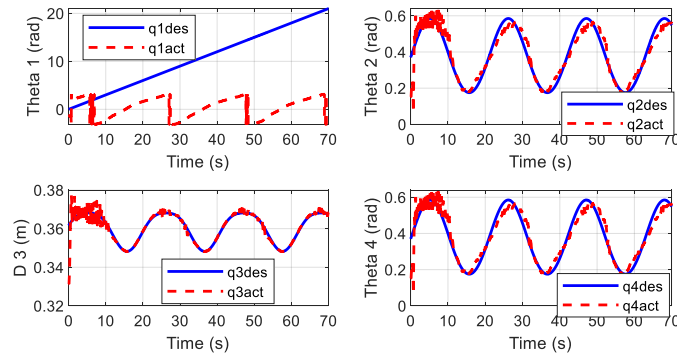


Figure. 5.13. One section experiment (OctArm tip section) — Desired and actual  $\theta_1$ ,  $\theta_2$ ,  $d_3$ , and  $\theta_4$  of the virtual RRPR rigid-link model in OctArm joint space.



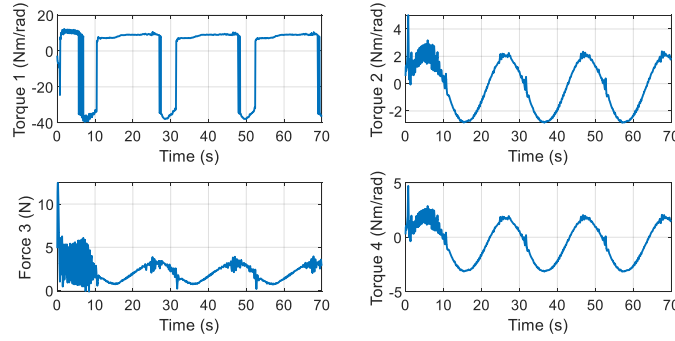


Figure. 5.14. One section experiment (OctArm tip section) — Actuation torques/force  $\tau_1$ ,  $\tau_2$ ,  $f_3$ , and  $\tau_4$ , applied to the corresponding joint space variables  $\theta_1$ ,  $\theta_2$ ,  $d_3$ , and  $\theta_4$  in virtual RRPR model.

#### 5.5.4 Two-section OctArm Experiment

The models for the complete, two-section continuum robot are formed in the previous sections by deriving the forward kinematics, inverse kinematics, and dynamics for the virtual RRPRRRPR rigid-link robot. After implementing the models into the system described in Figure. 5.2, the computed torques applied on all eight virtual joints are converted to six pressure signals which are used to actuate the OctArm mid and tip-sections. However, such an approach identifies several major drawbacks which lead to our eventual termination of controlling the two-section OctArm with the 8-DoF virtual robot model. First, compiling the experiment program in Simulink environment can consume approximately 90 minutes due to the size and complexity of the 8-DoF robot dynamics. Second, the inverse kinematics, which utilizes the pseudoinverse of the Jacobian matrix, fails to determine joint parameters that provide a valid constant curvature configuration for both mid and tip-sections. Specifically, the virtual robot joint variable pairs  $\theta_2$  and  $\theta_4$ , as well as  $\theta_6$  and  $\theta_8$  are not equal. Third, the inverse kinematics solutions are occasionally unreachable due to limitations on joint angles/length.

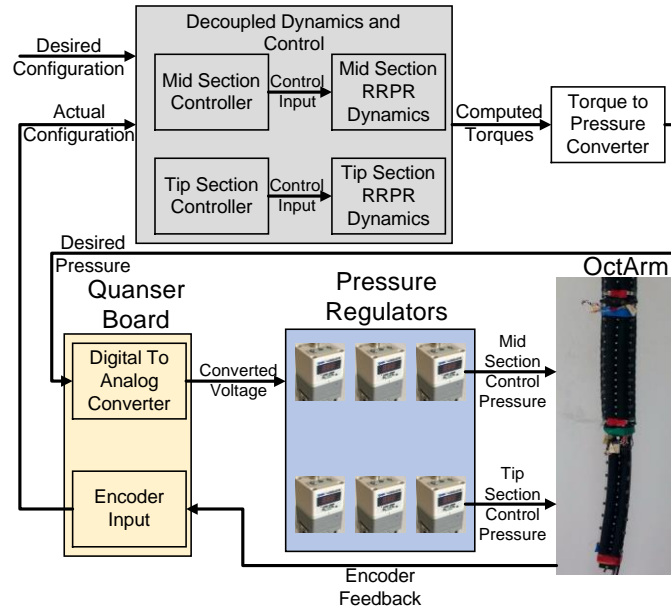


Figure. 5.15. Experimental control loop block diagram for two section OctArm decoupled virtual discrete-jointed model dynamics control.

Due to these three hindrances mentioned above, an alternative modeling approach for two section continuum robots is established: the 8-DoF RRPRRRPR rigid-body model is decoupled into two separate 4-DoF virtual discrete-jointed RRPR models whose effectiveness has been validated previously in both simulation and experiment. After the decoupling of the 8-DoF model, each of the two 4-DoF models received control input from separate controllers and generated two unique  $4 \times 1$  computed torque vectors to actuate each individual section; see Figure. 5.15. Two laboratory experiments on two-sections of the OctArm, each with distinct configuration space settings, are presented here to validate the effectiveness of the new approach in controlling multi-section continuum robots.

#### 5.5.4.1 Two section experiment 1

The desired and configuration space variables for the first experiment, whose video footage link is <https://urlzs.com/BLzyj>, is shown in Figure. 5.15. The tip-section arc length,

which is desired as a constant 0.38m, demonstrates a 5% overshoot before it immediately reaches steady state with a 3.1 second settling time; the tip-section curvature shows a similar pattern. As for the mid-section, due to the changing center of mass of the tip-section during the experiment, a sawtooth shape of the curvature is observed while the arc length yields a sinusoidal error of  $\pm 3.3\text{mm}$  with the frequency of orientation  $\phi$  shown in Figure. 5.17. The full  $360^\circ$  torsional displacement of the mid-section is accomplished smoothly whereas the tip-section orientation shows small sinusoidal fluctuation around the set point due to mid-section rotation. Collectively, the decoupled dynamics model controller demonstrates excellent performance with decent error convergence and fast response in the configuration space.

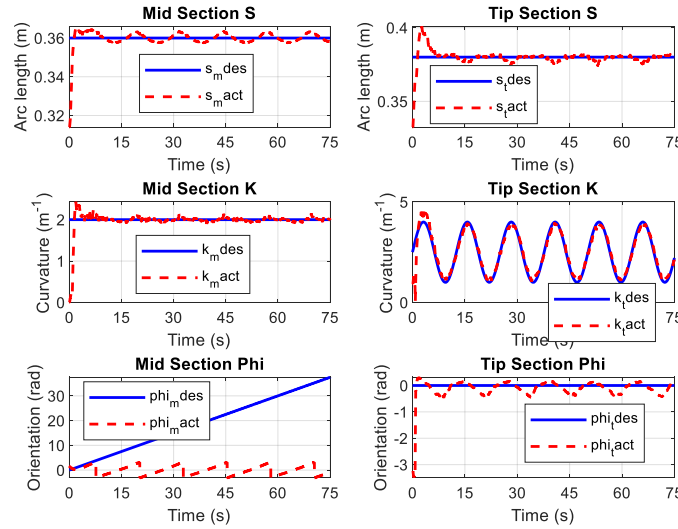


Figure. 5.15. Two section experiment 1 (OctArm tip and mid sections) — Desired and actual arc length  $s$ , curvature  $k$ , and orientation  $\phi$  in configuration space.

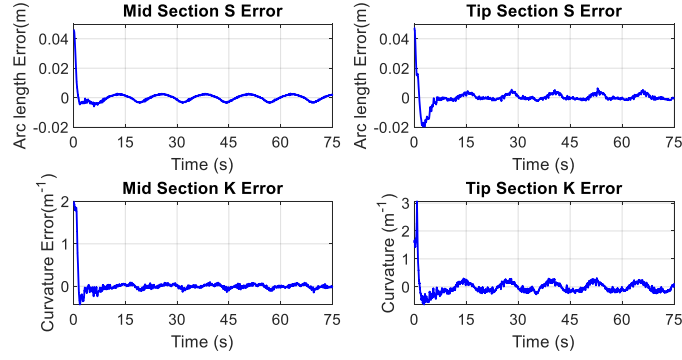


Figure. 5.17. Two section experiment 1 (OctArm tip and mid sections) — Arc length  $s$ , and curvature  $k$  error in configuration space.

The desired and actual joint space variables of the decoupled virtual robot model can be observed in Figure. 5.18. The variables  $\theta_1$ ,  $\theta_2$ ,  $d_3$ , and  $\theta_4$  represent the joint space of the mid-section while  $\theta_5$ ,  $\theta_6$ ,  $d_7$ , and  $\theta_8$  denotes that of the tip-section. All the joint variables converge to the desired set-point successfully thanks to the overwhelming tracking performance of the curvature and arc length. The resulting computed torques for each joint variable in the decoupled virtual robot model are illustrated in Figure. 5.19.

#### 5.5.4.2 Two section experiment 2

After the successful completion of experiment 1, a more complicated two section OctArm maneuver, whose video footage link is <https://urlzs.com/k7C98>, is tested to examine the control method resilience against demanding robot operations. The desired and actual configuration space variables are exhibited in Figure. 5.20. The arc length for both tip and mid-section display outstanding performance with minor overshoot on the tip-section. On the other hand, the mid-section curvature exhibits not only oscillatory motion but also high overshoot due to higher stiffness, which leads to mediocre manipulability. The tip-section arc length also experiences intense oscillations at the first sine wave trough and a major overshoot before it reaches a steady state after 22 seconds. Both the tip and

mid-section track the desired orientation well. Collectively, the performance of experiment 2 deteriorated compared to that of experiment 1, as shown in Figure. 5.21, where errors of both section configurations increased by a noticeable amount.

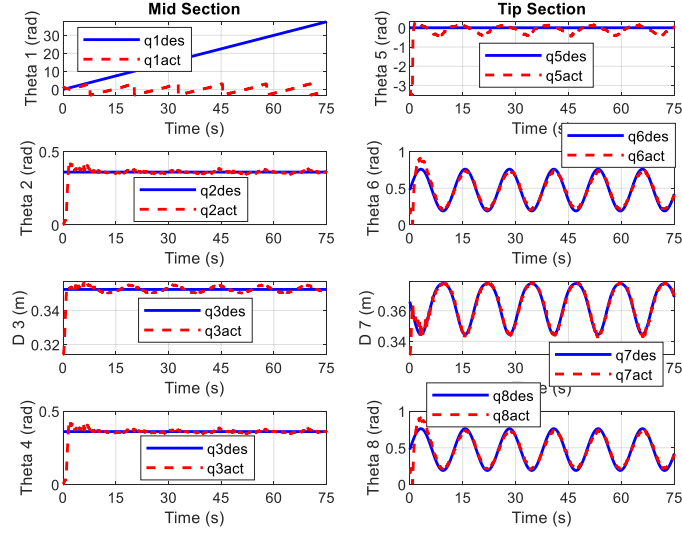


Figure. 5.18. Two section experiment 1 (OctArm tip and mid sections) — Desired and actual  $\theta_1, \theta_2, d_3, \theta_4, \theta_5, \theta_6, d_7$ , and  $\theta_8$  of the virtual discrete-jointed model in the joint space; the variables  $\theta_1, \theta_2, d_3, \theta_4$  represents the mid-section virtual RRPR model and the variables  $\theta_5, \theta_6, d_7, \theta_8$  represents the tip-section virtual RRPR model.

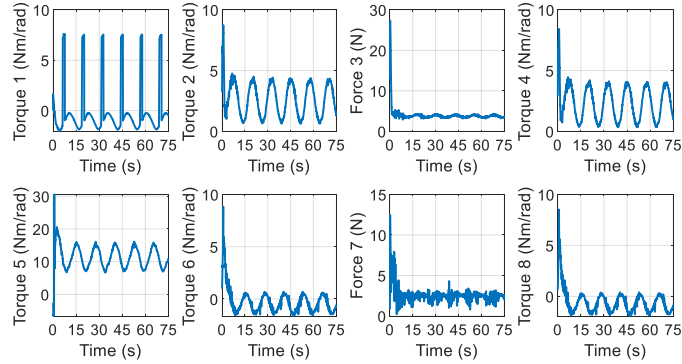


Figure. 5.19. Two section experiment 1 (OctArm tip and mid sections) — Actuation torques/force applied to the corresponding joint space variables:  $\tau_1$  to  $\theta_1, \tau_2$  to  $\theta_2, f_3$  to  $d_3, \tau_4$  to  $\theta_4, \tau_5$  to  $\theta_5, \tau_6$  to  $\theta_6, f_7$  to  $d_7$ , and  $\tau_8$  to  $\theta_8$ .

The joint space variables and the corresponding torques/forces responses can be found in Figure. 5.22 and 23. Due to the high-frequency torques  $\tau_2, \tau_4, \tau_6$ , and  $\tau_8$  being computed, shown in Figure. 5.23, some oscillatory tracking behavior on the robot curvature

related to revolute joints  $\theta_2$ ,  $\theta_4$ ,  $\theta_6$ , and  $\theta_8$  is observed before the system reaches steady state at 22 seconds and follows the desired joint space trajectories decently; see Figure. 5.22. Like the arc length  $s$  behavior, the prismatic joints  $d_3$  and  $d_7$  demonstrate excellent tracking performance.

#### 5.5.5 Discussion and Future Research

The main objective of the experiments was to evaluate the tracking capability of the proposed controller for multi-section continuum robots in configuration space. There are three critical findings inferred from the experimental evaluations on the OctArm. First, the virtual discrete-jointed robot model-based controller accomplishes the configuration space tracking for both the single section and two section OctArm trajectories satisfactorily. Second, the complicated 8-DoF dynamics model built for the two section OctArm proved to be infeasible to implement. Consequently, a decoupled dynamics model composed of two 4-DoF dynamic models, each responsible for formulating the control strategy for one of the two sections, was exploited. Finally, the configuration space errors exhibit sequential and cyclical nature in both one section and two section experiments. The cyclical pattern observed is likely due to unmodeled dynamics and the discrepancies between the physical system and the ideal model used. Corrections made to the model as well as compensation to the physical system could reduce or eliminate these behaviors.

Further studies should investigate the disturbance rejection capabilities of the proposed control method. Also, the proposed decoupling of virtual discrete-jointed dynamics model for the two-section OctArm control may seamlessly apply to continuum dynamics (Tatlicioglu et al., 2007) as well. The possibility of decoupling continuum

dynamics for the multi-section continuum robot control is conceptually fascinating and should be explored.

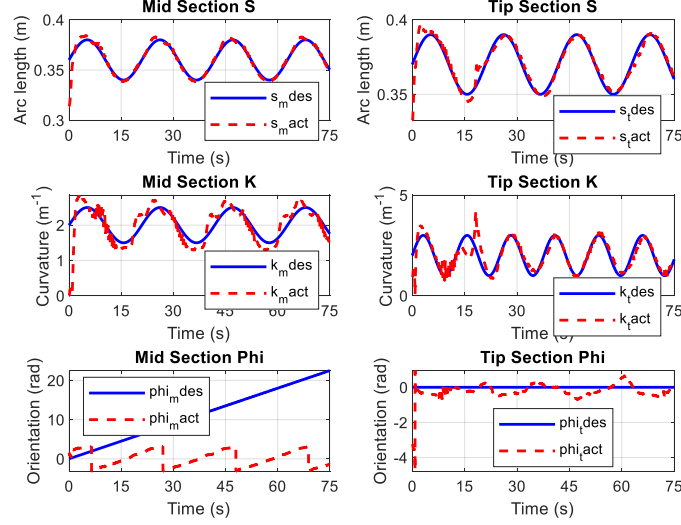


Figure. 5.20. Two section experiment 2 (OctArm tip and mid sections) — Desired and actual arc length  $s$ , curvature  $k$ , and orientation  $\phi$  in configuration space.

## 5.5. Conclusion

In this paper, a novel model-based dynamic feedback control architecture was introduced for spatial multi-section continuum robots. Inspired by conventional rigid link robot computed-torque control techniques, the control law utilizes the model of a virtual, conventional rigid link robot with discrete joints, in whose coordinates the controller is developed, to generate real-time control inputs for the continuum robot. The computed-torque input was translated to pneumatic pressures applied to each pneumatic artificial muscle in the actuator space of the continuum robot through a carefully designed converter. This controller was implemented on the OctArm—a pneumatically actuated spatial continuum manipulator with three sections—using a control architecture with both feedback linearization and PID controller. The forward and inverse kinematics, as well as dynamics model approximated by a virtual discrete-jointed robot model, are derived for

both single and two-section continuum robots. An alternative dynamic modeling approach based on the decoupling of the complex virtual discrete-jointed model was proposed to facilitate the implementation of the proposed controller on a two-section continuum robot. The proposed controller was successfully simulated and experimentally validated on both single and two sections of the OctArm. Accompanying this paper is video footage showing the configuration space tracking motion of the OctArm in 3D space as reported in the experimental results.

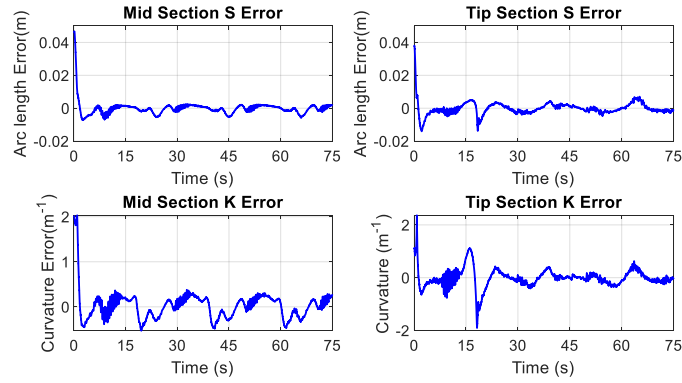


Figure. 5.21. Two section experiment 2 (OctArm tip and mid sections) — Arc length  $s$ , and curvature  $k$  error in configuration space.



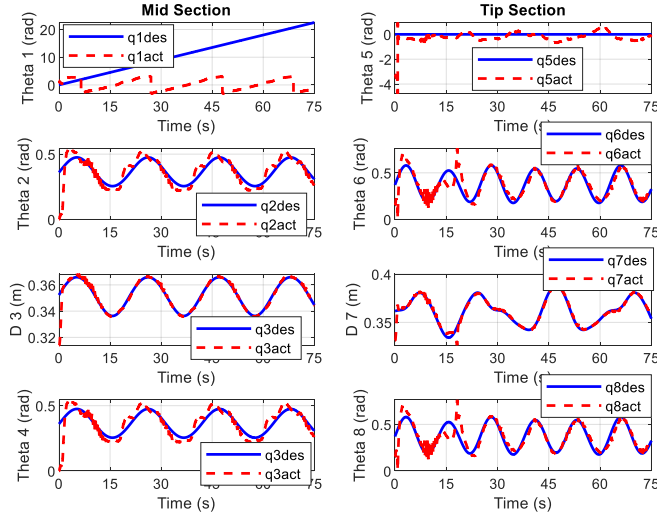


Figure. 5.22. Two section experiment 2 (OctArm tip and mid sections) — Desired and actual  $\theta_1, \theta_2, d_3, \theta_4, \theta_5, \theta_6, d_7$ , and  $\theta_8$  of the virtual discrete-jointed model in the joint space; the variables  $\theta_1, \theta_2, d_3, \theta_4$  represents the mid-section model and the variables  $\theta_5, \theta_6, d_7, \theta_8$  represents the tip-section model.

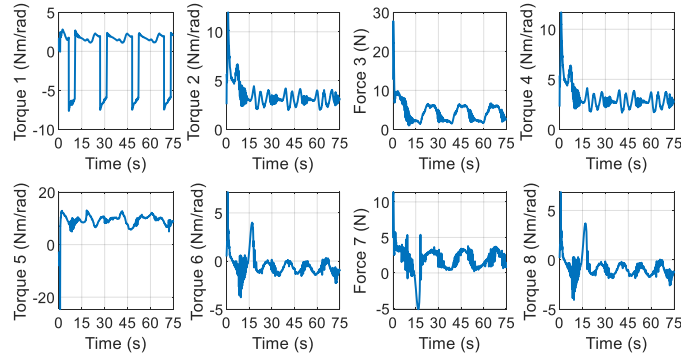


Figure. 5.23. Two section experiment 2 (OctArm tip and mid sections) — Actuation torques/force applied to the corresponding joint space variables:  $\tau_1$  to  $\theta_1, \tau_2$  to  $\theta_2, f_3$  to  $d_3, \tau_4$  to  $\theta_4, \tau_5$  to  $\theta_5, \tau_6$  to  $\theta_6, f_7$  to  $d_7$ , and  $\tau_8$  to  $\theta_8$ .

## CHAPTER SIX

### HAPTIC ASSISTIVE CONTROL WITH LEARNING BASED DRIVER INTENT RECOGNITION FOR SEMI-AUTONOMOUS VEHICLES

Semi-autonomous vehicles equipped with assistive control systems may experience degraded lateral behaviors when aggressive driver steering commands compete with high levels of autonomy. This challenge can be mitigated with effective operator intent recognition, which can configure automated systems in context-specific situations where the driver intends to perform a steering maneuver. In this article, an ensemble learning-based driver intent recognition strategy has been developed. A nonlinear model predictive control algorithm has been designed and implemented to generate haptic feedback for lateral vehicle guidance, assisting the drivers in accomplishing their intended action. To validate the framework, operator-in-the-loop testing with 30 human subjects was conducted on a steer-by-wire platform with a virtual reality driving environment. The roadway scenarios included lane change, obstacle avoidance, intersection turns, and highway exit. The automated system with learning-based driver intent recognition was compared to both the automated system with a finite state machine-based driver intent estimator and the automated system without any driver intent prediction for all driving events. Test results demonstrate that semi-autonomous vehicle performance can be enhanced by up to 74.1% with our proposed learning-based intent predictor. The proposed

holistic framework that integrates human intelligence, machine learning algorithms, and vehicle control can help solve the driver-system conflict problem leading to safer vehicle operations.

## **6.1 Introduction**

The introduction of computer-controlled electro-mechanical systems into ground vehicles has fostered semi-autonomous operation. Drive-by-wire systems, including steering, braking, and throttle, offer a pathway from driver to computer commanded vehicle inputs which promotes performance improvements. These mechatronic systems offer the potential to enhance steering functionality by enabling advanced driver-assistance features such as lane-keeping (LKA) that augment the interaction and collaboration between the human-vehicle to simplify the driving task and improve safety (Penmetsa et al., 2019). When the vehicle drifts towards the lane markers, LKA uses steering and/or selective braking to center the vehicle and prevent unattended single-vehicle lane departure events (Freeman et al., 2016). Advanced human-machine interaction modalities such as haptics can assist drivers in the vehicle cockpit (Wang et al., 2019b). Haptic assisted driving interfaces can provide tunable force feedback that meets the operator's need for vehicle steering while tailoring the driving experience. By integrating a robust haptic force feedback system into the drive-by-wire system, lane departure events can be anticipated and compensated within the LKA systems.

In general, lane keeping assistance technology operates efficiently for mild driving conditions. However, such systems can fail to respond to increased environment complexity and emergency situations. Furthermore, LKA sensors may have difficulty

recognizing fading lane markings and lanes changes due to construction, resulting in an undesirable actions or feature disabling. Human drivers, on the other hand, tend to solve complex problems, interpret emergency situations, and respond to uncertain settings better than automation (Cummings, 2017; Li et al., 2018). Therefore, haptic assistive control offers the opportunity to retain human abilities while leveraging the capacities of automatic vehicle systems through human-automation synergies.

Literature on haptic assistive control tends to emphasize control authority arbitration and transition between human and automation (D.A. and M., 2010). Muslim and Itoh (Muslim and Itoh, 2017) examined human-machine interactions during lane change with two levels of automation authority: sharing of steering control that provides haptic control guidance, and an automatic cooperative system that acts autonomously. Bhardwaj et al. (Bhardwaj et al., 2020) implemented three control authority schemes, namely, autopilot, active safety, and haptic shared control, and compared their performance by analyzing obstacle hits and metrics related to obstacle avoidance maneuvers. Boehm et al. (Boehm et al., 2016) constructed a system model that hybridizes power and information flow between the driver and steering wheel to describe modulating mechanical impedance to dynamically allocate authority. Various haptic control sharing paradigms have been proposed to combine human and automation control. Ghasemi et al. (Ghasemi et al., 2019) developed two sharing methods, input mixing and haptic shared control, to describe the communication channels open to the driver for monitoring automation behavior. Sentouh et al. (Sentouh et al., 2018) designed a two-level haptic shared control approach which offered a smooth switching between multiple controllers. Nishimura et al. (Nishimura et

al., 2015) evaluated the cooperative status between the human and automation within haptic shared control to solve intent inconsistency during lane-keeping.

The majority of haptic assistive control studies fall into two broad categories: (a) exploring communication, negotiation, and transition of control authority between human and automation, and (b) studying various control sharing paradigms that manage the changing roles for automation through various interfaces. However, the literature is short on considering intention recognition techniques to enable haptic assisted automated vehicles to generate human-like decision-making systems. For semi-automated vehicles, as categorized by SAE J3016 Automation Level 3, operators are typically required to intervene when unexpected conditions occur (On-Road Automated Driving (ORAD) committee, n.d.). Intent recognition enables haptic assistance to be allocated to maneuvers relevant to the driving situation and can help to avoid mismatches between the operator intention and the system's reaction. The incorporation of the driver intent recognition technique into haptic assistive control framework is conceptually intriguing, and this project seeks to fill this gap by examining the haptic assistive driving interface with learning-based driver intent recognition in the drive-by-wire setting. Such a driving interface naturally applies to the teleoperation of autonomous ground vehicles, which has become the essential and safe enabler of the new mobility in the foreseeable future.

Driver intent recognition (DIR) is a concept that contributes to a decision decision-making framework and plays a significant role in determining the appropriate state and subsequent course of driving actions when coping with different situations (Xing et al., 2019). Generative models like Hidden Markov Models (HMM) are widely used in existing

DIR studies. Li et al. (Li et al., 2016b) developed an integrated intention inference algorithm based on HMM and a Bayesian Filtering (BF) technique. Li et al. (Li et al., 2014) proposed a driver lane change/keep intention inference method based on a dynamic Bayesian network (BN). Kasper et al. (Kasper et al., 2012) designed a lane change detection method based on the object-oriented BN. Discriminative models such as Support Vector Machine (SVM) provide memory efficiency and effectiveness in high dimensional spaces (Doshi et al., 2011). Kumar et al. (Kumar et al., 2013b) constructed a multinomial classifier by combining SVM and BF. Kim et al. (Kim et al., 2017b) inferred driver intent by deploying artificial neural network (ANN) models to feed augmented information into a SVM. Human cognitive models were also adopted in the past. Salvucci et al. (Salvucci, 2006) introduced a real-time DIR system based on mind tracking architecture. Prior research mainly utilizes individual learning techniques to develop a single classification model for DIR.

In this study, a novel haptic assistive vehicle control strategy enhanced with machine learning-based operator intent recognition has been investigated (refer to Figure 6.1). The new control framework adjusts the vehicle desired trajectories based on the monitored drivers' preference. An ensemble meta-algorithm learning method determines the driver's intention. This approach generates and combines multiple machine learning models into a high quality prediction with more stable performance and decreased variance, bias, and standard deviation per an individual learner (Lessmann et al., 2015; Utami et al., 2014). The recognition results are used for path re-planning to match the driver's intention. The updated vehicle path is provided to the nonlinear model-predictive path-following

longitudinal and lateral controllers. To assess the assistive control framework, human subjects driving performance on four road scenarios has been evaluated in an immersive driving simulator environment.

The remainder of the article is organized as follows. The mathematical formulation and control structure are presented in Sections II and III, respectively. The driving intention recognition module and path planning algorithm are introduced in Section IV. The experimental setup with the accompanying operator-in-the-loop test results are summarized in Section V. Finally, Section VI offers the conclusion.

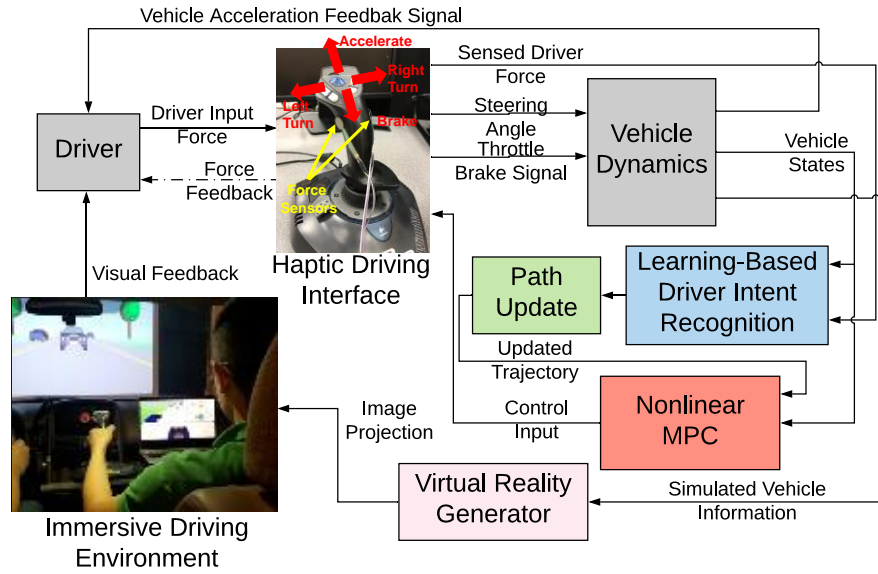


Figure 6.1. The illustration of the haptic assistive control framework with learning-based intent recognition.

## 6.2 Vehicle Dynamics

The remainder of the article is organized as follows. The mathematical formulation and control structure are presented in Sections II and III, respectively. The driving intention recognition module and path planning algorithm are introduced in Section IV. The

experimental setup with the accompanying operator-in-the-loop test results are summarized in Section V. Finally, Section VI offers the conclusion.

### 6.2.1 Chassis Dynamics

The governing equations of motion for the longitudinal velocity,  $v_x$ , lateral velocity,  $v_y$ , and yaw rate,  $\dot{\psi}$ , can be expressed as (Freeman et al., 2016)

$$\begin{aligned} m\dot{v}_x &= -m\dot{\psi}v_y + (F_{xfl} + F_{xfr})\cos\delta + F_{xrl} + F_{xrr} - (F_{yfl} + F_{yfr})\sin\delta \\ m\dot{v}_y &= -m\dot{\psi}v_x + (F_{xfl} + F_{xfr})\sin\delta + F_{yrl} + F_{yrr} + (F_{yfl} + F_{yfr})\cos\delta \\ I_z\ddot{\psi} &= l_f(F_{xfl} + F_{xfr})\sin\delta + l_f(F_{yfl} + F_{yfr})\cos\delta - l_r(F_{yrl} + F_{yrr}) \\ &\quad + \frac{l_w}{2}((F_{xfr} - F_{xfl})\cos\delta + (F_{xrr} - F_{xrl}) + (F_{yfl} - F_{yfr})\sin\delta) \end{aligned} \quad (6.1)$$

where  $\delta$  denotes the front wheel steer angle,  $m$  represents the vehicle total mass, and  $I_z$  is the vehicle yaw moment of inertia.

The longitudinal tire forces at the front left, front right, rear left, and rear right tires are  $F_{xfl}$ ,  $F_{xfr}$ ,  $F_{xrl}$ , and  $F_{xrr}$ , respectively. Similarly, the lateral forces may be stated as  $F_{yfl}$ ,  $F_{yfr}$ ,  $F_{yrl}$ , and  $F_{yrr}$ . The terms  $l_f$ ,  $l_r$ , and  $l_w$  refer to the distance from the center of gravity to the front wheels and rear wheels, as well as between the left and right wheels.

### 6.2.2 Wheel and Tire Dynamics

The vehicle simulation requires the tire/road interface forces and moments for the wheels. A general analytical tire model (Dugoff et al., n.d.) has been updated for combined wheel slip (Guntur and Sankar, 1980). The longitudinal wheel slip ratio,  $s_{xj}$ , becomes

$$s_{xj} = \begin{cases} \frac{r_{eff}\omega_{wj} - v_x}{v_x}, & v_x < r_{ref}\omega_{wj}; \text{ braking} \\ \frac{r_{eff}\omega_{wj} - v_x}{r_{eff}\omega_{wj}}, & v_x > r_{ref}\omega_{wj}; \text{ traction} \end{cases} \quad (6.2)$$



where the  $j$  subscript represents  $fl, fr, rl, rr$ . The term  $\omega_{wj}$  denotes the  $j$ th wheel's rotational speed.

The front and rear tire sideslip angles,  $\alpha_j$ , become

$$\alpha_{fl} = \alpha_{fr} = \delta - \left( \frac{v_y + l_f \dot{\psi}}{v_x} \right), \quad \alpha_{rl} = \alpha_{rr} = - \left( \frac{v_y - l_r \dot{\psi}}{v_x} \right) \quad (6.3)$$

The longitudinal and lateral tire force,  $F_{xj}$  and  $F_{yj}$ , may be written as

$$F_{xj} = C_{\sigma j} \left( \frac{s_{xj}}{1 + s_{xj}} \right) f(\lambda_j), \quad F_{yj} = C_{\alpha j} \left( \frac{\tan \alpha_j}{1 + s_{xj}} \right) f(\lambda_j) \quad (6.4)$$

where  $C_{\alpha j}$  and  $C_{\sigma j}$  are the cornering and longitudinal tire stiffnesses. Using the wheel slip ratio,  $s_{xj}$ , and tire sideslip angle,  $\alpha_j$ , from (2) and (3), the variable  $\lambda_j$  and the function  $f(\lambda_j)$  in Eq. (6.4) are given by

$$\lambda_j = \frac{\mu F_{zj} (1 + s_{xj})}{2 \sqrt{(C_{\sigma j} s_{xj})^2 + (C_{\alpha j} \tan \alpha_j)^2}}, \quad f(\lambda_j) = \begin{cases} (2 - \lambda_j) \lambda_j; & \lambda_j < 1 \\ 1; & \lambda_j \geq 1 \end{cases} \quad (6.5)$$

The term  $F_{zj}$  denotes the vertical force on the  $j$ th tire while the symbol  $\mu$  represents the tire-road friction coefficient.

The governing equation for the rotational wheel speed,  $\omega_{wi}$ , may be written as

$$I_w \dot{\omega}_{wj} = T_{dj} - T_{bj} - r_{eff} F_{xj}, \quad (j = fl, fr, rl, rr) \quad (6.6)$$

where  $I_w$  is the wheel inertia, and  $r_{eff}$  is the effective tire radius. The drive and braking torques are denoted as  $T_{dj}$  and  $T_{bj}$ .

### 6.3 Vehicle Control Methodologies

A fundamental component of the haptic assisted control system is an autonomous path-following controller. Over the years, the control of longitudinal and lateral dynamics of autonomous ground vehicles has been studied. Katriniok et al. (Katriniok et al., 2013) proposed a model-based predictive control approach for combined longitudinal and lateral vehicle guidance. Xu et al. (Xu et al., 2016) integrated adaptive and robust control algorithms for Kuafu-II autonomous vehicle. Guo et al. (Guo et al., 2016) constructed a coordinated steering and braking control strategy based on nonlinear backstepping and adaptive fuzzy sliding-mode control. Chebly et al. (Chebly et al., 2017) covers a coupled longitudinal and lateral dynamics control algorithm using Lyapunov functions. Guo (Guo, 2016) designed an adaptive coordinated control scheme to manage longitudinal and lateral motion using adaptive backstepping sliding mode control. Fergani et al. (Fergani et al., 2017) designed lateral/longitudinal flatness and  $H_\infty$  vertical dynamics control for coordination of suspension and steering/braking. Previous works have identified that the nonlinear control strategies are superior to linear controllers regarding the vehicle trajectory tracking capacities (Kayacan et al., 2018).

A nonlinear model predictive controller (NMPC) will be designed for the combined vehicle longitudinal and lateral dynamics (Findeisen and Allgower, 2002). NMPC accommodates fast-dynamic nonlinear systems by incorporating constraints on the state and control variables into the online optimization problem (refer to Figure 6.2). In this section, a reduced-order nonlinear vehicle model will be presented. The optimal control problem will be formulated as NMPC and solved. Finally, a nonlinear state estimator will be implemented to provide smooth filtered state estimation.

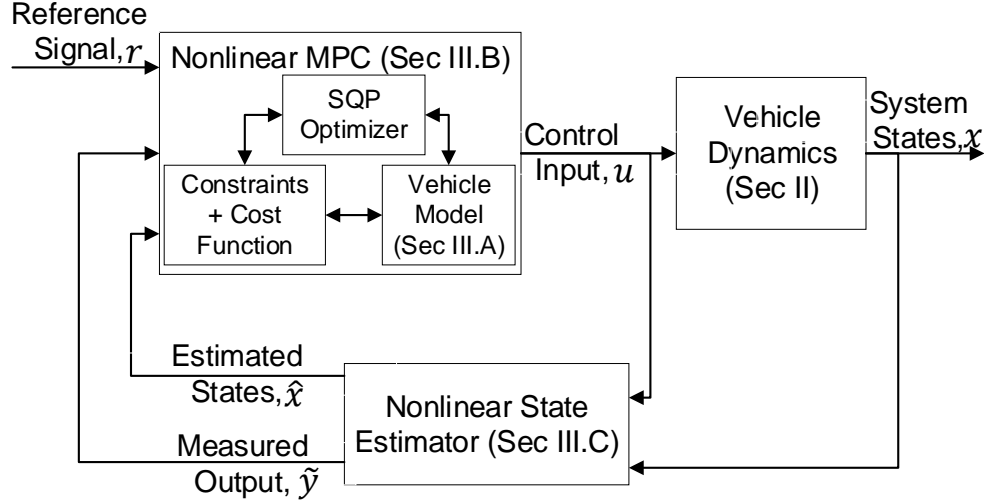


Figure 6.2. NMPC closed-loop control structure.

### 6.3.1 Nonlinear Vehicle Model for Control Synthesis

The vehicle dynamics model presented earlier is relatively complicated for control synthesis. This complexity results from the coupled vehicle dynamics and tire-road behavior. An alternative two-wheeled vehicle model is utilized to describe the longitudinal, lateral, and yaw motion dynamics. The lateral and yaw motion dynamics can be expressed as (Freeman et al., 2016)

$$\dot{v}_y = \frac{2C_{\alpha f}}{m} \delta - \frac{2C_{\alpha f} + 2C_{\alpha r}}{mv_x} v_y - \left( v_x + \frac{2C_{\alpha f} l_f - 2C_{\alpha r} l_r}{mv_x} \right) \dot{\psi} \quad (6.7)$$

$$\ddot{\psi} = \frac{2C_{\alpha f} l_f + 2C_{\alpha r} l_r}{I_z v_x} v_y - \left( \frac{2C_{\alpha f} l_f^2 + 2C_{\alpha r} l_r^2}{I_z v_x} \right) \dot{\psi} + \frac{2C_{\alpha f} l_f}{I_z} \delta \quad (6.8)$$

The longitudinal motion dynamics which directly maps the electric motor torque,  $T_{em}$ , to the change in vehicle speed,  $\dot{v}_x$ , becomes (Rajamani, 2006b)

$$\dot{v}_x = \frac{1}{I_{em}} \left( R_g r_{eff} T_{em} - c_a R_g^4 r_{eff}^4 \omega_{em}^2 - R_g^2 r_{eff}^2 F_{Rx} \right) \quad (6.9)$$

where  $R_g$  is the gear ratio,  $c_a$  is the aerodynamic drag coefficient,  $I_{em}$  is the electric motor moment of inertia,  $F_{Rx}$  is the tires rolling resistance which is proportional to the vehicle mass  $m$ . The electric motor torque,  $T_{em}$ , is dependent upon commanded electric power which is not addressed in this article. The electric motor angular speed,  $\omega_{em}$ , can be represented as

$$\dot{\omega}_{em} = T_{em} / I_{em} \quad (6.10)$$

The lateral and heading error,  $e_y$  and  $e_h$ , are defined as

$$\dot{e}_y = v_y + v_x e_h \quad (6.11)$$

$$\dot{e}_h = \dot{\psi} - \rho v_x \quad (6.12)$$

where  $\rho$  represents the road curvature.

The nonlinear vehicle dynamics model (7)-(12) can be expressed in state-space representation as

$$\dot{x}(t) = f(x(t), u(t)), \quad x(0) = x_0 \quad (6.13)$$

where  $x(t) \in \mathbb{R}^6$  and  $u(t) \in \mathbb{R}^3$  become

$$\begin{aligned} x(t) &= [v_y \quad \dot{\psi} \quad v_x \quad \omega_{em} \quad e_y \quad e_h]^T \\ u(t) &= [T_{em} \quad \delta \quad \rho]^T \end{aligned} \quad (6.14)$$

Note that the road curvature is not controllable since  $\rho$  depends on the road geometric design. However, the road curvature can describe the desired yaw rate,  $\dot{\psi}_{des} = \rho v_x$ , as a known or measured disturbance. Only  $T_{em}$  and  $\delta$  are the controllable variables.

### 6.3.2 Nonlinear Model Predictive Control

The set of admissible states, control inputs, and control input rates are denoted by  $X$ ,  $U$ , and  $\Delta U$  and assumed to satisfy the following assumptions:

**A1.**  $X \subseteq \mathbb{R}^6$  is connected,  $U \subseteq \mathbb{R}^3$  is compact and  $(0,0) \in X \times U$ . The sets  $U$  and  $\Delta U$  are given by box constraints of the form

$$\begin{aligned} X &:= \{x \in \mathbb{R}^m \mid x_{\min} \leq x \leq x_{\max}\} \\ U &:= \{u \in \mathbb{R}^m \mid u_{\min} \leq u \leq u_{\max}\} \\ \Delta U &:= \{\dot{u} \in \mathbb{R}^m \mid \dot{u}_{\min} \leq \dot{u} \leq \dot{u}_{\max}\} \end{aligned} \quad (6.15)$$

where  $x_{\min}$ ,  $x_{\max}$ ,  $u_{\min}$ ,  $u_{\max}$ ,  $\dot{u}_{\min}$ , and  $\dot{u}_{\max}$  are given constant vectors.

**A2.** The vector field  $f: \mathbb{R}^6 \times \mathbb{R}^3 \rightarrow \mathbb{R}^6$  is continuous and satisfies  $f(0,0) = 0$ .

**A3.** The system (13) has a unique continuous solution for any initial condition in the region of interest and any piecewise continuous and right continuous input function  $u(\cdot): [0, T_p] \rightarrow U$ .

The NMPC uses a predication model to calculate future system control on a finite prediction horizon,  $T_p$ . The cost function,  $J$ , minimizes the output errors and penalizes the electric motor torque and steer angle change for smooth driving experience. The cost function may be formulated as

$$J = \int_t^{t+T_p} [r(\tau) - y(\tau)]^T Q [r(\tau) - y(\tau)] + \dot{u}(\tau)^T R \dot{u}(\tau) d\tau \quad (6.16)$$

where  $y = [v_x \quad e_y \quad e_h]^T$  and  $r = [v_{xref} \quad 0 \quad 0]^T$  are the predicated and reference outputs. The term  $v_{xref}$  denotes the reference longitudinal speed. To avoid a drastic control input change, the control input rates may be expressed as  $\dot{u}$ . The weighting matrices,  $Q$  and  $R$ , represent the tracking errors and control input variations.

A sequential quadratic programming (SQP) algorithm was selected for this nonlinear MPC application. The NMPC problem may be formulated as (Findeisen and Allgower, 2002)

$$\arg \min_{u(\cdot)} J(x(t), u(\cdot); T_c, T_p) \quad (17a)$$

$$\text{subject to } \dot{x}(\tau) = f(x(\tau), u(\tau)) \quad (6.17b)$$

$$u(\tau) \in U, \forall \tau \in [t, t + T_c] \quad (6.17c)$$

$$\dot{u}(\tau) \in \Delta U, \forall \tau \in [t, t + T_c] \quad (6.17d)$$

$$u(\tau) = u(t + T_c), \forall \tau \in [t + T_c, t + T_p] \quad (6.17e)$$

$$x(\tau) \in X, \forall \tau \in [t, t + T_p] \quad (6.17f)$$

where  $T_c$  is the control horizon with  $T_c \leq T_p$ . The function  $f(x(\tau), u(\tau))$  denotes the continuous state space representation given by (13) and the term  $u(\cdot)$  is the optimization vector.

Let  $u^*(\cdot; x(t)): [t, t + T_p] \rightarrow U$  represent the optimal solution to the optimization problem. The open-loop optimal control problem will be solved repeatedly at the sampling instances  $t = s\phi, s = 0, 1, \dots$ , once new measurements are available. The closed-loop control is defined by the optimal solution at sampling instants

$$u(t) := u^*(t; x(t)) \quad (6.18)$$

To implement the NMPC to the combined vehicle longitudinal and lateral control design, the predicated and reference outputs terms of the nonlinear vehicle model in (16) can be substituted by  $y$  and  $r$ .

### 6.3.3 Nonlinear Estimation

An extended Kalman filter (EKF) estimates the state vector,  $\hat{x}$ , of the nonlinear vehicle system. The nonlinear vehicle system in (13) can be rewritten in the following state-space form

$$\begin{cases} \hat{x}(t) = f(\hat{x}(t), u(t)) + w(t) \\ \hat{y}(t) = \hat{y}(t) + v(t) \end{cases} \quad (6.19)$$

where  $w(t)$  and  $v(t)$  are the process and measurement noises respectively and the estimated output  $\hat{y}(t) = g(\hat{x}(t), u(t))$ . Both  $w(t)$  and  $v(t)$  are assumed to be the non-intercorrelated, stationary Gaussian white noise processes with mean and covariance,  $w(t) \sim (0, Q(t))$  and  $v(t) \sim (0, R(t))$ . The state estimation vector  $\hat{x}(t) = [\hat{v}_y, \hat{\psi}, \hat{v}_x, \hat{\omega}_{em}, \hat{e}_y, \hat{e}_h]^T$ , includes the five estimated states. The output vector,  $\hat{y}(t)$ , is composed of the measured longitudinal velocity,  $\tilde{v}_x$ , as well as measured vehicle lateral and heading error with respect to the road,  $\tilde{e}_y$  and  $\tilde{e}_h$ .

## 6.4 Driver Intent Recognition

During extended driving periods, the human operator may experience multiple driving condition changes in which emergency situations occur. To prevent potential traffic accident when completing lane change and obstacle avoidances, predicting the human driver's intention is critical. In this section, an ensemble learning based driver intent recognition method with verification will be presented.

#### 6.4.1 Feature Selection

The process of selecting a subset of driving variables and their attributes that are most relevant to the predictive model construction problem is called feature election. Four driver actions/behaviors are key:

1. Driver head orientation or eye movement by camera.
2. Secondary driver operation actions (e.g., controlling infotainment system) by camera or sensors.
3. Driver's operation behaviors (e.g., steering, throttle, brake patterns) by vehicle sensors.
4. Vehicle responses (e.g. vehicle speed, yaw rate) by vehicle sensors.

The driver-in-the-loop platform (shown in Figure 6.3) used in this study enables the collection of the driver's operation behavior and vehicle response information per the third and fourth methods.



Figure 6.3. Driver-in-the-loop simulation platform with joystick for throttle, brake, and steering commands.

The vehicle operating variables (F1-F15) and the driver behavior indicators (F16-F22) are listed in Table I. The maneuvers considered include lane keeping, lane change,



obstacle avoidance, highway exit, intersection turn, and inconsistent driving. All features are used to identify driver intention and a code may be assigned for each feature. F1-F15 are vehicle response related variables, and F16-F22 are driver operation behavior related features. To help the ensemble model distinguish between lane change and intersection turn/highway exit maneuvers, the current lane information,  $L_{ct}$ , is also considered. This information will record the lane in which the driver initiates a vehicle maneuver. With this information, the trained ensembled model can further classify a right lane change like maneuver as a highway exit maneuver should the current lane is the highway exit only lane. Similarly, the model can separate intersection turns from lane change by knowing whether the vehicle is in the turn lanes at an intersection.

#### 6.4.2 *Ensemble Learning Based Intent Recognition*

Ensemble learning is the technique by which multiple classifiers are combined to solve a computational intelligence problem. In machine learning, ensemble methods use several models to improve the final predictive performance. One common type of ensembles is Boosting, which employs models of the same type that complement one another. These models are obtained in an iterative way and their individual outputs are combined using a weighted vote scheme. Adaptive Boosting (AdaBoost) is a widely used boosting method and encompasses three major variants: AdaBoost.M1 for binary classification, AdaBoost.M2 for multi-class classification, and AdaBoost.R for regression problems. In this study, we propose to use the multi-class method for the driver intent recognition problem.

Table 6.1. Vehicle Operating variables and driver behavior indicators with corresponding feature code

Vehicle Operating Variable	Variable Description	Feature Code	Vehicle Operating Variable	Variable Description	Feature Code
$e_y$	Lateral Error	F1	$\omega_{wfl}, \omega_{wfr}, \omega_{wrl}, \omega_{wrr}$	Tire Rotational Speed	F12-15
$v_y$	Lateral Velocity	F2	$\delta$	Steer Angle	F16
$\dot{v}_y$	Lateral Acceleration	F3	$\dot{\delta}$	Steer Angle Speed	F17
$v_x$	Longitudinal Velocity	F4	$p_t$	Throttle Position	F18
$\dot{v}_x$	Longitudinal Acceleration	F5	$p_b$	Brake Position	F19
$\psi$	Yaw Angle	F6	$\dot{p}_t$	Throttle Position Change Rate	F20
$\dot{\psi}$	Yaw Rate	F7	$\dot{p}_b$	Brake Position Change Rate	F21
$\alpha_{fl}, \alpha_{fr}$	Front Tire Slip Angle	F8-F9	$F_H$	Applied Human Force	F22
$\alpha_{rl}, \alpha_{rr}$	Rear Tire Slip Angle	F10-F11			

The AdaBoost.M2 algorithm takes as input a training set of  $N$  examples  $S = \langle (o_1, p_1), \dots, (o_N, p_N) \rangle$  where  $o_i$  is an instance draw from feature space  $O$  and represented in a vector of feature attribute values, and  $p_i \in P = \{1, \dots, k\}$  is the class label associated with  $o_i$ . In this study, we assume that the set of possible labels  $P$  is of finite cardinality  $k = 5$ : lane keeping (LK), left lane-change (LLC), right lane-change (RLC), left obstacle avoidance (LOA), and right obstacle avoidance (ROA).

The multi-class algorithm has access to multiple weak learning algorithms. The weak learner generates hypotheses which have the form  $h: O \times P \rightarrow [0,1]$ . The hypothesis  $h(o, p)$  measures the degree to which it is believed that  $p$  is the correct label associated with instance  $o$ . In this study, a decision tree has been selected as the weak learner that will be combined with the other decision tree learners to predict driver intention. To formalize

the goal of each weak learner, a pseudo-loss  $\varepsilon$  of weak hypothesis  $h$  on training instance  $i$  which measures the goodness of the weak hypothesis is defined as

$$\varepsilon(h, i) = \frac{1}{2} \left( 1 - h(o_i, p_i) + \sum_{p \neq p_i} q(i, p) h(o_i, p) \right) \quad (6.20)$$

where the function  $q = \{1, \dots, N\} \times P \rightarrow [0, 1]$  is the label weighting function which assigns to each instance  $i$  in the training set a probability distribution. The terms  $h(o_i, p_i)$  and  $h(o_i, p)$  are the hypotheses generated by the weak learner with the correct label  $p_i$  and the incorrect label  $p$  associated with feature  $o_i$ . The weak learner's goal is to minimize the expected pseudo-loss for given distribution  $D$  and weighting function  $q$ .

The multi-class method can be initialized with the weight vector  $w_{i,p}^1 = D_1(i)/(k-1)$  for each instance  $i = 1, \dots, N$  and each incorrect label  $p \in P - \{p_i\}$ . The algorithm is then executed for  $t = 1, 2, \dots, T$  iterations with the following steps:

First, the weighting function  $q_t$  is set as

$$q_t(i, p) = \frac{w_{i,p}^t}{W_i^t}, \quad W_i^t = \sum_{p \neq p_i} w_{i,p}^t \quad (6.21)$$

for mislabels  $p \neq p_i$ . The mislabel distribution  $D_t$  may be set as

$$D_t(i) = \frac{W_i^t}{\sum_{i=1}^N W_i^t} \quad (6.22)$$

The mislabel distribution is a distribution defined over the set of all mislabels.

Second, the mislabel distribution  $D_t$  and weighting function  $q_t$  is supplied to a decision tree that is selected as the weak learner. In response, the decision tree will compute a hypothesis  $h_t: O \times P \rightarrow [0, 1]$ .

Third, the pseudo-loss of the hypothesis,  $h_t$ , is calculated as

$$\varepsilon_t(h_t) = \frac{1}{2} \sum_{i=1}^N D_t(i) \left( 1 - h_t(o_i, p_i) + \sum_{p \neq p_i} q_t(i, p) h_t(o_i, p) \right) \quad (6.23)$$

The decision tree's goal then is to minimize the pseudo-loss  $\varepsilon_t$ .

Fourth, the weights are then updated for the next iteration to be

$$w_{i,p}^{t+1} = w_{i,p}^t \beta_t^{(1/2)(1+h_t(o_i, p_i) - h_t(o_i, p))}, \quad \beta_t = \varepsilon_t / (1 - \varepsilon_t) \quad (6.24)$$

for each instance  $i = 1, \dots, N$  and each incorrect label  $p \in P - \{p_i\}$ .

Last, for a given instance  $o$ , the final hypothesis,  $h_f$ , outputs the label  $p$  that maximizes a weighted average of the weak hypothesis values  $h_t(o, p)$

$$h_f(o) = \arg \max_{p \in P} \sum_{t=1}^T \left( \log \frac{1}{\beta_t} \right) h_t(o, p) \quad (6.25)$$

#### 6.4.3 Training and Validation

To prepare a model that recognizes the driver's intentions based on the scanned vehicle sensor signals, the training and validation process will be discussed. The ensemble learning method will be applied to classify the human and vehicle behaviors. As shown Figure 6.4, the two main phases are offline training and online validation. The offline training phase begins by collecting the training samples from the driver-in-loop platform (refer to Figure 6.3). The sample data set contains 233,101 observations of five different driver activities: LK, LLC, RLC, LOA, and ROA. Each observation has 22 features extracted from the human behaviors and the vehicle responses data measured by the vehicle sensors. A total of 209,791 observations are used for model training, while the other applied for model verification. All the data are preprocessed before training to improve computational efficiency.

To evaluate whether an ensemble complies with the user-defined classification error and training time specification, the trained ensemble model is verified using a test dataset that provide an unbiased evaluation of a final model fit on the training dataset. The ensemble model accuracy is influenced by the values of number of decision trees, and the weak learner selected for the proposed ensemble. Noticing there is a tradeoff between training error and decision tree size, the trained ensemble should achieve a low training error with a tree that is not too large. We present a methodology for selecting a favorable accuracy-complexity tradeoff: grow the tree more carefully and try to end the growing process at an appropriate point early on. The test classification error and training time are plotted as a function of the number of trained trees in the ensemble in Figure 6.5. The ensemble achieves a classification error of under 1% using 44 or more trees. For 45 or more trees, the classification error decreases at a much slower rate. Considering that further expanding the tree size beyond 45 would not improve the ensemble accuracy significantly and that the additional training time due to increase in model complexity is undesirable, the number of trees selected is 45.

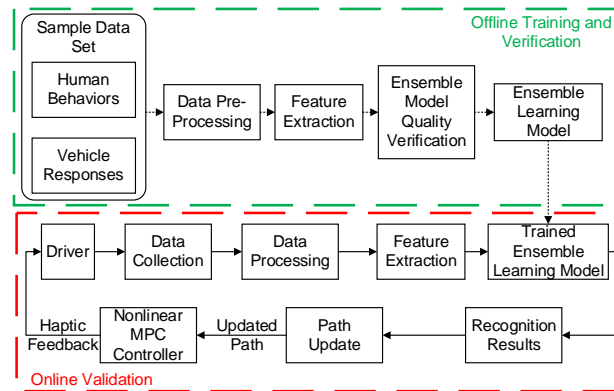


Figure 6.4. Driving intent recognition process implemented using ensemble learning approach.

The verification results of the driver intent detection for the proposed ensemble model are shown on a confusion matrix plot in Figure 6.6. The rows correspond to the true class and the columns correspond to the predicted class. The diagonal cells correspond to observations that are correctly classified. The off-diagonal cells correspond to incorrectly classified observations. These metrics are often called the precision (or positive predictive value) and false discovery rate, respectively. The results show that the average recognition accuracy is about 98.9%, and each categories recognition accuracy is more than 95%; therefore, the ensemble model achieves a great performance of driver intention recognition.

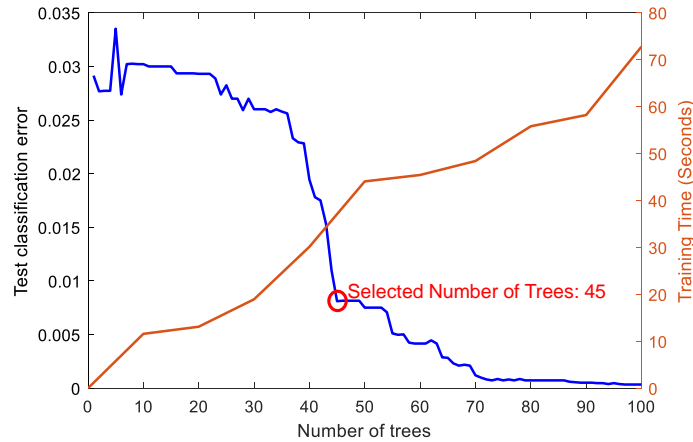


Figure 6.5. Misclassification of the test data (left vertical axis) and training time of 209,791 observations (right vertical axis) as a function of the number of trained trees in the ensemble.

The second phase, online validation, examines the ensemble model performance in a real-time operator-in-the-loop driving simulator. To assess the driver intent recognition accuracy, a real-world three-lane highway scenario is selected. On the test track, the driver performs obstacle avoidance and lane change maneuvers about traffic cones and slow-moving surrounding vehicles. In Figure 6.7, there are the LOA actions on the highway in (a), the RLC actions in (b), the ROA action in the (c), and the LLC action on in (d). The

driver intention recognition results for these maneuvers actions is plotted in the right-hand column. The step functions in these subplots indicate that the driver's intention shifted from one class to the other in the designed road scenario. From Figure 6.7, when the driver initiates the lane-change/obstacle avoidance maneuver, the step function accurately reflects where the intention change occurs. The online testing results apparently proves that the proposed ensemble model accomplishes a remarkable driver intent recognition performance.

True Class	1	99.9%		0.0%		0.1%
	2	4.2%	95.8%			
	3	0.3%		99.7%		
	4	0.4%			99.6%	
	5	0.4%				99.6%
		1	2	3	4	5
		Predicted Class				

Figure 6.6. A confusion matrix from true labels and predicted labels with number of trees  $N = 45$ . Class labels: 1=Lane keeping (LK), 2=Left lane change (LLC), 3=Right lane change (RLC), 4=Left obstacle avoidance (LOA), and 5=Right obstacle avoidance (ROA).

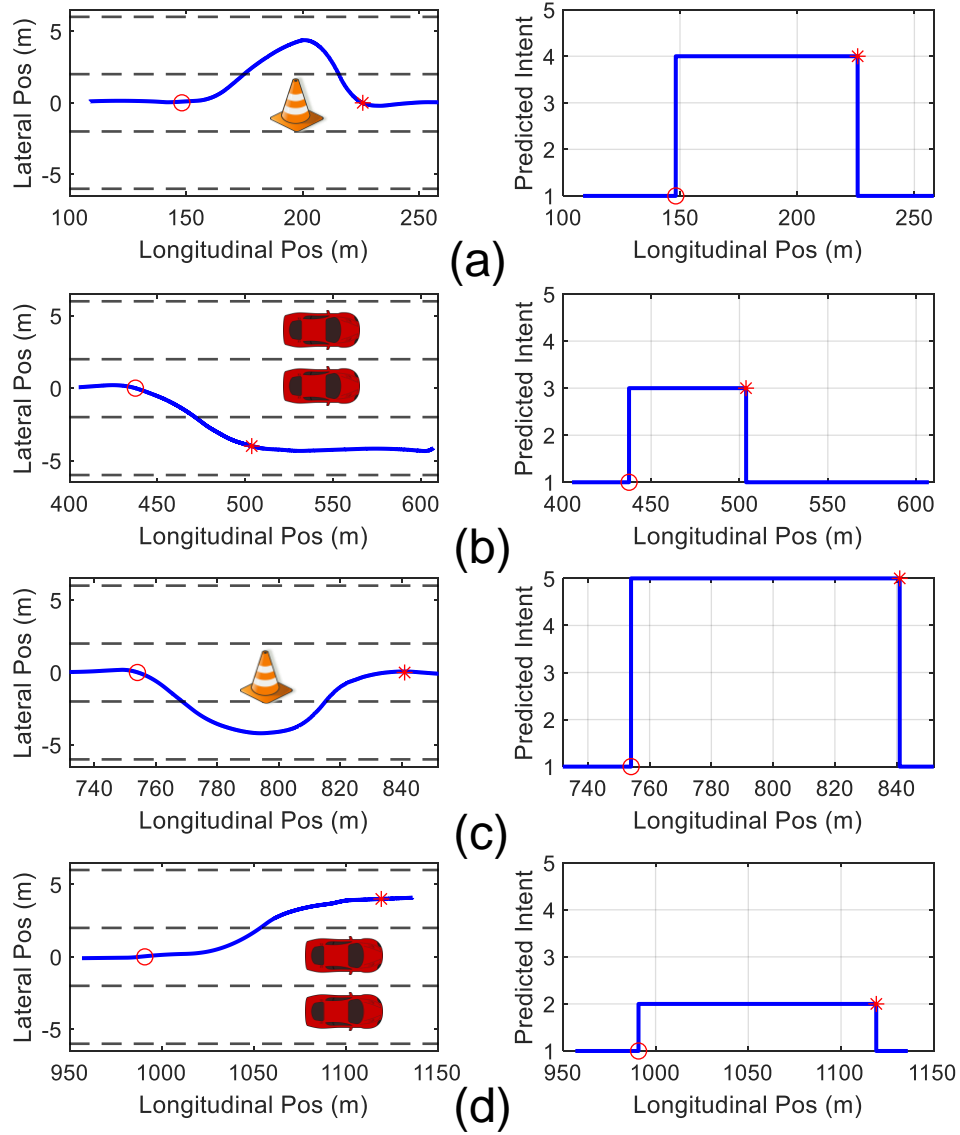


Figure 6.7. Ensemble model recognition result in the design scenario: vehicle trajectory on the left column and lane changing intention recognition result on the right column. Recognition Intent labels: 1=Lane keeping (LK), 2=Left lane change (LLC), 3=Right lane change (RLC), 4=Left obstacle avoidance (LOA), and 5=Right obstacle avoidance (ROA).

#### 6.4.4 Finite State Machine Based Intent Recognition

A finite state machine (FSM) based driver intent recognition technique was also designed for comparison purposes. The FSM uses predefined operating conditions to



classify vehicle behavior which is then selected based on real time driving events. For instance, the Stanford Racing Team used FSM to switch between 13 driving states (Montemerlo et al., 2009). Hülnhagen et al. (Hulnhagen et al., 2010) proposed a probabilistic FSM to capture the driving maneuver sequences. In this project, the FSM used four elements  $(W, E, e_0, A)$ . The first element, input set  $W = [\dot{v}_y \ \dot{\psi} \ \delta \ \dot{\delta} \ p_t \ p_b \ F_H \ L_{ct}]$ , is a set of variables concerning driver and vehicle response from Table I. The second element are all the driving state set  $E$  which divides the continuous driving task into a finite set of discrete lateral and longitudinal guidance states. These states correspond to all the maneuvers considered in this study. The third element  $e_0$  is the initial state Lane Keeping. The fourth element,  $A: E \times W \rightarrow E$ , denotes the state transition function that is represented by a set of state switch conditions based on the truth values of the Boolean variables from the input set. Due to space limitations, detailed state transition function and FSM diagram is omitted from the article.

#### 6.4.5 Path Update

The path update function, which generates new vehicle trajectories to comply with the inferred driver's intention, serves two purposes. First, the utility should accurately describe the evasive steering maneuvers that fulfills a comfortable, feasible, and safe lane change. In the presence of obstacles, it generates a new path description to overcome the event. Second, the path update algorithm should also generate the reference input for the vehicle control systems that provide driver assistive feedback. Many motion planning techniques have been investigated; a sigmoid polynomial function is selected to model lane change and obstacle avoidance. These trajectories generate optimal evasive path in terms

of vehicle constraints, speed, and comfort with low computational cost. A polynomial approach also supports the continuous concatenation of curves, which in turn, guarantees driver comfort.

The desired vehicle lane change trajectory,  $y_{LC}$ , which is shown in Figure 6.8a, is a fifth-degree polynomial model

$$y_{LC}(x_o) = \sum_{n=0}^5 a_n x_o^n \quad (26)$$

where  $x_o$  is the longitudinal offset from the starting point of the lane change maneuver. To ensure feasibility and driver comfort, the determination of polynomial coefficients  $a_n$  is based on several constraint equations which limit the lateral offset derivatives.

The polynomial parameters  $a_n$  are determined by applying the following boundary conditions to the splines,

$$\begin{aligned} y_{LC}(0) &= 0, y_{LC}(d_{LC}) = y_T \\ \frac{d}{dx_o} y_{LC}(0) &= 0, \frac{d}{dx_o} y_{LC}(d_{LC}) = 0 \\ \frac{d^2}{dx_o^2} y_{LC}(0) &= 0, \frac{d^2}{dx_o^2} y_{LC}(d_{LC}) = 0 \end{aligned} \quad (27)$$

where  $d_{LC}$  is the required distance to complete a lane change maneuver and  $y_T$  is the target lateral offset at the end of the maneuver.

The desired vehicle obstacle avoidance trajectory,  $y_{OA}$ , which is shown in Figure 6.8b, is defined as a function of two fifth order polynomials concatenated together,

$$y_{OA}(x) = \begin{cases} y_{OA1}(x_o) = \sum_{n=0}^5 b_n x_o^n, & \text{if } 0 \leq x_o < d_{OA} \\ y_{OA2}(x_o) = \sum_{n=0}^5 c_n x_o^n, & \text{if } d_{OA} \leq x_o \leq 2d_{OA} \end{cases} \quad (28)$$

where  $x_o$  is the longitudinal offset from the starting point of the obstacle avoidance maneuver, and  $d_{OA}$  denotes the distance between the obstacle and the obstacle avoidance maneuver starting location. The polynomial coefficients  $b_n$  and  $c_n$  are derived by imposing the following boundary conditions,

$$\begin{aligned} y_{OA}(0) &= 0, y_{OA}(d_{OA}) = y_T, y_{OA}(2d_{OA}) = 0 \\ \frac{d}{dx_o} y_{OA}(0) &= 0, \frac{d}{dx_o} y_{OA}(d_{OA}) = 0, \frac{d}{dx_o} y_{OA}(2d_{OA}) = 0 \\ \frac{d^2}{dx_o^2} y_{OA}(0) &= 0, \frac{d^2}{dx_o^2} y_{OA}(d_{OA}) = 0, \frac{d^2}{dx_o^2} y_{OA}(2d_{OA}) = 0 \end{aligned} \quad (29)$$

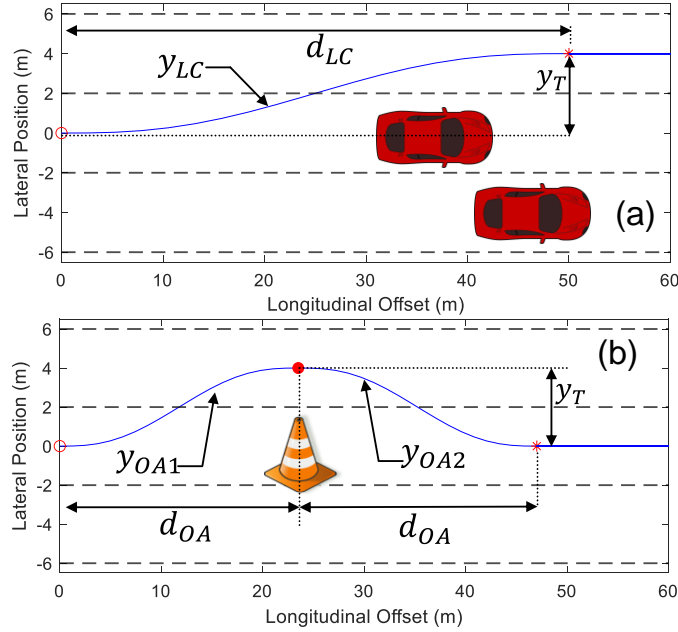


Figure. 6.8. Updated vehicle trajectory for driver intended maneuvers on three-lane highways: (a) lane change, and (b) obstacle avoidance. The red circle and asterisk are the start and the end of the maneuver.

The desired vehicle trajectory for right turn, left turn, and highway exit are designed to be circular segment of radius 15m, 25m, and 70m. The drivers are asked to follow the planned quarter circle track when passing through these maneuvers.

## **6.5 Experimental Results and Discussion**

An operator-in-the-loop driving simulator environment has been created to assess the efficacy of the proposed learning-based driver intent recognition with accompanying controllers. In this section, the virtual environment, testing methodology, and experimental results will be presented.

### *6.5.1 Test Environment*

To explore the real-time performance of each operator using the steering input devices, a fixed-base hardware-in-the-loop experimental test bench was created (refer to Figure 3). The driving simulator involves the synchronized operation of specialized hardware and software. The components included the haptic steering device with two force sensors, a high-resolution image projector, and a Honda CR-V static vehicle. The visual environment, created using the V-Realm Builder 2.0, was rendered by the 3D Animation toolbox and projected on a large screen. The vehicle model, including wheels and chassis, and nonlinear MPC controllers have been implemented in the MATLAB/Simulink environment (Wang et al., 2019b). The haptic steering device is connected via USB to the main PC and communicate through QUARC Real-Time Control Software to maintain timing and steering commands during the simulation. Attached to the haptic steering device were two force sensing resistors that measuring human forces applied to the driving interface through Arduino. The vehicle speed and recognized driver intent were displayed on the screen, and the audio feedback played through the cabin speakers.

A portable test environment was created in response to the COVID-19 pandemic which limited laboratory access. A laptop computer with integrated speaker system and

USB connected Joystick enabled outdoor testing. The primary difference between the two systems is the vehicle cabin vs bench, ambient light conditions, and size of the screen.

### 6.5.2 *Test Methodology*

A total of 25 human subjects drove the experimental system and completed pre- and post-test questionnaires (refer to Table B.1) (Wang et al., 2019b). The effects of FSM and learning based intent recognition models, with integrated NMPC, on driver preference and performance were investigated on highway and city road scenarios per Figure 6.9. The highway test track consisted of a series of lane keeping, obstacle avoidance, and lane change maneuvers. The urban roadway involved turns, intersections, and traffic characteristic of a populated city. To control for learning that may arise from repeated activities, a Latin square design ensured a randomized order of testing. After driving through each event, the drivers were requested to complete the post-test questionnaire and quantify the subjective measures of control and confidence, ease of driving, and safety.

The three driving configurations, C1 = No DIR, C2 = FSM DIR, and C3 = EL DIR were integrated with NMPC and coded in MATLAB. All configurations are equipped with a self-centering mechanism to emulate original equipment manufacturer (OEM) steering feel. A tradeoff exists between model sophistication and execution speed, so the scenery is limited. The best performance corresponds to the case when an operator completes an assigned task with the highest intent recognition accuracy and ideal handling performance (e.g., lateral and heading error, lateral acceleration, yaw rate).

### 6.5.3 Test Results

To evaluate the performance of the haptic assistive control system, two different roadways were considered.

#### 6.5.3.1 Highway Results

A highway scenario which features two obstacle avoidances, two lane changes, and one exit maneuver was initially considered as shown in Figure 6.9. The driver accelerates to a speed of 90 kph and then attempts to negotiate the course without striking the colored cones and/or other roadway vehicles.

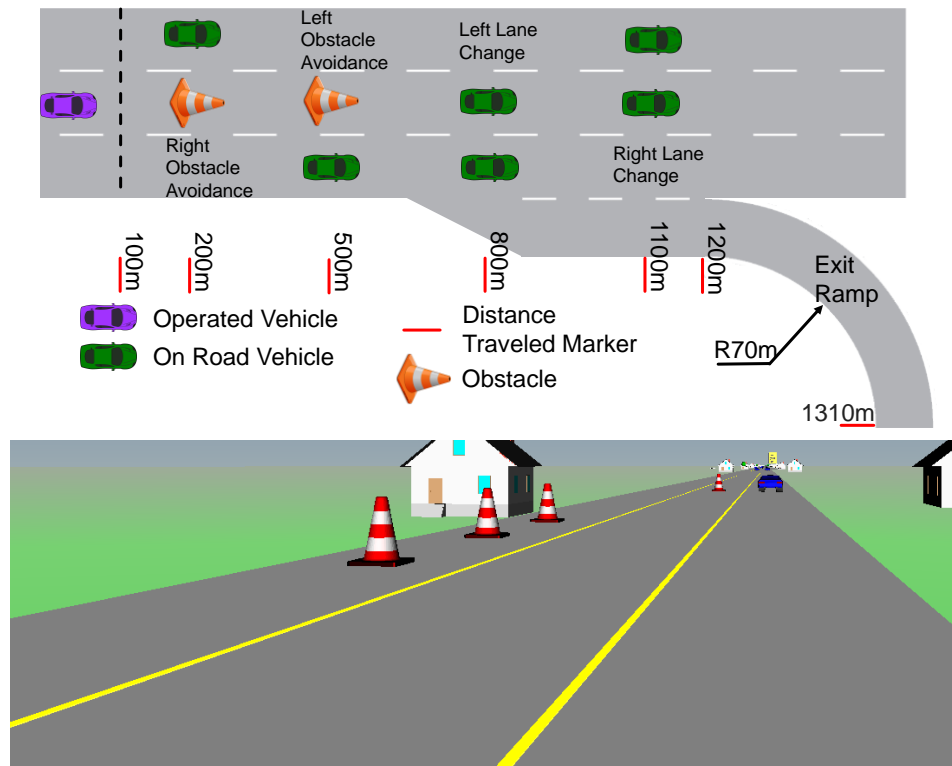


Figure 6.9. Highway scenario — (a) Test track, and (b) Animated simulator scene

To provide insight into the drivers' understanding and execution of the highway maneuver for each driving configuration, the overall RMS and maximum lateral acceleration ( $F3$ ),  $\bar{v}_y$  and  $\dot{v}_{ymax}$ , applied human force ( $F22$ ),  $\bar{F}_H$  and  $F_{Hmax}$ , and intent

recognition accuracy,  $\bar{R}\%$  and  $R\%_{max}$ , are listed in Table II. Configuration C1 offered decreased lateral accelerations of 44.4% and 10.7% when compared to C2 and C3, thus ensuring superior vehicle lateral stability and driver comfort. However, drivers exhibited poor steer angle actions and subsequent vehicle placement on the road during obstacle avoidance with C1 due to lack of supplemental vehicle control. The greater applied human force, as evident by the RMS value, for C1 indicated that the drivers operated the joystick with more effort than C2 and C3. Configuration C3 offered a higher level of driver intent recognition accuracy than C2 for this scenario by 38.9% with low driver workload. Configuration C2 proved to be marginally acceptable and led to misclassification of driver intent. Such misclassification can initiate unintended maneuvers that conflict with the driver's true intention and prompt safety concerns.

Table 6.2. Average of all  $N = 25$  human subjects' lateral acceleration  $\dot{v}_y$ , applied human force  $F_H$ , and intent recognition accuracy  $R\%$  for driving configurations, C1-C3, on highway scenario. Note that the bar represents the RMS value, while subscript *max* is the maximum value

Config	$\bar{\dot{v}}_y$ (deci-g's)	$\bar{F}_H$ (N)	$\bar{R}\%$ (%)	$\dot{v}_{y_{max}}$ (deci-g's)	$F_{H_{max}}$ (N)	$R\%_{max}$ (%)
C1	<b>0.50</b>	1.53	N/A	<b>7.21</b>	<b>7.05</b>	N/A
C2	0.90	1.26	70.35	7.61	9.68	100
C3	0.56	<b>0.94</b>	<b>97.72</b>	7.28	8.15	100

To demonstrate and compare the performance for C1-C3 during a left obstacle avoidance, the vehicle paths and optimal ISO 3888-2 trajectory are plotted in Figure 6.10a. Driver #12, who successfully completed this maneuver using both C1 and C3 traveled from the original to adjacent lane (450-500m) with minor lateral deviations. During the return sequence (500-530m), a noticeable steering difference between C1 and C3 was observed

with C3 outperforming C1 (e.g., maximum lateral error of 0.47m vs 2.27m). This difference indicates the proficiency of the nonlinear haptic feedback, C3, in recognizing obstacle avoidance intent. During the steering operation of C2 in Figure 6.10c, the driver applied a 2.3N force on the joystick at 457.9m. However, the FSM did not recognize the operator's intent until 469.8m when the driver increased the applied force to 9N which triggered the state transition, causing lateral instability and deteriorated performance. In comparison with C1, C2 and C3 actuated the joystick more aggressively, yielding the larger front wheel steer angle outputs shown in Figure 6.10b. In contrast, C1 required less effort as noted by the small steer angles, resulting in an easier and more comfortable steering experience. In general, C3 with accurate learning-based intent recognition and effective vehicle control, guaranteed the best vehicle lateral performance during highway obstacle avoidance.



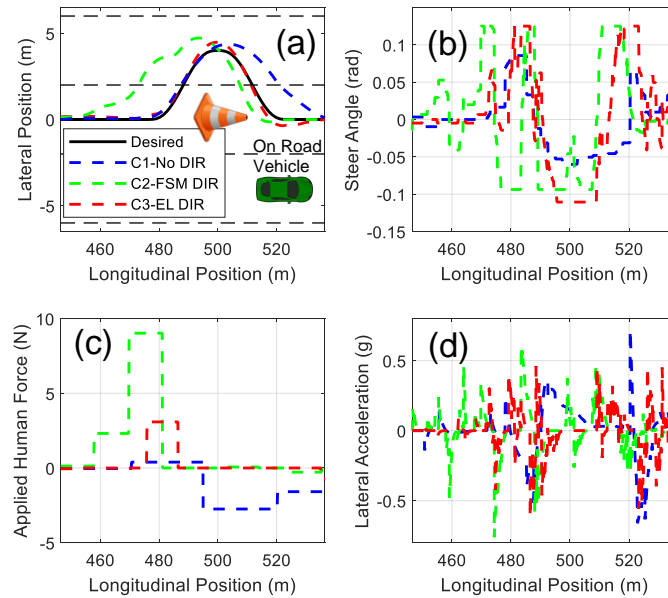


Figure 6.10. Driver #12 response — (a) Desired and actual vehicle trajectories, (b) Wheel steer angle, (c) Applied human force onto the joystick, and (d) Lateral acceleration when driving through the highway track with speed of 90kph under configurations C1-C3 for vehicle left obstacle avoidance of highway roadway.

The 5<sup>th</sup> operator's response during a left lane change is shown in Figure 6.11. The configuration C1 completed the maneuver effectively thanks to the familiarity with the classical driving techniques. Noticeably, configuration C2 again failed to recognize the driver's left lane change intent in Figure 6.11a in time, leading to an unintended weaving behavior from 730 to 760m. In contrast, configuration C3 accurately recognized the driver lane change intent at 750m, which ensured minimal lateral deviations and lateral acceleration for both lane changes. Moreover, the steering operation of C1 requires the driver to apply force to the joystick throughout the lane change maneuvers (Figure 6.11c). On the other hand, C3 perform the maneuver without much human intervention, as evident by the zero applied human force yielded after the haptic assistive control system take over. When driving with C2 and C3, the lateral accelerations are generally larger than those

driving with C1 as shown in Figure 6.11d. The maximum lateral acceleration the driver felt steering with configuration C2 reached up to 0.68g, which can lead to motion discomfort. Overall, the lateral performance of C1 during moderate highway lane change maneuvers can be improved by C3 with learning-based haptic assistive control.

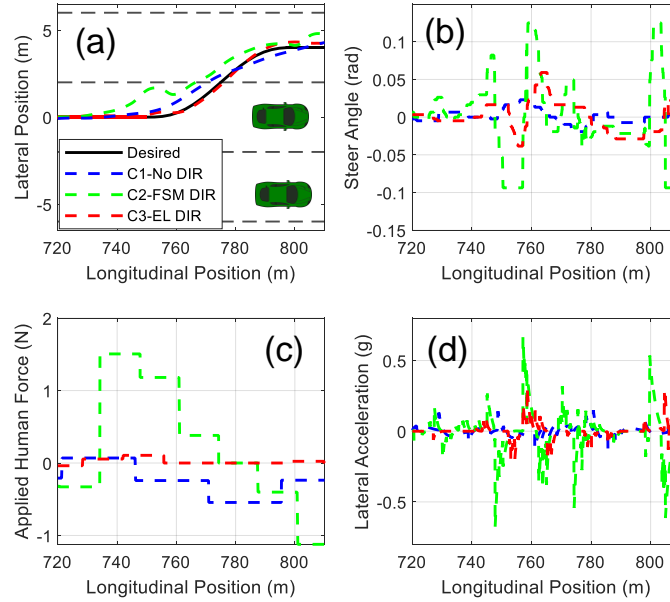


Figure 6.11. Driver #5 response — (a) Desired and actual vehicle trajectories, (b) Wheel steer angle, (c) Applied human force onto the joystick, and (d) Lateral acceleration when driving through the highway track with speed of 90kph under configurations C1-C3 for left lane change of highway roadway.

### 6.5.3.2 City Road Results

After the completion of the highway scenario, the driver then traveled on a city roadway which consisted of a 300m straight section with an initial speed of 30kph (a common city street speed limit) as shown in Figure 6.12. The driver then encounters a 15m radius right turn and a 25m radius left turn at two intersections. Each road feature contains a straight path section that allows the driver to change to the dedicated turn lane. The total distance traveled by the driver throughout the roadway has been marked on the map. The

city road design requires somewhat aggressive driving as evident by quick actions and higher lateral acceleration to better illustrate steering impact.

The 25 drivers' RMS and maximum lateral acceleration (F3), applied human force (F22), lateral error (F1), and intent recognition accuracy for all configurations on the city road are listed in Table III. Configuration C3 offered the best performance per trajectory tracking capability, higher intent recognition accuracy, and lowest driver workload. The performance of configuration C1 in a moderate left turn is acceptable, outperforming C2 and C3 for lateral stability and driver comfort. However, owing to inadequate vehicle control, drivers displayed weak paths with C1, as evident by the largest RMS and maximum lateral error. Configuration C2 offered a 23.59% lower level of intent recognition accuracy than C3. The C2 (FSM based intent recognition model) approach relies on the state transition function, which specifies the conditions under which the driver intent transition occurs. Drivers operated their vehicles in different ways, causing the state transition function to be effective in inferring intent for some people but ineffective for others. On the other hand, the C3 (ensemble learning based approach) method used the collected driving data to train the intent recognition model. Therefore, C3 achieved a higher accuracy than C2 by capturing important regularities inherent in the driving data.

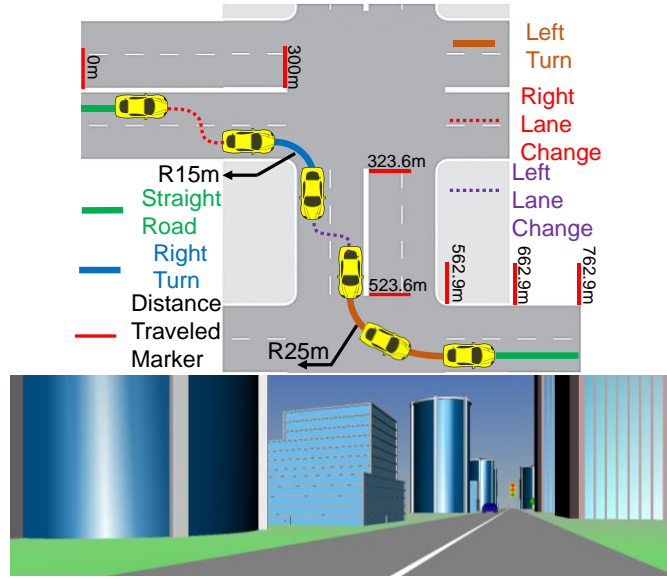


Figure 6.12. City road scenario — (a) Test track, and (b) Animated simulator

Table 6.3. Average of all  $N = 25$  human subjects' lateral acceleration  $\dot{v}_y$ , applied human force  $F_H$ , intent recognition accuracy  $R\%$ , and lateral error  $e_y$  for driving configurations, C1-C3, on city road scenario. Note that the bar represents the RMS value, while subscript *max* is the maximum value

Config	$\bar{\dot{v}}_y$ (deci- g's)	$\bar{F}_H$ (N)	$\bar{R}\%$ (%)	$\bar{e}_y$ (m)	$\dot{v}_{y\max}$ (deci- g's)	$F_{H\max}$ (N)	$R\%_{\max}$ (%)	$e_{y\max}$ (m)
C1	<b>0.66</b>	2.63	N/A	0.64	6.48	12.35	N/A	0.85
C2	0.75	1.03	72.89	0.22	<b>6.04</b>	5.91	100	0.58
C3	0.67	<b>0.90</b>	<b>95.39</b>	<b>0.20</b>	6.78	<b>4.87</b>	100	<b>0.47</b>

After moving into the right lane on the straight road, the driver faced two intersections at which the 15m radius right (300-323.6m) and the 25m radius left (523.6-562.9m) turn maneuvers were performed. The right turn required aggressive driving, considering the driver was tracking at 30kph with a centrifugal acceleration of 0.47g. The vehicle's lateral error, which is the orthogonal distance from the CG of the vehicle to the desired lane center, for Driver #8 is depicted in Figure 6.13a for C1-C3. Equipped with

basic self-centering and lane-keeping functionality, C1 demonstrated poor performance given the large lateral error. Meanwhile, C2 and C3 with the DIR based haptic assistive control lowered the maximum lateral error by 71.7% and 74.1% when negotiating the circular path in comparison to C1. Moreover, without proper vehicle control, C1 started to oversteer after entering the turn while braking and turning too much. With the addition of the intent recognition in the haptic assistive control, C2 and C3 eliminated any oversteer. The adoption of C2 and C3 also relieved the driver's burden as shown in Figure 6.13b; decreasing the maximum joystick applied force by 85.3% and 76.5%. Collectively, the FSM and learning-based DIR adopted in C2 and C3 improved the vehicle tracking performance and reduced the operator workload during these maneuvers.

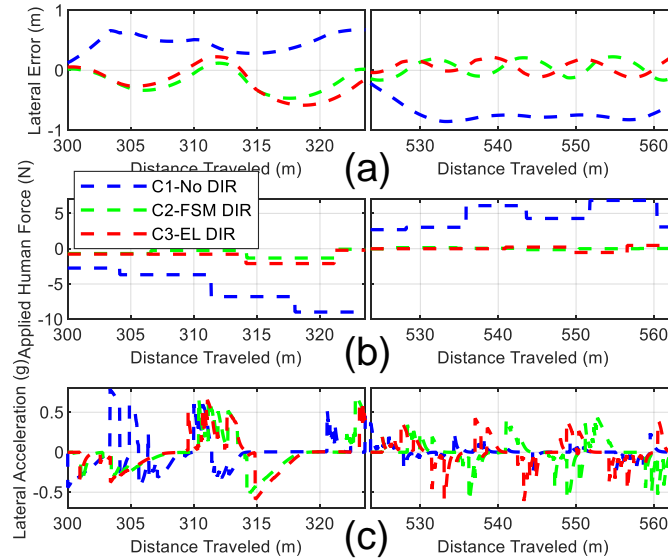


Figure 6.13. Driver #8 response — (a) Lateral error, (b) Applied human force on joystick, and (c) Lateral acceleration when driving

### 6.5.3.3 Post-Test Questionnaire Results

The human driver subjective reactions to the three driving configuration were evaluated through a questionnaire. As shown in Table A.I, nine questions requested

responses on a Likert scale of 1 to 7 in three aspects: (i) Degree to which participants felt a sense of confidence and control over the driving system (Questions 1-4, symbol O1), (ii) Perceived ease-of-use of the driving system (Questions 5 and 6, symbol O2), and (iii) Understood safety of the vehicle (Questions 7-9; symbol O3).

The normalized subjective reaction measures for the five driving configurations, C1-C3, and the driver observations, O1- O3, have been displayed in Figure 6.14. For the confidence and control measure, O1, the participants gave the highest rating to the driving system without DIR, C1, due to its familiarity. Results also show that C3 received complimentary remarks from the drivers for its operational comfortableness and additional safety assurance during obstacle avoidance. One crucial observation found in the analysis of ease-of-use, O2, was that C2 and C3 were significantly preferred over C1. Such a novel pattern may be explained by the proposed advanced haptic assistive control systems with DIR that demanded much less physical effort from the operator during both regular driving and evasive maneuvering. Finally, it was observed that the safety, O3, rating was inversely correlated with lane deviations. Consequently, most operators rated high scores on C2 and C3 for the capability of driving the vehicle safest during moderate turns/cornering and sharp intersection turns, respectively. There was also a significant positive correlation between safety ratings and intent recognition correctness, as the safety ratings given to the FSM based configuration, C2, which yields lower intention prediction precision, was less than those given to the learning based configuration, C3.

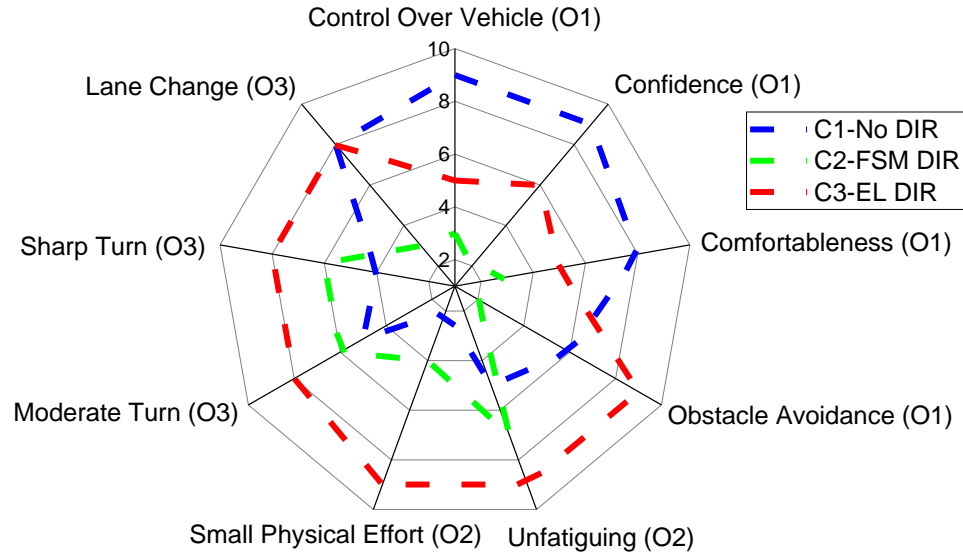


Figure 6.14. Nine subjective measures for three driving configurations C1-C3 based on human subjects' responses to the questionnaire in Table III normalized to 10. Symbols O1 to O3 correspond to Table III and capture the steering characteristic behind driver assessment.

## 6.6 Conclusion

The worldwide growth in semi-autonomous ground vehicles necessitates intelligent driving interfaces for the development of safety and situational awareness systems. In this study, a learning-based driver assistance system that combines path-planning, vehicle control, and intent recognition in a holistic haptic assistive control framework was designed and numerically evaluated for ground vehicles. A nonlinear model predictive controller was developed for the haptic driving interface longitudinal and lateral functionalities. Using ensemble methods, a machine learning based model was trained to utilize the driving data for predicting driver behavior transitions. Validation results by human subject testing indicated that the trained model can recognize driver intent transition patterns and predict with high accuracy. Furthermore, the comparison study with a finite state machine based model demonstrated the machine learning-based model superiority in intent prediction

accuracy. The learning-based model development cycle can be quite long, as the DIR model must be trained and validated. On the other hand, the state machine based model has the advantage of implementation simplicity and time-efficiency when driving data is unavailable. Overall, the proposed learning-based haptic assistive control system elevated the driver performance and reduced the operator burden during select maneuvers. In future work, the proposed system can migrate from on-board operation to the teleoperation of ground vehicles.



## APPENDIX

### Appendix A

#### Publications List (as First-Author)

##### **Journal Articles**

- C. Wang, Y. Wang, and J. Wagner, “Evaluation of Robust Haptic Interface for Semi-Autonomous Vehicles”, *SAE International Journal of Connected and Automated Vehicles*, vol. 2, no. 2, pp. 99-114, May 2019.
- C. Wang, C. Frazelle, J. Wagner, and I. Walker, “Dynamic Control of Multi-Section Three-Dimensional Continuum Manipulators Based on Virtual Discrete-Jointed Robot Models”, *IEEE/ASME Transactions on Mechatronics*, June 2020.
- C. Wang, K. Alexander, P. Pidgeon, and J. Wagner, “Design and Evaluation of a Driver Intent Based Mobile Control Interface for Ground Vehicles”, submitted to *International Journal of Vehicle Design*, October 2019.
- C. Wang, F. Li, Y. Wang, and J. Wagner, “Haptic Assistive Control with Learning Based Driver Intent Recognition for Semi-Autonomous Vehicles”, submitted to *IEEE Transactions on Haptics*, November 2020.

##### **Conference Proceedings**

- C. Wang, Y. Wang, and J. Wagner, “Evaluation of alternative steering devices with adjustable haptic feedback for semi-autonomous and autonomous vehicles”, in *Proceedings of SAE World Congress and Exhibition*, SAE Technical Paper 2018-01-0572, Detroit, MI, April 2018.
- C. Wang, J. Wagner, C. Frazelle, and I. Walker, “Continuum Robot Control Based on Virtual Discrete-Jointed Robot Models”, *IECON 2018 - 44th Annual Conference of the IEEE Industrial Electronics Society*, pp. 2508-2515, Washington, DC, October 2018.
- C. Wang, K. Alexander, P. Pidgeon, and J. Wagner, “Use of Cellphones as Alternative Driver Inputs in Passenger Vehicles”, in *Proceedings of SAE World Congress and Exhibition*, SAE Technical Paper 2019-01-1239, Detroit, MI, April 2019.
- C. Wang, C. Frazelle, J. Wagner, and I. Walker, “A Discrete-Jointed Robot Model Based Control Strategy for Spatial Continuum Manipulators”, *IECON 2020 - 46th Annual Conference of the IEEE Industrial Electronics Society*, pp. 543-549, Singapore, October 2020.

## REFERENCES

- Alleyne, A., 1997. A Comparison of Alternative Intervention Strategies for Unintended Roadway Departure (URD) Control. *Vehicle System Dynamics* 27, 157–186. <https://doi.org/10.1080/00423119708969327>
- Alt, B., Hermann, E., Svaricek, F., 2013. Second order sliding modes control for rope winch based automotive driver robot. *IJVD* 62, 147. <https://doi.org/10.1504/IJVD.2013.052707>
- Ancha, S., Baviskar, A., Wagner, J.R., Dawson, D.M., 2007. Ground vehicle steering systems: modelling, control, and analysis of hydraulic, electric and steer-by-wire configurations. *IJVD* 44, 188. <https://doi.org/10.1504/IJVD.2007.013225>
- Andonian, B., Rauch, W., Bhise, V., 2003. Driver Steering Performance Using Joystick vs. Steering Wheel Controls. Presented at the SAE 2003 World Congress & Exhibition, pp. 2003-01–0118. <https://doi.org/10.4271/2003-01-0118>
- Bajo, A., Goldman, R.E., Simaan, N., 2011. Configuration and joint feedback for enhanced performance of multi-segment continuum robots, in: 2011 IEEE International Conference on Robotics and Automation. Presented at the 2011 IEEE International Conference on Robotics and Automation (ICRA), IEEE, Shanghai, China, pp. 2905–2912. <https://doi.org/10.1109/ICRA.2011.5980005>
- Bajo, A., Simaan, N., 2016. Hybrid motion/force control of multi-backbone continuum robots. *The International Journal of Robotics Research* 35, 422–434. <https://doi.org/10.1177/0278364915584806>
- Baviskar, A., Wagner, J.R., Dawson, D.M., Braganza, D., Setlur, P., 2009. An Adjustable Steer-by-Wire Haptic-Interface Tracking Controller for Ground Vehicles. *IEEE Trans. Veh. Technol.* 58, 546–554. <https://doi.org/10.1109/TVT.2008.925317>
- Bhardwaj, A., Ghasemi, A.H., Zheng, Y., Febbo, H., Jayakumar, P., Ersal, T., Stein, J.L., Gillespie, R.B., 2020. Who's the boss? Arbitrating control authority between a human driver and automation system. *Transportation Research Part F: Traffic Psychology and Behaviour* 68, 144–160. <https://doi.org/10.1016/j.trf.2019.12.005>
- Black, J., Freeman, P.T., Wagner, J.R., Iyasere, E., Dawson, D.M., Switzer, F.S., 2014. Evaluation of driver steering preferences using an automotive simulator. *IJVD* 66, 124. <https://doi.org/10.1504/IJVD.2014.064548>
- Black, J., Iyasere, E., Wagner, J., 2011. Creation of a driver preference objective metric to evaluate ground vehicle steering systems, in: Proceedings of the 2011 American Control Conference. Presented at the 2011 American Control Conference, IEEE, San Francisco, CA, pp. 1867–1872. <https://doi.org/10.1109/ACC.2011.5990751>
- Boehm, P., Ghasemi, A.H., O'Modhrain, S., Jayakumar, P., Gillespie, R.B., 2016. Architectures for Shared Control of Vehicle Steering\*\*The authors wish to acknowledge the financial support of the Automotive Research Center (ARC) under Cooperative Agreement W56HZV-04-2-0001 with the U.S. Army Tank Automotive Research, Development and Engineering Center (TARDEC) Warren, MI. *IFAC-PapersOnLine* 49, 639–644. <https://doi.org/10.1016/j.ifacol.2016.10.637>

- Braganza, D., Dawson, D.M., Walker, I.D., Nath, N., 2007. A Neural Network Controller for Continuum Robots. *IEEE Trans. Robot.* 23, 1270–1277. <https://doi.org/10.1109/TRO.2007.906248>
- Camarillo, D.B., Carlson, C.R., Salisbury, J.K., 2009. Configuration Tracking for Continuum Manipulators With Coupled Tendon Drive. *IEEE Trans. Robot.* 25, 798–808. <https://doi.org/10.1109/TRO.2009.2022426>
- Camarillo, David B., Carlson, C.R., Salisbury, J.K., 2009. Task-Space Control of Continuum Manipulators with Coupled Tendon Drive, in: Khatib, O., Kumar, V., Pappas, G.J. (Eds.), *Experimental Robotics*. Springer Berlin Heidelberg, Berlin, Heidelberg, pp. 271–280. [https://doi.org/10.1007/978-3-642-00196-3\\_32](https://doi.org/10.1007/978-3-642-00196-3_32)
- Chan, B., 2011. Electronic Stability Control as Standard on Heavy Duty Emergency Vehicles: A Simulation Analysis. Presented at the Commercial Vehicle Engineering Congress, pp. 2011-01–2151. <https://doi.org/10.4271/2011-01-2151>
- Chebly, A., Talj, R., Charara, A., 2017. Coupled Longitudinal and Lateral Control for an Autonomous Vehicle Dynamics Modeled Using a Robotics Formalism. *IFAC-PapersOnLine* 50, 12526–12532. <https://doi.org/10.1016/j.ifacol.2017.08.2190>
- Conrad, B., Zinn, M., 2015. Closed loop task space control of an interleaved continuum-rigid manipulator, in: 2015 IEEE International Conference on Robotics and Automation (ICRA). Presented at the 2015 IEEE International Conference on Robotics and Automation (ICRA), IEEE, Seattle, WA, USA, pp. 1743–1750. <https://doi.org/10.1109/ICRA.2015.7139423>
- Cummings, M., 2017. Artificial intelligence and the future of warfare. Chatham House for the Royal Institute of International Affairs London.
- D.A., A., M., M., 2010. Neuromuscular Analysis as a Guideline in designing Shared Control, in: Hosseini, M. (Ed.), *Advances in Haptics*. InTech. <https://doi.org/10.5772/8696>
- Dadras, S., 2017. Path Tracking Using Fractional Order Extremum Seeking Controller for Autonomous Ground Vehicle. Presented at the WCX<sup>TM</sup> 17: SAE World Congress Experience, pp. 2017-01–0094. <https://doi.org/10.4271/2017-01-0094>
- Davila, J., Fridman, L., Levant, A., 2005. Second-order sliding-mode observer for mechanical systems. *IEEE Trans. Automat. Contr.* 50, 1785–1789. <https://doi.org/10.1109/TAC.2005.858636>
- Doshi, A., Morris, B.T., Trivedi, M.M., 2011. On-road prediction of driver's intent with multimodal sensory cues. *IEEE Pervasive Comput.* 10, 22–34. <https://doi.org/10.1109/MPRV.2011.38>
- Dugoff, H., Fancher, P.S., Segel, L., 1970. An Analysis of Tire Traction Properties and Their Influence on Vehicle Dynamic Performance. Presented at the International Automobile Safety Conference, p. 700377. <https://doi.org/10.4271/700377>
- Dugoff, H., Fancher, P.S., Segel, L., n.d. Tire Performance Characteristics Affecting Vehicle Response to Steering and Braking Control Inputs. The University of Michigan Ann Arbor, Michigan, Highway Safety Research Institute Institute of Science and Technology.

- Ellensohn, F., Schwienbacher, M., Venrooij, J., Rixen, D., 2018. Motion Cueing Algorithm for a 9 DoF Driving Simulator: MPC with Linearized Actuator Constraints. Presented at the WCX World Congress Experience, pp. 2018-01–0570. <https://doi.org/10.4271/2018-01-0570>
- Elvin, D., Gambrell, P., 2002. Adapting Vehicles for the Disabled Driver. Presented at the International Body Engineering Conference & Exhibition and Automotive & Transportation Technology Congress, pp. 2002-01–2082. <https://doi.org/10.4271/2002-01-2082>
- Enriquez, M., Afonin, O., Yager, B., Maclean, K., 2001. A pneumatic tactile alerting system for the driving environment, in: Proceedings of the 2001 Workshop on Perceptive User Interfaces - PUI '01. Presented at the the 2001 workshop, ACM Press, Orlando, Florida, p. 1. <https://doi.org/10.1145/971478.971506>
- Fahami, S.M.H., Zamzuri, H., Mazlan, S.A., 2015. Development of Estimation Force Feedback Torque Control Algorithm for Driver Steering Feel in Vehicle Steer by Wire System: Hardware in the Loop. International Journal of Vehicular Technology 2015, 1–17. <https://doi.org/10.1155/2015/314597>
- Falkenhahn, V., Hildebrandt, A., Neumann, R., Sawodny, O., 2017. Dynamic Control of the Bionic Handling Assistant. IEEE/ASME Trans. Mechatron. 22, 6–17. <https://doi.org/10.1109/TMECH.2016.2605820>
- Falkenhahn, V., Hildebrandt, A., Sawodny, O., 2014. Trajectory optimization of pneumatically actuated, redundant continuum manipulators, in: 2014 American Control Conference. Presented at the 2014 American Control Conference - ACC 2014, IEEE, Portland, OR, USA, pp. 4008–4013. <https://doi.org/10.1109/ACC.2014.6858736>
- Fergani, S., Menhour, L., Senname, O., Dugard, L., D'Andréa-Novel, B., 2017. Integrated vehicle control through the coordination of longitudinal/lateral and vertical dynamics controllers: Flatness and LPV/H $\infty$ -based design: VDC: Flatness and LPV/ H $\infty$ -Based Design. Int. J. Robust. Nonlinear Control 27, 4992–5007. <https://doi.org/10.1002/rnc.3846>
- Findeisen, R., Allgower, F., 2002. An Introduction to Nonlinear Model Predictive Control. Presented at the Systems and control: 21th Benelux meeting, Eindhoven: Technische Universiteit Eindhoven, Veldhoven, Netherlands.
- Frazelle, C.G., Kapadia, A.D., Walker, Ian.D., 2018. A Nonlinear Control Strategy for Extensible Continuum Robots, in: 2018 IEEE International Conference on Robotics and Automation (ICRA). Presented at the 2018 IEEE International Conference on Robotics and Automation (ICRA), IEEE, Brisbane, QLD, pp. 7727–7734. <https://doi.org/10.1109/ICRA.2018.8463187>
- Freeman, P., Jensen, M., Wagner, J., Alexander, K., 2015. A Comparison of Multiple Control Strategies for Vehicle Run-Off-Road and Return. IEEE Trans. Veh. Technol. 64, 901–911. <https://doi.org/10.1109/TVT.2014.2329264>
- Freeman, P., Samant, S., Wagner, J.R., Alexander, K., Pidgeon, P., 2013. Evaluation of an Automotive Simulator Based Driver Safety Training Program for Run-Off-the-Road and Recovery. Presented at the SAE 2013 World Congress & Exhibition, pp. 2013-01–1260. <https://doi.org/10.4271/2013-01-1260>

- Freeman, P., Wagner, J., Alexander, K., 2016. Run-off-road and recovery – state estimation and vehicle control strategies. *Vehicle System Dynamics* 54, 1317–1343. <https://doi.org/10.1080/00423114.2016.1200728>
- Gambrell, P., Elvin, D., 2002. The Application of New Technologies in the Motor Car - Positives and Negatives for the Disabled Driver. Presented at the International Body Engineering Conference & Exhibition and Automotive & Transportation Technology Congress, pp. 2002-01–2083. <https://doi.org/10.4271/2002-01-2083>
- George Thuruthel, T., Ansari, Y., Falotico, E., Laschi, C., 2018. Control Strategies for Soft Robotic Manipulators: A Survey. *Soft Robotics* 5, 149–163. <https://doi.org/10.1089/soro.2017.0007>
- Ghasemi, A.H., Jayakumar, P., Gillespie, R.B., 2019. Shared control architectures for vehicle steering. *Cogn Tech Work* 21, 699–709. <https://doi.org/10.1007/s10111-019-00560-9>
- Gravagne, I.A., Walker, I.D., 2002. Uniform regulation of a multi-section continuum manipulator, in: *Proceedings 2002 IEEE International Conference on Robotics and Automation* (Cat. No.02CH37292). Presented at the 2002 IEEE International Conference on Robotics and Automation, IEEE, Washington, DC, USA, pp. 1519–1524. <https://doi.org/10.1109/ROBOT.2002.1014759>
- Greigarn, T., Poirot, N.L., Xu, X., Cavusoglu, M.C., 2019. Jacobian-Based Task-Space Motion Planning for MRI-Actuated Continuum Robots. *IEEE Robot. Autom. Lett.* 4, 145–152. <https://doi.org/10.1109/LRA.2018.2881987>
- Grissom, M.D., Chitrakaran, V., Dienno, D., Csencits, M., Pritts, M., Jones, B., McMahan, W., Dawson, D., Rahn, C., Walker, I., 2006. Design and experimental testing of the OctArm soft robot manipulator, in: Gerhart, G.R., Shoemaker, C.M., Gage, D.W. (Eds.), . Presented at the Defense and Security Symposium, Orlando (Kissimmee), FL, p. 62301F. <https://doi.org/10.1117/12.665321>
- Gunta, R., Sankar, S., 1980. A Friction Circle Concept for Dugoff's Tyre Friction Model. *International Journal of Vehicle Design* 1, 373–377. <https://doi.org/10.1504/IJVD.1980.061234>
- Guntur, R., Sankar, S., 1980. A Friction Circle Concept for Dugoff's Tyre Friction Model. *International Journal of Vehicle Design* 1, 373–377. <https://doi.org/10.1504/IJVD.1980.061234>
- Guo, J., 2016. Coordinated Longitudinal and Lateral Control of Autonomous Electric Vehicles in a Platoon. Presented at the SAE-TONGJI 2016 Driving Technology of Intelligent Vehicle Symposium, pp. 2016-01–1875. <https://doi.org/10.4271/2016-01-1875>
- Guo, J., Hu, P., Wang, R., 2016. Nonlinear Coordinated Steering and Braking Control of Vision-Based Autonomous Vehicles in Emergency Obstacle Avoidance. *IEEE Trans. Intell. Transport. Syst.* 17, 3230–3240. <https://doi.org/10.1109/TITS.2016.2544791>
- Hannan, M.W., Walker, I.D., 2003. Kinematics and the Implementation of an Elephant's Trunk Manipulator and Other Continuum Style Robots. *J. Robotic Syst.* 20, 45–63. <https://doi.org/10.1002/rob.10070>

- Hannan, M.W., Walker, I.D., 2001. Analysis and experiments with an elephant's trunk robot. *Advanced Robotics* 15, 847–858. <https://doi.org/10.1163/156855301317198160>
- Heathershaw, A., 2000. Optimizing Variable Ratio Steering for Improved On-Centre Sensitivity and Cornering Control. Presented at the SAE 2000 World Congress, pp. 2000-01–0821. <https://doi.org/10.4271/2000-01-0821>
- Hesheng Wang, Weidong Chen, Xiaojin Yu, Tao Deng, Xiaozhou Wang, Pfeifer, R., 2013. Visual servo control of cable-driven soft robotic manipulator, in: 2013 IEEE/RSJ International Conference on Intelligent Robots and Systems. Presented at the 2013 IEEE/RSJ International Conference on Intelligent Robots and Systems (IROS 2013), IEEE, Tokyo, pp. 57–62. <https://doi.org/10.1109/IROS.2013.6696332>
- Hulnhagen, T., Dengler, I., Tamke, A., Dang, T., Breuel, G., 2010. Maneuver recognition using probabilistic finite-state machines and fuzzy logic, in: 2010 IEEE Intelligent Vehicles Symposium. Presented at the 2010 IEEE Intelligent Vehicles Symposium (IV), IEEE, La Jolla, CA, USA, pp. 65–70. <https://doi.org/10.1109/IVS.2010.5548066>
- Hwang, J., Huh, K., Na, H., Jung, H., Kang, H., Yoon, P., 2008. Development of a Model Based Predictive Controller for Lane Keeping Assistance. Presented at the SAE World Congress & Exhibition, pp. 2008-01–1454. <https://doi.org/10.4271/2008-01-1454>
- ISO 3888-2:2011 [WWW Document], n.d. . International Organization for Standardization. URL <http://www.iso.org/cms/render/live/en/sites/isoorg/contents/data/standard/05/72/57253.html> (accessed 7.31.19).
- Jalali, K., Uchida, T., McPhee, J., Lambert, S., 2013. Development of an Advanced Fuzzy Active Steering Controller and a Novel Method to Tune the Fuzzy Controller. *SAE Int. J. Passeng. Cars – Electron. Electr. Syst.* 6, 241–254. <https://doi.org/10.4271/2013-01-0688>
- Jensen, M., Freeman, P., Wagner, J., Alexander, K., 2013. Controller design and evaluation for vehicle run-off-the-road and recovery, in: 2013 European Control Conference (ECC). Presented at the 2013 European Control Conference (ECC), IEEE, Zurich, pp. 962–967. <https://doi.org/10.23919/ECC.2013.6669117>
- Jensen, M.J., Tolbert, A.M., Wagner, J.R., Switzer, F.S., Finn, J.W., 2011. A Customizable Automotive Steering System With a Haptic Feedback Control Strategy for Obstacle Avoidance Notification. *IEEE Trans. Veh. Technol.* 60, 4208–4216. <https://doi.org/10.1109/TVT.2011.2172472>
- Joshi, A., 2018. Hardware-in-the-Loop (HIL) Implementation and Validation of SAE Level 2 Automated Vehicle with Subsystem Fault Tolerant Fallback Performance for Takeover Scenarios. *SAE Intl. J CAV* 1, 13–32. <https://doi.org/10.4271/12-01-01-0002>
- Kalinowski, J., Drage, T., Bräunl, T., 2014. Drive-By-Wire for an Autonomous Formula SAE Car. *IFAC Proceedings Volumes* 47, 8457–8462. <https://doi.org/10.3182/20140824-6-ZA-1003.01156>

- Kamal, S., Chalanga, A., Moreno, J.A., Fridman, L., Bandyopadhyay, B., 2014. Higher order super-twisting algorithm, in: 2014 13th International Workshop on Variable Structure Systems (VSS). Presented at the 2014 13th International Workshop on Variable Structure Systems (VSS), IEEE, Nantes, France, pp. 1–5. <https://doi.org/10.1109/VSS.2014.6881129>
- Kang, C.M., Sung Gu, Y., Jeon, S.J., Son, Y.S., Kim, W., Lee, S.-H., Chung, C.C., 2016. Lateral Control System for Autonomous Lane Change System on Highways. SAE Int. J. Passeng. Cars - Mech. Syst. 9, 877–884. <https://doi.org/10.4271/2016-01-1641>
- Kapadia, A., Walker, I.D., 2011. Task-space control of extensible continuum manipulators, in: 2011 IEEE/RSJ International Conference on Intelligent Robots and Systems. Presented at the 2011 IEEE/RSJ International Conference on Intelligent Robots and Systems (IROS 2011), IEEE, San Francisco, CA, pp. 1087–1092. <https://doi.org/10.1109/IROS.2011.6094873>
- Kapadia, A.D., Fry, K.E., Walker, I.D., 2014. Empirical investigation of closed-loop control of extensible continuum manipulators, in: 2014 IEEE/RSJ International Conference on Intelligent Robots and Systems. Presented at the 2014 IEEE/RSJ International Conference on Intelligent Robots and Systems (IROS 2014), IEEE, Chicago, IL, USA, pp. 329–335. <https://doi.org/10.1109/IROS.2014.6942580>
- Kapadia, A.D., Walker, I.D., Dawson, D.M., Tatlicioglu, E., 2010. A Model-based Sliding Mode Controller for Extensible Continuum Robots, in: Proceedings of the 9th WSEAS International Conference on Signal Processing, Robotics and Automation, ISPRA'10. World Scientific and Engineering Academy and Society (WSEAS), Stevens Point, Wisconsin, USA, pp. 113–120.
- Kasper, D., Weidl, G., Dang, T., Breuel, G., Tamke, A., Wedel, A., Rosenstiel, W., 2012. Object-Oriented Bayesian Networks for Detection of Lane Change Maneuvers. IEEE Intell. Transport. Syst. Mag. 4, 19–31. <https://doi.org/10.1109/MITS.2012.2203229>
- Katriniok, A., Maschuw, J.P., Christen, F., Eckstein, L., Abel, D., 2013. Optimal vehicle dynamics control for combined longitudinal and lateral autonomous vehicle guidance, in: 2013 European Control Conference (ECC). Presented at the 2013 European Control Conference (ECC), IEEE, Zurich, pp. 974–979. <https://doi.org/10.23919/ECC.2013.6669331>
- Katzourakis, D.I., Abbink, D.A., Happee, R., Holweg, E., 2011. Steering Force Feedback for Human–Machine-Interface Automotive Experiments. IEEE Trans. Instrum. Meas. 60, 32–43. <https://doi.org/10.1109/TIM.2010.2065550>
- Katzschmann, R.K., Santina, C.D., Toshimitsu, Y., Bicchi, A., Rus, D., 2019. Dynamic Motion Control of Multi-Segment Soft Robots Using Piecewise Constant Curvature Matched with an Augmented Rigid Body Model, in: 2019 2nd IEEE International Conference on Soft Robotics (RoboSoft). Presented at the 2019 2nd IEEE International Conference on Soft Robotics (RoboSoft), IEEE, Seoul, Korea (South), pp. 454–461. <https://doi.org/10.1109/ROBOSOFT.2019.8722799>

- Kayacan, E., Saeys, W., Ramon, H., Belta, C., Peschel, J.M., 2018. Experimental Validation of Linear and Nonlinear MPC on an Articulated Unmanned Ground Vehicle. *IEEE/ASME Trans. Mechatron.* 23, 2023–2030. <https://doi.org/10.1109/TMECH.2018.2854877>
- Kim, I.-H., Bong, J.-H., Park, J., Park, S., 2017a. Prediction of Driver's Intention of Lane Change by Augmenting Sensor Information Using Machine Learning Techniques. *Sensors* 17, 1350. <https://doi.org/10.3390/s17061350>
- Kim, I.-H., Bong, J.-H., Park, J., Park, S., 2017b. Prediction of Driver's Intention of Lane Change by Augmenting Sensor Information Using Machine Learning Techniques. *Sensors* 17, 1350. <https://doi.org/10.3390/s17061350>
- Kumar, P., Perrollaz, M., Lefevre, S., Laugier, C., 2013a. Learning-based approach for online lane change intention prediction, in: 2013 IEEE Intelligent Vehicles Symposium (IV). Presented at the 2013 IEEE Intelligent Vehicles Symposium (IV), IEEE, Gold Coast City, Australia, pp. 797–802. <https://doi.org/10.1109/IVS.2013.6629564>
- Kumar, P., Perrollaz, M., Lefevre, S., Laugier, C., 2013b. Learning-based approach for online lane change intention prediction, in: 2013 IEEE Intelligent Vehicles Symposium (IV). Presented at the 2013 IEEE Intelligent Vehicles Symposium (IV), IEEE, Gold Coast City, Australia, pp. 797–802. <https://doi.org/10.1109/IVS.2013.6629564>
- Lessmann, S., Baesens, B., Seow, H.-V., Thomas, L.C., 2015. Benchmarking state-of-the-art classification algorithms for credit scoring: An update of research. *European Journal of Operational Research* 247, 124–136. <https://doi.org/10.1016/j.ejor.2015.05.030>
- Li, F., Wang, W., Feng, G., Guo, W., 2014. Driving Intention Inference Based on Dynamic Bayesian Networks, in: Wen, Z., Li, T. (Eds.), *Practical Applications of Intelligent Systems*. Springer Berlin Heidelberg, Berlin, Heidelberg, pp. 1109–1119. [https://doi.org/10.1007/978-3-642-54927-4\\_106](https://doi.org/10.1007/978-3-642-54927-4_106)
- Li, K., Wang, X., Xu, Y., Wang, J., 2016a. Lane changing intention recognition based on speech recognition models. *Transportation Research Part C: Emerging Technologies* 69, 497–514. <https://doi.org/10.1016/j.trc.2015.11.007>
- Li, K., Wang, X., Xu, Y., Wang, J., 2016b. Lane changing intention recognition based on speech recognition models. *Transportation Research Part C: Emerging Technologies* 69, 497–514. <https://doi.org/10.1016/j.trc.2015.11.007>
- Li, M., Cao, H., Song, X., Huang, Y., Wang, J., Huang, Z., 2018. Shared Control Driver Assistance System Based on Driving Intention and Situation Assessment. *IEEE Trans. Ind. Inf.* 14, 4982–4994. <https://doi.org/10.1109/TII.2018.2865105>
- Lin, H., Antsaklis, P.J., 2009. Stability and Stabilizability of Switched Linear Systems: A Survey of Recent Results. *IEEE Transactions on Automatic Control* 54, 308–322. <https://doi.org/10.1109/TAC.2008.2012009>
- MacAdam, C.C., 1988. Development of driver/vehicle steering interaction models for dynamic analysis (No. UMTRI-88-53). University of Michigan Transportation Research Institute.



- MacAdam, C.C., 1981. Application of an Optimal Preview Control for Simulation of Closed-Loop Automobile Driving. *IEEE Trans. Syst., Man, Cybern.* 11, 393–399. <https://doi.org/10.1109/TSMC.1981.4308705>
- MacAdam, C.C., 1980. An Optimal Preview Control for Linear Systems. *J. Dyn. Sys., Meas., Control* 102, 188. <https://doi.org/10.1115/1.3139632>
- Mahl, T., Hildebrandt, A., Sawodny, O., 2014. A Variable Curvature Continuum Kinematics for Kinematic Control of the Bionic Handling Assistant. *IEEE Trans. Robot.* 30, 935–949. <https://doi.org/10.1109/TRO.2014.2314777>
- Mahvash, M., Dupont, P.E., 2011. Stiffness Control of Surgical Continuum Manipulators. *IEEE Trans. Robot.* 27, 334–345. <https://doi.org/10.1109/TRO.2011.2105410>
- Mandhata, U., Wagner, J., Switzer, F., Dawson, D., Summers, J., 2010. A Customizable Steer-By-Wire Interface for Ground Vehicles. *IFAC Proceedings Volumes* 43, 656–661. <https://doi.org/10.3182/20100712-3-DE-2013.00002>
- Mandhata, U.B., Jensen, M.J., Wagner, J.R., Switzer, F.S., Dawson, D.M., Summers, J.D., 2012. Evaluation of a customizable haptic feedback system for ground vehicle steer-by-wire interfaces, in: 2012 American Control Conference (ACC). Presented at the 2012 American Control Conference - ACC 2012, IEEE, Montreal, QC, pp. 2781–2787. <https://doi.org/10.1109/ACC.2012.6314906>
- Marchese, A.D., Rus, D., 2016. Design, kinematics, and control of a soft spatial fluidic elastomer manipulator. *The International Journal of Robotics Research* 35, 840–869. <https://doi.org/10.1177/0278364915587925>
- Marchese, A.D., Tedrake, R., Rus, D., 2015. Dynamics and trajectory optimization for a soft spatial fluidic elastomer manipulator, in: 2015 IEEE International Conference on Robotics and Automation (ICRA). Presented at the 2015 IEEE International Conference on Robotics and Automation (ICRA), IEEE, Seattle, WA, USA, pp. 2528–2535. <https://doi.org/10.1109/ICRA.2015.7139538>
- Matsuura, Y., Kitazawa, S., Hiraike, Y., 2004. A Study of Driver's Maneuver Characteristics Using the Joy-Stick Device. Presented at the SAE 2004 World Congress & Exhibition, pp. 2004-01–0452. <https://doi.org/10.4271/2004-01-0452>
- Medeiros-Ward, N., Cooper, J.M., Doxon, A.J., Strayer, D.L., Provancher, W.R., 2010. Bypassing the Bottleneck: The Advantage of Fingertip Shear Feedback for Navigational Cues. *Proceedings of the Human Factors and Ergonomics Society Annual Meeting* 54, 2042–2047. <https://doi.org/10.1177/154193121005402405>
- Mehdizadeh, E., Kabganian, M., Kazemi, R., 2011. A new force feedback for Steer-by-Wire vehicles via virtual vehicle concept, in: IEEE Conference on Decision and Control and European Control Conference. Presented at the 2011 50th IEEE Conference on Decision and Control and European Control Conference (CDC-ECC 2011), IEEE, Orlando, FL, USA, pp. 2281–2286. <https://doi.org/10.1109/CDC.2011.6160941>
- Middleton, R., Goodwin, G., 1986. Adaptive computed torque control for rigid link manipulators, in: 1986 25th IEEE Conference on Decision and Control. Presented at the 1986 25th IEEE Conference on Decision and Control, IEEE, Athens, Greece, pp. 68–73. <https://doi.org/10.1109/CDC.1986.267156>

- Mills, V.D., Wagner, J.R., 2003. Behavioural modelling and analysis of hybrid vehicle steering systems. *Proceedings of the Institution of Mechanical Engineers, Part D: Journal of Automobile Engineering* 217, 349–361. <https://doi.org/10.1243/095440703321645061>
- Montemerlo, M., Becker, J., Bhat, S., Dahlkamp, H., Dolgov, D., Ettinger, S., Haehnel, D., Hilden, T., Hoffmann, G., Huhnke, B., Johnston, D., Klumpp, S., Langer, D., Levandowski, A., Levinson, J., Marcil, J., Orenstein, D., Paefgen, J., Penny, I., Petrovskaya, A., Pflueger, M., Stanek, G., Stavens, D., Vogt, A., Thrun, S., 2009. Junior: The Stanford Entry in the Urban Challenge, in: Buehler, M., Iagnemma, K., Singh, S. (Eds.), *The DARPA Urban Challenge*, Springer Tracts in Advanced Robotics. Springer Berlin Heidelberg, Berlin, Heidelberg, pp. 91–123. [https://doi.org/10.1007/978-3-642-03991-1\\_3](https://doi.org/10.1007/978-3-642-03991-1_3)
- Muslim, H., Itoh, M., 2017. Haptic Shared Guidance and Automatic Cooperative Control Assistance System: Performance Evaluation for Collision Avoidance during Hazardous Lane Changes. *SICE Journal of Control, Measurement, and System Integration* 10, 460–467. <https://doi.org/10.9746/jcmsi.10.460>
- Nahak, S., Kota, N., 2013. Modeling & Simulation of Joystick Operated Steering System. Presented at the 8th SAEINDIA International Mobility Conference & Exposition and Commercial Vehicle Engineering Congress 2013 (SIMCOMVEC), pp. 2013-01–2865. <https://doi.org/10.4271/2013-01-2865>
- Nishimura, R., Wada, T., Sugiyama, S., 2015. Haptic Shared Control in Steering Operation Based on Cooperative Status Between a Driver and a Driver Assistance System. *Journal of Human-Robot Interaction* 4, 19–37. <https://doi.org/10.5898/JHRI.4.3.Nishimura>
- Norfleet, D., Wagner, J., Alexander, K., Pidgeon, P., 2009. Automotive Driving Simulators: Research, Education, and Entertainment. *SAE Int. J. Passeng. Cars – Electron. Electr. Syst.* 2, 186–193. <https://doi.org/10.4271/2009-01-0533>
- Nozaki, H., Mizuno, K., Yoshino, T., 2012. Effect of Rear-Wheel Active Steering and Variable Steering Wheel Gear Ratio on Proportional Derivative Steering Assistance. Presented at the SAE 2012 Commercial Vehicle Engineering Congress, pp. 2012-01–1936. <https://doi.org/10.4271/2012-01-1936>
- On-Road Automated Driving (ORAD) committee, n.d. Taxonomy and Definitions for Terms Related to Driving Automation Systems for On-Road Motor Vehicles. SAE International. [https://doi.org/10.4271/J3016\\_201806](https://doi.org/10.4271/J3016_201806)
- Pedley, M., n.d. Tilt Sensing Using a Three-Axis Accelerometer 22.
- Penmetsa, P., Hudnall, M., Nambisan, S., 2019. Potential safety benefits of lane departure prevention technology. *IATSS Research* 43, 21–26. <https://doi.org/10.1016/j.iatssr.2018.08.002>
- Petermeijer, S.M., Abbink, D.A., Mulder, M., de Winter, J.C.F., 2015. The Effect of Haptic Support Systems on Driver Performance: A Literature Survey. *IEEE Trans. Haptics* 8, 467–479. <https://doi.org/10.1109/TOH.2015.2437871>
- Pohl, J., Ekmark, J., 2003. Development of a Haptic Intervention System for Unintended Lane Departure. Presented at the SAE 2003 World Congress & Exhibition, pp. 2003-01–0282. <https://doi.org/10.4271/2003-01-0282>

- Polling, D., Mulder, M., van Paassen, M.M., Chu, Q.P., 2005. Inferring the driver's lane change intention using context-based dynamic Bayesian networks, in: 2005 IEEE International Conference on Systems, Man and Cybernetics. Presented at the 2005 IEEE International Conference on Systems, Man and Cybernetics, IEEE, Waikoloa, HI, USA, pp. 853–858. <https://doi.org/10.1109/ICSMC.2005.1571253>
- Q8-USB Data Acquisition Device - Quanser [WWW Document], n.d. URL <https://www.quanser.com/products/q8-usb-data-acquisition-device/> (accessed 6.18.19).
- Rajamani, R., 2006a. Vehicle Dynamics and Control, 1st ed. Springer, USA.
- Rajamani, R., 2006b. Vehicle Dynamics and Control. Springer US, Boston, MA.
- Roadway Departure Safety - Safety | Federal Highway Administration [WWW Document], n.d. URL [https://safety.fhwa.dot.gov/roadway\\_dept/](https://safety.fhwa.dot.gov/roadway_dept/) (accessed 9.4.19).
- Robinson, G., Davies, J.B.C., 1999. Continuum robots - a state of the art, in: Proceedings 1999 IEEE International Conference on Robotics and Automation (Cat. No.99CH36288C). Presented at the International Conference on Robotics and Automation, IEEE, Detroit, MI, USA, pp. 2849–2854. <https://doi.org/10.1109/ROBOT.1999.774029>
- Rodríguez, J.-L., Velázquez, R., 2012. Haptic Rendering of Virtual Shapes with the Novint Falcon. *Procedia Technology* 3, 132–138. <https://doi.org/10.1016/j.protcy.2012.03.014>
- Saleh, L., Chevrel, P., Mars, F., Lafay, J.-F., Claveau, F., 2011. Human-like cybernetic driver model for lane keeping. *IFAC Proceedings Volumes* 44, 4368–4373. <https://doi.org/10.3182/20110828-6-IT-1002.02349>
- Salvucci, D.D., 2006. Modeling Driver Behavior in a Cognitive Architecture. *Hum Factors* 48, 362–380. <https://doi.org/10.1518/001872006777724417>
- Sentouh, C., Nguyen, A.-T., Floris, J., Popieul, J.-C., 2018. Multiple Controller Switching Concept for Human-Machine Shared Control of Lane Keeping Assist Systems, in: 2018 IEEE International Conference on Systems, Man, and Cybernetics (SMC). Presented at the 2018 IEEE International Conference on Systems, Man, and Cybernetics (SMC), IEEE, Miyazaki, Japan, pp. 2730–2735. <https://doi.org/10.1109/SMC.2018.00466>
- Setlur, P., Wagner, J., Dawson, D., Powers, L., 2003. A hardware-in-the-loop and virtual reality test environment for steer-by-wire system evaluations, in: Proceedings of the 2003 American Control Conference, 2003. Presented at the 2003 American Control Conference, IEEE, Denver, CO, USA, pp. 2584–2589. <https://doi.org/10.1109/ACC.2003.1243466>
- Setlur, P., Wagner, J.R., Dawson, D.M., Braganza, D., 2006. A Trajectory Tracking Steer-by-Wire Control System for Ground Vehicles. *IEEE Trans. Veh. Technol.* 55, 76–85. <https://doi.org/10.1109/TVT.2005.861189>

- Shakeri, G., Brewster, S.A., Williamson, J., Ng, A., 2016. Evaluating Haptic Feedback on a Steering Wheel in a Simulated Driving Scenario, in: Proceedings of the 2016 CHI Conference Extended Abstracts on Human Factors in Computing Systems - CHI EA '16. Presented at the the 2016 CHI Conference Extended Abstracts, ACM Press, Santa Clara, California, USA, pp. 1744–1751. <https://doi.org/10.1145/2851581.2892497>
- Shaw, G., Dalrymple, G., Ragland, C., 1999. Reducing the Risk of Driver Injury from Common Steering Control Devices in Frontal Collisions. Presented at the International Congress & Exposition, pp. 1999-01–0759. <https://doi.org/10.4271/1999-01-0759>
- Sheng Fu, Saeidi, H., Sand, E., Sadrfaidpour, B., Rodriguez, J., Yue Wang, Wagner, J., 2016. A haptic interface with adjustable feedback for unmanned aerial vehicles (UAVs) -model, control, and test, in: 2016 American Control Conference (ACC). Presented at the 2016 American Control Conference (ACC), pp. 467–472. <https://doi.org/10.1109/ACC.2016.7524958>
- Shimizu, Y., Kawai, T., Yuzuriha, J., 1999. Improvement in Driver-Vehicle System Performance by Varying Steering Gain with Vehicle Speed and Steering Angle: VGS (Variable Gear-Ratio Steering System). Presented at the International Congress & Exposition, pp. 1999-01–0395. <https://doi.org/10.4271/1999-01-0395>
- Siciliano, B., 1990. Kinematic control of redundant robot manipulators: A tutorial. *J Intell Robot Syst* 3, 201–212. <https://doi.org/10.1007/BF00126069>
- Simulink - Simulation and Model-Based Design [WWW Document], n.d. URL <https://www.mathworks.com/products/simulink.html> (accessed 6.18.19).
- Stanton, N.A., Young, M., McCaulder, B., 1997. Drive-by-wire: The case of driver workload and reclaiming control with adaptive cruise control. *Safety Science* 27, 149–159. [https://doi.org/10.1016/S0925-7535\(97\)00054-4](https://doi.org/10.1016/S0925-7535(97)00054-4)
- Tagne, G., Talj, R., Charara, A., 2016. Design and Comparison of Robust Nonlinear Controllers for the Lateral Dynamics of Intelligent Vehicles. *IEEE Trans. Intell. Transport. Syst.* 17, 796–809. <https://doi.org/10.1109/TITS.2015.2486815>
- Tang, Z., Heung, H.L., Tong, K.Y., Li, Z., 2019. A Novel Iterative Learning Model Predictive Control Method for Soft Bending Actuators, in: 2019 IEEE International Conference on Robotics and Automation (ICRA). Presented at the 2019 IEEE International Conference on Robotics and Automation (ICRA), IEEE, Montreal, Canada, pp. 4004–4010.
- Tatlcioglu, E., Walker, I.D., Dawson, D.M., 2007. Dynamic Modelling for Planar Extensible Continuum Robot Manipulators, in: Proceedings 2007 IEEE International Conference on Robotics and Automation. Presented at the Proceedings 2007 IEEE International Conference on Robotics and Automation, pp. 1357–1362. <https://doi.org/10.1109/ROBOT.2007.363173>
- Trivedi, D., Rahn, C.D., Kier, W.M., Walker, I.D., 2008. Soft robotics: Biological inspiration, state of the art, and future research. *Applied Bionics and Biomechanics* 5, 99–117. <https://doi.org/10.1080/11762320802557865>

- Utami, I.T., Sartono, B., Sadik, K., 2014. Comparison of Single and Ensemble Classifiers of Support Vector Machine and Classification Tree. *Journal of Mathematical Sciences and Applications* 2, 17–20. <https://doi.org/10.12691/jmsa-2-2-1>
- Vaddi, P.K.R., Vinjamuri, S., Cheruvu, K., 2014. Steer Assistance Control for Improved Vehicle Response. Presented at the SAE 2014 World Congress & Exhibition, pp. 2014-01–0109. <https://doi.org/10.4271/2014-01-0109>
- van Ginkel, J., 2014. Estimating the Tire-Road Friction Coefficient Based on Tire Force Measurements. Delft University of Technology, Delft, Netherland.
- Vepa, R., 2017. Nonlinear Control of Robots and Unmanned Aerial Vehicles An Integrated Approach, 1st ed. CRC Press.
- Walker, I.D., 2013. Continuous Backbone “Continuum” Robot Manipulators. *ISRN Robotics* 2013, 1–19. <https://doi.org/10.5402/2013/726506>
- Walker, I.D., Dawson, D.M., Flash, T., Grasso, F.W., Hanlon, R.T., Hochner, B., Kier, W.M., Pagano, C.C., Rahn, C.D., Zhang, Q.M., 2005. Continuum robot arms inspired by cephalopods, in: Gerhart, G.R., Shoemaker, C.M., Gage, D.W. (Eds.), . Presented at the Defense and Security, Orlando, Florida, USA, p. 303. <https://doi.org/10.1117/12.606201>
- Wang, C., Alexander, K., Pidgeon, P., Wagner, J., 2019a. Use of Cellphones as Alternative Driver Inputs in Passenger Vehicles. Presented at the WCX SAE World Congress Experience, pp. 2019-01–1239. <https://doi.org/10.4271/2019-01-1239>
- Wang, C., Wagner, J., Frazelle, C.G., Walker, I.D., 2018a. Continuum Robot Control Based on Virtual Discrete-Jointed Robot Models, in: IECON 2018 - 44th Annual Conference of the IEEE Industrial Electronics Society. Presented at the IECON 2018 - 44th Annual Conference of the IEEE Industrial Electronics Society, IEEE, D.C., DC, USA, pp. 2508–2515. <https://doi.org/10.1109/IECON.2018.8591387>
- Wang, C., Wang, Y., Wagner, J.R., 2019b. Evaluation of a Robust Haptic Interface for Semi-Autonomous Vehicles. *SAE Intl. J CAV* 2, 12-02-02–0007. <https://doi.org/10.4271/12-02-02-0007>
- Wang, C., Wang, Y., Wagner, J.R., 2018b. Evaluation of Alternative Steering Devices with Adjustable Haptic Feedback for Semi-Autonomous and Autonomous Vehicles. Presented at the WCX World Congress Experience, pp. 2018-01–0572. <https://doi.org/10.4271/2018-01-0572>
- Webster, R.J., Jones, B.A., 2010. Design and Kinematic Modeling of Constant Curvature Continuum Robots: A Review. *The International Journal of Robotics Research* 29, 1661–1683. <https://doi.org/10.1177/0278364910368147>
- Wong, J.Y., 2008. Theory of ground vehicles, 4th ed. ed. Wiley, Hoboken, N.J.
- World report on disability 2011 [WWW Document], n.d. URL <https://apps.who.int/iris/handle/10665/44575> (accessed 7.31.19).
- Wu, Y., Wang, L., Li, F., 2018. Research on Variable Steering Ratio Control Strategy of Steer-by-Wire System. Presented at the Intelligent and Connected Vehicles Symposium, pp. 2018-01–1583. <https://doi.org/10.4271/2018-01-1583>

- Xing, Y., Lv, C., Wang, Huaji, Wang, Hong, Ai, Y., Cao, D., Velenis, E., Wang, F.-Y., 2019. Driver Lane Change Intention Inference for Intelligent Vehicles: Framework, Survey, and Challenges. *IEEE Trans. Veh. Technol.* 68, 4377–4390. <https://doi.org/10.1109/TVT.2019.2903299>
- Xu, L., Wang, Y., Sun, H., Xin, J., Zheng, N., 2016. Integrated Longitudinal and Lateral Control for Kuafu-II Autonomous Vehicle. *IEEE Trans. Intell. Transport. Syst.* 17, 2032–2041. <https://doi.org/10.1109/TITS.2015.2498170>
- Zhang, N., Wang, M., 2005. Dynamic Modeling of Hydraulic Power Steering System with Variable Ratio Rack and Pinion Gear. *JSME Int. J., Ser. C* 48, 251–260. <https://doi.org/10.1299/jsmec.48.251>
- Zheng, H., Hu, J., Yang, S., 2016. Variable Steering Ratio Design for Vehicle Steer-by-Wire System with Joystick. Presented at the SAE 2016 World Congress and Exhibition, pp. 2016-01–0455. <https://doi.org/10.4271/2016-01-0455>